

# Università degli Studi di Bologna

---

---

FACOLTÀ DI SCIENZE MATEMATICHE, FISICHE E NATURALI

Dipartimento di Astronomia

## MULTIWAVELENGTH STUDY OF CLUSTER MERGERS AND CONSEQUENCES FOR THE RADIO EMISSION PROPERTIES OF GALAXY CLUSTERS

DOTTORATO DI RICERCA IN ASTRONOMIA

XIX CICLO – FIS/05

Coordinatore Chiar.mo Prof. LAURO MOSCARDINI

Tesi di Dottorato  
di:

**SIMONA GIACINTUCCI**

Relatore:  
Chiar.mo Prof.

**DANIELE DALLACASA**

Co-relatori:

Dr.ssa **TIZIANA VENTURI**

Dr. **SANDRO BARDELLI**

---

---



**QUESTA TESI E' STATA SVOLTA  
NELL'AMBITO DELLE ATTIVITA' DI RICERCA  
DELL' ISTITUTO DI RADIOASTRONOMIA  
DELL' ISTITUTO NAZIONALE DI ASTROFISICA  
(BOLOGNA)**



# Contents

<b>Abstract</b>	<b>1</b>
<b>1 Cluster mergers and non-thermal phenomena</b>	<b>5</b>
1.1 Cluster mergers . . . . .	6
1.1.1 Merger shock waves . . . . .	6
1.1.2 Turbulent gas motions . . . . .	9
1.2 Non-thermal properties of galaxy clusters . . . . .	10
1.3 General properties of cluster scale radio sources . . . . .	12
1.4 Radio halos . . . . .	13
1.5 Radio relics . . . . .	16
1.6 Non-thermal phenomena & cluster merger connection . . . . .	18
1.7 Thermal-non-thermal connection in radio halo clusters . . . . .	19
1.8 Origin of the radio emitting electrons in radio halos . . . . .	21
1.9 The re-acceleration scenario for radio halos . . . . .	23
1.9.1 Statistical calculations . . . . .	24
1.10 Models for the radio relic formation . . . . .	25
1.10.1 Shock acceleration . . . . .	26
1.10.2 Adiabatic compression . . . . .	27
1.11 Observational study of cluster mergers . . . . .	28
1.11.1 Multifrequency analysis of individual galaxy clusters . . . . .	29
1.12 The GMRT Radio Halo Survey . . . . .	30
<b>2 Cluster selection and observations</b>	<b>33</b>
2.1 The sample . . . . .	33
2.2 Radio observations . . . . .	34
2.3 The Giant Metrewave Radio Telescope . . . . .	35

2.4	GMRT observations and data reduction . . . . .	37
2.4.1	Recording . . . . .	37
2.4.2	Data editing . . . . .	38
2.4.3	Bandpass calibration . . . . .	38
2.4.4	Calibration and Imaging . . . . .	39
2.5	VLA observations and data reduction . . . . .	40
2.5.1	RXCJ2003.5–2323 . . . . .	40
2.5.2	A 521 . . . . .	41
2.6	X-ray data . . . . .	41
2.6.1	Chandra data reduction and analysis . . . . .	42
<b>3</b>	<b>The radio halo in Abell 3562</b>	<b>47</b>
3.1	The merging environment of A 3562 . . . . .	49
3.2	Radio analysis . . . . .	51
3.2.1	High resolution images . . . . .	52
3.2.2	Low resolution images . . . . .	53
3.2.3	General comments on the radio emission in A 3562 . . . . .	56
3.3	Spectral index images and integrated spectra . . . . .	57
3.3.1	Spectral properties of the radio halo . . . . .	57
3.3.2	Spectral properties of the head–tail radio galaxy J1333–3141 . . . . .	59
3.4	Origin of the radio halo . . . . .	60
3.4.1	Study of the integrated radio spectrum . . . . .	61
3.4.2	Origin of the radio emitting electrons . . . . .	62
3.5	X-ray versus radio analysis . . . . .	62
3.5.1	X–radio morphological comparison . . . . .	62
3.5.2	Point–to–point comparison . . . . .	65
3.6	Cluster merger and origin of the diffuse radio emission . . . . .	68
3.6.1	Self-consistency of re–acceleration . . . . .	69
3.6.2	Observational evidence . . . . .	70
3.6.3	The extent of the radio emission . . . . .	71
3.6.4	A radio bridge between the radio halo and J1332–3146a? . . . . .	72
3.7	Summary of the A 3562 analysis . . . . .	73

<b>4</b>	<b>The giant radio halo in A 209</b>	<b>77</b>
4.1	The merging environment of A 209 . . . . .	79
4.2	The giant radio halo . . . . .	81
4.2.1	GMRT 610 MHz observations . . . . .	81
4.3	X-ray Chandra Analysis . . . . .	86
4.3.1	Image analysis . . . . .	86
4.3.2	Spectral analysis . . . . .	87
4.4	Optical analysis . . . . .	92
4.5	Combined radio, optical and X-ray analysis . . . . .	95
4.5.1	Optical versus X-ray . . . . .	95
4.5.2	Radio vs X-ray . . . . .	96
4.6	The proposed merging scenario . . . . .	97
4.7	Origin of the radio halo . . . . .	99
<b>5</b>	<b>The giant radio halo in A 697</b>	<b>101</b>
5.1	The merging environment of A 697 . . . . .	102
5.2	The giant radio halo . . . . .	104
5.2.1	GMRT 610 MHz observations . . . . .	104
5.2.2	The morphology . . . . .	107
5.2.3	The radio spectrum . . . . .	109
5.2.4	Equipartition magnetic field . . . . .	109
5.3	X-ray Chandra analysis . . . . .	110
5.3.1	Image analysis . . . . .	110
5.3.2	Spectral analysis . . . . .	112
5.4	Optical analysis . . . . .	115
5.5	Combined radio, optical and X-ray analysis . . . . .	120
5.5.1	Optical versus X-ray . . . . .	120
5.5.2	Radio vs X-ray . . . . .	122
5.6	Multiple group accretion or cluster major merger? . . . . .	122
5.7	Origin of the radio halo . . . . .	126
<b>6</b>	<b>The radio relic in Abell 521</b>	<b>127</b>
6.1	Multiple merging events in A 521 . . . . .	128
6.2	Radio analysis . . . . .	131

6.2.1	GMRT observations at 610 MHz . . . . .	131
6.2.2	The radio morphology . . . . .	133
6.2.3	VLA observations at 4.9 and 8.4 GHz . . . . .	135
6.2.4	The radio relic . . . . .	136
6.2.5	The radio galaxy J0454–1016a . . . . .	136
6.3	Spectral analysis . . . . .	140
6.3.1	Integrated radio spectrum of the relic . . . . .	140
6.3.2	Integrated radio spectrum of J0454–1016a . . . . .	141
6.3.3	Spectral index image . . . . .	142
6.3.4	Equipartition magnetic field . . . . .	145
6.4	Origin of the radio relic . . . . .	145
6.5	Is there a shock in the external region of A 521? . . . . .	147
6.6	Summary and future perspectives . . . . .	149
<b>7</b>	<b>The giant radio halo in RXCJ 2003.5–2323</b>	<b>151</b>
7.1	Radio observations . . . . .	153
7.1.1	GMRT 610 MHz images . . . . .	153
7.1.2	VLA 1.4 GHz images . . . . .	155
7.2	Observational properties of the radio halo . . . . .	156
7.3	Polarisation properties of the halo . . . . .	159
7.4	The halo integrated spectrum and magnetic field . . . . .	159
7.5	Radio halo–cluster merger connection: is there a merger? . . . . .	160
7.6	Origin of the clumps and filaments . . . . .	162
7.7	Summary of the analysis of RXCJ2003.5–2323 . . . . .	163
<b>8</b>	<b>Multiple diffuse radio sources in RXCJ 1314.4–2515</b>	<b>165</b>
8.1	Evidence for a merger in RXCJ 1314.4–2525 . . . . .	166
8.2	GMRT 610 MHz observations . . . . .	167
8.3	The radio relics . . . . .	169
8.3.1	The morphology . . . . .	169
8.3.2	The integrated spectrum and magnetic field . . . . .	172
8.3.3	Origin of the relics . . . . .	172
8.4	The radio halo . . . . .	174
8.4.1	Origin of the radio halo . . . . .	177

8.5	Need for an energetic cluster merger . . . . .	178
8.6	Analysis of the cluster dynamics from archival data . . . . .	179
8.6.1	Optical analysis . . . . .	179
8.6.2	X-ray analysis . . . . .	180
8.7	Open issues and future observations . . . . .	181
<b>9</b>	<b>Final considerations and conclusions</b>	<b>183</b>
9.0.1	Summary of the observational results . . . . .	183
9.0.2	The $\text{Log}L_X\text{-Log}P_{1.4\text{GHz}}$ correlation for radio halos . . . . .	185
9.0.3	Diffuse radio sources and cluster merger dynamics . . . . .	186
9.0.4	Future perspectives . . . . .	188
	<b>Bibliography</b>	<b>191</b>



# Abstract

In the present thesis a thorough multiwavelength analysis of a number of galaxy clusters known to be experiencing a merger event is presented.

The bulk of the thesis consists in the analysis of deep radio observations of six merging clusters, which host extended radio emission on the cluster scale. A composite optical and X-ray analysis is performed in order to obtain a detailed and comprehensive picture of the cluster dynamics and possibly derive hints about the properties of the ongoing merger, such as the involved mass ratio, geometry and time scale. The combination of the high quality radio, optical and X-ray data allows us to investigate the implications of the ongoing merger for the cluster radio properties, focusing on the phenomenon of cluster scale diffuse radio sources, known as *radio halos* and *relics*.

A total number of six merging clusters was selected for the present study: **A 3562, A 697, A 209, A 521, RXCJ 1314.4–2515 and RXCJ 2003.5–2323**. All of them were known, or suspected, to possess extended radio emission on the cluster scale, in the form of a radio halo and/or a relic.

High sensitivity radio observations were carried out for all clusters using the Giant Metrewave Radio Telescope (GMRT) at low frequency (i.e.  $\leq 610$  MHz), in order to test the presence of a diffuse radio source and/or analyse in detail the properties of the hosted extended radio emission. For three clusters, the GMRT information was combined with higher frequency data from Very Large Array (VLA) observations. A re-analysis of the optical and X-ray data available in the public archives was carried out for all sources. Proprietary deep XMM-Newton and Chandra observations were used to investigate the merger dynamics in A 3562.

Thanks to our multiwavelength analysis, we were able to confirm the existence of a radio halo and/or a relic in all clusters, and to connect their properties and origin to the reconstructed merging scenario for most of the investigated cases.

- The existence of a small size and low power radio halo in A 3562 was successfully explained in the theoretical framework of the particle re-acceleration model for the origin of radio halos, which invokes the re-acceleration of pre-existing relativistic electrons in the intracluster medium by merger-driven turbulence.
- A giant radio halo was found in the massive galaxy cluster A 209, which has likely undergone a past major merger and is currently experiencing a new merging process in a direction roughly orthogonal to the old merger axis. A giant radio halo was also detected in A 697, whose optical and X-ray properties may be suggestive of a strong merger event along the line of sight. Given the cluster mass and the kind of merger, the existence of a giant radio halo in both clusters is expected in the framework of the re-acceleration scenario.
- A radio relic was detected at the outskirts of A 521, a highly dynamically disturbed cluster which is accreting a number of small mass concentrations. A possible explanation for its origin requires the presence of a merger-driven shock front at the location of the source. The spectral properties of the relic may support such interpretation and require a Mach number  $M \lesssim 3$  for the shock.
- The galaxy cluster RXCJ 1314.4–2515 is exceptional and unique in hosting two peripheral relic sources, extending on the Mpc scale, and a central small size radio halo. The existence of these sources requires the presence of an ongoing energetic merger. Our combined optical and X-ray investigation suggests that a strong merging process between two or more massive subclumps may be ongoing in this cluster. Thanks to forthcoming optical and X-ray observations, we will reconstruct in detail the merger dynamics and derive its energetics, to be related to the energy necessary for the particle re-acceleration in this cluster.
- Finally, RXCJ 2003.5–2323 was found to possess a giant radio halo. This source is among the largest, most powerful and most distant ( $z=0.317$ ) halos imaged so far. Unlike other radio halos, it shows a very peculiar morphology with

bright clumps and filaments of emission, whose origin might be related to the relatively high redshift of the hosting cluster. Although very little optical and X-ray information is available about the cluster dynamical stage, the results of our optical analysis suggest the presence of two massive substructures which may be interacting with the cluster. Forthcoming observations in the optical and X-ray bands will allow us to confirm the expected high merging activity in this cluster.

Throughout the present thesis a cosmology with  $H_0 = 70 \text{ km s}^{-1} \text{ Mpc}^{-1}$ ,  $\Omega_m=0.3$  and  $\Omega_\lambda=0.7$  is assumed.



# Chapter 1

## Cluster mergers and non-thermal phenomena

Galaxy clusters are the largest and most massive gravitationally bound blocks of the large scale structure of the Universe, with a total mass ranging from  $\sim 10^{14} M_{\odot}$  to  $\gtrsim 10^{15} M_{\odot}$ . They include from few hundreds to thousands of galaxies within a radius of the order of  $\sim 1\text{--}2$  Mpc (e.g. Abell 1958; Abell, Corwin & Olowin 1989). The volume between galaxies is totally filled with hot ( $\sim 10^7 - 10^8$  K) and rarefied gas (density  $\sim 10^{-4}\text{--}10^{-2}$  cm $^{-3}$ ), referred to as *intracluster medium* (ICM; see Molendi 2004 for a review), which emits at X-ray wavelengths through thermal Bremsstrahlung. Galaxies and gas account for only a little fraction of the total mass of a galaxy cluster ( $\sim 5\%$  and  $\sim 15\%$  respectively), which is mostly dominated by dark matter, whose distribution can be inferred thanks to its gravitational effects on the luminous matter (e.g. weak lensing; Bartelmann & Schneider 2001).

In the current picture of the large scale structure formation in the Universe, known as Cold Dark Matter (CDM) scenario, massive galaxy clusters are recognized to assemble and grow in a hierarchical way, through the gravitational accretion of smaller mass condensations, as galaxy groups and less massive clusters, and through the major merging with sub-clusters of similar mass. This picture is supported from both numerical and observational results, showing that galaxy clusters indeed form and evolve through merging processes at the nodes of the filamentary structure of the Universe (e.g. Katz & White 1993; Borgani et al. 2004; Durrett et al. 1998; Bardelli et al. 2000; Adami et al. 2005).

## 1.1 Cluster mergers

Cluster mergers are among the most spectacular and energetic phenomena in the Universe, and play a fundamental role in determining the observed structure and dynamical properties of massive galaxy clusters. The total kinetic energy released by the collision of two massive subclusters can reach and exceed a value of the order of  $\sim 10^{64}$  ergs (Markevitch, Sarazin & Vikhlinin 1999). Such huge amount of kinetic energy is mostly converted into thermal energy (on a typical time scale of  $\sim 1$  Gyr) by large scale hydrodynamical shock waves, driven in the gaseous atmosphere of the cluster (Sec. 1.1.1). Furthermore, it is expected that a fraction of the merger energy is dissipated also through large scale turbulent motions of the gas (Sec. 1.1.2).

### 1.1.1 Merger shock waves

Cluster mergers are expected to drive large scale gas motions with bulk velocities of the order of  $\sim 1000$ – $2000$  km s $^{-1}$  (e.g. Sarazin 2002). Such velocity is comparable to the expected sound speed of  $\sim 1000$ – $1500$  km s $^{-1}$  in the ICM. Hence the motions involved in mergers are moderately supersonic and consequently they lead to the formation of shock waves.

The expected Mach number of these shocks is  $M \equiv v_s/c_s \lesssim 3$ , where  $v_s$  is the shock velocity relative to the pre-shock gas and  $c_s = \sqrt{(5/3)P/\rho}$  is the sound speed in the pre-shock gas, being  $P$  and  $\rho$  its pressure and density respectively (e.g. Sarazin 2002). Shocks with higher Mach numbers might be driven in more peripheral regions of clusters, or in the gas of low mass and colder subclusters merging with massive clusters (provided that the subcluster is less dense than the main cluster).

The formation of shock waves with  $M \lesssim 3$  is also indicated by both the hydrodynamical simulations of cluster mergers (e.g. Schindler & Müller 1993; Roettiger, Stone & Burns 1999; Ricker & Sarazin 2001; Ryu et al. 2003; Pfrommer et al. 2006) and semi-analytical calculations (e.g. Gabici & Blasi 2003).

In Figure 1.1 we report an example of a numerical simulation of a cluster merger with different impact parameters (from Ricker & Sarazin 2001). The mass ratio between the colliding subclusters is 1:1. As clear from the first panels (on the left), at an early stage of the merger (i.e. before the first encounter between the cores), the region between the two subcluster centres is heated by two shocks which bound it on either side. In a more advanced stage, these shocks cross the subcluster centres

and move to the outer regions of the merging system (middle panels). Eventually, after a time of the order of  $\sim 3.5$  Gyr from the first core crossing, the subcluster cores start to oscillate (right panel) until the system has completely merged and the dynamical equilibrium is restored.

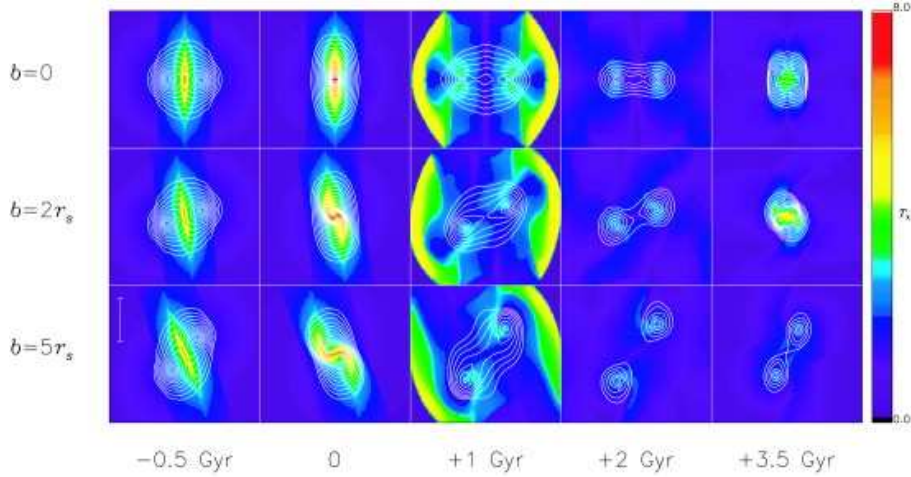


Figure 1.1: Hydrodynamical simulation of the 2–10 keV emission-weighted temperature distribution (colour map) and X-ray surface brightness (contours) of an 1:1 merger for different impact parameters  $b$  (from Ricker & Sarazin 2001). The colorbar gives the temperature scale in keV. For each panel,  $t = 0$  corresponds to the time at which the luminosity of the system reaches its maximum value.

As clear from the simulation in Figure 1.1, merger shock waves are responsible for irreversible changes in the intracluster medium. During their propagation, the shock fronts compress and heat the gas to temperatures up to several keV, and also increase its entropy. Furthermore, the heating and compression associated with merger shocks can produce a significant, temporary increase of the cluster X-ray luminosity up to a factor  $\sim 10$  (e.g. Ricker & Sarazin 2001; Randall, Sarazin & Ricker 2002; see also panel corresponding to  $t=0$  in Fig. 1.1).

Observationally, the detection of merger shock front is rare and rather difficult with the available X-ray instrumentation for a number of reasons. Merger shocks are characterised by low Mach numbers, and hence the associated gas density jump is expected to be relatively small. This implies that a shock could be detected only if it has not yet moved to the low surface brightness external regions of the cluster, where the background emission dominates and it becomes difficult to detect the expected density edge. However, even if the shock front is still well within the inner and brighter cluster region, it can be difficult to observe it because of the merger

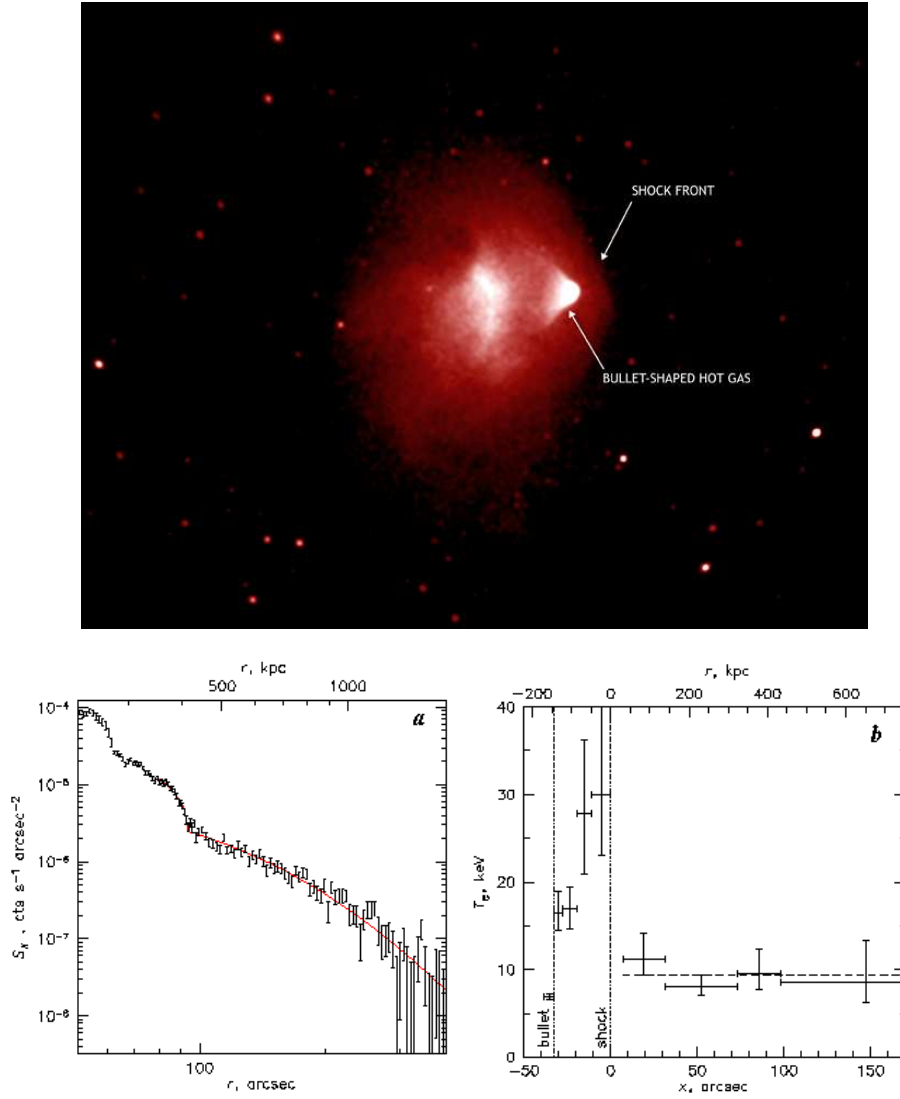


Figure 1.2: Shock front in 1E 0657–56. *Upper panel* – Chandra image of the cluster (Credit: NASA/CXC/CfA/M. Markevitch et al.) *Middle panel* – X–ray surface brightness profile across the shock. The solid line is best–fit model for the shock jump (from Markevitch 2006). *Lower panel* – X–ray projected temperature profile across the shock (from Markevitch 2006).

geometry, i.e. if the merger is not occurring on the plane of the sky. In this case the density and temperature edges could be smoothed by projection effects.

Regions with higher gas temperature and entropy with respect to the average cluster values have been detected in many merging clusters, and interpreted as evidence of shock heating (e.g. Henry & Briel 1995 & 1996; Markevitch, Sarazin & Irwin 1996; Markevitch & Vikhlinin 2001; Markevitch et al. 2003; Kempner & David 2004; Govoni et al. 2004). However, only two shock fronts, exhibiting both a clear

sharp gas density edge and an unambiguous temperature jump have been detected so far by the X-ray Chandra observatory, which provides the highest resolution X-ray imaging capability at present. Such shocks were found by Markevitch et al. (2002 & 2006) in the highly disturbed galaxy cluster 1E 0657–56 (also known as *bullet cluster*), and by Markevitch et al. (2005) in A 520. The impressive X-ray image of the bow shock in 1E 0657–56, and the clear jumps in the X-ray surface brightness and projected temperature profiles across the discontinuity are reported in Figure 1.2.

Merger shock fronts may have been found also in two other merging clusters, i.e. A 3667 (Vikhlinin, Markevitch & Murray 2001) and A 754 (Krivonos et al. 2003; Henry, Finoguenov & Briel 2004), but an obvious detection of a temperature discontinuity across the putative front is still missing.

### 1.1.2 Turbulent gas motions

It is expected that cluster mergers may excite a non-negligible amount of turbulent motions in the gas of the colliding subclusters. This idea is mainly supported by the results of numerical simulations of cluster mergers (e.g. Roettiger, Stone & Burns 1999; Ricker & Sarazin 2001; Takizawa 2005; Dolag et al. 2005; Vazza et al. 2006), which provide a detailed description of the gas dynamics in response to such high energetic events.

In particular, numerical simulations predict that the turbulent pressure in the ICM can account for up to  $\sim 20\text{--}35\%$  of the thermal pressure (e.g. Sunyaev, Norman & Bryan 2003; see also the recent analysis in Vazza et al. 2006), and similar estimates are also obtained from semi-analytical calculations (e.g. Cassano & Brunetti 2005, Vazza et al. 2006).

An image of a galaxy cluster simulation from Vazza et al. (2006) is reported in Figure 1.3. The cluster is undergoing a merging event with a less massive subcluster (mass ratio 1:10). The simulation shows that large scale turbulent eddies are injected in the intracluster medium by the infall of the subcluster (see also the simulations in Dolag et al. 2005). Such eddies dissipate a fraction of the merger energy through the whole cluster volume over a typical timescale of the order of  $\sim 1$  Gyr. The largest eddies decay with time into more random and turbulent velocity fields, and eventually a turbulent cascade is developed.

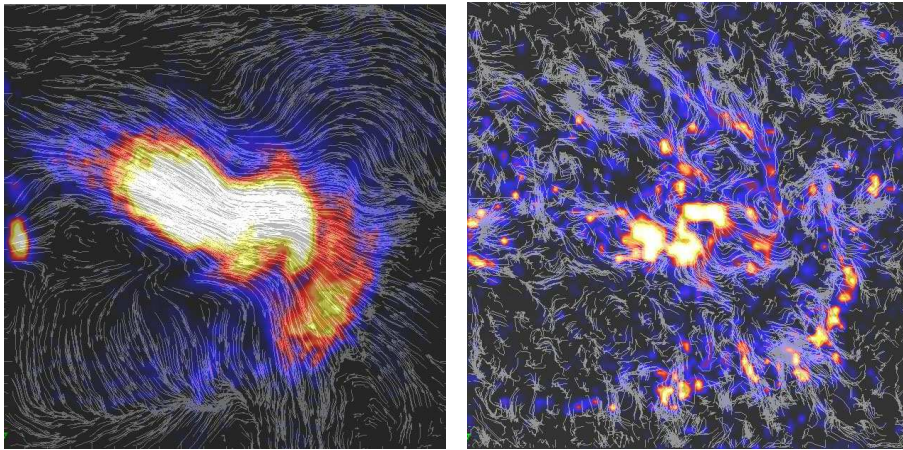


Figure 1.3: Bi-dimensional map of the central  $\sim (1.3 \text{ Mpc})^2$  of a simulation of a galaxy cluster from Vazza et al. (2006). A subcluster 10 times less massive is being accreted by the cluster (entering from the left). The streamlines on the left depict the velocity defined with respect to the centre of mass velocity; on the right they depict the local velocity residuals, after subtraction of the global mean bulk velocity of the cluster.

Unfortunately, the current instrumentation does not allow to directly probe and measure turbulence in galaxy clusters. The only instrument expected to be able to detect the turbulent broadening of the lines of heavy ions in excess of the thermal broadening (Inogamov & Sunyaev 2003) was the X-ray Spectrometer on board of the satellite Suzaku (ASTRO-E2), but a malfunction of the vacuum system caused the shutdown of that instrument.

On the other hand, few existing observational results might provide hints of the existence of turbulent motions in galaxy clusters. For example, signature of mildly supersonic turbulence may have been revealed by the spatially resolved pseudo-pressure image of the Coma cluster, obtained by Schuecker et al. (2004) from high sensitivity X-ray XMM-Newton observations. An indirect observational indication for turbulent motions in the Perseus cluster may come from the lack of resonant scatterings in this cluster (Churazov et al. 2003; Gastaldello & Molendi 2004).

## 1.2 Non-thermal properties of galaxy clusters

From a theoretical point of view, merger-driven shock waves and turbulence may play an important role in determining the non-thermal properties of the intracluster medium. Shocks may efficiently accelerate supra-thermal particles in the ICM up to relativistic energies, thus contributing to the injection of relativistic hadrons and

electrons in the cluster volume (e.g. Gabici & Blasi 2003; Ryu et al. 2003). Shocks and turbulence may also re-accelerate pre-existing relativistic particles mixed with the thermal ones within the ICM (e.g. the paper reviews Brunetti 2003 & 2004 and references therein).

The most striking and firm evidence for the existence of large scale non-thermal phenomena in galaxy clusters comes from the radio band. In addition to the individual radio sources associated with cluster galaxies, the radio observations reveal that a fraction of massive and X-ray luminous clusters host spectacular diffuse radio sources, which extend on the cluster scale and whose synchrotron emission arises directly within the ICM (see Sec. 1.3). These extended sources, referred to as *radio halos* (Sec. 1.4) and *relics* (Sec. 1.5), probe the existence of widespread relativistic electrons and large scale magnetic fields in galaxy clusters.

Evidence for relativistic electrons in the intracluster medium may also be supported by the hard X-ray (HXR) excess emission possibly detected in few galaxy clusters (e.g. Coma, Fusco-Femiano et al. 1999, 2004, Rephaeli & Gruber 2002; A2256, Fusco-Femiano et al. 2000, 2005; Rephaeli & Gruber 2003), thanks to the sensitivity and wide spectral coverage of the Beppo-SAX and Rossi X-ray Timing Explorer (RXTE) X-ray satellites. This phenomenon consists of an excess of emission in the hard region of the X-ray band (i.e.  $\gtrsim 10$  keV) with respect to the high energy extrapolation of the thermal emission at lower energies, which is due to the thermal Bremsstrahlung from the ICM.

The most likely interpretation of the non-thermal HXR emission is Inverse Compton (IC) radiation from high energy relativistic electrons, scattering the photons of the cosmic microwave background (CMB; e.g. Fusco-Femiano et al. 2003). Since all clusters with a possible HXR excess detection also host a radio halo, it is expected that these particles may be the same relativistic electrons responsible for the diffuse synchrotron emission (see Sec. 1.8).

The existence of the HXR excess in galaxy clusters is still matter of debate (e.g. Rossetti & Molendi 2004; Fusco-Femiano, Landi & Orlandini 2007). If definitely confirmed (e.g. from Suzaku observations or future X-ray observatories such as NEXT), the HXR excess may represent an important tool to unambiguously determine the amount of the ICM energy in the form of relativistic electrons and magnetic field.

### 1.3 General properties of cluster scale radio sources

Cluster scale diffuse radio sources are large regions of emission, which extend on a scale of several hundreds of kpc, but can reach and exceed the Mpc scale. Such emission is classified as *radio halo* and *relic* according to the source overall morphology and location within the cluster region. In particular, radio halos show a roughly regular structure and are typically observed at the cluster centre (see Sec. 1.3), while relics are characterised by a more irregular morphology and peripheral location (see Sec. 1.5).

The origin of these extended radio sources can not be obviously attributed to an individual optical galaxy, neither can be explained as the integrated contribution from a number of unresolved discrete radio galaxies. Such diffuse emission must therefore originate within the intracluster medium (e.g. Kempner & Sarazin 2001; the review paper by Feretti 2003 and references therein).

The integrated radio spectrum of halos and relics usually shows a power law shape with a steep spectral index, i.e.  $\alpha \gtrsim 1$ , assuming that the radio flux density is  $S(\nu) \propto \nu^{-\alpha}$ . This clearly implies a non-thermal origin for the emission, which is attributed to synchrotron radiation from relativistic electrons with energies of the order of GeV. These electrons must coexist with the thermal particles within the ICM, and require to be accelerated in large scale magnetic fields.

The energy density and magnetic field strength associated with halos and relics are usually estimated using the standard equipartition assumption e.g. Pacholczyk, 1970). The typical value of the minimum energy density in these sources is of the order of  $\sim 10^{-14}$ – $10^{-13}$  erg cm<sup>-3</sup>, and the corresponding equipartition magnetic field is in the range 0.1–1  $\mu$ G (e.g. Govoni & Feretti 2004). Magnetic field intensities  $\sim 2$ – $5$  times higher are obtained if the contribution of low energy electrons is taken into account in the calculation, by adopting a low energy cut-off in the electron spectrum instead of a low-frequency cut-off in the emitted one (e.g. Brunetti, Setti & Comastri 1997)

Both radio halos and relics are characterised by very low surface brightness, with values of the order of  $\simeq 1 \mu$ Jy arcsec<sup>-2</sup> at 1.4 GHz. Given such low surface brightness, combined with their large extent and steep spectra, the detection and study of these sources can be difficult. In order to detect and properly image the whole extended emission associated with halos and relics, high sensitivity, low angular resolution

(i.e. many tens of arcsec) and low frequency data ( $\nu \leq 1.4$  GHz) are required. On the other hand, radio images with an angular resolution of the order of few arcsec are also needed to discriminate between real diffuse emission and the blend of discrete radio galaxies. Hence it is important to combine the information from low-resolution observations with high resolution images from interferometric data, with high sensitivity to extended structures, as for example the Giant Metrewave Radio Telescope (GMRT; Sec. 2.3) and the Very Large Array (VLA).

Since the detection of the first radio halo in the Coma cluster (referred to as Coma C; Wilson et al. 1970), the number of discovered cluster radio halos and relics has significantly increased in the last 30 years, especially thanks to the better sensitivity of modern radio telescopes and the combination of single dish and interferometric information. At present a total of about 20 radio halos have been detected (Giovannini, Tordi & Feretti 1999; Kempner & Sarazin 2001; Giovannini & Feretti 2002; Bacchi et al. 2003; Venturi et al. 2007), and  $\sim 20$  relics (including candidates) are known (Kempner & Sarazin 2001; Giovannini & Feretti 2004; Venturi et al. 2007). These numbers indicate that these sources are relatively rare.

## 1.4 Radio halos

Radio halos are observed in the central regions of galaxy clusters. They usually show a fairly regular morphology, with a radio surface brightness distribution which is peaked at the cluster centre and smoothly decreases towards the cluster periphery.

Their largest linear size (LLS) ranges from few hundreds of kpc up to and well beyond the Mpc scale. The sources with  $LLS \gtrsim 700$  kpc are referred to as *giant* radio halos (GHR), according to the definition in Cassano & Brunetti (2005; scaling for the different cosmology adopted in the present work). The prototype of the class of giant radio halos is Coma C in the Coma cluster (Wilson et al. 1970; Schlickeiser, Sievers & Thiemann 1987; Kim et al. 1990; Giovannini et al. 1993; Deiss et al. 1997; Thierbach, Klein & Wielebinski 2003), which has a largest linear size of  $\sim 800$  kpc. The 327 MHz image of this source is reported in Figure 1.4 (left panel).

In Figure 1.5 we report the radio images of three other examples of giant radio halos, overlaid on the X-ray Chandra images of the hosting clusters. All sources have a LLS considerably greater than 1 Mpc. For comparison in Figure 1.6 we report the VLA 1.4 GHz images of the small size radio halos in A 2218 ( $LLS \sim 380$  kpc;

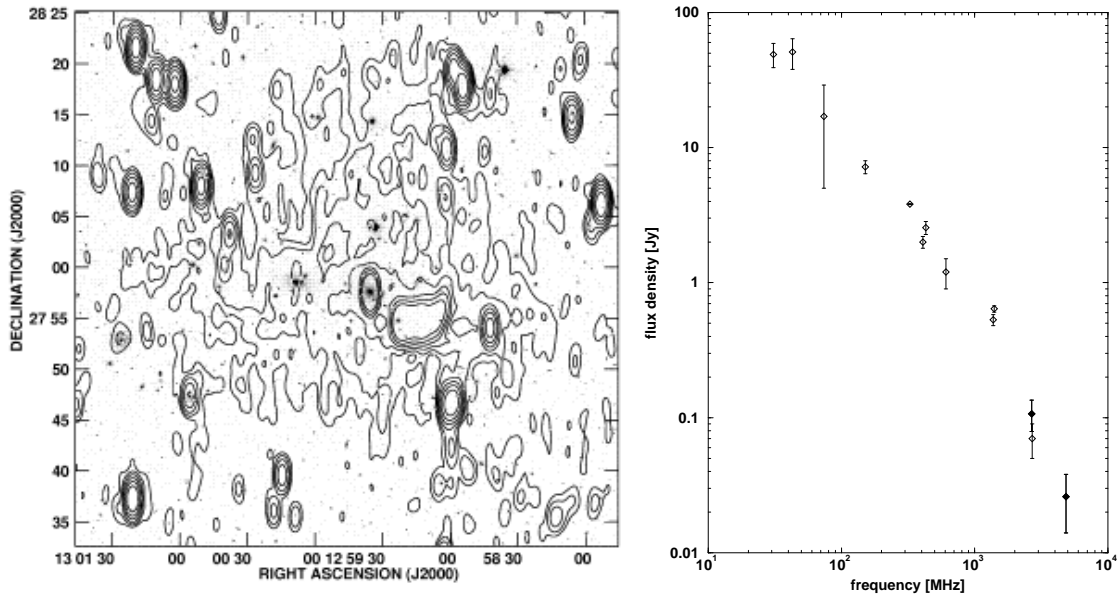


Figure 1.4: *Left panel* – 327 MHz contours of the giant radio halo in the Coma cluster, superposed to the optical image (from Feretti et al. 2004). The resolution of the radio image is  $55'' \times 125''$ . Contour levels are 3, 6, 12, 25, 50, 100 mJy b<sup>-1</sup>. *Right panel* – Integrated radio spectrum of Coma C between 30.9 MHz and 4.9 GHz (from Thierbach, Klein & Wielebinski 2003).

Giovannini & Feretti 2000, Govoni et al. 2004) and A 3562 (LLS $\sim$  470 Kpc; Venturi et al. 2003; also analysed in the present work in Chapter 3). As clear from Figure 1.5, GRHs typically cover a region which is significantly larger than the core region of the hosting cluster, while smaller radio halos (Fig. 1.6) extend on a scale which is comparable or only slightly larger than the cluster core radius.

The integrated radio spectrum of halos is that typical of aged radio sources, i.e. steep with a  $\alpha \gtrsim 1$ , with average values of the order of  $\alpha \sim 1.2$ – $1.3$  (see for example the spectrum of the Coma cluster radio halo reported in the right panel of Figure 1.4). In the most cases with adequate frequency coverage, a spectral steepening at high frequency is reported (e.g. Coma C in the right panel of Fig. 1.4, Thierbach, Klein & Wielebinski 2003; A 754, Bacchi et al. 2003; A 1914, Komissarov & Gubanov 1994; A 2319, Feretti, Giovannini & Böhringer 1997; see also A 3562 in Chapter 3).

The analysis of the spectral index distribution in few well-studied radio halos revealed the presence of inhomogeneities on small scales, which may reflect the complex form of the energy distribution of the radio emitting particles in these

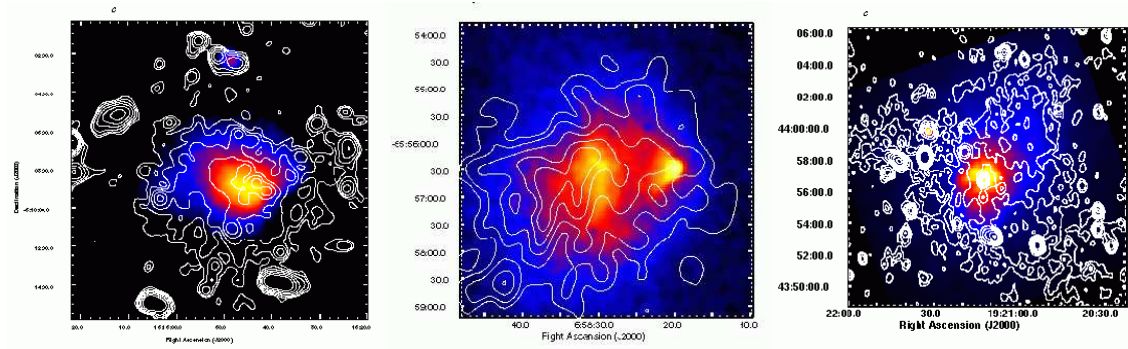


Figure 1.5: Radio contours of the giant radio halos in A 2163 (LLS  $\sim 1.9$  Mpc; left), 1E 0657-56 (LLS  $\sim 1.4$  Mpc; centre) and A 2319 (LLS  $\sim 1$  Mpc; right), superposed to the cluster X-ray Chandra image (from Govoni et al. 2004). *Left panel* – The radio image is at 1.4 GHz (VLA) and has a resolution of  $30'' \times 30''$ . Contour levels are spaced by a factor 2, starting from  $0.1 \text{ mJy b}^{-1}$ . *Central panel* – The radio image is at 1.3 GHz (ATCA; Liang et al. 2000) and has a resolution of  $24'' \times 22''$ . Contour levels are spaced by a factor 2, starting from  $2.7 \text{ mJy b}^{-1}$ . *Right panel* – The radio image is at 1.4 GHz (VLA) and has a resolution of  $29'' \times 20''$ . Contour levels are spaced by a factor 2, starting from  $0.1 \text{ mJy b}^{-1}$ .

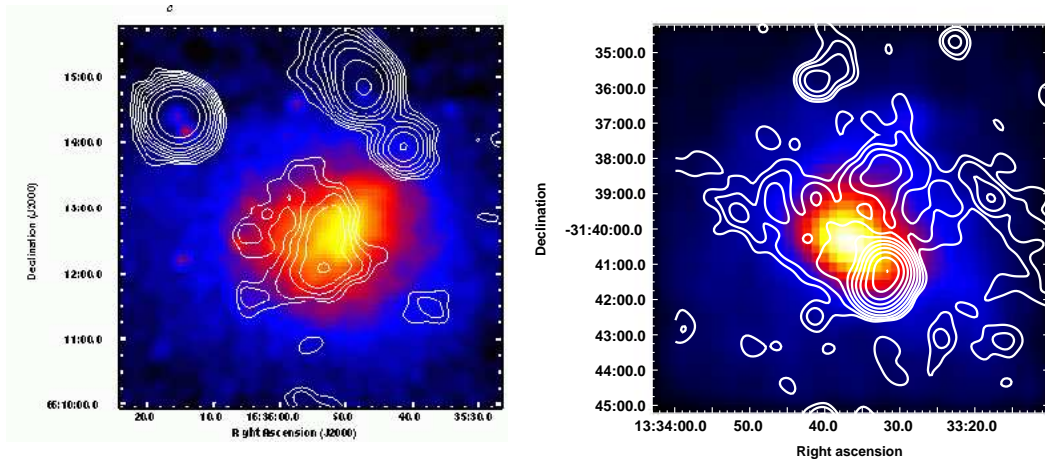


Figure 1.6: *Left panel* – VLA 1.4 GHz contours of the radio halo in A 2218 (LLS  $\sim 380$  kpc), on the cluster X-ray Chandra image (from Govoni et al. 2004). The resolution of the radio image is  $35'' \times 35''$ . Contour levels are spaced by a factor 2, starting from  $0.24 \text{ mJy b}^{-1}$ . *Right panel* – VLA-1.4 GHz contours of the radio halo in A 3562 (LLS  $\sim 470$  kpc; Venturi et al. 2003), on the cluster X-ray ROSAT image. The resolution of the radio image is  $42'' \times 35''$ . Contour levels are spaced by a factor 2, starting from  $0.12 \text{ mJy b}^{-1}$  (see also Chapter 3).

sources (e.g. A 665 and A 2163, Feretti et al. 2004; A 2256, Clarke & Enßlin 2006; A 2744 and A 2219, Orrú et al. 2007; see also A 3562 in Chapter 3).

The emission from radio halos is characterized by a low or negligible polarisation,

with upper limits for the fractional polarisation  $< 5 - 10\%$  (e.g.  $\sim 10\%$  in Coma, Giovannini et al. 1993;  $\sim 6.5\%$  in A 2219, Feretti et al. 2001;  $\sim 4\%$  in A 2163, Bacchi et al. 2003). Recently, high sensitivity VLA observations at 1.4 GHz of A 2255 led to the first detection of significant polarisation in a radio halo (Govoni et al. 2005). This source shows a very complex and filamentary structure, with the brightest filaments strongly polarised at levels of  $\sim 20 - 40\%$ , while the upper limit to the fractional polarisation in the fainter regions of the halo was estimated to be  $\lesssim 15\%$ .

## 1.5 Radio relics

Radio relics are similar to halos in their low surface brightness, large ( $\sim$  Mpc) size and steep spectrum. However, they are usually found at the outskirts of the cluster X-ray emission, and typically exhibit an irregular and highly elongated morphology, with a variety of structures (such as sheet, arc, and toroid) and sharp emission edges.

The prototype of the class of cluster radio relics is 1253+275 in the Coma cluster (Ballarati et al. 1981; Giovannini, Feretti & Stanghellini 1991; Thierbach, Klein & Wielebinski 2003; also reported in the left panel of Fig. 1.7).

Impressive cases of double radio relics, extending on both sides of the cluster X-ray emission and almost symmetrically located with respect to the cluster centre, have been observed in A 3667 (Rottgering et al. 1997; Roettiger, Burns & Stone 1999; Johnston-Hollitt, Ekers & Hunstead 2001) and A 3376 (Bagchi et al. 2005 & 2006), also reported in the left panel of Figure 1.8.

Clusters hosting both a central radio halo and a peripheral relic are also known, as for example Coma (Giovannini et al. 1993) and A 2256 (Bridle & Fomalont 1976; Clarke & Enßlin 2006), whose 1.4 GHz image on the cluster Chandra X-ray emission is reported in the right panel of Figure 1.8. Up to date, the unique galaxy cluster in which two relic sources and one radio halo have been detected is RXCJ 1314.4–2515 (Feretti et al. 2005; Venturi et al. 2007; also analysed in the present work in Chapter 8).

Unfortunately, the available data and detailed knowledge of the physical properties of radio relics are still poor, and the number of well studied sources is limited. Integrated radio spectra over a wide range of frequencies are available for few relics only. One of the relics with accurate flux density measurements at

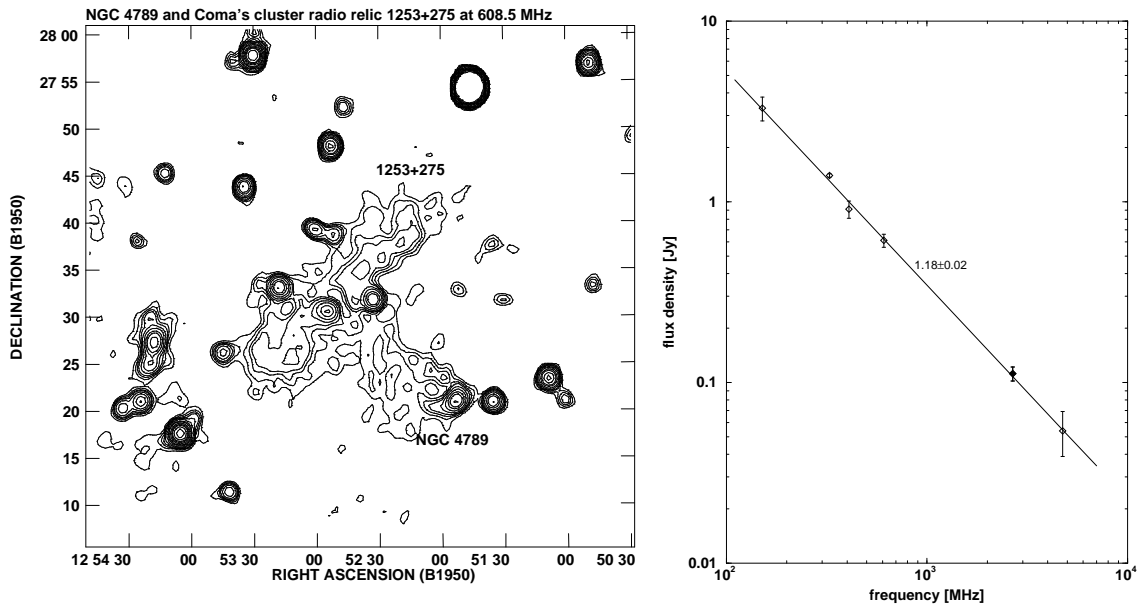


Figure 1.7: *Left panel* – 608 MHz image of the radio relic 1253+275 in the Coma cluster (from Giovannini, Feretti & Stanghellini 1991) and the nearby narrow angle tail radio galaxy NGC 4789. *Right panel* – Integrated radio continuum spectrum of 1253+275 between 151 MHz and 4.75 GHz. The solid line is the best power-law fit to the data and has  $\alpha=1.18\pm 0.02$  (reproduced from Thierbach, Klein & Wielebinski 2003).

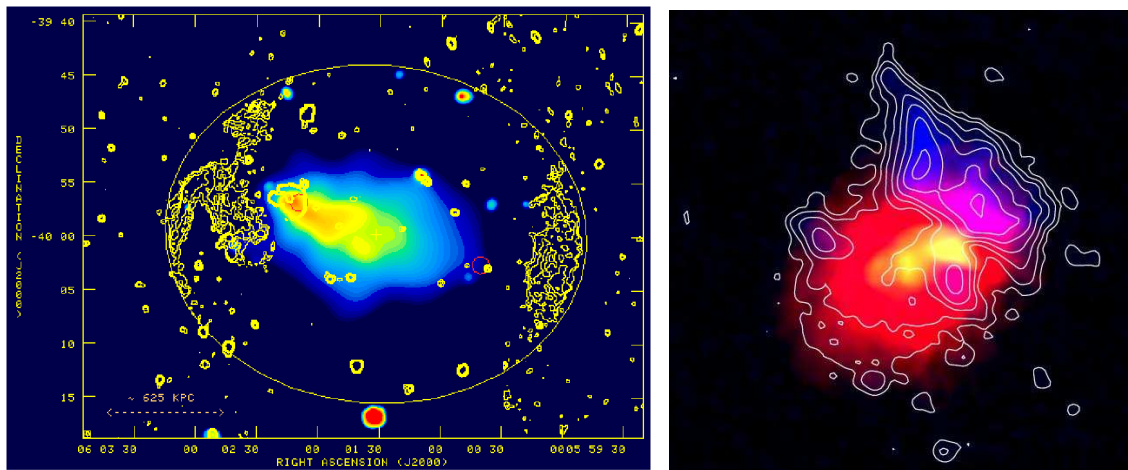


Figure 1.8: *Left panel* – VLA 4 GHz image of the radio relics (yellow contours; resolution  $20''$ ) in A 3376, on the ROSAT PSPC image (from Bagchi et al. 2006). *Right panel* – VLA 1.4 GHz image of the radio relic and halo (white contours; resolution  $80''$ ) in A 2256, on the X-ray Chandra image (from Clarke & Enßlin 2006).

many different frequencies is 1253+275 in the Coma cluster (Thierbach, Klein & Wielebinski 2003). As clear from the right panel of Figure 1.7, the total spectrum

of this source is well fitted by a power law with  $\alpha \sim 1.2$  extending on about two orders of magnitude in frequency (Thierbach, Klein & Wielebinski 2003).

Unlike radio halos (Sec. 1.4), no steepening at high frequency is observed in the spectrum of this relic. However, given the lack of multifrequency radio information for most relics, it is not possible to determine whether the absence of a high frequency steepening is a common feature within this class of radio sources.

The few images of the spectral index distribution in relics reported in the literature (e.g. A 3667, Rottgering et al. 1997; 1235+275, Giovannini et al. 1991; A 2256, Clarke & Enßlin 2006; A 2744, Orrú et al. 2007; see also A 521 in Chapter 6) show indication of a spectral steepening along the source minor axis, with the flattest spectrum in the more external side of the relic with respect to the cluster centre.

Finally, the radio emission from relics is usually highly polarised, with typical linear polarisation up to  $\sim 25 - 30\%$  at 1.4 GHz (e.g. 1253+275, Thierbach, Klein & Wielebinski 2003). Higher polarisation levels were found in the A 2256 relic, where a linear polarization fraction up to 45% was detected at 1.4 GHz, with an average polarisation of  $\sim 20\%$  across the source (Clarke & Enßlin 2006).

## 1.6 Non-thermal phenomena & cluster merger connection

The observational evidence points to a tight connection between cluster mergers and radio halos and relics. So far, these sources have been detected only in X-ray luminous galaxy clusters which manifest clear signature of ongoing or recent merging activity.

In particular the clusters hosting a radio halo and/or a relic usually exhibit substructures in the spatial and velocity distributions of optical galaxies, as well as substructures and distortions in the X-ray brightness distribution (Schuecker et al. 2001). They often show temperature gradients and shock heated regions (e.g. Markevitch et al. 1998; Markevitch & Vikhlinin 2001). An anticorrelation with the presence of a dense cool core is observed (e.g. Feretti 1999), further indication that the cluster has undergone a recent merger event, as strong mergers are expected to disrupt the cool core, as shown for example by the simulations in Gómez et al. (2002). Furthermore, as pointed out by Buote (2001), these clusters possess large values of the dipole power ratio, which indicate high dynamical disturbance and

departure from the equilibrium.

Although not all merging clusters host a diffuse radio source, there is still no evidence of any radio halo or relic in a cluster where the presence of a merger can be firmly excluded.

## 1.7 Thermal–non–thermal connection in radio halo clusters

A connection between the properties of radio halos and the thermal properties of the hosting clusters seems supported by a number of observational results.

- By inspecting the 1.4 GHz NRAO VLA Sky Survey (NVSS; Condon et al. 1998), Giovannini, Tordi & Feretti (1999) found that  $\simeq 5\%$  of the galaxy clusters in a complete X–ray flux–limited sample at  $z \leq 0.2$  (extracted from Ebeling et al. 1996) possess a diffuse halo source. The halo fraction increases with the X–ray luminosity of the hosting cluster, up to  $\sim 30\text{--}35\%$  for clusters with X–ray luminosity larger than  $10^{45}$  erg s $^{-1}$  (Giovannini & Feretti 2002). This suggests a preferential location of radio halos in X–ray luminous clusters, which are also characterised by high temperature ( $kT \gtrsim 7$  keV) and large mass ( $\gtrsim 10^{15} M_{\odot}$ ).
- It has been found that the 1.4 GHz radio power of halos correlates with the cluster X–ray luminosity (Colafrancesco et al. 1999; Bacchi et al. 2003), as well as with the temperature of the thermal gas (Liang et al. 2000), and the total cluster mass (Govoni et al. 2001a).

In Figure 1.9 we report the  $\text{Log}L_X\text{--}\text{Log}P_{1.4\text{GHz}}$  diagram for all galaxy clusters known to host a radio halo, regardless of their size<sup>1</sup> (see Cassano, Brunetti and Setti 2006, and references therein). The clusters with a detected giant radio halo (i.e. with  $\text{LLS} \gtrsim 700$  kpc, see Sec. 1.4) are reported as black circles. The filled ones are the clusters at redshift  $z > 0.2$ , the empty circles are those at  $z < 0.2$ . The cluster hosting a radio halo with  $\text{LLS} < 700$  kpc are shown as triangles. The black ones represent A 2218 ( $z=0.176$ ; Giovannini & Feretti 2000) and A 401 ( $z=0.0737$ ; Bacchi et al. 2003), while the red triangle is A 3562

---

<sup>1</sup>We do not include the clusters hosting the so–called *mini–halos*, as for example A 2390 (Bacchi et al. 2003) and Perseus (Gitti, Brunetti & Setti 2002). Unlike radio halos, these sources are thought to be associated with cool core clusters with no evidence for ongoing merging processes (e.g. Tribble 1993; Sijbring 1993; Gitti, Brunetti & Setti 2002).

( $z=0.048$ ; Venturi et al. 2003; also studied in the present work in Chapter 3). The solid line is the best-fit of the correlation found for giant radio halos by Cassano, Brunetti & Setti (2006), which can be expressed as:

$$\log \left( \frac{P_{1.4\text{GHz}}}{3.16 \times 10^{24} h_{70}^{-1} \text{W Hz}^{-1}} \right) = A_f + B_f \log \left( \frac{L_{X[0.1-2.4\text{keV}]}}{10^{45} h_{70}^{-1} \text{erg s}^{-1}} \right) \quad (1.1)$$

where  $A_f = 0.159 \pm 0.060$  and  $B_f = 1.97 \pm 0.25$ .

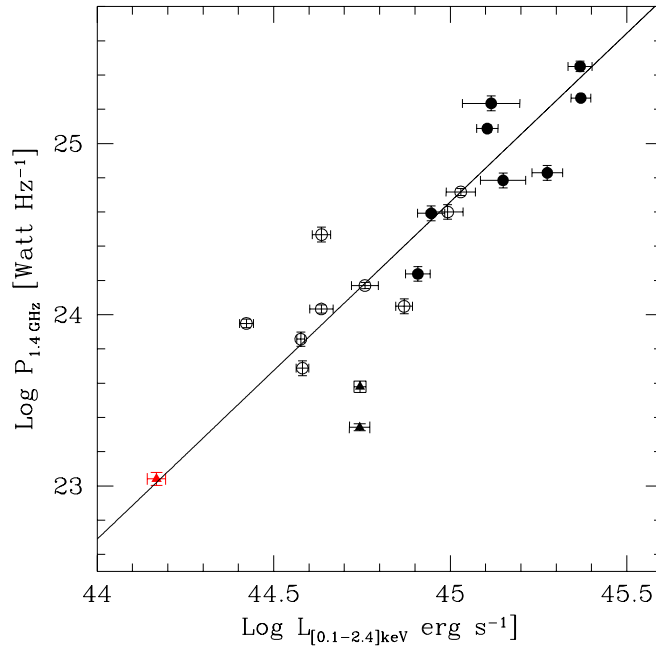


Figure 1.9:  $\text{Log}L_X\text{--}\text{Log}P_{1.4\text{GHz}}$  diagram for all clusters with detected radio halos. Empty and filled black circles are the giant radio halos at  $z < 0.2$  and  $z > 0.2$  respectively. Black triangles are the radio halos in A 2218 (Giovannini & Feretti 2000) and A 401 (Bacchi et al. 2003). The red triangle is A 3562 (Venturi et al. 2003; Chapter 3). The solid line is the best-fit correlation found for giant radio halos by Cassano, Brunetti & Setti (2006).

As clear from Figure 1.9, the most powerful radio halos are found in clusters with the highest X-ray luminosity, which are also the most distant.

- A spatial correlation is observed between the radio brightness of the halo source and the X-ray brightness of the parent cluster, as detected by X-ray ROSAT (Govoni et al. 2001b) and Chandra observations (Kempner and David 2004; Govoni et al. 2004).

## 1.8 Origin of the radio emitting electrons in radio halos

The large linear size of cluster radio halos poses the question of their origin, since the diffusion time the relativistic electrons need to cover the observed size of such sources is  $\sim 30$ – $100$  times longer than their radiative ages. This is known as the *diffusion problem* and was first pointed out by Jaffe (1977).

The radiative lifetime of a population of relativistic electrons losing energy through synchrotron radiation and IC scattering of the CMB photons is given by

$$\tau(\text{yr}) = \frac{24.5}{(B^2 + B_{\text{CMB}}^2)\gamma} \quad (1.2)$$

where  $B$  is the magnetic field intensity (in G),  $\gamma$  is the electron Lorentz factor, and  $B_{\text{CMB}} = 3.18(1 + z^2) \mu\text{G}$  is the magnetic field equivalent to the CMB.

In the ICM, the typical aging time scale of the relativistic electrons is relatively short ( $\sim 10^7$ – $10^8$  years; e.g. Sarazin 1999), while their expected diffusion velocity is of the order of the Alfvén speed ( $\sim 100 \text{ km s}^{-1}$ ). Hence it is plausible that electrons may not be able to diffuse over a region of  $\gtrsim 10$ – $50$  kpc size within their radiative lifetime.

This implies that, in order to justify the presence of cluster scale diffuse radio emission, a mechanism of particle acceleration is required, whose efficiency must be comparable to the energy loss processes (e.g. Petrosian 2001, Brunetti et al. 2001 and references therein).

Many theoretical possibilities have been investigated to explain the origin of the relativistic electrons responsible for the diffuse radio halos in galaxy clusters. They can be divided into two main classes: i) *primary models* and ii) *secondary models*.

### i) Primary models

As first proposed by Jaffe (1977) and Roland (1981), relativistic particles may be injected in the intracluster medium by a variety of processes which are active during the life of a cluster, as for example the Active Galactic Nucleus (AGN) activity in radio galaxies, star formation, supernovae and galactic winds. Furthermore, ultra-relativistic electrons (i.e. with  $\gamma > 10^3$ ) may be injected by merger shocks (Sarazin 1999), or continuously accelerated *in-situ* by turbulence (Schlickeiser, Sievers & Thiemann 1987). An alternative possibility is that pre-existing relativistic

electrons (with  $\gamma \gtrsim 10\text{--}100$ ) might be re-accelerated by merger-driven turbulence (*re-acceleration scenario*), as first proposed by Petrosian (2001) and Brunetti et al. (2001).

## ii) Secondary models

In this class of models, first proposed by Dennison (1980), the radio emitting electrons are continuously injected in the cluster volume as secondary products of the hadronic interactions of cosmic rays in the ICM (see also Colafrancesco & Blasi 1998; Dolag & Enßlin 2000). The inelastic proton-proton collisions may produce charged pions, which in turn decay and inject electrons and positrons in the ICM. Since the relativistic protons have a mean radiative lifetime which is of the order of the Hubble time, the large extent of the radio halo emission may be explained in the framework of these models, without invoking any (re-)acceleration mechanism.

Although the origin of the emitting particles responsible for cluster scale radio halos is still a matter of debate (e.g. Enßlin 2004), the above two models predict a number of observational properties for the radio halo emission and for the hosting cluster, which may be exploited to discriminate among the models by comparing their predictions with the observations.

On the basis of the current radio data, a firm conclusion can not be derived yet. However, the properties of few well-studied radio halo clusters seem to support the presence of *in-situ* particle re-acceleration mechanisms in the ICM (e.g. Brunetti 2003 & 2004; Blasi 2004; Feretti et al. 2004; Hwang 2004; Reimer et al. 2004).

In particular, the main observational evidence for *in-situ* particle re-acceleration can be summarised as follows:

- i) *linear size* – the large extent of radio halos implies that these sources may not be powered by merger shock waves (Sec. 1.1.1), since the shock-accelerated electrons have a short path-length due to the IC losses, and can travel only a short distance from the front, emitting synchrotron radiation just around the shock rim (e.g. Miniati et al. 2001). Shock acceleration may be responsible for the origin of radio relics, as discussed in Section 1.10;
- ii) *radial radio profile* – the radial synchrotron profiles of giant radio halos are found to be broader than the profiles of the X-ray emission from the hot

intracluster medium (e.g. Govoni et al. 2001b). This implies that the spatial distribution of relativistic electrons is broader than that of the thermal particles, and hence provides important constraints to the secondary models.

In particular, if central  $\mu\text{G}$  magnetic fields and a relatively rapid decrease of the field strength going outward are assumed (as expected on the basis of theoretical arguments; e.g. Dolag, Bartelmann & Lesch 2002), the secondary models require a very high density of relativistic hadrons in the cluster outskirts (e.g. Brunetti 2003). This is due to the fact that the production rate of secondary particles depends on the density of the thermal gas. Hence, higher magnetic fields in the core region and a less steep radial decline of its intensity would be required to explain the observed profiles (Pfrommer & Enßlin 2004);

- iii) *synchrotron spectra* – the integrated radio spectrum of few well-studied radio halos shows a high frequency steepening (e.g. right panel of Fig. 1.7; Giovannini et al. 1993; Thierbach, Klein & Wielebinski 2003; see also A 3562 in Chapter 3). Such steepening may reflect the presence of a high energy break or a cut-off in the energy spectrum of the emitting electrons. Furthermore the images of the spectral index distribution of an increasing number of radio halos show a progressive steepening of the radio spectrum from the centre to the periphery of the cluster (e.g. Coma, Giovannini et al. 1993; A 665 and A 2163, Feretti et al. 2004). The observed radial steepening may be theoretically explained as due to the presence of a high energy cut-off in the electron spectrum combined with a radial decrease of the ICM magnetic field strength (Brunetti et al. 2001; Kuo et al. 2003). The presence of such high energy cut-off is naturally expected in the framework of the re-acceleration models (Petrosian 2001; Brunetti et al. 2001).

## 1.9 The re-acceleration scenario for radio halos

As pointed out in Section 1.8, there is increasing evidence that the radio properties of radio halos may be naturally accounted for by the re-acceleration scenario, in which a population of relic electrons in the ICM are continuously re-accelerated by some kind of fluid turbulence generated during merging events (Petrosian 2001; Brunetti et al. 2001).

Many theoretical possibilities have been investigated within this framework. Based on relatively simple assumptions, specific magneto-turbulent models for Alfvénic electron acceleration in galaxy clusters were developed by Ohno, Takizawa & Shibata (2002), Fujita, Takizawa & Sarazin (2003) and Brunetti et al. (2004).

### 1.9.1 Statistical calculations

Recently Cassano & Brunetti (2005; hereinafter CB05) presented the results of statistical semi-analytical calculations in the framework of the re-acceleration scenario. These calculations are capable to describe the evolution of the thermal properties of the ICM and of non-thermal component in galaxy clusters in a self-consistent way.

For a number of synthetic cluster merging histories (reproduced by using the Press & Schechter formalism; Press & Schechter 1974), CB05 estimated the injection rate of turbulence during each merging event. They calculated the evolution of the spectrum of the relativistic electrons in the ICM (and of the ensuing diffuse radio emission) during the cluster life by taking into account both the electron acceleration due to magneto-sonic (MS) waves and the relevant energy losses of the electrons.

The results in CB05 showed that non-thermal radio emission with the typical radio luminosity of the observed radio halos may be efficiently powered by turbulent re-acceleration during cluster major mergers (with mass ratio  $\gtrsim 1:5$ ), provided that a non-negligible fraction of the merger-driven turbulence is channeled into MS waves.

Furthermore, they derived the probability to develop a giant radio halo as a function of the mass of the parent cluster. Their calculations indicate that only massive clusters (i.e. with  $M \gtrsim 10^{15} M_{\odot}$ ) can host a giant radio halo, and that the probability to form these diffuse radio sources shows an abrupt increase for clusters with  $M \gtrsim 2 \times 10^{15} M_{\odot}$ . The comparison of such predictions with the observed occurrence of giant radio halos in clusters in the redshift range  $z=0 \div 0.2$  (Giovannini, Tordi & Feretti 1999; Sec. 1.7) provided very consistent results.

### Evolution with redshift

Based on the calculations in CB05, Cassano, Brunetti & Setti (2006; hereinafter CBS06) determined the evolution of the probability to form a giant radio halo as function of the cluster mass and redshift. Such calculations include the possible

dependence of the magnetic field intensity ( $B$ ) from the cluster mass (i.e.  $B \propto M^\alpha$ , with  $\alpha \geq 0.6$ ; see CBS06 for details). Furthermore, they calculated the expected radio luminosity function and number counts of giant radio halos (above a given radio flux density at 1.4 GHz) in different redshift bins.

The main results of those calculations can be summarised as follows:

- i. giant radio halos can be powered by magneto-turbulent re-acceleration up to a redshift  $z \sim 0.5-0.6$ ;
- ii. for a given mass of the hosting cluster, the probability to form a GRH generally decreases with redshift. In particular, for a galaxy cluster with  $M \sim 2 \times 10^{15} M_\odot$ , the probability is  $\sim 10\%$  for  $0.2 < z < 0.4$  and,  $\sim 30\%$  for  $z < 0.2$ ;
- iii. for a given redshift, the probability to find a GRH generally increases with the cluster mass. At  $z = 0.3$ , such probability is  $< 5\%$  in a Coma-like cluster ( $M \sim 1.8 \times 10^{15} M_\odot$ ),  $\sim 25\%$  in clusters with  $M \geq 2 \times 10^{15} M_\odot$ , and reaches  $\sim 50-60\%$  for  $M > 3 \times 10^{15} M_\odot$ ;
- iv. the shape of the radio luminosity function of giant radio halos (left panel of Fig. 1.10) is characterised by the presence of a cut-off at low synchrotron radio powers, which reflects the inefficiency of particle acceleration in the case of less massive galaxy clusters. Furthermore, the radio halo number density shows a negative evolution with redshift;
- iv. given that the anticorrelation between the halo number density and the redshift (left panel of Fig. 1.10) is strongly compensated by the increasing volume at larger  $z$ , the bulk of the radio halo formation is expected in massive clusters ( $M \gtrsim 2 \times 10^{15} M_\odot$ ) in the redshift range  $z=0.1-0.3$ , as clear from Figure 1.10 (right panel) which shows the expected total number of GRH above the flux density  $S_{1.4\text{GHz}} = 5 \text{ mJy}$  as function of redshift.

## 1.10 Models for the radio relic formation

The current theoretical models for the origin of radio relics predict a connection between these sources and the presence of a shock wave, driven by a cluster merging episode, and propagating through the X-ray gas. In particular, relics

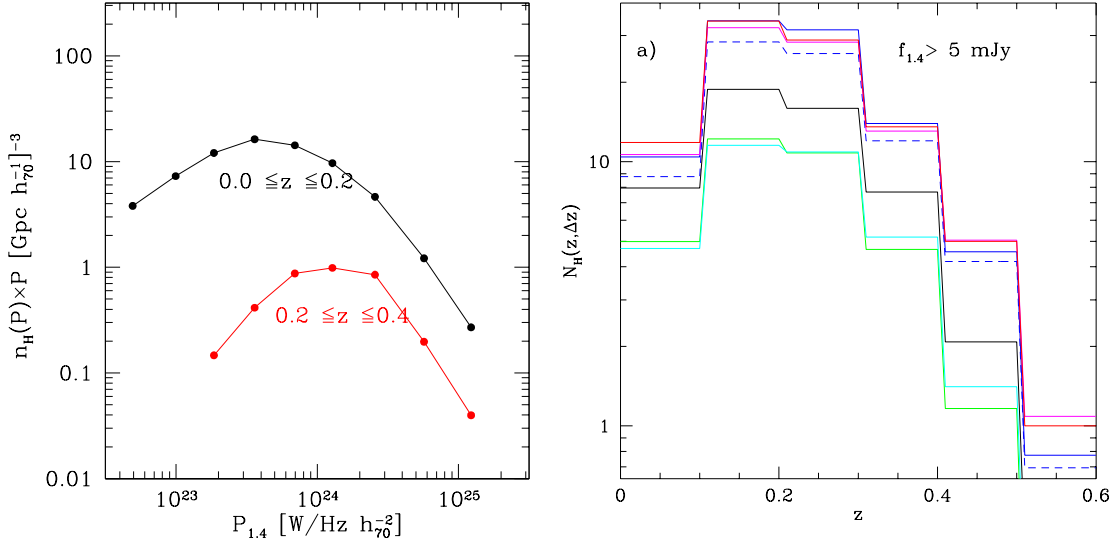


Figure 1.10: *Left panel* – Expected radio luminosity function in the redshift bins  $z=0.0\div 0.2$  (black line) and  $z=0.2\div 0.4$  (red line) from CBS06. *Right panel* – Expected total number of giant radio halos above the flux density  $S_{1.4\text{GHz}}=5\text{ mJy}$  as function of  $z$  (reproduced from CBS06). The colours of the lines indicate different combination of the parameters in the calculation (see CBS06 for details).

may be produced by particle diffusive shock acceleration (Sec. 1.10.1) or adiabatic compression of *fossil* radio plasma (Sec. 1.10.2), although both mechanisms may play a role. Furthermore shocks may also re-accelerate seed relativistic particles in the intracluster medium (see Markevitch et al. 2005 for a detailed discussion).

### 1.10.1 Shock acceleration

In the first models developed for the formation of radio relics, the radio emitting electrons are accelerated up to relativistic energies directly from the ICM thermal pool, through Fermi-I diffusive shock acceleration (Enßlin et al. 1998; Röttgering et al. 1997).

In the case of a fully ionized plasma as the ICM, the spectrum of the electrons accelerated by the shock is a power law in energy, whose slope  $\delta$  is related to the shock Mach number  $M$  according to the following equation:

$$\delta = 2 \frac{M^2 + 1}{M^2 - 1} + 1 \quad (1.3)$$

(e.g. Blandford & Eichler 1987), where the effect of particle aging  $\Delta(\delta) = 1$  is included. The spectral index of the ensuing radio emission  $\alpha = (\delta - 1)/2$  is thus

related to the Mach number of the shock.

If the shocks driven during mergers are weak (i.e.  $M \lesssim 3$ , as suggested by semi-analytical calculations and numerical simulations; see Sec. 1.1.1), they are expected to accelerate steep particle spectra, which may be consistent with the steep integrated spectra observed in radio relics (Sec. 1.5).

Once accelerated by the shock, the electrons are short-lived because of the IC and synchrotron losses, and thus their spectrum will quickly steepen. In this case, it is expected that the spectral index distribution of the radio emission in relics exhibits a steepening going from the current shock location (where the observed  $\alpha$  is the electron injection spectral index) to the trailing edge (in the observer projection; Enßlin et al. 1998).

Furthermore, it is expected that the shock may cause the magnetic field to become aligned with the shock plane. This may explain the high levels of polarisation in radio relics, since it implies that even an originally isotropic distribution of magnetic fields would exhibit a preferred orientation after the shock crossing, which may be observable by a global polarisation signature.

### 1.10.2 Adiabatic compression

An alternative model for the relic origin is the adiabatic compression of fossil radio plasma as result of the passage of a merger shock (Enßlin & Gopal-Krishna 2001).

Such fossil radio plasma may be the former outflow of a radio galaxy in which the central engine of the AGN has ceased to inject fresh relativistic plasma. The high energy electrons, related to the previous AGN activity, have suffered for major energy losses due to Inverse Compton and synchrotron radiation, and are able to produce radio emission only below the detectable limit with the current radio instrumentation, which may be eventually detected at very low frequencies (tens of MHz). For this reason, these cocoons of aged radio plasma are also called *radio ghosts* (Enßlin 1999).

When a radio ghost is crossed by a merger shock wave, propagating with a typical velocity of few  $1000 \text{ km s}^{-1}$ , the cocoon is compressed adiabatically and not shocked because of the much higher sound speed within it. Enßlin & Gopal-Krishna (2001) proposed that such compression may increase the magnetic field strength and re-energize the electron population in such fossil radio plasma, thus leading to

observable synchrotron emission.

In this case the pre-existing relativistic electrons are expected to produce diffuse radio emission in front of the bow shock, and then rapidly lose their energy while moving away from the front. Hence a steepening in the spectral index distribution of the relic is expected also in this scenario.

The numerical magneto-hydrodynamical simulations by Enßlin & Brüggen (2002) of a fossil radio cocoon crossed by a shock wave predict a variety of radio morphologies and polarisation properties, which may be reasonably well matched by the available high sensitivity radio images of cluster radio relics.

An important requirement in this scenario is that the electron population is not older than  $\sim 0.2\text{--}2$  Gyr (Enßlin & Gopal-Krishna 2001), and therefore the presence of an active radio galaxy in the proximity of the relic is required. In the case of the radio relic 1253+275 in the Coma cluster (see left panel of Fig. 1.7), a possible morphological connection between the diffuse source and the nearby radio galaxy NGC 4789 was pointed out by Giovannini, Feretti & Stanghellini (1991). This feature may suggest that the relic might be indeed fossil radio plasma that has been revived by a shock.

Given that merger shock waves should be very frequent during the life of a galaxy cluster, the requirement of both a shock wave and fossil radio plasma may be an attractive explanation for the rarity of radio relics (Sec. 1.3).

## 1.11 Observational study of cluster mergers

The observations suggest that merging events are relatively common within the population of galaxy clusters. In particular optical and X-ray studies show that a large fraction of clusters (30–40 %) have substructures (Girardi et al. 1997; Jones & Forman 1999), indicating frequent occurrence of merging processes. Strong evidence has been accumulated in the literature for a connection between mergers and cluster scale radio halos and relics (Sec.1.6). However, as pointed out in Section 1.3, only a fraction of merging clusters host diffuse radio emission. Hence it is important to investigate in detail the cluster merger phenomenon, in order to connect the physics of cluster mergers to the possible presence of extended radio emission in the form of a radio halo or relic.

Such investigation can be carried out through the multifrequency analysis of

individual galaxy clusters with high quality and high sensitivity observations in the radio, X-ray and optical bands, and whose properties are suggestive of merging activity (Sec. 1.11.1).

On the other hand, it is important to study the statistical properties of large sample of galaxy clusters, in order to derive a global understanding of the effect of merging phenomena on the cluster radio properties. Furthermore, the statistical analysis is fundamental to test the predictions of the theoretical models for the origin of non-thermal phenomena in galaxy clusters and thus to discriminate between the available scenarios (see Sec. 1.12).

### 1.11.1 Multifrequency analysis of individual galaxy clusters

Combined optical and X-ray studies are particularly successful in revealing the dynamics of merging clusters (e.g. Bardelli et al. 2002; Boschin et al. 2004; Girardi et al. 2006). The optical information is complementary to the X-ray information, since galaxies and gas are expected to react on different time scales during a merger (see for example the numerical simulations by Roettiger, Loken & Burns 1997). Furthermore, while the X-ray observations provide information about projected physical quantities, the optical data allow to analyse the cluster also in the redshift space.

In particular, the high quality X-ray spectral and imaging data provided by the Chandra and XMM-Newton observations allow to derive high resolution temperature and density images of galaxy clusters, in which signature of merging events may be searched for, such as substructure in the gas density distribution, multiple peaks, distortions, edges and tails of emission, temperature and pressure gradients, bow shocks and cold fronts (e.g. Henry, Finoguenov & Briel 2004; Finoguenov, Böhringer & Zhang 2005; Mazzotta, Fusco-Femiano & Vikhlinin 2002; Markevitch & Vikhlinin 2001, 2007).

In the optical band, the cluster dynamical state can be determined by analysing the line-of-sight velocity distribution of cluster member galaxies, as well as the presence of substructures and segregation in the galaxy distribution projected on the plane of the sky (e.g. Girardi & Biviano 2002). The combination of the spatial and kinematics analysis of member galaxies allows to measure the amount of substructure and identify possible pre-merging subclusters or merger remnants.

A more comprehensive picture of the dynamics in cluster mergers can be obtained by combining the results of the optical and X-ray studies with the weak lensing analysis, which allow to reconstruct the distribution of the total mass in the merging system. As an example, Figure 1.11 shows the comparison between the optical, X-ray and mass distributions in the two merging clusters A 1758N and A 1758S carried out in the recent work by Okabe & Umetsu (2007).

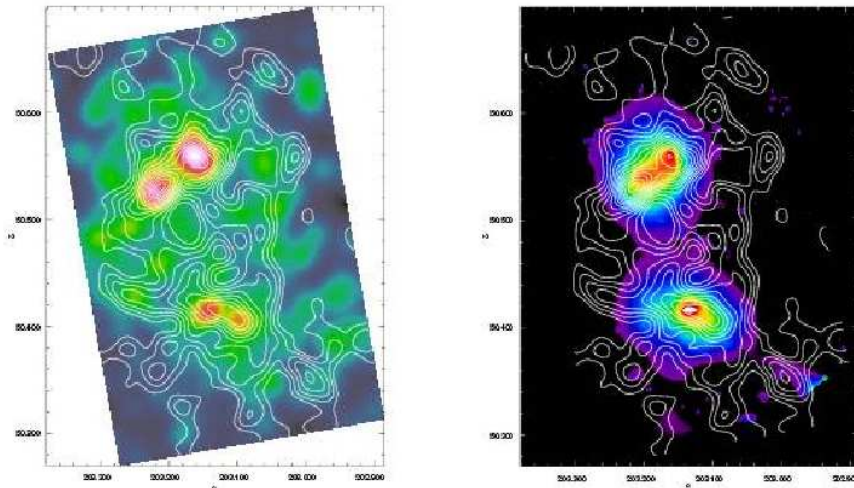


Figure 1.11: Comparison between the hot gas, optical galaxy and mass distribution in the merging cluster A 1758 (from Okabe & Umetsu 2007). *Left panel* – Contours of the reconstructed mass distribution from the weak lensing analysis, overlaid on the galaxy density distribution in the R band, smoothed to the same angular resolution of the mass image. *Left panel* – The same mass contours overlaid on the smoothed XMM–Newton X-ray image (0.5–7.0 keV)

## 1.12 The GMRT Radio Halo Survey

The Giant Metrewave Radio Telescope (GMRT) Radio Halo Survey (Venturi et al. 2007; Venturi et al. in prep.) was carried out at 610 MHz using the Indian radio interferometer GMRT (see Sec. 2.3 for a description of the telescope).

The survey was designed to search for new radio halos and relics in galaxy clusters in the redshift range  $0.2 \leq z \leq 0.4$ , and statistically investigate the connection between the presence of such non-thermal phenomena and the merging activity of the hosting cluster. Furthermore, the survey aims to derive the fraction of massive galaxy clusters in this redshift interval hosting a giant radio halo (the statistical information for  $z < 0.2$  is already available in the literature, see Sec. 1.7),

and compare this number with the predictions of the re-acceleration model for the origin of these sources in the same redshift interval (Sec. 1.9.1 and Fig. 1.10).

A statistical sample of galaxy clusters was extracted from the ROSAT–ESO Flux Limited X–ray (REFLEX) galaxy cluster catalogue (Böhringer et al. 2004), and the combination of the ROSAT Brightest Cluster Sample (BCS; Ebeling et al. 1998) and the extended BCS (Ebeling et al. 2000) catalogues. From these catalogues all galaxy clusters with X–ray luminosity  $L_{X[0.1-2.4\text{keV}]} \geq 5 \times 10^{44} \text{ erg s}^{-1}$  were selected. In order to ensure a good u–v coverage with the GMRT, declination limits were also imposed. To summarise the selection criteria:

- \*  $0.2 \leq z \leq 0.4$ ;
- \*  $L_{X[0.1-2.4\text{keV}]} \geq 5 \times 10^{44} \text{ erg s}^{-1}$ ;
- \*  $-30^\circ < \delta < +2.5^\circ$  for the REFLEX catalogue;
- \*  $+15^\circ < \delta < +60^\circ$  for the eBCS catalogue.

The limit in the X–ray luminosity was chosen in order to select massive galaxy clusters, since the value of the mass threshold for the formation of a giant radio halo predicted by the re-acceleration model (Sec. 1.9.1) corresponds to a cluster virial mass  $M_V \gtrsim 10^{15} M_\odot$ . Assuming the  $L_X - M_V$  correlation in CBS06, the adopted limit reflects a virial mass limit of  $M_V \geq 1.4 \times 10^{15} M_\odot$ .

A total sample of 50 galaxy clusters was obtained, 27 clusters selected from the REFLEX catalogue and 23 from the BCS+eBCS catalogue. The sample includes seven clusters which are known to host a radio halo from the literature. Among the remaining clusters, 610 MHz GMRT observations were carried out for 34 sources with no radio information available either in the literature or public archives at the time the observing proposals were submitted. The survey was performed during three different observing runs (January and August 2005, August 2006), for a total of  $\sim 90$  hours of observations.

The choice of the GMRT was motivated by the observational evidence that radio halos and relics are characterised by steep radio spectrum and very low surface brightness (Sec. 1.3). Thus an instrument capable of high sensitivity at low frequency as the GMRT was preferred (see Sec. 2.3 for a description of the GMRT). The survey was carried out at 610 MHz, since this frequency offers the best compromise among

sensitivity and range of angular resolutions, allowing to reduce confusion limitations at a very low level.

The results of the REFLEX subsample were recently presented in Venturi et al. (2007), and the analysis of the combined REFLEX+BCS sample will be carried out in forthcoming papers (Venturi et al. in preparation, Cassano et al. in preparation).

## Chapter 2

# Cluster selection and observations

### 2.1 The sample

The main purpose of the present work is to connect the physics of the hot intracluster medium and cluster mergers to the presence of cluster scale diffuse radio emission (Sec. 1.3), through a composite radio, optical and X-ray analysis of a number of galaxy clusters which are known to be undergoing or have recently experienced a merging event. As pointed out in Section 1.11.1, the combined X-ray/optical approach is a powerful tool to investigate and possibly determine the dynamics, geometry and time scale of the merger.

With this aim we selected four examples of merging clusters with high quality data both in the optical and X-ray bands, and performed deep radio observations in order to test the presence and understand the origin and properties of the hosted diffuse radio halos or relics in connection with the cluster merging activity. Three of these clusters were observed as part of the larger project of the GMRT Radio Halo Survey described in Section 1.12. From the total sample built for the survey, two further clusters were extracted for the present study: they both host diffuse radio emission on cluster scale, but the knowledge of their dynamical state is very poor, due to the lack of deep optical information and high resolution X-ray observations. Therefore, a detailed multiwavelength study is not possible for these clusters, which were analysed mainly in the radio band.

The six galaxy clusters studied in the present work are listed in Table 2.1, where the following information is reported: (1) the cluster name, (2) and (3) J2000 coordinates, (4) redshift, (5) X-ray luminosity in the 0.1–2.4 keV band, (6) velocity dispersion, (7) and (8) estimates of the virial mass  $M_V$  and virial radius

Table 2.1: Galaxy cluster sample.

Cluster Name	RA <sub>J2000</sub>	DEC <sub>J2000</sub>	z	L <sub>X [0.1–2.4keV]</sub> 10 <sup>44</sup> erg s <sup>-1</sup>	σ <sub>v</sub> km s <sup>-1</sup>	M <sub>V</sub> 10 <sup>15</sup> M <sub>⊙</sub>	R <sub>V</sub> Mpc
◇ A 209	01 31 53.0	-13 36 34	0.206	6.29 (a)	1394 (c)	1.58	2.69
◇ A 521	04 54 09.1	-10 14 19	0.248	8.18 (a)	1325 (d)	1.89	2.78
◇ A 697	08 42 53.3	+36 20 12	0.282	10.57 (b)	1334 (e)	2.25	2.90
A 3562	13 33 36.3	-31 39 40	0.048	1.48 (a)	987 (f)	0.59	2.11
◇ RXCJ 1314.4–2515	13 14 28.0	-25 15 41	0.244	10.94 (a)	1100 (g)	2.30	2.98
◇ RXCJ 2003.5–2323	20 03 30.4	-23 23 05	0.317	9.25 (a)	–	2.05	2.75

Notes to Table 2.1: ◇ marks the clusters which are part of the GMRT Radio Halo Survey (Sec. 1.12); (a) Böhringer et al. (2004); (b) Ebeling et al. (1998); (c) Mercurio et al. (2003); (d) Ferrari et al. (2003); (e) Girardi, Boschini & Barrena (2006); (f) Bardelli et al. 1998b; (g) Valtchanov et al. (2002).

R<sub>V</sub> respectively. M<sub>V</sub> and R<sub>V</sub> were determined using the correlation between the X-ray luminosity and M<sub>V</sub> reported in Cassano, Brunetti & Setti (2006), which has a statistical dispersion of ∼ 30%. If we account for the uncertainty of the virial mass values given in Table 2.1, our estimates are consistent with the values of M<sub>V</sub> obtained from the cluster velocity dispersion in the literature (see Notes to Tab. 2.1 for references).

The clusters observed as part of the GMRT Radio Halo Survey and included in the present thesis due to the presence of extended cluster scale radio emission are marked as ◇ in the table. for RXCJ 1314.4–2515 and RXCJ 2003.5–2323 the analysis is carried out mostly in the radio band and further work in the optical and X-ray bands is in progress.

## 2.2 Radio observations

Table 2.2 summarises all radio observations used for the analysis of the galaxy clusters listed in Table 2.1. The columns in the table provide the following information: (1) cluster name, (2) array used for the observation, (3) observing date, (4) and (5) observing frequency and total bandwidth (MHz), (6) total time on source (minutes), (7) half power bandwidth (HPWB) of the full array (arcsec × arcsec, position angle p.a. in degrees), and (7) rms level (1σ) in the full resolution image (μJy b<sup>-1</sup>).

All clusters were observed at low frequency with the GMRT. Furthermore VLA

observations were carried out at 4.9 and 8.4 GHz for A 521, and at 1.4 GHz for RXCJ 2003.5–2323. VLA archival data at 1.4 GHz were used for the analysis of A 521. Finally, published VLA and Australia Telescope Compact Array (ATCA) data at 1.4 GHz were used for the study of A 3562 (Venturi et al. 2000; Venturi et al. 2003; Giacintucci et al. 2004).

Table 2.2: Summary of the radio observations.

Cluster	Telescope	Obs. date	$\nu$ MHz	$\Delta\nu$ MHz	t min	HPWB, p.a. (full array), "×", °	rms $\mu\text{Jy b}^{-1}$
A 209	GMRT	01/05	610	32	240	8.0×5.0, 64	60
A 521	GMRT	01/05	610	32	210	5.0×4.0, 52	30
	VLA–CnB (a)	09/02	1400	25	330	12.8×6.7, 79	15
	VLA–CnB	10/06	4860	50	60	4.0×2.0, –82	15
	VLA–BnA	06/06	4860	50	110	1.0×0.8, –68	10
	VLA–BnA	06/06	8430	50	170	0.6×0.5, 82	10
A 697	GMRT	09/05	610	32	80	6.2×4.5, 65	25
(b) A 3562	GMRT	01/03	235	8	420	17.4×11.5, 11	800
	GMRT	02/03	327	16	420	15.0×8.0, 26	300
	GMRT	01/03	610	8	420	7.3×5.0, 7	150
	ATCA–6C (c)		1380	128	120	10.2×6.5, 41	100
	VLA–DnC (d)	07/00	1400	50	240	41.9×35.1, 55	50
RXCJ1314.4–2515	GMRT	01/05	610	32	150	8.0×5.0, 15	65
RXCJ2003.5–2323	VLA–CnB	10/06	1400	25	540	12.6×9.2, 85	20
	GMRT	01/05	610	32	240	6.9×5.0, –3	40

Notes to Table 2.2: (a) archival data; (b) this cluster was observed using the GMRT simultaneously at 235 and 610 MHz; (c) from Venturi et al. (2000); (d) from Venturi et al. (2003) and Giacintucci et al. (2004).

## 2.3 The Giant Metrewave Radio Telescope

The GMRT is the world largest radio interferometer at meter wavelengths. It is operated by the National Centre for Radio Astrophysics (NCRA) of the Tata Institute of Fundamental Research (TIFR, India) and is located at  $\sim 80$  km North of Pune. The instrument is an aperture synthesis array, composed of 30 fully steerable parabolic dishes of 45 m diameter each (see Fig. 2.1): 14 antennas are located in a compact central array, covering a region of about  $1 \text{ km}^2$ , and 16 are distributed along three arms to form an approximately Y-shaped configuration, with a longest

baseline of  $\sim 25$  km.

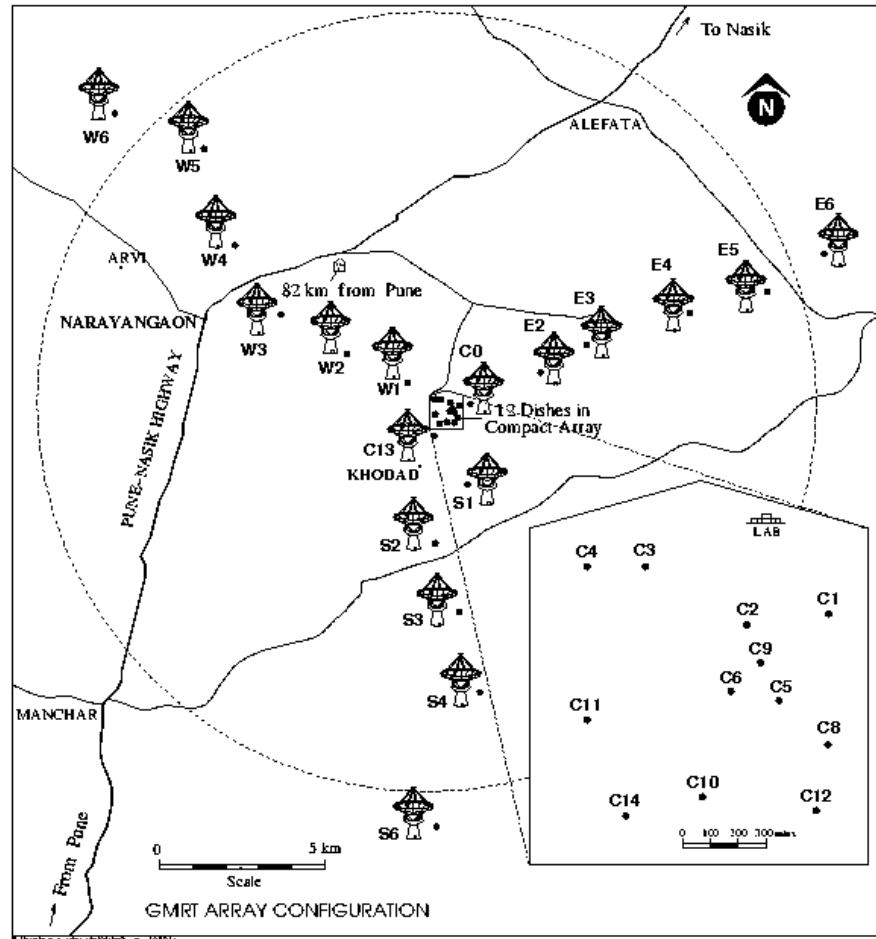


Figure 2.1: Locations of the GMRT antennas.

The array currently operates in five frequency bands centered around 150, 235, 327, 610 and 1280 MHz. The main system parameters are summarised in Table 2.3.

At each frequency, two simultaneous observing bands are provided, namely the *upper side band* (USB) and *lower side band* (LSB), with a bandwidth of 16 MHz each at 327, 610 and 1280 MHz and 8 MHz at 235 and 150 MHz. Simultaneous dual-frequency observations are possible at 235 and 610 MHz, with an 8 MHz bandwidth at each frequency. Dual polarization information (right RR and left LL) is provided at all frequencies. When the array observes in simultaneous mode at 235/610 MHz,

Table 2.3: GMRT Parameters.

	Frequency (MHz)				
	150	235	327	610	1280
Primary Beam (arcmin)	186	114	81	43	24
HPWB Full Array (arcsec)	20	13	9	5	2
HPWB Central Compact Array (arcsec)	420	270	200	100	40
Largest Detectable Structure (arcmin)	68	44	32	17	7
Sensitivity ( $\mu\text{Jy b}^{-1}$ ) *	46	17	10	9	13

Note to Table 2.3: \* theoretical value for assumed bandwidth of 16 MHz, 10 hours integration time and natural weighting.

LL polarisation is recorded at 235 MHz, and RR at 610 MHz.

The GMRT u–v coverage ensures a good sensitivity both to compact and extended sources. In particular the baselines obtained by the antennas in the compact central array are similar in length to the VLA D–array configuration, while the baselines between the arm antennas are comparable in length to the VLA B–array. Hence, a single observation with the GMRT samples the u–v plane adequately on the short as well as on the long baselines, thus providing high sensitivity imaging over a wide range of angular resolutions (Tab. 2.3). Therefore GMRT is a very suitable instrument to study diffuse, low surface brightness and steep spectrum radio sources such as cluster scale radio halos and relics (Sec. 1.3). The possibility to obtain both high resolution (few arcsec) and low resolution (few tens of arcsec) images at all frequencies (see Sec. 2.4.4 for details) allows to discriminate between real diffuse emission and a blend of individual radio galaxies, and to detect and remove single radio sources possibly embedded in the halo/relic emission.

## 2.4 GMRT observations and data reduction

### 2.4.1 Recording

The 610 MHz observations reported in Table 2.2 were performed using both the USB and LSB for all sources, except for A 3562, whose observations were carried out simultaneously at 235/610 MHz. The 327 MHz data of A 3562 were recorded using the USB only.

All data were collected in spectral–line mode over 64 channels at 235 MHz,

and 128 channels/band at all other frequencies, with a spectral resolution of 125 kHz/channel. A calibration source (e.g. 3C 48, 3C 147, 3C 286) was observed at the beginning and end of each observing session, in order to determine and correct for the bandpass shape and for the initial amplitude and phase calibration. A nearby phase calibrator was observed each  $\sim 20$  minutes for each source, in order to monitor any time-dependent phase and amplitude fluctuations of the telescope, and thus apply the phase calibration.

The visibility data were first converted to FITS format using the *gwfits* software available at the GMRT site, and then reduced and analysed using the National Radio Astronomy Observatory (NRAO) Astronomical Image Processing System (AIPS) package.

### 2.4.2 Data editing

Low frequency observations may suffer from strong radio frequency interference (RFI) and ionospheric scintillation, which may significantly affect the quality of the data and the achievable sensitivity in the image. Hence, in addition to the normal flagging of bad baselines, antennas and time ranges, an accurate editing of the visibility data was carried out in order to identify and remove those data affected by narrow band RFI and scintillation, especially at frequencies  $\nu \leq 610$  MHz.

### 2.4.3 Bandpass calibration

The bandpass calibration was carried out using the flux density calibrator. An RFI-free channel was chosen to calibrate the bandpass for each antenna.

At 235 and 327 MHz, the bandpass calibration solutions were applied to the data by running the AIPS task *flgit*. This task subtracts a continuum from the channels in the  $u-v$  plane, determined on the basis of the bandpass shape and using a specified set of channels. The data whose residuals exceed a chosen threshold are then flagged.

In order to find a compromise between the data set size and the need to minimize bandwidth smearing within the primary beam, after bandpass calibration the central channels of each data set were compressed into 6 channels of  $\sim 1$  MHz each at 235 MHz, and  $\sim 2$  MHz each at 327 MHz and 610 MHz.

#### 2.4.4 Calibration and Imaging

The USB and LSB data sets were calibrated and reduced separately. In order to improve the quality of the final image, phase self-calibration was applied to each data set.

The large field of view of the GMRT leads to significant errors if the whole field is imaged directly, due to the non-planar nature of the sky. To minimize these errors, the wide-field imaging technique was implemented in each step of the phase self-calibration process, using 25 facets which cover a total field of view in the range  $\sim 1^2 \div 3.5^2$  square degree, depending on the frequency and resolution. The facets were imaged separately, with a different assumed phase centre, and then recombined to deal with the transformation from planes to sphere. The final images from each individual data set were then corrected for the primary beam of the GMRT using an 8th-order polynomial function with the coefficients reported in the online GMRT user manual<sup>1</sup>. Finally they were combined in the image plane to obtain the final image, which was weighted by the rms noise levels of each individual image.

In those cases where no strong radio sources were found within the imaged field at 610 MHz (i.e. A 3562, A 697 and A 521), the USB and LSB self-calibrated data sets were averaged again from 6 channels to 1 single channel and then combined together to produce the final images.

For each cluster, images over a wide range of resolutions were produced, in order to fully exploit the information GMRT can provide. The full resolution images (Tab. 2.2) were obtained by means of uniform weighting. The low resolution images, which are more adequate to image extended and low surface brightness sources, were produced using natural weighting and a Gaussian taper to down-weight long baseline information.

The sensitivity of the observations ( $1\sigma$  level) achieved in the full resolution images are reported in Tab. 2.2. The spread in the noise level depends mostly on the total time on source and on the presence of strong point-like radio sources in the imaged field. In this latter case, the dynamic range is limited by the presence of phase artefacts around the brightest sources, which have not been successfully corrected during self-calibration (see Fig. 2.2). Furthermore, residual RFI still affecting the data at 235 and 327 MHz led to a lower sensitivity than the expected value (see

---

<sup>1</sup>[http://www.gmrt.ncra.tifr.res.in/gmrt\\_hpagen/Users/doc/manual/UsersManual/node1.html](http://www.gmrt.ncra.tifr.res.in/gmrt_hpagen/Users/doc/manual/UsersManual/node1.html)

Tables 2.3 and 2.2).

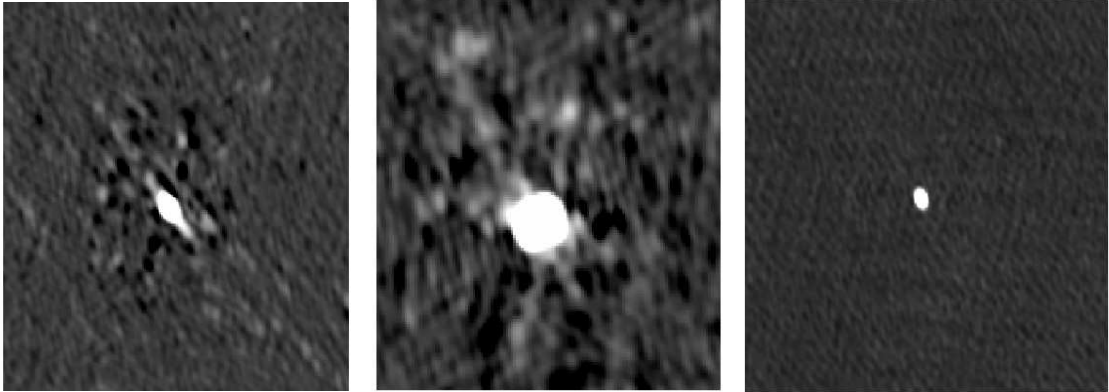


Figure 2.2: *Left and central panels* – Residual phase artefacts visible around two bright radio sources in the RXCJ 1314.4–2515 field (Tab. 2.2). The grayscale ranges between  $-1.5$  and  $172.0$   $\text{mJy b}^{-1}$  in the left panel and between  $-0.9$  and  $199.5$   $\text{mJy b}^{-1}$  in the central panel. *Right panel* – Case of a faint radio source where residual phase artefacts are absent. The grayscale ranges between  $-0.25$  and  $23.9$   $\text{mJy b}^{-1}$ .

The average residual amplitude errors in the data are of the order of  $\lesssim 5\%$  at all the frequencies. Larger amplitude errors were estimated for A 3562, i.e.  $\sim 10\%$  at 610 MHz,  $\sim 20\%$  at 327 MHz, and  $\sim 15\%$  at 235 MHz.

## 2.5 VLA observations and data reduction

VLA observations were carried out at 1.4 GHz for the galaxy cluster RXCJ2003.5–2323, and at 4.9 GHz and 8.5 GHz for A 521 (see Tab. 2.2).

### 2.5.1 RXCJ2003.5–2323

RXCJ2003.5–2323 was observed in the hybrid CnB configuration, in order to optimize the  $u$ – $v$  coverage at the low declination of the source. The observations were carried out into two different runs (Tab. 2.2), for a total integration time of  $\sim 9$  hours on source. The cluster was observed using the standard polarisation mode at 1.4 GHz, and spectral line correlator mode in order to better filter out the RFI in the observing band and properly image the whole cluster field with wide field imaging. We used 8 channels for each of the two IFs, centered at 1385 MHz and 1465 MHz, with a total bandwidth of 25 MHz/IF. 3C 286 and 3C 343 were observed for the bandpass and primary flux density calibration, and for the calibration of the polarisation electric vector. The phase calibration was obtained from the nearby

calibrator 1923–210, while multiple observations of 1949–199 over a large range of parallactic angles were used to calibrate the polarisation leakage for each antenna. Calibration and imaging were performed using the AIPS package. The data sets from the two different days were calibrated separately. After bandpass calibration, the 8 channels/IF of each data set were averaged to 1 single channel of  $\sim 22$  MHz. Each data set was self-calibrated in phase only, implementing the wide-field imaging technique to compensate for the non-coplanar geometry of the VLA. We used a total of 18 facets to cover the primary beam area and bright outlying sources. The final self-calibrated data set were then combined together to produce the final images. Both uniform and natural weighting were used for the total intensity image I, and for the images in the Stokes parameters Q and U. The polarised intensity images were derived from the Q and U images.

### 2.5.2 A 521

The region of the radio relic in A 521 (see Chapter 6) was observed at 8.4 GHz with the VLA in the hybrid BnA configuration, suitable for the low declination of the source. The 4.9 GHz observations were performed using both the BnA and CnB configurations (see Tab. 2.2 for details). A bandwidth of 50 MHz was used for each of the two IF channels at each frequency. All observations include full polarisation information, with 3C 48 as primary amplitude and absolute electric vector position angle calibrator. The source 0501–019 was used as phase and instrumental polarisation calibrator. The data were calibrated and reduced using the pilot pipeline for the VLA data processing, a facility recently started at NRAO. The semi-automatic pipeline is implemented in the AIPS package, and provided high quality calibrated data sets at each frequency. The pipeline products were further phase self-calibrated in AIPS, in order to correct for residual phase variations, and used to produce the final images.

## 2.6 X-ray data

High resolution X-ray observations from the Chandra and XMM-Newton observatories were used for the analysis of the galaxy clusters listed in Table 2.4. The table gives (1) the cluster name, (2) the X-ray satellite used for the observation (C for Chandra, X for XMM-Newton), (3) detector where the aimpoint lies, (4)

Table 2.4: Summary of the X-ray observations.

Cluster name	Satellite	Detector	Obs. Id	Exposure ks
√ A 697	C	ACIS-I	4271	19
√ A 521	C	ACIS-I	901	39
	C	ACIS-S	430	39
√ A 209	C	ACIS-I	522	9
	C	ACIS-I	3579	9
A 3562	C	ACIS-I	4167	20
	X	EPIC pn	0105261301	33
	X	EPIC pn	0105261401	7
	X	EPIC pn	0105261501	7
	X	EPIC pn	0105261601	15
	X	EPIC pn	0105261701	14
	X	EPIC pn	0105261801	4

√ marks the archival observations re-processed in the present work; C and X stand for Chandra and XMM-Newton respectively.

archive number of the observation, and (5) exposure time in ks after removal of flaring episodes. The archival Chandra data of the clusters marked as √ in Table 2.4 were re-processed in the present work. The data reduction and analysis are described in Section 2.6.1. The proprietary XMM-Newton data of A 3562 were first presented in Finoguenov et al. (2004), while the Chandra data are from Ettori et al. (in preparation).

### 2.6.1 Chandra data reduction and analysis

The Chandra data reduction and analysis were carried out using the version 3.3.3 of the Chandra Interactive Analysis of Observations (CIAO) package. The level=1 event files were retrieved from the public Chandra archive and re-processed using the standard procedure. The CIAO *acis\_process\_events* tool was used to correct the data for the charge transfer inefficiency (CTI) effect and apply the re-computation of event grades. The tool was also used to update the gain maps of the Advanced CCD Imaging Spectrometer (ACIS) with the latest version provided within CALDB 3.2.3, and to correct for its time dependence (T\_GAIN

correction). For the observations telemetered in VFaint mode, which provides a better rejection of the particle-induced background, *acis\_process\_events* was run with the option *check\_vf\_pha = yes*, to filter out additional events due to particle background. The standard filtering was performed, excluding known bad CCD columns, hot pixels, chip node boundaries, and events with ASCA grades 1, 5, and 7, as well as bad aspect intervals. The background light curves were carefully examined in order to detect and remove possible background flaring episodes during the observation, following the recommendations given in the cookbook provided by M. Markevitch<sup>2</sup>. The time intervals which exhibited background count rate fluctuations larger than 20% from the quiescent rate were excluded. The background mean count rate in the observation was then compared to the background values tabulated by M. Markevitch<sup>3</sup>. A good consistency within less than 10% was found for all observations.

The cleaned event files were then used for the image and spectral analysis. The blank-sky background files corresponding to the configuration and period of the observation<sup>4</sup> were used in the analysis. The background files was reprocessed and reprojected to match the observation. Since the background may change slightly with time, we normalized the blank-sky by requiring the same event count rate in the 9.5–12 keV band as the observation.

### Image Analysis

The cleaned event files were binned to produce images of each cluster in the selected energy range. Each image was background subtracted using the corresponding blank-sky. The image was then divided for the exposure map, obtained using the CIAO tool *mkeexpmap*, to correct for vignetting effect and exposure variations across the field of view.

In order to highlight the cluster diffuse X-ray emission and detect possible substructures within the gas distribution, a wavelet analysis was performed. The images were smoothed implementing the wavelet-smoothing algorithm from the A. Vikhlinin's *zhtools* package (Vikhlinin et al. 1998).

The presence of possible X-ray surface brightness gradients and discontinuities,

---

<sup>2</sup>[http://cxc.harvard.edu/cal/Acis/Cal\\_prods/bkgrnd/acisbg/COOKBOOK](http://cxc.harvard.edu/cal/Acis/Cal_prods/bkgrnd/acisbg/COOKBOOK)

<sup>3</sup><http://cxc.harvard.edu/contrib/maxim/acisbg/data/README>

<sup>4</sup><http://cxc.harvard.edu/contrib/maxim/acisbg/data/>

suggested by the wavelet re-constructed image, was checked by extracting brightness profiles on the unsmoothed, background subtracted and vignetting corrected image.

### Spectral Analysis

The spectral analysis was performed using CIAO and the version 12.1 of the X-Ray Spectral Fitting Package (XSPEC). After the detection and removal of possible point sources within the cluster emission, the spectra of the selected regions were extracted using CIAO. The Redistribution Matrix File (RMF) and Auxiliary Response File (ARF) were calculated using the CIAO tools *mkacisrmf* and *mkwarf* respectively. The spectra for each data set were then grouped, so that each bin contained at least 20 counts, and finally fitted in XSPEC, restricting the energy range to a minimum value of 0.6 keV and a maximum of 8 keV. Due to the uncertainties in the ACIS calibration below 0.6 keV, we excluded less energetic photons from the spectral analysis in order to avoid systematic bias. The effective cut at high energies is generally lower than 7–8 keV, since the signal to noise ratio (S/N) for a thermal spectrum rapidly decreases above 5 keV. In the case of different observations for the same cluster (e.g. A 209), the spectra (along with the RMFs and ARFs) were extracted separately, and then simultaneously fitted using the same spectral model.

In all cases, an absorbed thermal model (*wabs mekal*) was chosen for the spectral fitting. The column density  $n_{\text{H}}$  was fixed to the Galactic value provided by Dickey & Lockman (1990) for the corresponding region of the sky. The redshift was fixed to the cluster one.

The goodness of the fit was evaluated on the basis of the reduced  $\chi^2$  value and the null hypothesis probability, which is the probability to have a value of  $\chi^2$  as large or larger than observed if the model is correct. If this probability is small then the model is not a good fit. In general the threshold for an acceptable fit is set to few % (see for example Balestra et al. 2007).

A comparison with the results obtained using the Cash statistics (on the ungrouped spectrum) revealed a good agreement for all the observations.

### Hardness Ratio Image

The hardness ratio images were obtained using two images extracted in the 0.2–2.5 keV (*soft*) and 2.5–9 keV (*hard*) energy bands, both background subtracted and

vignetting corrected. Point sources were detected and removed using the CIAO tools *wavdetect* and *dmfilth*. The images were adaptively smoothed with *csmooth*, using the same identical smoothing pattern, derived with a minimum significance of  $5\sigma$  and a maximum significance of  $10\sigma$ . Finally the smoothed images were combined as (*hard - soft/hard + soft*) to obtain the hardness ratio image. The temperature calibration was carried out with the *fakeit* tool in XSPEC. The theoretical conversion factors were computed using an absorbed thermal model (*wabs mekal*), with a column density fixed to the Galactic value, an abundance  $Z = 0.3 Z_{\odot}$ , and  $z$  fixed to the cluster redshift. The model was convolved with the Chandra response, using the ARF and RMF files corresponding to the configuration and period of the observation.



## Chapter 3

# The radio halo in Abell 3562

The galaxy cluster A 3562 ( $z=0.048$ ,  $L_{X[0.1-2.4\text{keV}]} = 1.48 \times 10^{44} \text{ erg s}^{-1}$ , virial mass  $M_v = 5.9 \times 10^{14} M_\odot$ ) is located in the Shapley Concentration supercluster, one of most dynamically active regions in the local Universe. The cluster main properties are reported in Table 2.1.

Recent X-ray XMM-Newton observations provided strong evidence that the cluster has recently experienced a severe gravitational interaction with a nearby massive group of galaxies (Finoguenov et al. 2004, hereinafter FHB04).

At the radio wavelengths, A 3562 hosts one of the smallest and the less powerful radio halo known to date. Hints of the presence of such diffuse radio emission were found by Venturi et al. (2000; hereinafter VBM00) on the basis of an 843 MHz image from the Molonglo Observatory Synthesis Telescope (MOST; reported in the right panel of Fig. 3.1), and inspection of the 1.4 GHz NVSS image (left panel of Fig. 3.1). Thanks to high sensitivity observations, carried out using the VLA at 1.4 GHz, the existence of a radio halo at the cluster centre was confirmed by Venturi et al. (2003; hereinafter VBD03) and Giacintucci et al. (2004; hereinafter GVB04). The 1.4 GHz image of the halo is reported in Figure 3.2.

The X-ray properties of A 3562, such as the luminosity and temperature (reported in Tab. 2.1), are not as high as typically found in other clusters hosting a radio halo (Sec. 1.7). However, VBD03 showed that the A 3562 halo follows and extends the correlation found between the halo 1.4 GHz radio power and the X-ray luminosity of the hosting cluster, down to lower values of all quantities involved (see Fig. 1.9 in Sec. 1.7). For this reason the halo source in A 3562 plays a special role in our understanding of the origin of cluster diffuse radio emission and its connection to the X-ray properties and merging activity of the hosting cluster. In particular,

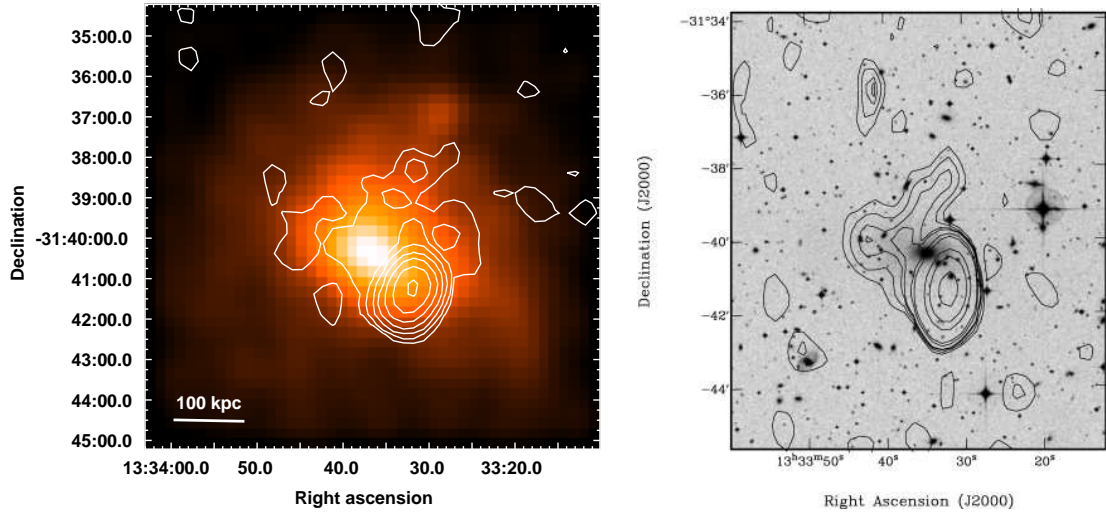


Figure 3.1: *Left panel* – 1.4 GHz NVSS image of the central region of A 3562, overlaid on the X-ray smoothed ROSAT–PSPC image. Radio contours are spaced by a factor 2, starting from  $\pm 1$  mJy  $\text{b}^{-1}$ . The resolution is  $45'' \times 45''$ , p.a.  $0^\circ$ . *Right panel* – 843 MHz MOST contours of the central region in A 3562, superposed to the optical DSS image. The resolution is  $81'' \times 43''$ , p.a.  $0^\circ$ . Contour levels are 2, 2, 3, 4, 4.5, 7.5, 10, 30, 50 and 100 mJy  $\text{b}^{-1}$ .

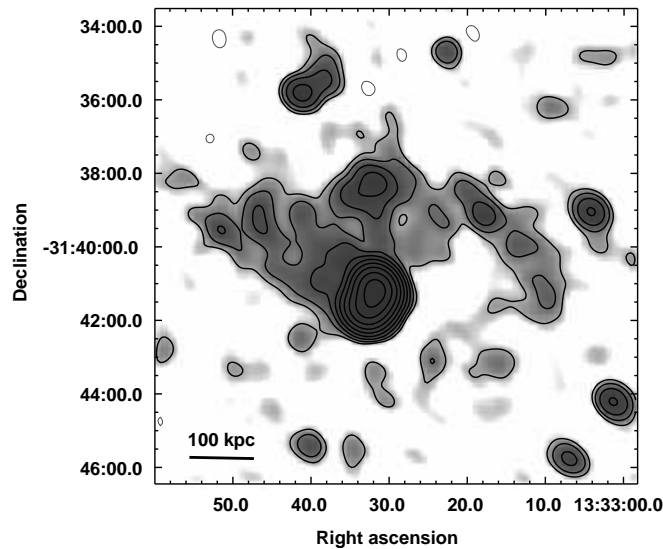


Figure 3.2: VLA 1.4 GHz radio image (grey scale and contours) of central radio halo in A 3562. The  $1\sigma$  level in the image is  $50 \mu\text{Jy} \text{b}^{-1}$ . Radio contours are spaced by a factor 2, starting from  $\pm 0.15$  mJy  $\text{b}^{-1}$ . The resolution is  $41.9'' \times 35.1''$ , p.a.  $55^\circ$ .

A 3562-like halos may help to understand the missing link between the massive and X-ray luminous clusters with a giant radio halo (i.e.  $LLS_{\sim} > 700$  kpc; see Sec. 1.4) and those without (or undetected).

The Chapter is organised as follows: a brief description of the complex merging environment of A 3562 is given in Section 3.1; in Section 3.2 the detailed analysis of the morphological and spectral properties of the radio halo is presented, using the low frequency GMRT observations and 1.4 GHz VLA and ATCA data (Tab. 2.2); in Section 3.4 we discuss the origin of the radio emitting electrons in the halo; a composite radio/X-ray investigation of the A 3562 region is carried out in Section 3.5 using XMM-Newton and Chandra observations (Tab. 2.4); in Section 3.6 we propose a possible cluster merger scenario to account for the observed properties of the radio emission in the A 3562 region; finally a summary of our results is given in Section 3.7.

At the redshift of A 3562 ( $z=0.048$ ), the cosmology adopted in this work leads to a linear scale of  $1'' = 0.94$  kpc.

### 3.1 The merging environment of A 3562

A 3562 belongs to the Shapley Concentration supercluster, one of the largest concentrations of mass in the local Universe (e.g. Zucca et al. 1993), where major cluster merging processes and group accretion are known to take place (Bardelli et al. 1996 and 1998a; Ettori, Fabian & White 1997). The optical and X-ray observations reveal that the Shapley Concentration has a remarkable structure dominated by a central high density core, whose X-ray emission is shown in Figure 3.3. The core is centered on the so-called *A 3558 complex*, a chain composed by the three clusters A 3562, A 3558, and A 3556 and the two groups of galaxies SC 1327–312 and SC 1329–313. Given its highly disturbed dynamical state, the A 3558 complex is considered one of the most spectacular and outstanding examples of cluster merger, as extensively outlined by studies in the optical and X-ray bands (Bardelli et al. 1996, 1998a, 1998b, 2000 and 2002; Ettori, Fabian & White 1997 and Ettori et al. 2000).

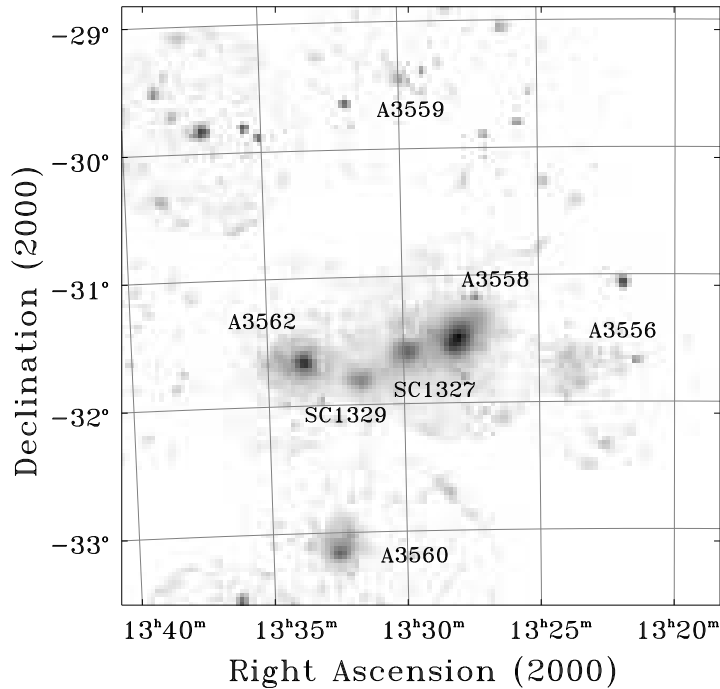


Figure 3.3: Mosaic of the core of the Shapley Supercluster obtained from ROSAT Position Sensitive Proportional Counter (PSPC) images in the 0.4–2 keV band (from Ettori, Fabian & White 1997).

Some of the main observational evidences supporting a strong merging activity in the A3558 complex can be briefly summarised as follows:

- i. a filamentary, physical structure of low surface brightness X-ray emission connects the central cluster A3558 to the two SC groups and A3562, and probably also to A3556 (Kull & Böhringer 1999; see also Fig. 3.3);
- ii. the distribution of the hot gas remarkably follows the two-dimensional distribution of the optical galaxies over the whole complex (Bardelli et al. 1998a);
- iii. the entire structure hosts a large number of subcondensations, as revealed by the detailed substructure analysis in Bardelli et al. (1998a).

Furthermore, the observed galaxy distribution resembles the results of the numerical simulations for the case of two colliding galaxy clusters (Roettiger, Loken & Burns 1997). This favoured the idea that the whole region may be the result of a past major merger between A3558 and another massive cluster, whose remnants

are A 3562, SC 1329–313 and SC 1327–312 (Bardelli et al. 1998b). This scenario may be supported by the very recent combined Chandra and XMM–Newton analysis of the main cluster A 3558, performed by Rossetti et al. (2006). A cold front was detected in the North–western region of the cluster by those authors, who proposed, as possible interpretation for its origin, either the *sloshing* of the A 3558 core in response to an off–axis merger with the nearby SC group or a past merger with a more massive cluster.

A detailed study of the hydrodynamic state of A 3562 and the nearby companion SC 1329–313 group was carried out by FHB04 using deep XMM–Newton observations. That work revealed that the region of A 3562 and SC 1329–313 is clearly perturbed, suggesting a recent interaction between the cluster and the group. In particular FHB04 proposed that SC 1329–313 has recently ( $\sim 1$  Gyr ago) passed North of A 3562, and induced a *sloshing* of the cluster core in the North–South direction.

## 3.2 Radio analysis

Low frequency observations of the region of A3562 and the nearby group SC 1329–313 were carried out using the GMRT at 235, 327 and 610 MHz (see Tab. 2.2 and Sec. 2.2 for details on the observations and Sec. 2.4 for the data reduction).

We produced images over a range of angular resolutions. In Section 3.2.1 we present the full resolution images of the central portion of A 3562, which show the emission from the head–tail radio galaxy J1333–3141 located (in projection) in the proximity of the cluster centre. The low resolution images, which allow to properly image and study the diffuse radio emission associated with the central radio halo, are presented and discussed in Section 3.2.2.

The details of all radio images presented here are given in Table 3.1, where the following information is reported: (1) source name, (2) frequency, (3) angular resolution (arcsec  $\times$  arcsec, position angle p.a. in degrees), (4) rms level ( $1\sigma$ ), (5) total flux density, and (6) source largest linear size (LLS, in kpc).

The 1.4 GHz radio information is from VBD03 and GVB04 for the radio halo (VLA data; Tab 2.2), and VBM00 (ATCA data; Tab 2.2) for the J1333–3141 head–tail radio galaxy, which is completely embedded in the radio halo emission. The values of the radio halo flux density in Table 3.1 refer to the diffuse emission only

Table 3.1: Details of the A 3562 images.

Source	$\nu$ MHz	HPWB, p.a. "×", °	rms mJy b <sup>-1</sup>	S <sub>tot</sub> mJy	LLS kpc
J1333–3141	1380	15.0×8.00, 26	0.10	109.3 ± 10.9	~80
	610	7.3×5.0, 7	0.15	195.7 ± 19.6	~80
	327	15.0×8.0, 26	0.30	293.3±58.7	~90
	240	17.4×11.5, 11	0.80	322.2±48.3	~90
Radio halo	1400	41.9×35.1, 55	0.05	20±2	~470
	610	30.0×20.0, 7	0.15	90±9	~470
	327	41.9×35.1, 55	0.25	195±39	~530
	240	41.9×35.1, 55	0.80	220±33	~350

and are determined after the subtraction of the J1333–3141 radio galaxy and point-like sources from the total flux density measured from the full resolution images, where they stand out well from the diffuse emission of the halo.

### 3.2.1 High resolution images

The high resolution images of the central region of A 3562 are shown in Figure 3.4. At this resolution the radio emission at the cluster centre is clearly dominated by the head–tail radio galaxy J1333–3141. This source is entirely surrounded by the extended radio halo (see low resolution images in Section 3.2.2). Residuals of the diffuse emission from the halo are clearly visible in the 235 MHz and 327 MHz images in Figure 3.4.

J1333–3141 is associated with the cluster elliptical galaxy MT 4108 ( $b_J = 17.25$ ,  $v = 14438 \text{ km s}^{-1}$ ), located at a projected distance of  $\sim 1'$  from the cluster dominant cD galaxy (VBM00). A detailed morphological and spectral analysis of this radio galaxy was carried out by VBD03, using VLA data at 330 MHz, 1.4, 4.86 and 8.46 GHz, in addition to ATCA data at 1.38 and 2.36 GHz published in VBM00. This study led to conclude that this source is the best candidate for the replenishment of the relativistic electrons which feed the radio halo (see Section 3.4).

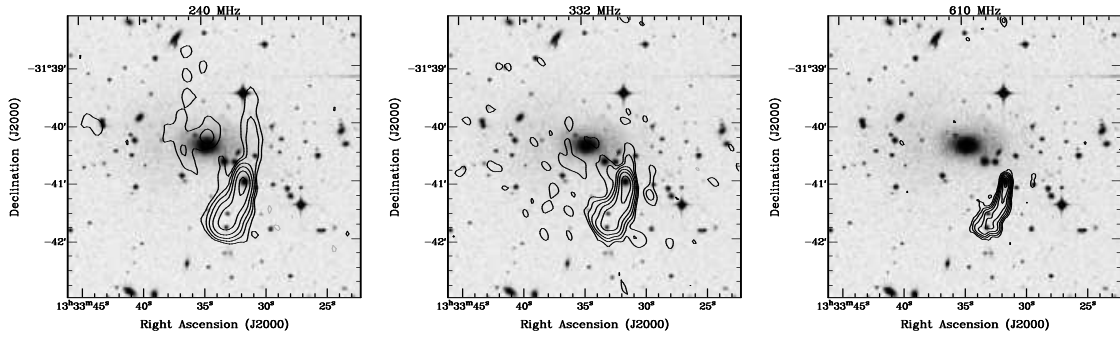


Figure 3.4: Radio contours of the high resolution images of the head–tail radio galaxy J1331–3141 at 235 MHz (left), 327 MHz (centre) and 610 MHz (right), overlaid on the DSS–1 optical frame. The  $1\sigma$  level in the image is 0.80, 0.30 and 0.15 mJy b $^{-1}$  respectively. Contours are scaled by a factor 2, starting from  $\pm 3\sigma$ . The resolution is  $17.4'' \times 11.5''$  in p.a.  $11^\circ$  at 235 MHz,  $15.0'' \times 8.0''$  in p.a.  $26^\circ$  at 327 MHz and  $7.3'' \times 5.0''$  in p.a.  $7^\circ$  at 610 MHz.

### 3.2.2 Low resolution images

At each frequency, we produced low resolution images of the A 3562 region, which are more adequate to image the diffuse emission associated with the halo. The best compromise between the low resolution needed and the sensitivity requested to reliably image and analyse the source was reached down–weighting the long spacing visibilities in order to have resolutions in the range  $30'' - 40''$ . For a proper comparison with the VLA 1.4 GHz image of the halo in VBD03 (here shown in Fig. 3.2), the 235 MHz and 327 MHz images are presented with the same resolution, i.e.  $41.9'' \times 35.1''$ , in p.a.  $55^\circ$ . Since the 610 MHz data were not used for a point–to–point analysis with the VLA 1.4 GHz data, in Figure 3.5 the 610 MHz image of the radio halo is shown with the resolution of  $30'' \times 20''$ , which better highlights the small scale features of the source.

Figure 3.6 shows the 235 MHz contours of the radio halo, and Figure 3.7 shows the radio emission at 327 MHz from the whole region of A 3562 and SC 1329–313, overlaid on the DSS–2 optical image, including both the radio halo and the diffuse source J1332–3146a in the SC group.

As clear from Figures 3.5, 3.6 and 3.7, the overall morphology of the radio halo at all frequencies shows the same irregular and complex structure, which extends along the North East–South West direction. A very faint filament of emission is detected West of the head–tail radio galaxy both in the 327 MHz and 610 MHz images. This is similar to what is found at 1.4 GHz (VBD03 and Fig. 3.2 in this

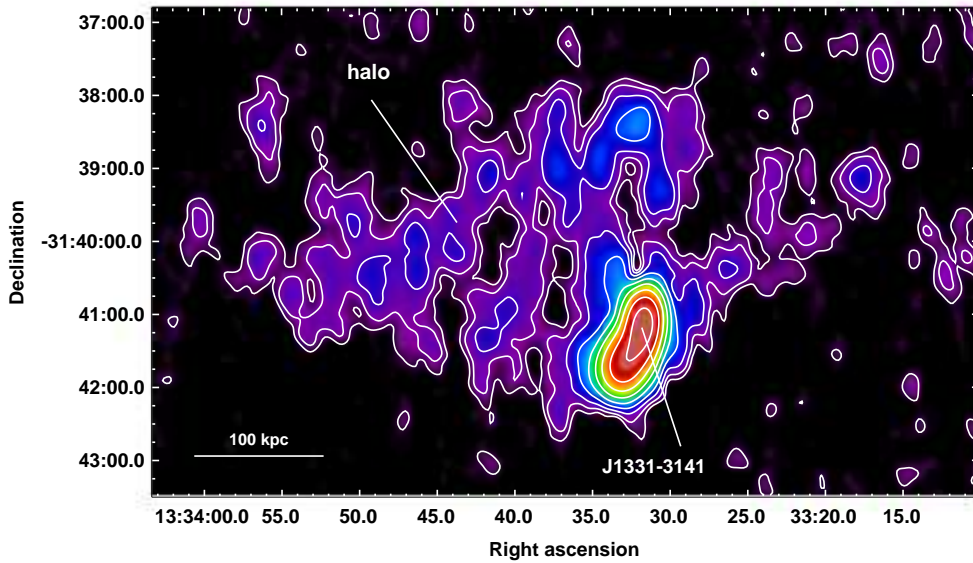


Figure 3.5: GMRT 610 MHz low resolution image (colours and contours) of the central radio halo in A 3562. The  $1\sigma$  level is  $0.15 \text{ mJy b}^{-1}$ . Contours levels are  $-0.5, 0.25, 0.5, 1.0, 2.0, 4.0, 8.0, 16.0, 32.0, 64.0 \text{ mJy b}^{-1}$ . The resolution is  $30'' \times 20''$ .

work). The largest angular size of the halo is  $\text{LLS} \sim 8'$  ( $\sim 470 \text{ kpc}$ ) at 1.4 GHz and 610 MHz, and  $\sim 9'$  ( $\sim 530 \text{ kpc}$ ) in the 327 MHz image (Tab. 3.1). Note that these values do not include the extension of the western filament.

The noise in the 235 MHz image ( $1\sigma = 0.80 \text{ mJy b}^{-1}$ ; Fig. 3.6) is considerably higher than in the other images (see Tab. 3.1), therefore the lowest contour is ten times higher than at 610 MHz (Fig. 3.5), and the total size of the halo at 235 MHz is smaller than at the other frequencies. However, there is a clear indication that the region covered by the halo emission is consistent with the morphology in Figures 3.5 and 3.7. For this reason, in order to determine the total flux density of the radio halo at 235 MHz, we integrated the measurement over the whole region of emission covered at the other three frequencies (see Tab. 3.1). This value is considerably higher than the one derived integrating only the portion of emission included in the  $3\sigma$  level (from  $\text{RA} = 13^{\text{h}}33^{\text{m}}20^{\text{s}}$  to  $13^{\text{h}}33^{\text{m}}45^{\text{s}}$ ), in support of the presence of positive residuals in this region. In particular, the flux density within the  $3\sigma$  level is  $S_{235\text{MHz}} \sim 170 \text{ mJy}$ , i.e. 60 mJy less than the value given in Table 3.1. For comparison, the flux density measured in regions of similar size outside the cluster

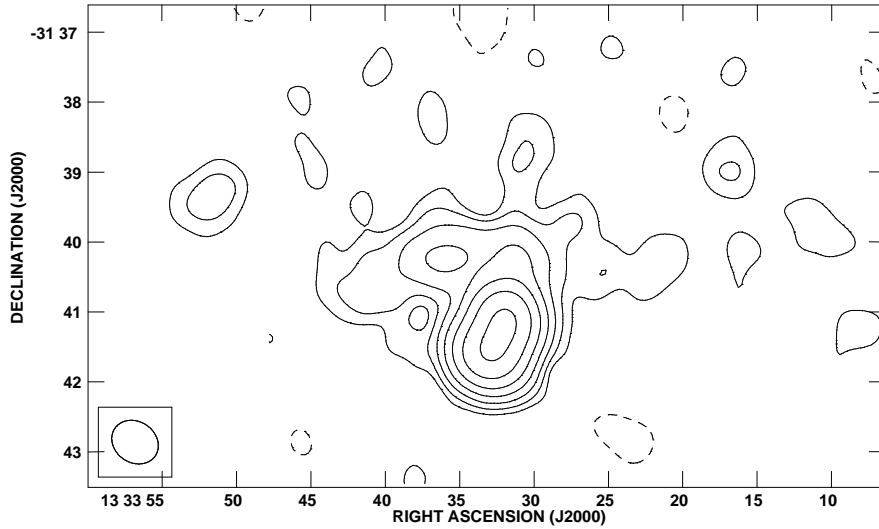


Figure 3.6: Low resolution image at 235 MHz of the central radio halo in A 3562. The resolution is  $41.9'' \times 35.1''$ . The  $1\sigma$  level is  $0.80 \text{ mJy b}^{-1}$ . Contours levels are spaced by a factor 2, starting from  $\pm 2.4 \text{ mJy b}^{-1}$ .

centre is of the order of the image noise. As a further check of our estimate of the radio halo size at 235 MHz, we integrated the flux density over an even wider region, obtaining flux density values consistent with the one given in Table 3.1 (within the errors).

The linear size of this radio halo is among the smallest found thus far. This is not unexpected, since giant radio halos (i.e. with  $LLS \gtrsim 700 \text{ kpc}$ , see Section 1.4) are usually found in massive and X-ray luminous galaxy clusters, while A 3562 does not show extreme X-ray properties (Tab. 2.1). A possible explanation for the relatively small size of the halo is discussed in Section 3.6.3.

The diffuse source J1332–3146a is visible in the bottom-right portion of Figure 3.7. This source is associated with the brightest galaxy in the group SC 1329–313. Its extended emission at 327 MHz is strongly elongated to the North-East direction and points toward the centre of A 3562. The full resolution images at 235 MHz and 327 MHz of J1332–3146a (not presented here) show no sign of the compact component associated with the optical galaxy nucleus and detected at 610 MHz (image not shown here) and at higher frequency (VBM00, GVB04, and Fig. 3.12 in this work). This suggests that the radio nucleus of the optical counterpart is self-absorbed at low frequencies, and that the extended radio emission is not connected to the present

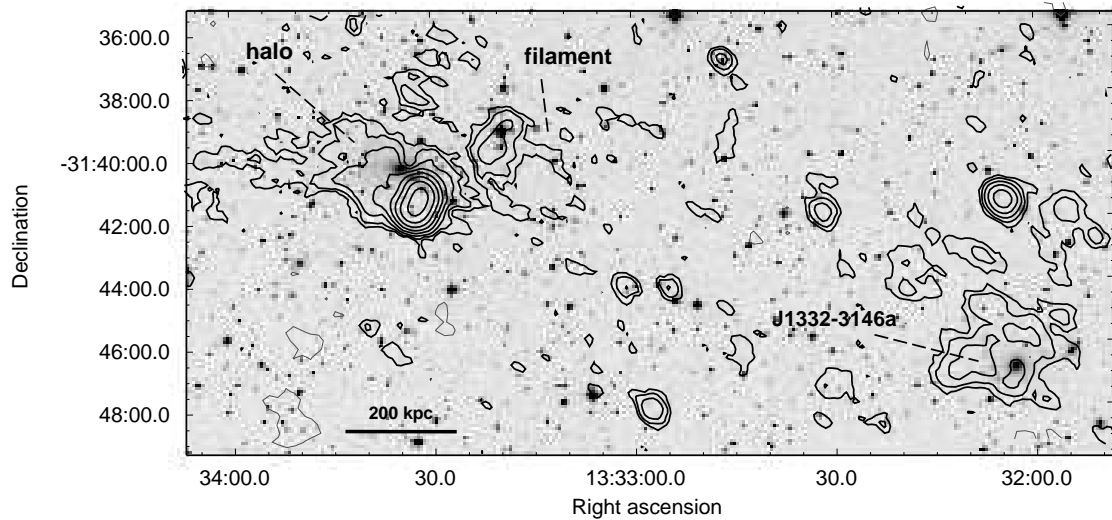


Figure 3.7: Low resolution image at 327 MHz of the region including the centre of A 3562 and the extended radio galaxy J1332–3146a (on the right) overlaid on the optical DSS–2 frame. The resolution is  $41.9'' \times 35.1''$ . Contours levels spaced by a factor 2, starting from  $\pm 1 \text{ mJy b}^{-1}$ .

activity of the AGN. We also note that the radio spectrum of J1332–3146a is steep, with a spectral index between 235 MHz and 1.4 GHz of  $\alpha = 1.2 \pm 0.1$ .

### 3.2.3 General comments on the radio emission in A 3562

The low resolution images, presented in Section 3.2.2, show that the radio emission in A 3562 is characterised by some interesting and peculiar features, and suggest some connection between the centre of A 3562 and the region of SC 1329–313. The radio halo has an irregular shape, with a filament of emission pointing South–West, i.e. toward the SC group. This is particularly clear at 327 MHz (Fig. 3.7) and at 1.4 GHz (VBD03, and also Fig. 3.12). The 327 MHz image in Figure 3.7 also shows that the source J1332–3146a is extended in the direction of A 3562, and that positive residuals (at the  $3\sigma$  level and higher) are present between these two regions. These features were noticed also at 1.4 GHz (GVB04; see also Fig. 3.12), and the combination of these two pieces of information is suggestive of the possibility that very low surface brightness emission, undetectable with the present radio instruments, permeates the whole region between the centre of A 3562 and SC 1329–313.

### 3.3 Spectral index images and integrated spectra

Spectral index imaging and integrated radio spectra are powerful tools in understanding the origin of the radio halo emission and of the re-acceleration processes on cluster scale. However, only very recently it has become possible to make images of the spectral index distribution in radio halos, and to obtain measures in the low frequency domain ( $\nu < 1.4$  GHz) of their integrated spectra. In particular, at present, spectral index maps are available for few cluster radio halos only (Feretti et al. 2004; Orrú et al. 2006; Clarke & Enßlin 2006; Orrú et al. 2007), while a good total spectrum is available only for the Coma giant radio halo (see right panel of Fig. 1.4 in Sec. 1.4; Thierbach, Klein & Wielebinski 2003), and for the central region of the radio halo in the cluster 1E 0657–56 (Liang et al. 2000).

Using the data presented here and those published in VBM00, VBD03 and GVB04, we produced the images of the spectral index distribution for the A 3562 radio halo (Sec. 3.3.1) and the head–tail radio galaxy J1333–3141 (Sec. 3.3.2), which is located (at least in projection) within the halo emission.

#### 3.3.1 Spectral properties of the radio halo

In order to determine the distribution of the spectral index over the radio halo, the GMRT image at 327 MHz (Fig. 3.7) was compared with the VLA image at 1.4 GHz (Fig. 3.2). Both images were produced with the same cell size, u–v range and restoring beam ( $41.9'' \times 35.1''$ , in p.a.  $55^\circ$ ). The images were aligned, clipped at a  $3\sigma$  level and combined to create the spectral index map within the Synage++ package (Murgia 2001). We note that the shortest baseline is the same at 327 MHz and 1.4 GHz (i.e.  $\sim 0.10$  k $\lambda$ ).

Figure 3.8 shows the spectral index image of the halo (colours) with 327 MHz contours overlaid. It is clear that the region of the head–tail J1333–3141 has a flat to normal spectrum, with  $\alpha$  in the range  $\sim 0 \div 0.7$ . The spectrum of the radio halo is steep, with an average value  $\alpha \simeq 1.5 \pm 0.1$  and knots steepening up to  $\alpha \simeq 2.0 \pm 0.2$ . Inspection of Figure 3.8 suggests that there is a clear separation between the region dominated by the head–tail and the region dominated by the halo, i.e. there is a sharp transition in the spectral index distribution of these two components, being

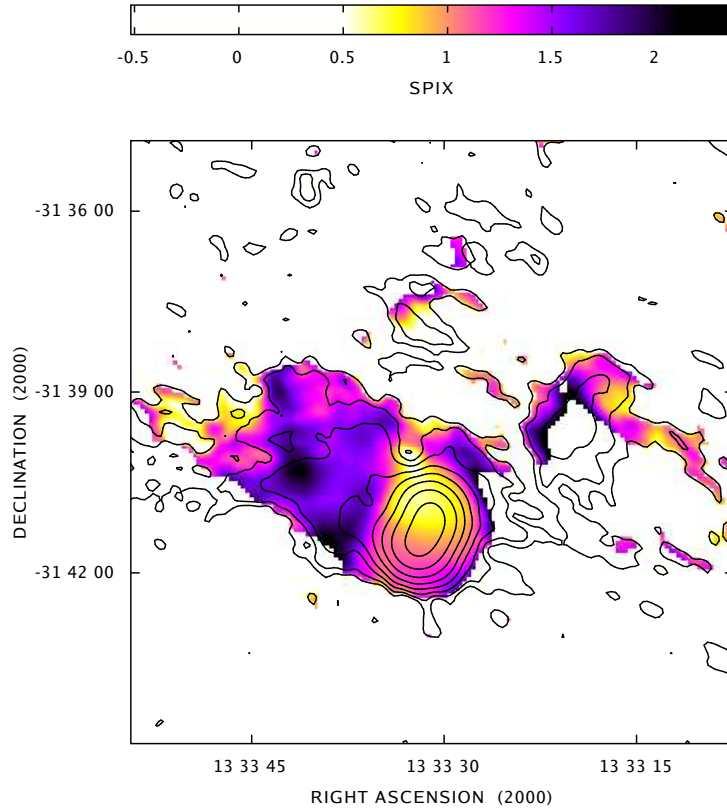


Figure 3.8: Color scale image of the spectral index distribution over the radio halo between 327 MHz and 1400 MHz, as computed from images with a restoring beam of  $41.9'' \times 35.1''$ , in p.a.  $55^\circ$ . Overlaid are the GMRT 327 MHz radio contours at levels 1, 2, 4, 8, 16, 32, 64, 128  $\text{mJy b}^{-1}$ .

the latter substantially steeper.

The integrated synchrotron spectrum of the radio halo in the frequency range 235 MHz–1400 MHz is shown in Figure 3.9 (points; see also Sec. 3.4.1 for discussion). The spectrum was determined by using the flux densities given in Table 3.1 and the MOST 843 MHz image in VBM00 (see also right panel of Fig. 3.1), who reported a flux density of  $S_{843\text{MHz}} = 59 \pm 6 \text{ mJy}$  for the halo emission. The radio spectrum of the halo appears to be very steep between 1400 MHz and 843 MHz, with a spectral index  $\alpha$  in the range  $\sim 1.9 - 2.3$  (VBD03). Between 843 MHz and 327 MHz the spectral index is  $\alpha \sim 1.3 \pm 0.2$ , and below 327 MHz the spectrum possibly flattens ( $\alpha \sim 0.4 \pm 0.7$ ).

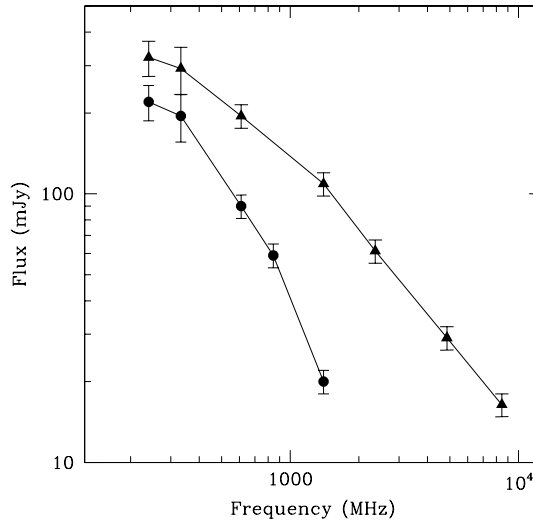


Figure 3.9: Radio spectra of the halo source (points) and of the head-tail J1333–3141 (triangles) in A3562. The 843 MHz value for the halo is from VBM00. For the head-tail, the 2.36 GHz flux density is taken from VBM00, and the 330 MHz, 4.86 GHz and 8.46 GHz values are from VBD03

### 3.3.2 Spectral properties of the head-tail radio galaxy J1333–3141

Figure 3.10 (left panel) shows the spectral index image of J1333–3141 (colours), obtained by comparison of the GMRT 327 MHz image and the ATCA image at 1.4 GHz (contours; VBM00), produced with the same cell size,  $u$ - $v$  range and restoring beam ( $15.0'' \times 8.0''$ , in p.a.  $26^\circ$ ). As described for the radio halo in Section 3.3.1, the images were aligned and clipped at the  $3\sigma$  level before combining them.

The spectral index distribution clearly shows that we are dealing with a tailed radio galaxy. The flattest region ( $\alpha \sim 0$ ) is coincident with the core region imaged at high resolution and high frequency in VBD03 (e.g. the VLA 8.46 GHz image reported in the right panel of Fig. 3.10, where the core is labelled as C). The significant transverse steepening corresponds to the beginning of the tail (the peak in the 1.4 GHz image). The spectral index smoothly steepens along the tail up to a value of  $\sim 1$ .

The total synchrotron spectrum of the source J1333–3141 in the frequency range 235 MHz–8.46 GHz is shown in Figure 3.9 (triangles). The spectrum can be described as a power law with  $\alpha = 0.96 \pm 0.04$  between 610 MHz and 8.46 GHz, with a flattening at frequencies  $\nu < 327$  MHz. Figure 3.9 also highlights the well known different spectral shape of halo sources and extended radio galaxies at frequencies

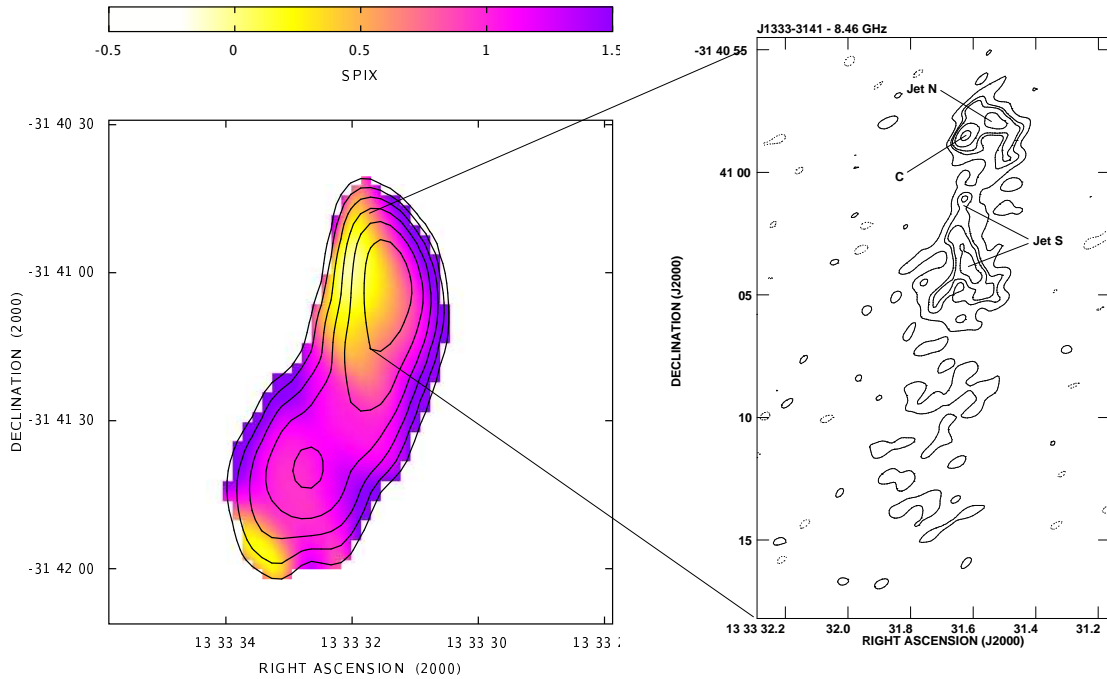


Figure 3.10: *Left panel* – Colour scale image of the spectral index distribution over the head–tail radio galaxy J1333–3141, between 327 MHz and 1380 MHz, as computed from images with a restoring beam of  $15.0'' \times 8.0''$ , in p.a.  $26^\circ$ . Overlaid are the ATCA 1.4 GHz radio contours at levels 0.5, 1.0, 2.0, 4.0, 8.0, 16.0  $\text{mJy b}^{-1}$ . *Right panel* – VLA 8.46 GHz image of J1333–3141. The resolution is  $0.88'' \times 0.51''$ , in p.a.  $-53^\circ$ . Contours are -0.09, 0.09, 0.18, 0.23, 0.32, 0.54  $\text{mJy b}^{-1}$ . The peak in the image is 0.64  $\text{mJy b}^{-1}$ . C is the radio core, jet N and jet S indicate the northern and western jets respectively (from VBD03).

$\nu > 330$  MHz (e.g. the halo source Coma–C in Fig. 1.4 and low luminosity radio galaxies, Parma et al. 2002).

### 3.4 Origin of the radio halo

As discussed in Section 1.9, a promising possibility for the explanation of radio halos is provided by electron re–acceleration due to merger–driven turbulence. In this case the main feature of the synchrotron spectrum emitted by these electrons is the steepening at high radio frequencies, provided that the maximum energy of the accelerated electrons is of the order of the energy of the radio emitting electrons.

### 3.4.1 Study of the integrated radio spectrum

Figure 3.11 shows the energy spectrum ( $\nu - \nu F(\nu)$ ) of the radio halo in A 3562 (see Sec. 3.3.1) compared to the expectations from different models for the origin of the radio emitting electrons (see Figure caption).

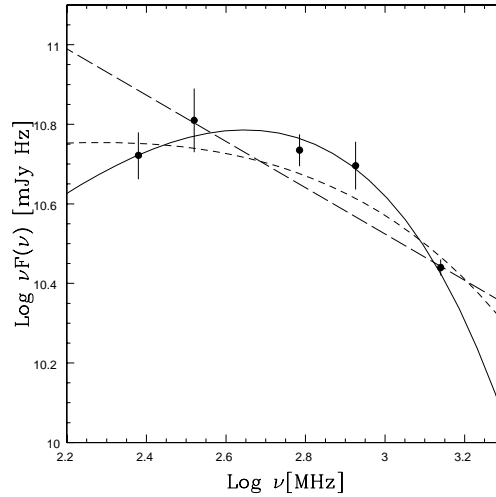


Figure 3.11: Energy spectrum of the radio halo in A 3562 compared with the expectations from three models for the origin of the emitting electrons. The *long dashed line* represents the emission from a power law energy distribution of the emitting electrons; this model is normalized at the 327–1400 MHz emission. The *short dashed line* is a turbulent–acceleration model of electrons which are accelerated and emit in a region which is larger than the typical scale of variation of the magnetic field intensity (the slope of the model is similar to what is reported in Brunetti 2004, Fig. 21). The *solid line* is obtained assuming that particles are accelerated with a fixed acceleration efficiency and emit in a region of constant magnetic field intensity.

Despite the relatively large error bars at low frequencies, the data points and their statistical trend strongly constrain the current models for the formation of this radio halo. It is clear that the observations are not consistent with a simple power law spectrum (long dashed line in Fig. 3.11), as expected, for example, from secondary models (Sec. 1.8). The A 3562 halo shows a steepening of the radio spectrum with frequency: this provides evidence for widespread particle acceleration in the emitting region. In the specific particle turbulent–acceleration model, which seems to better describe the observed spectral behaviour (solid line in Fig. 3.11), it is assumed that the electrons are accelerated and emit in a region where the magnetic field strength is approximately constant (reasonably assumed of the order of  $\mu\text{G}$ ). This implies that the scale of the diffuse radio source is comparable to (or smaller than) the scale

of the variation of the magnetic field intensity in the ICM.

The magnetic field in the ICM is believed to be amplified during the cluster formation mostly due to dynamo amplification and shear flows and thus its strength should decrease with distance from the cluster centre. Detailed MHD numerical simulations show that the radial profile of the field intensity in massive clusters is expected to be almost flat in the core region, and it rapidly decreases with distance (Dolag et al. 2002). The average size of the halo in A 3562 is of the order of the cluster core radius and this is consistent with the above scenario in which particles are emitting in a region with a relatively uniform magnetic field intensity.

### 3.4.2 Origin of the radio emitting electrons

The head–tail radio galaxy J1331–3141 is completely embedded (in the plane of the sky) in the radio halo emission (see Fig. 3.5). Hence it is the best candidate to provide the electron population in the central part of the cluster.

VBD03 computed the number of electrons the radio galaxy injected in the intracluster medium in order to check if it is high enough to feed the halo. They found that this number is sufficient if the galaxy has been radio active over a considerable fraction of the time  $t_{\text{cross}}$  needed to cross the halo region ( $\sim 470$  kpc), where  $t_{\text{cross}} \sim 5 \times 10^8$  years, assuming that the galaxy velocity is of the order of the dispersion velocity in the cluster ( $\sigma_v = 987$  km s $^{-1}$ , Bardelli et al. 1998b).

## 3.5 X-ray versus radio analysis

In order to complete the analysis of the A 3562 radio halo and understand its origin and connection to the cluster merger history, a composite X/radio analysis was performed by using (a) the radio image at 1.4 GHz first presented in VBD03; (b) XMM–Newton data presented in FHB04; (c) Chandra observations (Ettori et al. in preparation). We refer to Table 2.4 for the details on the X–ray observations.

### 3.5.1 X–radio morphological comparison

Figure 3.12 shows the overlay of the radio contours at 1.4 GHz on the XMM–Newton mosaic of the A 3562 region, obtained by FHB04 in the 0.8–2 keV band.

In Figure 3.13 the radio emission of the halo at 1.4 GHz is compared with the pseudo–entropy (upper panel) and pseudo–pressure (lower panel) images of A 3562,

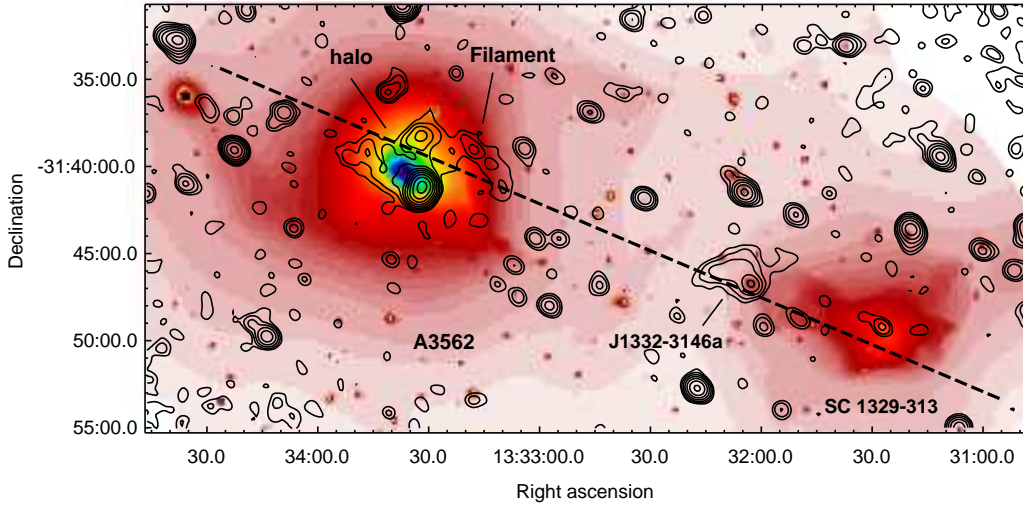


Figure 3.12: VLA–1.4 GHz contours of the radio emission from A 3562 and SC 1329–313, superposed to the XMM–Newton mosaic in the 0.8–2 keV band. The  $1\sigma$  level in the radio image is  $50 \mu\text{Jy b}^{-1}$ . The radio contours are spaced by a factor 2, starting from  $\pm 0.15 \text{ mJy b}^{-1}$ . The resolution of the radio image is  $41.9'' \times 35.1''$ , in p.a.  $55^\circ$ .

derived by FHB04 and defined as  $S = T/\sqrt[3]{I}$  and  $P = T \times \sqrt{I}$  respectively (Churazov et al. 2003; Briel, Finoguenov & Henry 2003), where  $I$  is the surface brightness in the 0.8–2 keV band and  $T$  is the temperature.

Figure 3.12 clearly indicates that A 3562 and SC 1329–313 *feel each other* both in the radio and X–ray bands. In particular:

- i) the X–ray brightness of A 3562 is slightly elongated toward SC 1329–313, whose emission strongly points to the centre of A 3562;
- ii) the weak filament of radio emission at the western end of the halo points toward SC 1329–313, while the extended emission of J1332–3146a (located at the border of the X–ray emission of SC 1329–313) is strongly elongated toward A 3562;
- iii) the radio halo extends mostly in the North–East direction;
- iv) the radio and X–ray emission in A 3562, the radio galaxy J1332–3146a and the X–ray emission of SC 1329–313 are almost perfectly aligned, as indicated from

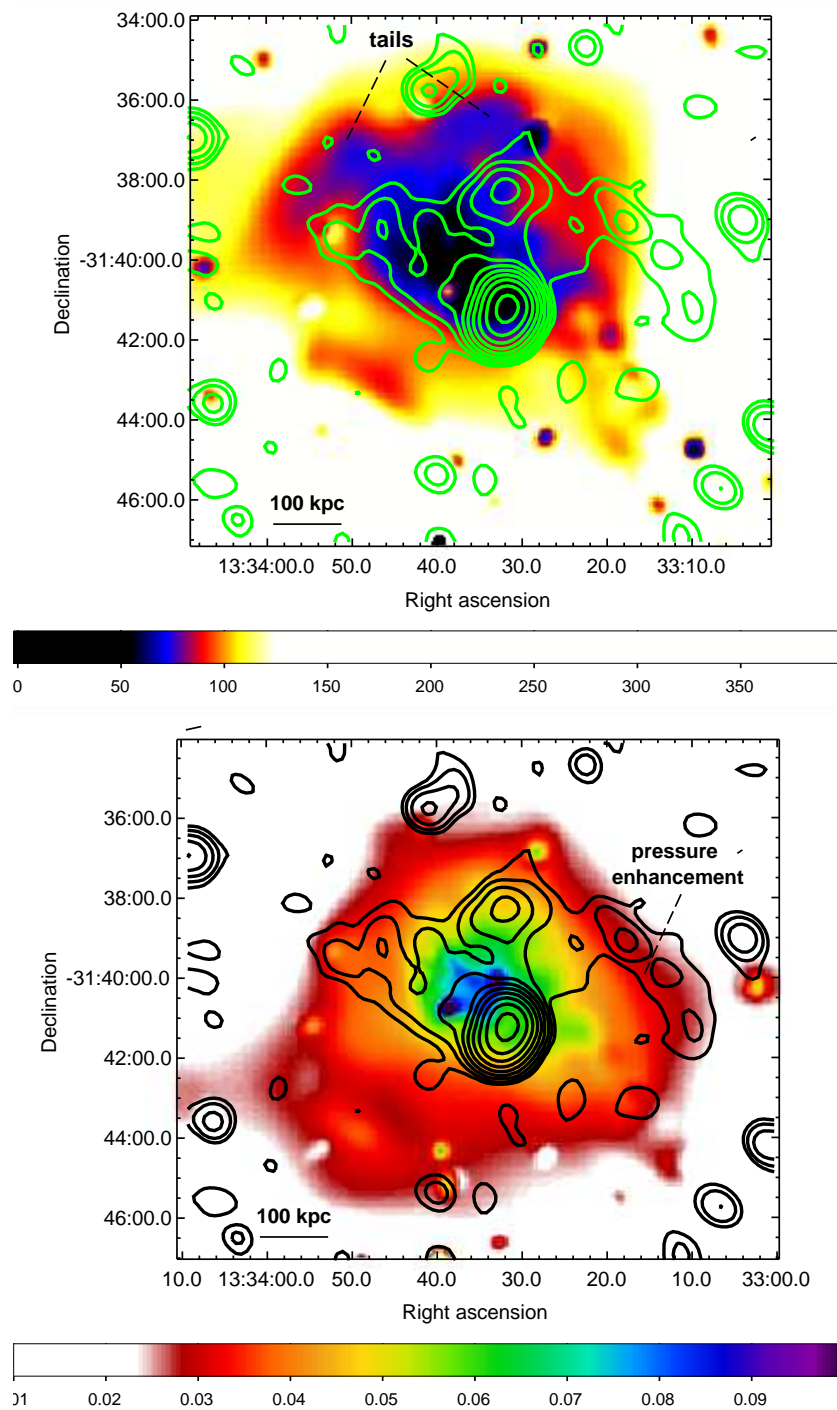


Figure 3.13: VLA-1.4 GHz image of the radio halo at the centre of A 3562, overlaid on the XMM-Newton pseudo-entropy (upper panel) and pseudo-pressure (lower panel) images of the cluster. The radio image is the same as Figure 3.12.

the dashed line in Figure 3.12.

Figure 3.13 zooms into the A 3562 centre. It is noteworthy that the pressure

(lower panel), the entropy (upper panel), and the halo radio emission extend to North–East with respect to the cluster centre. The inner region of the pseudo–entropy distribution shows two tails toward North. Hereinafter, these features will be referred to as pseudo–entropy tails. The South–Eastern part of the radio halo has a sharp edge, and closely follows the morphology of the entropy image.

From the lower panel of Figure 3.13, it is also evident that the western radio filament pointing to South–West remarkably follows (at least in projection) the region of enhanced gas pressure discussed in FHB04.

### 3.5.2 Point–to–point comparison

A point–to–point analysis of the radio (1.4 GHz flux density and 327–1400 MHz spectral index) and the X–ray (surface brightness, temperature, entropy, pressure) quantities was performed, by using both the Chandra and XMM–Newton data.

Following Govoni et al. (2001b), we constructed a grid covering the cluster region, and the mean radio and X–ray quantities were determined for every grid cell, as well as the root–mean–square (rms), which can be assumed as an estimate of the error. The whole analysis has been carried out using the IDL and the Synage++ packages. In order to perform a proper comparison, an image of the halo after subtraction of the central head–tail J1333–3141 was used. In Figure 3.14 the radio halo 1.4 GHz emission (after subtraction of the head–tail) is shown as contours, superposed to the Chandra X–ray surface brightness image. The figure also reports the grid used for the analysis, which covers the whole region of the X–ray emission. The size of each grid cell is  $70'' \times 70''$ , and was chosen in order to select statistically independent regions.

As noted in the comparison between the radio halo and the XMM–Newton images (Sec. 3.5), a strong spatial correlation is found between the radio halo emission and the inner region of the emission from the X–ray plasma.

The presence of correlation between radio and X–ray quantities was investigated through a Spearman test, which evaluates a rank correlation coefficient  $r_s$  on given data arrays. The absolute value of  $r_s$  can range between 0 (no correlation is present) and 1 (perfect correlation). The test returns also  $P_{sp}$ , the two–sided significance of the agreement of the rank correlation coefficient  $r_s$  with the null–hypothesis of

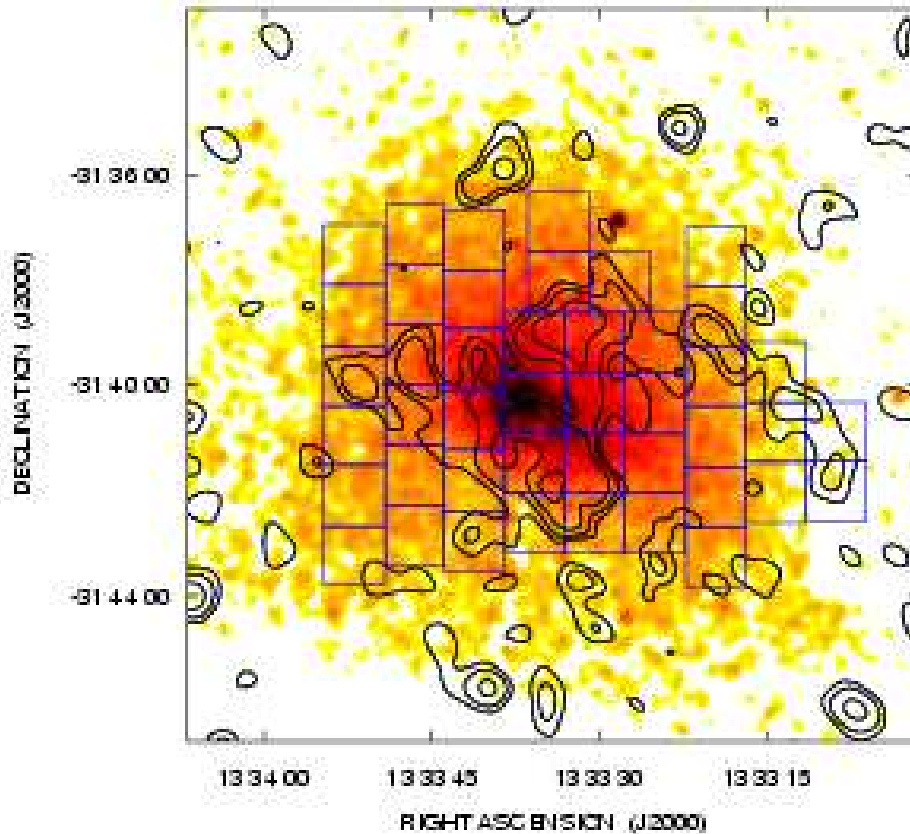


Figure 3.14: Grid used for the comparison of the radio and X-ray images of the cluster A 3562. The size of each grid cell is  $70'' \times 70''$ . The grid is overlaid on the Chandra X-ray surface brightness image (colour). Contours represent the VLA-1.4 GHz image of the halo, after subtraction of the central head-tail J1333-3141. Radio contours are spaced by a factor 2, starting from  $0.15 \text{ mJy b}^{-1}$ . The angular resolution of the radio image is  $41.9'' \times 35.1''$ . The X-ray image has been obtained from the Chandra raw image (resolution  $2'' \times 2''$ ) after a smoothing with a box of  $60''$  width.

no-correlation between the data arrays. A small value of  $P_{sp}$  indicates a significant (anti-)correlation if  $r_s$  is (negative) positive.

The most significant correlation is given by the Chandra X-ray surface brightness versus the radio flux density at 1400 MHz (Fig. 3.15). In the figure filled triangles represent the data from the cells with radio emission; filled dots represent the data from the cells which cover the western filament. For completeness some upper limits (not included in the statistical analysis) are also shown, which represent cells with no detected radio emission above the  $1\sigma$  level. For these two quantities  $r_s = +0.65$  is found; the probability that the relative distribution of values

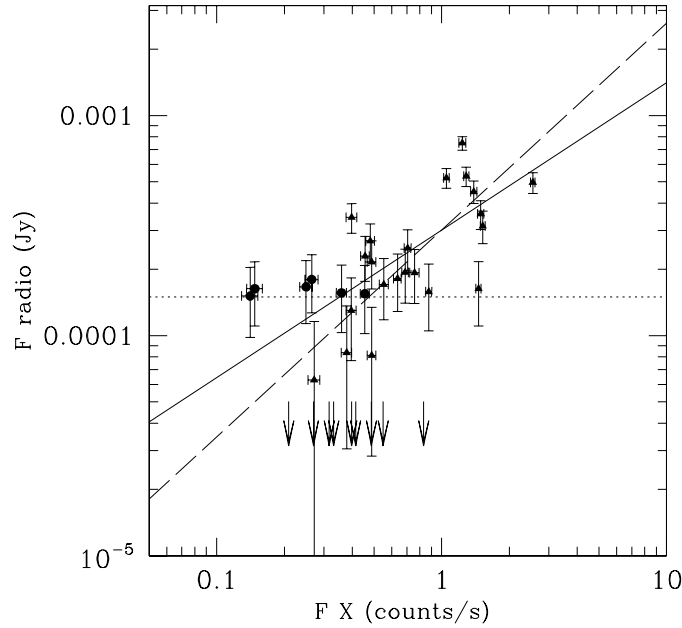


Figure 3.15: Relation between the radio flux density at 1.4 GHz and the Chandra X-ray flux for the cluster A3562. Data points represent the mean flux density in each cell of the grid constructed over the cluster region (Fig.3.14). The error-bars are the rms of flux distribution. The filled dots indicate the values derived for the grid cells containing the weak filamentary structure of the radio halo extending toward South-West. The upper limits represent cells with no detected radio emission above the  $1\sigma$  level. The dotted line is the radio  $3\sigma$  level. The solid line is the best fit of the data including all the boxes. The long-dashed line is the best fit obtained excluding the western filament.

is not correlated is  $P_{\text{sp}} = 1.5 \times 10^{-4}$ . In this case the weighted best fit is given by  $\log F_{\text{radio}} = (0.67 \pm 0.12) \log F_X - (3.52 \pm 0.05)$ , which is consistent with a sub-linear correlation, as found in some other radio halos (Govoni et al. 2001b). A correlation between the radio flux and X-ray brightness is also confirmed by the analysis of the XMM-Newton data. It is worth noticing that if the western filament of the halo is excluded from the statistical analysis, the significance of the correlation slightly decreases to  $r_s = +0.60$  ( $P_{\text{sp}} = 3.3 \times 10^{-3}$ ), meaning that the filament plays a marginal role in the overall significance of the  $F_{\text{radio}} - F_X$  correlation, while the slope of the correlation steepens from sub-linear to linear, with  $\log F_{\text{radio}} = (0.94 \pm 0.13) \log F_X - (3.52 \pm 0.05)$  (Fig. 3.15).

Furthermore, higher radio flux densities are measured in regions with lower values of the X-ray gas temperature and entropy levels ( $r_s \sim -0.6$ ), and higher gas pressure estimates ( $r_s \sim +0.6$ ). A weak evidence ( $|r_s| \leq 0.4$ ) for a spatial

correlation between the spectral index image of the radio halo (Fig. 3.8) and the projected X-ray quantities was detected. Note that these results do not depend on the choice of the position of the boxes used to cover the cluster emission (Fig. 3.14), providing different configurations very similar results.

### 3.6 Cluster merger and origin of the diffuse radio emission

In the framework of the re-acceleration scenario for the origin of radio halos (Sec. 1.9), it has been pointed out that, independently of the details of the turbulence injection process during a cluster merger, magneto-sonic (MS) waves with scales  $< 100$  kpc may efficiently accelerate relativistic electrons in the ICM up to the energies ( $\gamma \sim 10^4$ ) required to emit the synchrotron radiation observed in the radio band (Cassano & Brunetti 2005).

Given the high quality of the X-ray and radio data and the evidence for particle re-acceleration from the halo integrated radio spectrum (Sect. 3.3.1), we attempt to explain the origin of the diffuse radio emission in A 3562 as due to electron acceleration driven by the turbulence generated by the merger between A 3562 and SC 1329–313.

The proposed scenario for the origin of the radio halo is based on the following points.

- 1) *Merger Kinematics* – Making use of several arguments, FHB04 derived the kinematics of the collision between SC 1329–313 and A 3562. They suggested that about 1 Gyr ago SC 1329–313 passed  $\sim 500$  kpc North of the core of A 3562 (corresponding to  $\sim 0.25$  virial radii, see Tab. 2.1) coming from East, with a relative velocity of the order of  $1700 \text{ km s}^{-1}$ , and it was gravitationally deflected toward the southwestern direction. The mass ratio between A 3562 and SC 1329–313 is 3:1 (Ettori, Fabian & White 1997). As a consequence of this passage, the core of A 3562 acquired a velocity component in the North–South direction, and it started *sloshing*, with an oscillation amplitude of the order of  $\sim 200$  kpc and a period of  $\sim 1$  Gyr (FHB04).
- 2) *Magnetic field and Merger* – The change of the core velocity at the oscillation apogee causes the escape of low-entropy gas. This produces the entropy tails, as discussed in FHB04 (see also the upper panel of Fig. 3.13). Since the

magnetic field is frozen into the thermal plasma, it is expected that the escape of the gas should flatten the profile of the field strength toward the region North of the A 3562 core.

- 3) *Turbulence and particle acceleration* – Another expected by-product of the interaction between SC 1329–313 and A 3562 is the injection of turbulence in the ICM (Sec. 1.1.2). Although the injection mechanism of the turbulence is very complex and depends on many unknown parameters, it is expected that large scale turbulence may be efficiently injected in the volume swept by the head of SC 1329–313 (i.e. by the self bounded subclump which is gradually stripped during the crossing of the main cluster by the effect of the ram pressure) and in the central region of A 3562 by the North–South oscillation of the core. As shown by analytical arguments and by numerical simulations (see Sec. 1.1.2), once injected these large scale eddies diffuse through a larger volume so that one may reasonably assume that turbulence fills at some level the region of the core of A 3562 and a large fraction of the volume between the cores of the two subclusters (actually from the bridge toward the North).

The effect of the turbulence on the process of particle acceleration and amplification of the magnetic field depends on the strength of the turbulence in this region. Provided that a fraction  $\eta_{\text{MS}} \sim 0.005 - 0.1 \times (10^{-3}/n_{\text{th}})(10^8/T)$  (being  $n_{\text{th}}$  the number of thermal particles) of the thermal energy of the ICM is channelled into MHD waves (depending on the specific MHD mode; see Brunetti 2004 and Cassano & Brunetti 2005), this may switch on the diffuse radio emission observed near the centre of A 3562.

### 3.6.1 Self-consistency of re-acceleration

If electrons are re-accelerated, as indeed suggested by the curved radio spectrum of A 3562 (Fig. 3.11), similar to the Coma radio halo (right panel of Fig. 1.4; Thierbach, Klein & Wielebinski, 2003), then the source age can be estimated by the cascading time-scale of the turbulence injected on the scales of the instabilities generated during the merging process.

The decay time scale of the MS waves is approximately  $\tau_{kk} \sim v_{\text{MS}}/kv_k^2$  (e.g. Yan & Lazarian 2004), where  $v_{\text{MS}}$  is the magnetosonic velocity,  $v_k$ <sup>1</sup> is the velocity of

---

<sup>1</sup>We used  $v_k^2 \sim \eta_{\text{MS}} \frac{E_{\text{th}}}{2\rho}$  ( $\rho$  = density of the thermal ICM,  $E_{\text{th}}$  = thermal energy) using a Kraichnan

the turbulent eddies and  $k$  is the wavenumber. Given the physical conditions in the ICM of A 3562, it is:

$$\tau_{kk}(\text{Gyr}) \simeq 0.7 \frac{L}{\text{Mpc}} \eta_{MS}^{-1} \quad (3.1)$$

where  $\eta_{MS} = E_{MS}/E_{th}$  is the ratio between the energy in the form of MS waves and the thermal energy in the emitting region ( $\eta_t \sim 0.2 - 0.9$  in Cassano & Brunetti 2005 is a few times  $\eta_{MS}$  here), and  $L$  is the maximum injection scale of the MHD turbulence.

The analysis of the entropy map (upper panel of Fig. 3.13) limits the scale of the Rayleigh–Taylor instabilities, driven by the core oscillation, to  $\sim 500$  kpc; the corresponding cascading time–scale (Eq. 3.1) is  $\tau_{kk} = 0.7 \left(\frac{\eta_{MS}}{0.5}\right)^{-1}$  Gyr; this should be considered a lower limit, since the oscillation of the core (and hence the growth of the instabilities) is still ongoing.

At the same time, large scale turbulence may be injected at the passage of SC 1329–313 North of the A 3562 core. In this case, the initial scale of the instabilities should be of the order of the diameter of the core of SC 1329–313, and thus the cascading time should be  $\sim 1$  Gyr. Note that both these cascading time scales are of the order of the time scale of the merging, and of the core oscillation in A 3562 (FHB04).

Thus the proposed scenario is self–consistent: there is enough time for the development of a turbulence cascade, necessary for particle acceleration; at the same time, the epoch of turbulence injection is recent enough to expect that turbulence is not yet completely dissipated at present.

### 3.6.2 Observational evidence

The observed correlations between radio and X–ray quantities (Sec. 3.5) support the proposed scenario.

- If turbulence is injected by the passage of SC 1329–313 through the cluster volume and by the oscillation of the A 3562 core, then it should be fairly uniform on several hundreds kpc scale. Thus, if the energy density of the turbulence is smaller than that of the thermal plasma, its intensity should not significantly depend on the X–ray quantities (e.g. temperature and thermal

---

spectrum.

density). In this case, once the relevant wave-damping processes are taken into account (e.g. Cassano & Brunetti 2005), the efficiency of the particle acceleration due to MS waves should scale with the temperature as  $1/\sqrt{T}$  and thus an anticorrelation between the non-thermal emission and the higher temperature patches is expected.

- On the other hand, since the magnetic field  $B$  is frozen into the ICM, higher synchrotron emissivity ( $\propto B^2$ ) is expected in regions with higher density  $n_{\text{th}}$ , provided that relativistic electrons are accelerated in these regions. Thus the significant correlation between radio and X-ray ( $\propto n_{\text{th}}^2$ ) flux could be driven by this effect.
- The freezing of the magnetic field into the ICM could also account for the observed anti-correlation between the radio flux and the entropy, provided that higher values of  $B$  are found in regions with lower entropy.
- Similarly, the observed correlation between the radio flux and the thermal pressure is expected if the measured values of the pressure are mainly determined by the values of the gas density.

### 3.6.3 The extent of the radio emission

The observed extent of the radio emission is slightly smaller than the entropy tails of A 3562. As discussed in Section 1.9.1, cluster mergers may efficiently power giant radio halos in the case of massive clusters only, with  $M \geq 10^{15} M_{\odot}$ . A 3562 is slightly below this mass threshold ( $M_V \simeq 6 \times 10^{14} M_{\odot}$ ), and the presence of a giant radio halo is indeed not expected. In this case, however, it might be supposed that diffuse synchrotron emission may be revealed on smaller scales in the cluster core region and toward the North of the core, where the strength of the magnetic field is likely to be stronger and possibly amplified by the interaction between the cluster and the nearby group.

The clear steepening of the radio spectrum (Fig. 3.11) strengthens this interpretation, since it proves that the energy of the electrons accelerated in the core region is just sufficient to emit synchrotron radiation up to frequencies around 1 GHz.

Given the shape of the observed radio spectrum, we point out that even assuming

that the acceleration efficiency is maintained outside the radio emitting region, a drop in the magnetic field strength by a factor of  $\sim 2$  outside this region would cause a sharp decrement of the synchrotron emissivity at 610 MHz, i.e. a factor of  $\sim 7 - 8$ .

#### 3.6.4 A radio bridge between the radio halo and J1332–3146a?

Figure 3.7 and the 1.4 GHz images presented in Figure 3.12 show outstanding features of extended radio emission. In particular, the western filament of the radio halo, the extension of J1332–3146a in the direction of the A 3562 centre, and the presence of positive residuals of radio emission at 1.4 GHz and 327 MHz are all perfectly aligned. Furthermore, the radio/XMM–Newton overlay of Figure 3.12 shows that the X–ray emission is also aligned along the same direction.

The scenario proposed in Section 3.6 could account for these observed signatures, at least at a qualitative level. It seems reasonable to expect that the motion of SC 1329–313 to South–West and the gravitational interaction with A 3562 have actually produced a *channel* of turbulence, which may have affected the ICM and relativistic particles over the whole distance between the group and the cluster. If this is the case, the energy rate injected into MHD modes along the bridge should be roughly of the order of  $\gtrsim 5 \times 10^{-29} \text{ erg s}^{-1} \text{ cm}^{-3}$  (here, for simplicity, we assume MS waves and a reference value of  $B \sim 0.5 \mu\text{G}$  and  $T \sim 5 \times 10^7 \text{K}$ ), which immediately would imply that the fluid turbulence in this low density region should be strong, from slightly subsonic to mildly supersonic depending on the efficiency of the radiation process of MS waves.

The radio images suggest that the western filament and the extension of J1332–3146a are the peaks of a bridge of very low brightness extended radio emission, which happens to be below the sensitivity limits of the current radio interferometers. This was noticed also in GVB04, based on 1.4 GHz data. The new GMRT data, in particular the 327 MHz image, further strengthen this possibility. We note that the spectrum of J1332–3146a is steep, with  $\alpha = 1.2$  between 235 MHz and 1.4 GHz, which is consistent with what is found in cluster–type radio sources such as halos and relics (Sec. 1.3).

### 3.7 Summary of the A 3562 analysis

We presented and discussed the low-frequency GMRT images at 235 MHz, 327 MHz and 610 MHz of the radio halo at the centre of A 3562.

The most important results of these observations, obtained by combining them with the 1.4 GHz VLA data published in VBD03 and GVB04, and the Chandra and XMM–Newton X-ray observations carried out by Ettori et al. (in prep.) and FHB04 respectively, can be summarised as follows:

- 1) A 3562 is characterized by extended radio emission on the cluster scale in the form of a radio halo;
- 2) the halo in A 3562 is among the smallest found thus far. Its LLS is of the order of  $\sim 500$  kpc at all the observed frequencies from 1.4 GHz to 327 MHz;
- 3) the point-to-point spectral index image of the halo between 327 and 1400 MHz shows a complex structure. Beyond the existence of a region with an average value of  $\alpha \sim 1.5 \pm 0.1$ , there are a number of knots steepening up to  $\sim 2.0 \pm 0.2$ . Our images also show that the spectrum of the electron populations of the radio halo and of the tailed source J1333–3141 embedded in it are clearly different;
- 4) with all the available data we could derive the integrated radio spectrum of the halo in the range 235 MHz–1.4 GHz, with 5 data points. The spectrum is very steep between 1400 MHz and 843 MHz, with a spectral index  $\alpha$  in the range  $\sim 1.9 - 2.3$  (VBD03). Between 843 MHz and 327 MHz the spectral index is  $\alpha \sim 1.3 \pm 0.2$ , and below 327 MHz the spectrum possibly flattens to  $\alpha \sim 0.4 \pm 0.7$ . We also derived the spectrum for the extended source J1332–3146a, and found that it is also steep, with  $\alpha = 1.2 \pm 0.1$  in the 235 MHz–1.4 GHz frequency range;
- 5) the radio and X-ray images show that A 3562 and the group SC 1329–313 *feel each other*, i.e. the extended features of the two regions point toward each other in both bands. Beyond the presence of a radio halo at its centre, the radio galaxy J1332–3146a (located South–West of A 3562) shows low brightness extended emission in the direction of the radio halo, suggestive of a possible connection between the two features. This possibility is reinforced by the

presence of positive residuals between the two diffuse radio sources both at 327 MHz and at 1.4 GHz (GVB04);

- 6) a spatial correlation is found between the radio halo and the quantities derived from the XMM–Newton and Chandra observations, like the X–ray surface brightness, the temperature, the pseudo–entropy and pseudo–pressure maps. All the observables show an extension toward North, and a sharp edge South of the core region in A 3562. A significant point–to–point linear positive correlation holds between the 1400 MHz flux density of the halo and the X–ray flux density. Such correlation is expected, given the correlations observed between the halo emission and the pseudo–pressure and pseudo–entropy maps of A 3562. Furthermore, the western filament of the radio halo, pointing to South–West, follows remarkably (at least in projection) a region of enhanced gas pressure.

These results provide further observational support to a scenario of cluster merger between A 3562 and SC 1329–313. In particular, the radio halo in A 3562 may be the result of particle re–acceleration induced by turbulence injected in the ICM by the passage of SC 1329–313 North of the core of A 3562, and by the oscillation of the cluster core in the North–South direction. The proposed scenario may explain the properties of the radio halo, including its relatively small size, the morphology and extent of the pseudo–entropy tails as derived from the XMM–Newton observations, as well as the statistical correlations between the radio and X–ray observables.

We further speculate that the alignment of the western filament of the radio halo with the extended emission around J1332–3146a and the positive residuals of radio emission between the centre of A 3562 and the group SC 1329–313, are also related to the turbulence induced by this merger event.

It has been shown that cluster mergers involving massive ( $M > 10^{15} M_{\odot}$ ) and luminous ( $L_X > 10^{45} \text{ erg s}^{-1}$ ) clusters may develop the energy and turbulence required to produce Mpc–scale radio emission, in the form of giant radio halos (Cassano & Brunetti 2005; see also Sec 1.9.1). On the other hand, it might be expected that slightly less massive systems may also produce diffuse radio emission, although less extended and less powerful than that of giant radio halos. Indeed, the case of A 3562 shows that merger events involving clusters with mass  $M \sim 6 \times 10^{14} M_{\odot}$  may produce signatures in the radio band, at a level comparable to the detection

limit of the instrumentation currently available. Therefore we expect that future observational facilities, such as LOFAR and the Square Kilometre Array (SKA), will substantially contribute to our knowledge and understanding of the cluster merger phenomenon.



## Chapter 4

# The giant radio halo in A 209

Abell 209 is a richness class R=3, X-ray luminous and massive galaxy cluster ( $L_{X[0.1-2.4\text{keV}]} \sim 6 \times 10^{44} \text{ erg s}^{-1}$ , virial mass  $M_v \sim 1.6 \times 10^{15} M_{\odot}$ ) at the redshift  $z=0.206$ . Its main properties are reported in Table 2.1.

The cluster is known to be currently undergoing a strong dynamical evolution. The presence of a merging process, involving two or more massive subclusters, is suggested by the extensive optical studies in the literature (Mercurio et al. 2003 and 2004b, hereinafter MGB03 and MBM04 respectively; Mercurio 2003; hereinafter M04; Haines et al. 2004). This scenario is supported also by the X-ray data (Rizza et al. 1998; MGB03 and M04), and by the results of the weak lensing analysis (Dahle et al. 2002; Paulin-Henriksson et al. 2007).

At radio wavelengths, the possible presence of cluster scale diffuse emission in A 209 was pointed out by Giovannini, Tordi & Feretti (1999) on the basis of the 1.4 GHz image from the NVSS (here shown in Fig. 4.1 on the POSS-2 optical image). The image suggests the existence of extended emission at the cluster centre (cross in the figure), however its presence is uncertain, due to the strong discrete radio sources, which are unresolved at the resolution of the NVSS ( $45'' \times 45''$ ). The existence of such diffuse emission, in the form of a giant radio halo, was confirmed by VLA 1.4 GHz data (Giovannini et al. 2006) and by our GMRT 610 MHz observations (Venturi et al. 2007; this work), performed as part of the GMRT Radio Halo Survey (Sec. 1.12).

In this Chapter we carry out a thorough multiband study of the radio halo and of the merging environment in A 209 by using our 610 MHz data (Tab. 2.2), combined

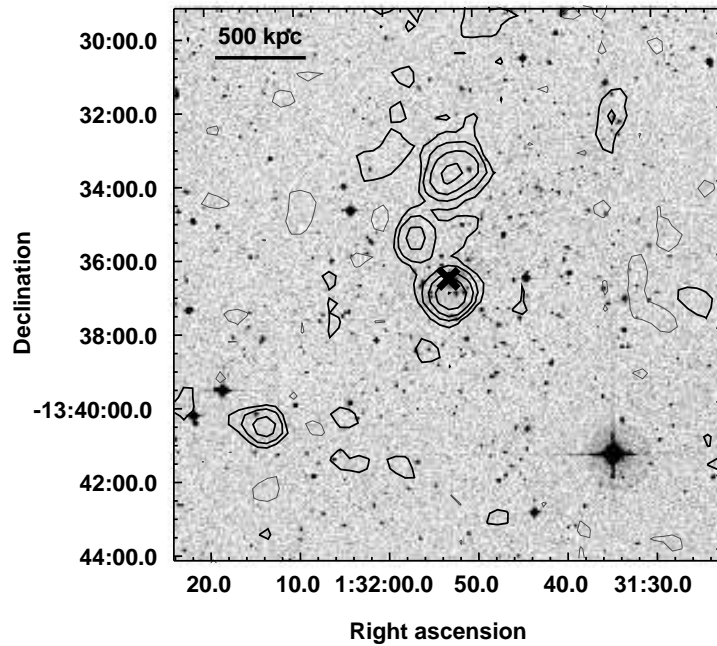


Figure 4.1: 1.4 GHz NVSS image of A 209, overlaid on the POSS-2 optical frame. The  $1\sigma$  level in the image is  $0.45 \text{ mJy b}^{-1}$ . Contour levels are spaced by a factor 2, starting from  $\pm 1 \text{ mJy b}^{-1}$ . The resolution is  $45'' \times 45''$ , p.a.  $0^\circ$ . The cross indicates the X-ray centre of the cluster (Tab. 2.1).

with the optical information from the literature and APM survey (Maddox et al. 1990), and X-ray Chandra observations from the public archive (Tab. 2.4).

The Chapter is organised as follows: in Section 4.1 we summarise the main results of the optical, X-ray and weak-lensing studies performed in the literature, which provide evidence for a recent merger in A 209; in Section 4.2 we present our GMRT 610 MHz observations and study the radio halo properties; in Section 4.3 we re-analyse the X-ray archival Chandra observations of the cluster; the optical analysis of the galaxy distribution as derived from the APM is given in Section 4.4; the combined X-ray/optical analysis of the cluster is carried out in Section 4.5, where we also analyse the radio halo in connection with the X-ray properties of the hosting cluster; the proposed merging scenario and the connection between the halo and the ongoing merger are discussed in Sections 4.6 and 4.7 respectively.

At the redshift of A 209 ( $z=0.206$ ), the cosmology adopted in this work leads to a linear scale of  $1'' = 3.38$  kpc.

#### 4.1 The merging environment of A 209

The optical properties of A 209 were investigated in detail using ESO–New Technology Telescope (NTT) observations by MGB03, and with the Canada–France Hawaii Telescope (CFHT) data by MBM04. All those studies point toward a young dynamical state for this cluster, which is likely to have recently experienced a strong merger event.

The main results of the optical analysis in MGB03 and MBM04 supporting such scenario can be summarised as follows:

- i. the cluster is characterised by a very high value of the line of sight velocity dispersion ( $\sigma_v \sim 1400$  km s<sup>-1</sup>; also reported in Tab. 2.1);
- ii. the galaxy velocity distribution is better described by the contribution of three Gaussians, rather than one single component. These velocity clumps are located at the mean redshifts 0.199, 0.208 and 0.215;
- iii. the intermediate and high velocity clumps are also segregated in the projected distribution of member galaxies, being the high velocity galaxies located in the southeastern region of the cluster, and the low velocity ones in the northwestern part;
- iv. a velocity gradient is present in the NW/SE direction, i.e. along the axis connecting the two main redshift clumps;
- v. the bright ( $R < 19.5$ ) and faint ( $R > 19.5$ ) galaxies are spatially segregated. The bright ones are centered around the dominant cD galaxy, while the fainter galaxies show many clumps aligned South–East of the cD;
- vi. the halo of the central cD galaxy is elongated in the NW/SE direction.

The above results indicate that the cluster has a preferential NW/SE direction in the optical band. This is also true for the cluster X–ray properties. The X–ray emission, as detected by ROSAT HRI (Rizza et al. 1998), Chandra (MGB03 and

M04a; this work) and XMM–Newton (Marty et al. 2003; Paulin–Henriksson et al. 2007; see also right panel of Fig. 4.2) is elongated along such direction. Furthermore the cluster X–ray images show two peaks of emission along the same NW/SE axis. The main one is approximately coincident with the peak of the brightest galaxies, while the secondary peak is likely associated with the main optical clump of fainter galaxies, located South–East of the cD (MGB03).

The weak lensing analysis carried out by Dahle et al. (2002) and more recently by Paulin–Henriksson et al. (2007) shows that the major axis of the reconstructed mass distribution is roughly aligned with the optical and X–ray axis (see Fig. 4.2). However, the centres of the X–ray emission, dark matter and galaxy distribution all appear offset from each other, as clear from Figure 4.2. In particular, the figure indicates that the centre of the mass distribution (red diamond) lies between the X–ray and galaxy distribution centres. This result was interpreted as evidence for a recent merging process between two subclusters along the NW/SE axis, where the X–ray, optical and mass distribution offsets may be due to the different behaviour of the dark matter, galaxies and gas during a merging process.

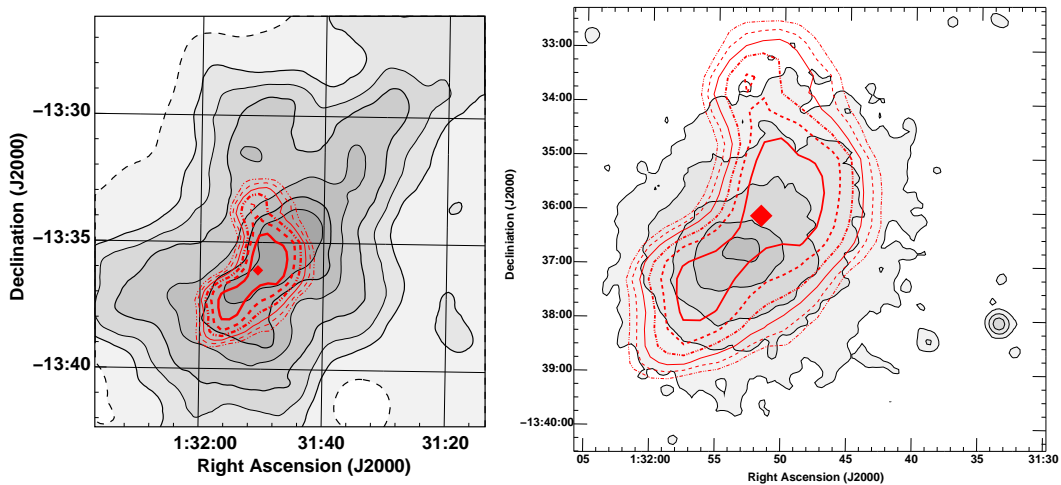


Figure 4.2: Comparison of the weak lensing mass reconstruction with the galaxy distribution (left panel) and X–ray XMM–Newton image (right panel) for A 209 from Paulin–Henriksson et al. (2007). The red isodensity contours correspond to mass densities from  $5 \times 10^{13} M_{\odot} \text{ arcmin}^{-2}$  (thin dot–dashed curve) to  $1 \times 10^{14} M_{\odot} \text{ arcmin}^{-2}$  (thick solid curve), with each contour separated by  $1 \times 10^{13} M_{\odot} \text{ arcmin}^{-2}$ . The red diamond indicates the cluster centre of mass. *Left panel* – The grey scale filled black contours are the surface density of  $R < 23.0$  galaxies, corresponding to 0 (dashed curve), 2 (solid), 3.3, 5, 7.5, 10.0 and 12.5 cluster galaxies  $\text{arcmin}^{-2}$ . *Right panel* – The grey scale filled black contours are the X–ray emission, as detected by XMM–Newton. The X–ray contours are spaced by a factor 2.

To summarise, all the observational properties of A 209 suggest that the main cluster, which hosts the cD, is currently merging with a massive subclump along the NW/SE axis. The presence of a velocity gradient supports the idea that the process is not occurring in the plane of the sky. Furthermore, both the weak lensing analysis and the strong luminosity segregation found in the bi-dimensional galaxy distribution suggest an advanced stage for the merger (as found for example for the Coma cluster by Biviano et al. (1996), where a similar luminosity segregation is observed). The brightest galaxies are in fact expected to trace the cores of the merging subclusters, whose high density allows them to survive for a relatively long time after the merging (e.g. the numerical simulations by González-Casado, Mamon & Salvador-Sole 1994).

## 4.2 The giant radio halo

### 4.2.1 GMRT 610 MHz observations

A 209 was observed using the GMRT at 610 MHz, as part of the REFLEX subsample selected for the GMRT Radio Halo Survey (Sec. 1.12). We observed the cluster for a total of  $\sim 4$  hours, and obtained a sensitivity of  $1\sigma = 60 \mu\text{Jy b}^{-1}$  in the full resolution image ( $8.0'' \times 5.0''$ ). The details of the observations are given in Table 2.2 and Section 2.2. The data reduction was carried out as described in Section 2.4.

The 610 MHz image of the radio emission from A 209 at the resolution of  $21.0'' \times 18.0''$  is presented in Figure 4.3. The solid circle has a radius corresponding to the cluster virial radius ( $R_V \sim 2.7$  Mpc; Tab. 2.1), and the dashed circle indicates the region covered by the optical analysis in MGB03 and MGM04 (Sec. 4.1).

The whole cluster virial region appears rich of discrete radio sources. At the cluster centre, a chain of sources extends in the North–South direction. Hints of a bridge of low surface brightness emission connecting these sources are also visible in the image.

Figure 4.4 shows the radio contours of the central portion of A 209 at two different resolutions, both superposed to the POSS–2 optical image. A number of individual radio sources is detected, labelled from A to H in the figure. We searched for optical identification by inspecting the POSS–2 image, and by using the spectroscopic catalogue in MGM04 and the APM information. The source list is given in Table 4.1, which reports the radio position, the 610 MHz flux density

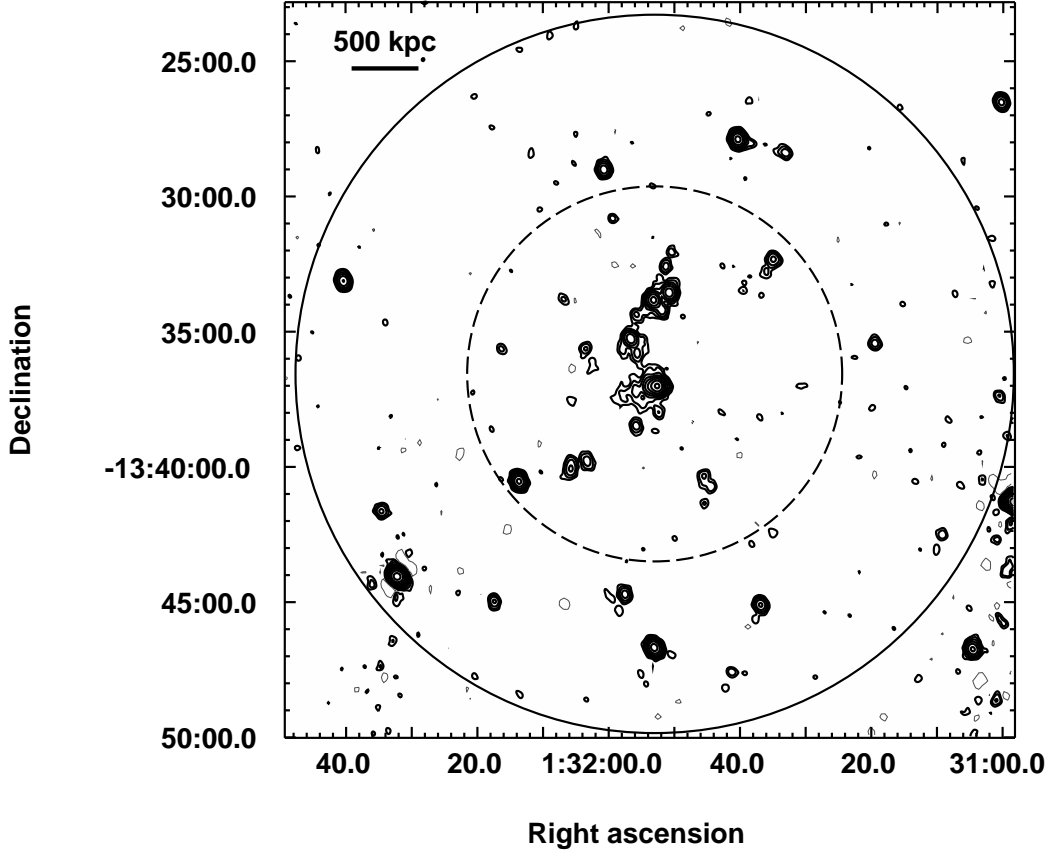


Figure 4.3: GMRT 610 MHz radio contours of the central  $25' \times 25'$  region containing A 209. The  $1\sigma$  level in the image is  $50 \mu\text{Jy b}^{-1}$ . Contour levels are scaled by a factor 2, starting from  $\pm 0.2 \text{ mJy b}^{-1}$ . The resolution is  $21.0'' \times 18.0''$ , p.a.  $13^\circ$ . The solid circle is centered on the X-ray centre of the cluster, and has a radius corresponding to the virial radius  $R_v = 13.28'$  (i.e. 2.69 Mpc). The dashed circle is the region covered by the optical analysis in MGB03 and MGM04.

measured on the full resolution image (upper panel of Fig. 4.4), the optical catalogue and the coordinates, magnitude  $R$  and redshift of the optical counterpart. As clear from Table 4.1, all sources have an optical counterpart, except for the double source C (Fig. 4.4), which has no associated optical object either on the POSS-2 plate or in the optical catalogues. Among the optically identified radio sources, 4 are located at the redshift of A 209 (A, B, F and H), while no redshift information is available for the others.

In addition to the individual radio galaxies listed in Table 4.1, positive residuals of radio emission are visible in the region between the head-tail radio galaxy A and source C in the high resolution image of Figure 4.4 (upper panel), suggesting

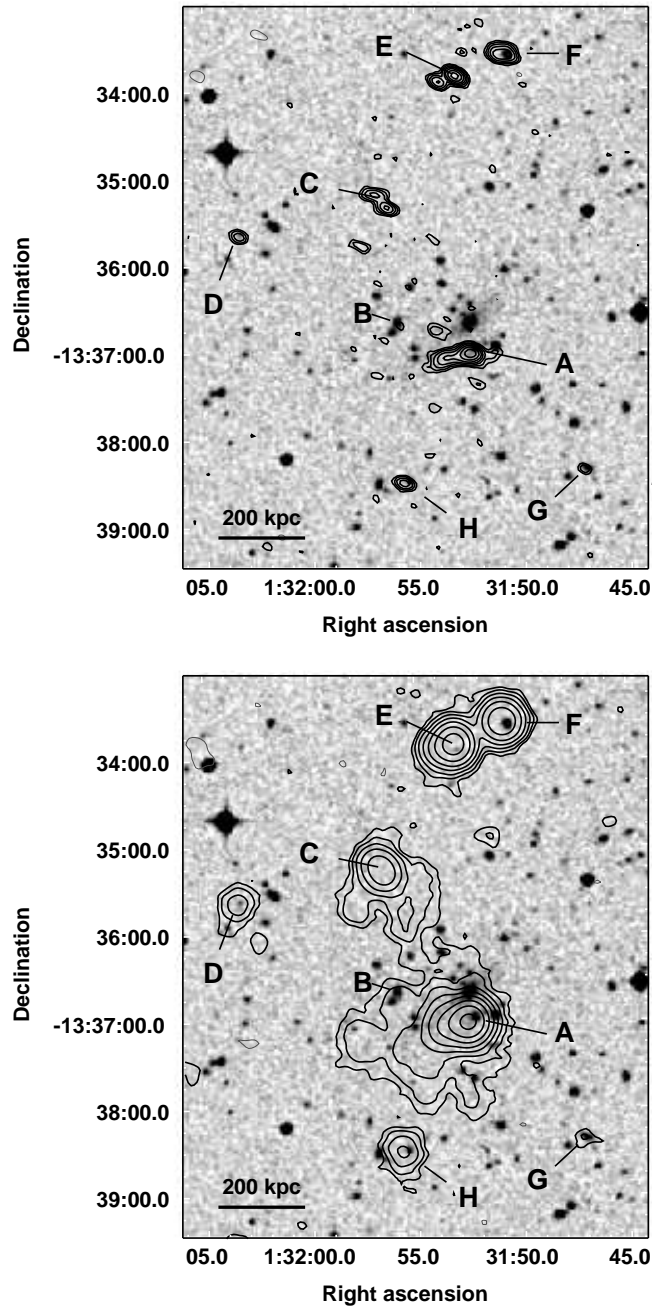


Figure 4.4: GMRT 610 MHz radio contours of the central region of A 209, overlaid on the POSS-2 optical plate. The  $1\sigma$  level is  $60 \mu\text{Jy b}^{-1}$ . Contours are spaced by a factor 2, starting from  $\pm 0.18 \text{ mJy b}^{-1}$ . The individual radio galaxies are labelled from A to G. *Upper panel* – The resolution is  $8.0'' \times 5.0''$ , p.a.  $64^\circ$ . *Lower panel* – The resolution is  $18.0'' \times 17.0''$ , p.a.  $0^\circ$ .

the presence of extended emission with a very low surface brightness. The image at the resolution of  $18.0'' \times 17.0''$ , given in the lower panel of Figure 4.4, confirms

Table 4.1: Individual radio galaxies at the A 209 centre.

Radio source	Radio position		$S_{610 \text{ MHz}}$ mJy	Optical catalogue	Optical Position		R	z
	RA <sub>J2000</sub>	DEC <sub>J2000</sub>			RA <sub>J2000</sub>	DEC <sub>J2000</sub>		
A	01 31 52.5	-13 37 01	42.4	MGM04#54	01 31 52.3	-13 36 58	17.19	0.202
B	01 32 55.8	-13 36 42	0.3	MGM04#64	01 31 55.9	-13 36 40	17.66	0.200
C	01 31 56.7	-13 35 16	6.9	—	—	—	—	—
D	01 32 03.4	-13 35 39	1.4	APM	01 32 03.4	-13 35 38	19.79	—
E	01 31 53.6	-13 33 52	22.2	APM	01 31 53.0	-13 33 54	20.77	—
F	01 31 50.8	-13 33 36	12.4	MGM04#46	01 31 50.6	-13 33 36	17.28	0.206
G	01 31 47.2	-13 38 22	0.6	APM	01 31 47.0	-13 38 21	17.86	—
H	01 31 55.7	-13 38 30	2.6	MGM04#63	01 31 55.5	-13 38 29	18.34	0.214

the presence of a diffuse radio component embedding the central head-tail (A) and extending toward C.

In order to highlight such extended component, we produced a low resolution image ( $32.0'' \times 30.0''$ ) of the diffuse emission only. The image, shown in Figure 4.5, was obtained after subtraction of all the individual sources visible in the high resolution image from the u-v data.

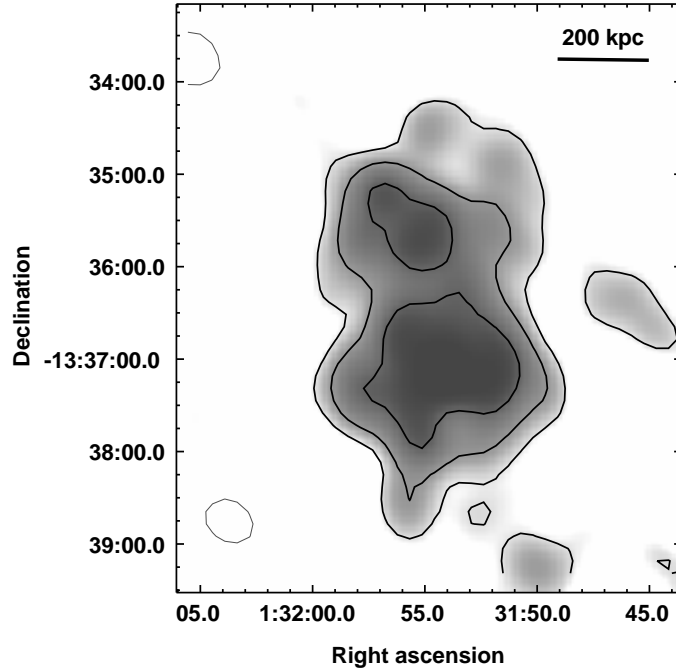


Figure 4.5: GMRT 610 MHz gray scale and radio contours of the giant radio halo in A 209 after subtraction of the individual sources (from A to H in Fig. 4.4). The resolution is  $32.0'' \times 30.0''$ , p.a.  $30^\circ$ . The  $1\sigma$  level in the image is  $150 \mu\text{Jy b}^{-1}$ . Contours are spaced by a factor 2, starting from  $\pm 0.35 \text{ mJy b}^{-1}$ .

Table 4.2: Properties of the giant radio halo in A 209

$S_{610\text{ MHz}}$ (mJy)	$24.0 \pm 3.6$
$\log P_{610\text{ MHz}}$ ( $\text{W Hz}^{-1}$ )	24.46
Largest Angular Size (arcmin)	$\sim 4$
Largest Linear Size (Mpc)	$\sim 810$ kpc

Figure 4.5 indicates that the diffuse emission extends on the cluster scale, permeating the whole central region of A 209. Its largest angular size is  $\sim 4'$ , which corresponds to a largest linear size  $\text{LLS} \sim 810$  kpc at the redshift of the hosting cluster. Such extent, coupled with its central location, implies that this source belongs to the class of giant radio halos (i.e.  $\text{LLS} \gtrsim 700$  kpc; Sec. 1.4). The main properties of the halo are given in Table 4.2.

The halo morphology in Figure 4.5 is elongated in the North–South direction. Unlike many giant radio halos known in the literature, which usually exhibit a roughly regular flux density distribution peaked at the cluster centre (see for example Fig. 1.5 in Sec. 1.4), this source shows an unusual surface brightness distribution, characterised by two peaks of emission. This peculiar morphology may be partially due to the difficulty to subtract the extended individual sources embedded in the halo emission, in particular the head–tail radio galaxy A, located just South of the cluster centre (see upper panel in Fig. 4.4)

Our image in Figure 4.5 is in partial agreement with the size and morphology of the VLA 1.4 GHz image shown by Giovannini et al. (2006), where a largest linear size exceeding the Mpc scale is reported.

The halo flux density, measured after subtraction of the individual radio sources (Fig. 4.4; Tab. 4.1) is  $S_{610\text{ MHz}} = 24.0 \pm 3.6$  mJy, which implies a total radio power of  $\log P_{610\text{ MHz}}(\text{W Hz}^{-1}) = 24.46$  (also reported in Tab. 4.2). The difficulty in subtracting the extended radio galaxies in Fig. 4.4 (upper panel) reflects the large error associated with the flux density measurement.

Additional GMRT 610 MHz observations were carried out for A 209 in August 2006, in order to better image and study the central radio halo, as well as to understand the reason of the discrepancy between our image (Fig. 4.5) and the VLA 1.4 GHz image in Giovannini et al. (2006). The data reduction is still in progress.

### 4.3 X-ray Chandra Analysis

In the light of the new results in the radio band (Sec. 4.2), we re-analysed the two X-ray Chandra observations of A 209 available in the public archive (Obs.Id 522 and 3579, performed during the Chandra periods C and D respectively; see Tab. 2.4 for the observation details). The 522 observation (i.e. the oldest one) was studied also by MGB03 and M04 (Sec. 4.1). Here we present and discuss only the results obtained from the combined analysis of the two observations relevant for the study of the radio halo and its connection with the merging environment of A 209.

The two datasets were reprocessed separately as described in Section 3.5.2, and then combined together to study the cluster X-ray surface brightness distribution (Sec. 4.3.1) and for the spectral analysis (Sec. 4.3.2).

#### 4.3.1 Image analysis

The wavelet-reconstructed image of the cluster X-ray emission in the 0.5–5.0 keV energy range is shown in the left panel of Figure 4.6. The image was produced by applying the wavelet decomposition tool (Vikhlinin et al. 1998) the image obtained by the sum of the images (both background subtracted and exposure map divided) from the two different observations of the cluster (see Sec. 2.6.1 for details).

As clear from Figure 4.6, the X-ray surface brightness distribution shows a complex structure, with a *jellyfish-like* shape elongated in the NW/SE direction. At the cluster centre three distinct peaks of emission are detected by the wavelet analysis.

A zoom on this region is given in the right panel of Figure 4.6, where the X-ray contours are superposed to the optical frame from the POSS-2. The dashed white ellipses indicate the position of the peaks detected in the X-ray image given in the left panel. The central brightest peak is roughly coincident with the central cD galaxy, as already found by MGB03 and M04 (Sec. 4.1). The south-eastern peak was detected also by those authors, who suggested a possible association with the main optical clump of faint galaxies, located South-East (in the plane of the sky) of the central cD (Sec. 4.1). Our analysis led to detect a third small substructure West of the cD galaxy. No obvious identification with any galaxy or optical clump is found for this peak.

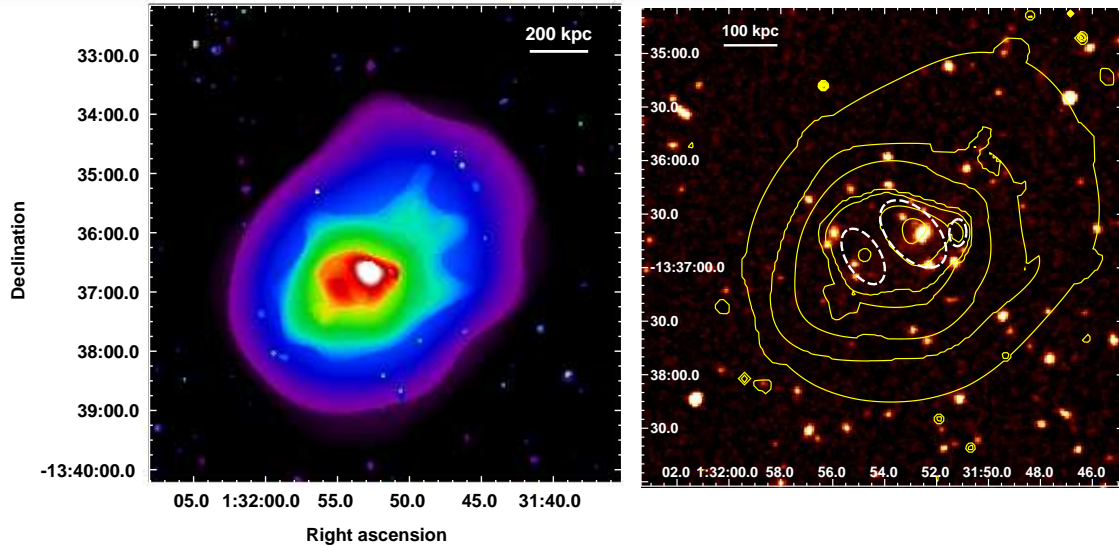


Figure 4.6: *Left panel* – Wavelet-reconstructed Chandra image of A 209 in the 0.5–5 keV band. The image is divided for the exposure map and background subtracted. *Right panel* – X-ray contours of the inner part of the image given in the left panel, overlaid on the optical image of the central region of A 209 from the POSS-2. Contour levels are logarithmically spaced by a factor  $\sqrt{2}$ . The dashed ellipses indicate the three substructures detected by the wavelet analysis.

### 4.3.2 Spectral analysis

The spectra were extracted separately for the two observations, along with the relative ARF and RMF files, and then fitted simultaneously as described in Section 2.6.1. The adopted energy range is 0.8–8.0 keV and the model used for the fit is the absorbed thermal model *wabs mekal* available in the XSPEC package. We fixed the local absorption to the Galactic neutral hydrogen column density  $N_{\text{H}} = 1.6 \times 10^{20} \text{ cm}^{-2}$ , as estimated from the radio data (Dickey & Lockman 1990). The redshift parameter was fixed to the cluster value  $z=0.206$ . Background spectra were extracted using the blank sky observations corresponding to the periods of the two observations (Sec. 2.6.1). The  $\chi^2$  statistics was used to evaluate the goodness of the best-fit models. A consistency check of the results was carried out comparing them with the spectral results obtained using the Cash statistics. All errors are given at the 90% confidence level.

#### Cluster average temperature

We determined the average temperature of A 209 by extracting the spectrum from each observation within a circular region with radius  $r=3'$  ( $\sim 600 \text{ kpc}$ ) and centered

on the main X-ray peak (upper panels in Fig. 4.7).

The extracted spectra were grouped to obtain a minimum of 20 counts per bin and then they were fit simultaneously. The spectra and the best fit models are shown in the lower panel of Figure 4.7. The best fit temperature and abundance values are given in Table 4.3, where we also report the reduced  $\chi^2$ , degree of freedom and null hypothesis probability of the best-fit model (see Sec. 2.6.1 for details). No significant difference was found using a local background instead of the blank sky observations. Furthermore, we obtained very consistent results using the Cash statistics.

Our estimate of the cluster temperature ( $T = 7.4_{-0.4}^{+0.6}$ ) is not consistent with the higher value  $T = 10.2_{-1.2}^{+1.4}$  keV obtained by MGB03 and M04 within the same  $3'$  radius circular region using the Chandra 522 observation only, i.e. the oldest among the currently available datasets (Tab. 2.4). The reason of such discrepancy is unclear. MGB03 and M04 do not provide the relevant details which would be needed for a careful comparison, such as for example the version of the Chandra calibration database used to re-process the data and the energy range adopted for the spectral fit.

On the other hand, significant discrepancies in the temperature values estimated by the same Chandra observations but re-processed with old and new CALDB versions, are reported in the literature for some galaxy clusters (e.g. MS 1054–0321, Jeltema et al 2001, Gioia et al. 2004 and Jee et al. 2005), especially if the observations were carried out during period C, as the 522 observation of A 209.

A preliminary spectral analysis of archival XMM–Newton observations of A 209 (Obs. Id. 0084230301; Giacintucci et al. in preparation) provides a temperature  $T=7.3_{-0.5}^{+0.6}$  within the same  $3'$  radius region. This value is in very good agreement with our Chandra result.

### Hardness ratio image

In order to search for possible substructures in the gas temperature distribution, we produced the hardness ratio image of the cluster, as described in Section 2.6.1.

We created two images (one for each Chandra observation) in the 0.2–2.5 keV energy band, both background subtracted and vignetting corrected, and summed them to obtain the *soft* image of the cluster. The same procedure was applied to produce the cluster *hard* image in the 2.5–5 keV energy range.

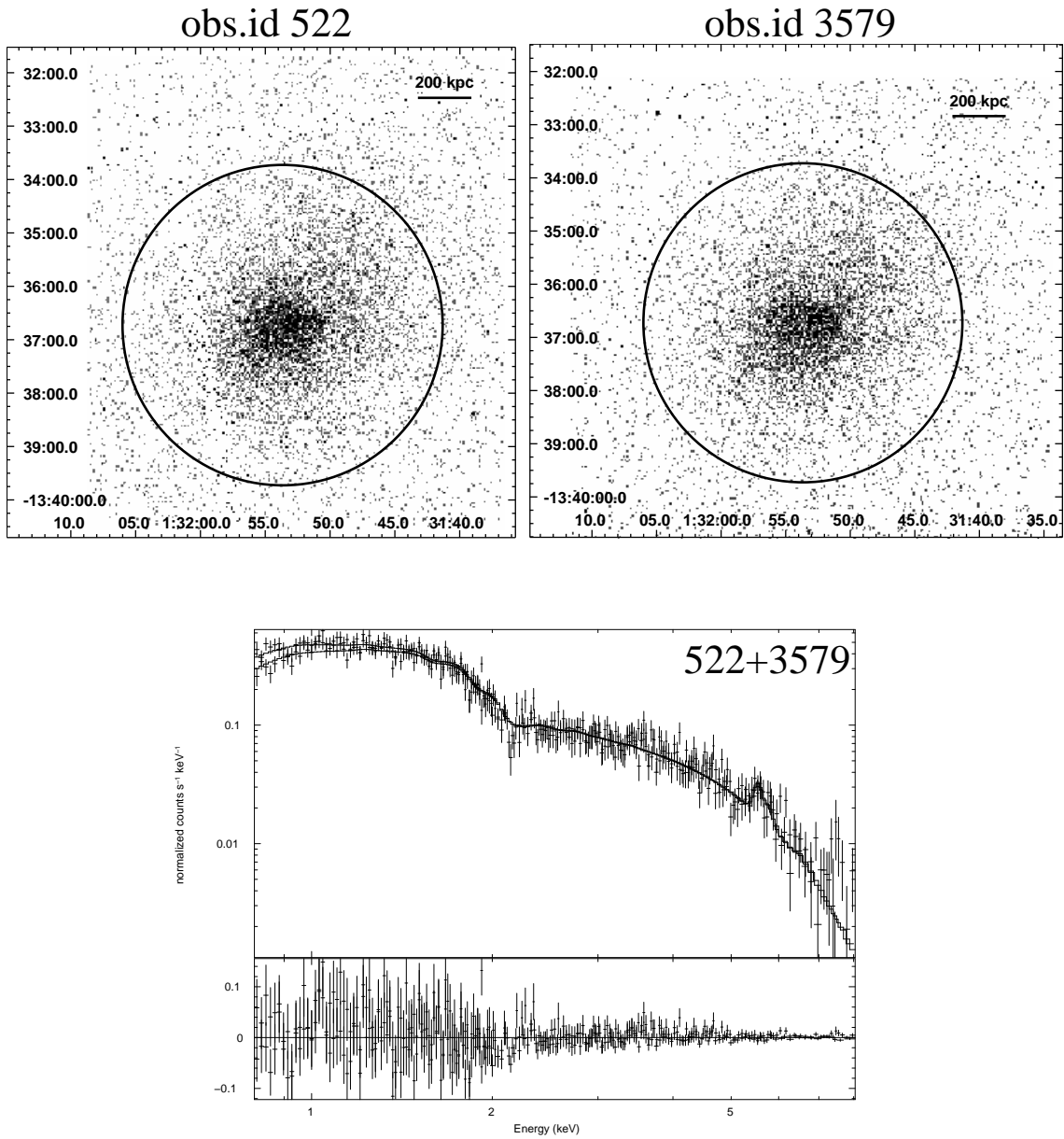


Figure 4.7: *Upper panel* – Chandra images of A 209 in the 0.5–5 keV energy band from the archival observations 522 (left) and 3579 (right). The images are background subtracted, vignetting corrected, and binned to  $1''$  pixels. The regions used to estimate the cluster temperature are indicated by the black circles, both having a radius of  $3'$  ( $\sim 600$  kpc). *Lower panel* – Spectra of A 209 extracted from the regions reported in the upper panel. Solid lines are the best fit models. The bottom section shows the residuals

Table 4.3: Spectral fit results.

Region	T * keV	Z/Z <sub>⊙</sub> *	χ <sub>red</sub> <sup>2</sup> [d.o.f.]	Null-hyp. Prob.
Whole cluster (r=3')	7.4 <sup>+0.6</sup> <sub>-0.4</sub>	0.29 <sup>+0.10</sup> <sub>-0.10</sub>	0.98 [387]	0.613
A	10.4 <sup>+3.4</sup> <sub>-2.2</sub>	0.3 **	1.14 [106]	0.159
B	8.1 <sup>+1.4</sup> <sub>-1.2</sub>	0.3 **	0.93 [130]	0.706
C	6.8 <sup>+0.9</sup> <sub>-0.9</sub>	0.3 **	1.07 [139]	0.274
D	6.1 <sup>+0.8</sup> <sub>-0.8</sub>	0.3 **	0.99 [152]	0.527

\* errors are at the 90% confidence level.

\*\* fixed in the fit.

After removal of point sources, the *soft* and *hard* images were adaptively smoothed using the same scales, with a minimum significance of  $5\sigma$  and a maximum significance of  $10\sigma$ . Finally the smoothed images were combined as  $(hard - soft) / (hard + soft)$  to obtain the hardness ratio image shown in Figure 4.8. In the figure we also report the temperature calibration carried out using the *fakeit* tool in XSPEC (see Sec. 2.6.1 for details). The three peaks of emission detected at the cluster centre by the wavelet analysis (Fig. 4.6) are reported as dashed black ellipses.

As evident from Figure 4.8, A 209 does not possess a strong cool core. The innermost portion of the cluster (i.e. the region containing the three dashed ellipses in the figure) is characterised by an average hardness ratio  $\langle HR \rangle \simeq -0.54$ , which corresponds to the temperature  $\langle T \rangle \simeq 6$  keV. Furthermore, the core region does not appear isothermal, but shows substructure on the smaller scale. In particular, the region associated with the eastern peak appears slightly colder ( $\langle T \rangle \simeq 5$  keV) than the regions centered on the central and western peaks ( $\langle T \rangle \simeq 6$  keV).

The most striking feature in Figure 4.8 is the presence of a hard region North–West of the core, where the hardness ratio ranges between  $-0.45$  and  $-0.41$ . These values imply a very hot temperature for this region, i.e. from  $T \sim 10$  keV up to  $T \gtrsim 12$  keV. A colder region ( $\langle T \rangle \simeq 4$  keV) is visible in Figure 4.8, roughly opposite to the hottest region with respect to the cluster centre.

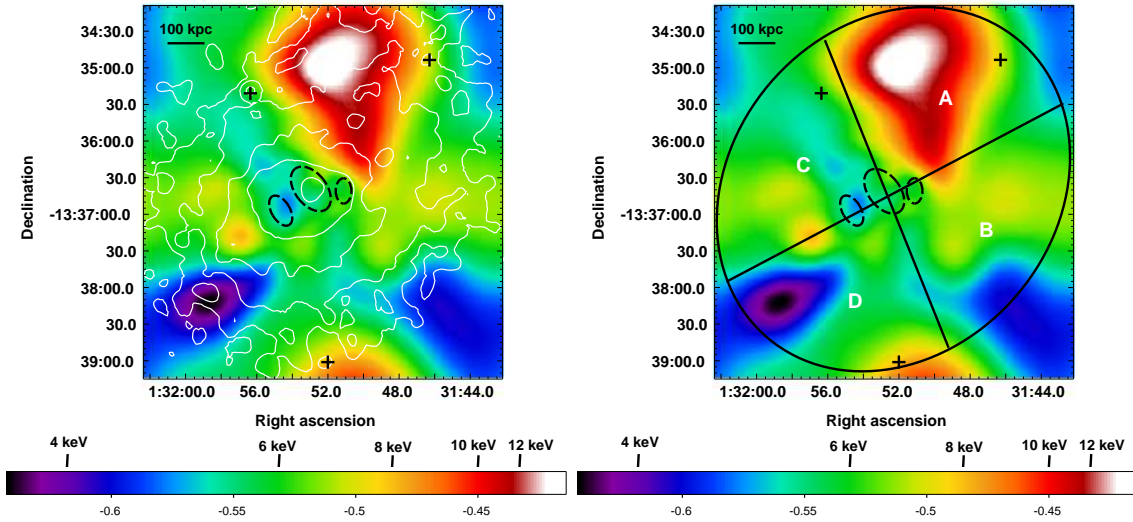


Figure 4.8: *Left panel* – Hardness ratio image of A 209 (colours) overlaid on the 0.5–5 keV brightness contours of the cluster (white), spaced by a factor of  $\sqrt{2}$ . The black dashed ellipses indicate the central substructures detected by the wavelet analysis. The black crosses show the position of the point sources which were removed. The temperature calibration is reported. *Right panel* – Hardness ratio map of A 209 (same as *left panel*). A, B, C and D indicate the regions used for the spectral fits.

In order to check the significance of the substructures observed in the hardness ratio distribution, we extracted the spectra in the four sectors labelled from A to D in Figure 4.8 (right panel), and fitted them with the *wabs mekal* model in the 0.8–8.0 keV range. Given the low statistics a spectral fit for each of the three central substructures (dashed black ellipses) is not possible. This does not allow us to confirm the different temperature values suggested by the hardness ratio image for such structures.

The results of the spectral fits for regions A, B, C, and D are summarised in Table 4.3 (errors are given at the 90% significance level). In Figure 4.9 we compare the temperature values for these regions with each other.

Despite the large errors due to the low statistics, Table 4.3 and Figure 4.9 confirm that the northwestern region of the cluster (A) is hotter than the other sectors. In particular the estimated temperature for A is significantly higher (at more than 90% significance level) than the value obtained for sector D, which contains the cold region detected in the hardness ratio image (Fig. 4.8). Regions B and C have temperatures which are consistent with each other within the errors.

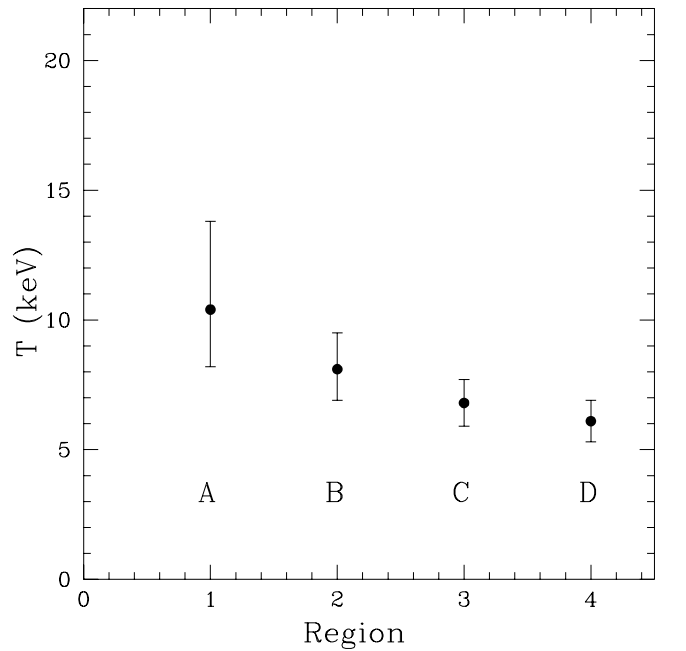


Figure 4.9: Best fit temperature associated with the X-ray regions defined in right panel of Figure 4.8. Errors are at the 90% confidence level.

#### 4.4 Optical analysis

We re-analysed the bi-dimensional galaxy distribution in the A 209 region using the information from the APM catalogue, which is complete up to the magnitude  $R = 20.5$ .

From this catalogue we extracted all galaxies with  $R \leq 20.5$  located within a circular region of  $\sim 10'$  radius (i.e.  $\sim 2.0$  Mpc) from the cluster X-ray centre (Tab. 2.1). We used the bi-dimensional version of the Adaptive Kernel Algorithm DEDICA (Bardelli et al. 1998a) to enhance possible substructures in the projected galaxy distribution.

The isodensity contours of the reconstructed galaxy density field (yellow), as derived from the  $R \leq 20.5$  APM sample, are shown in the two upper panels of Figure 4.10, superposed to the POSS-2 optical image of A 209. In panel *a*) the galaxy density image is defined on the basis of the galaxy number, while in panel *b*) the density is weighted for the galaxy luminosity.

The two optical distributions show different features and contain important pieces of information. Three significant substructures (labelled as G1, G2 and G3) are clearly visible in both panels of Figure 4.10:

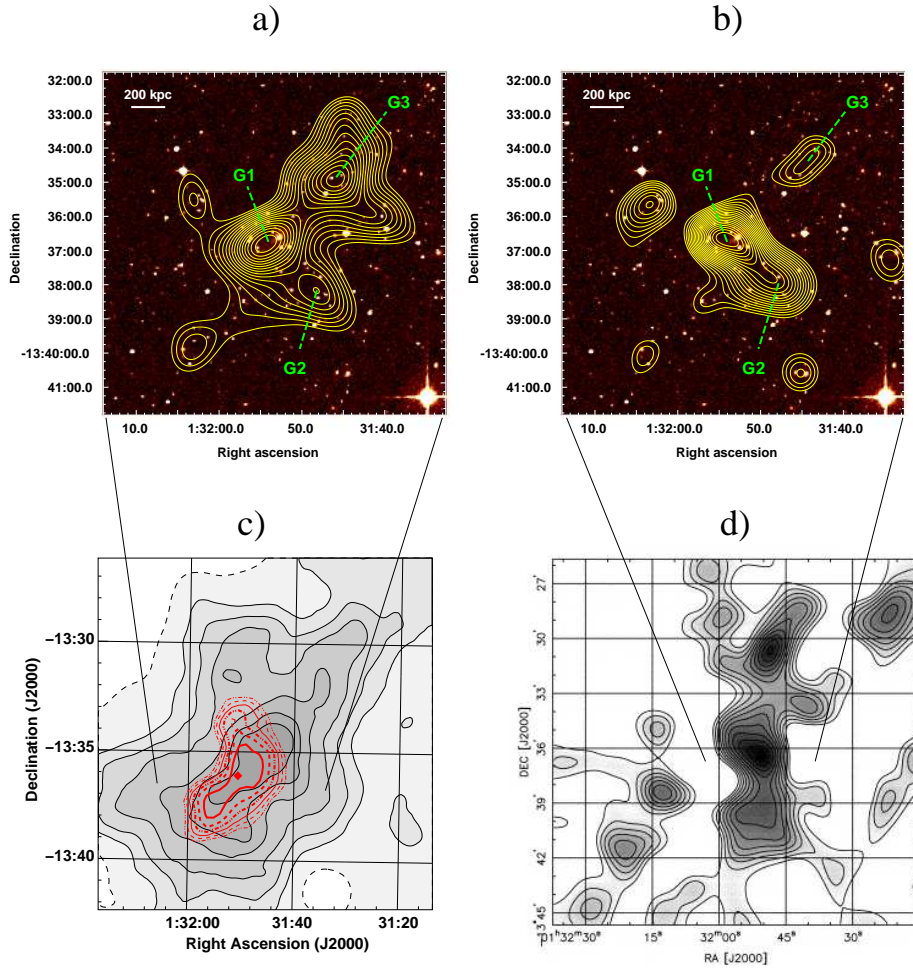


Figure 4.10: Panels a) and b) – Isodensity contours of the reconstructed galaxy density field (yellow) as derived from the  $R \leq 20.5$  APM sample, overlaid on the POSS–2 image of A 209 (colour). G1, G2 and G3 indicate the optical substructures. In panel a) the density map is defined on the basis of the galaxy number. Panel b) shows the luminosity–weighted density map. Panel c) – Weak lensing mass reconstruction (red contours) on the galaxy distribution (grey scale and black contours) from Paulin–Henriksson et al. (2007). See caption of Fig. 4.2 for details. Panel d) – Projected mass density inferred from the weak lensing analysis by Dahle et al. (2002).

- the main one (G1) is associated with the cluster central region and contains 25 objects (including the dominant cD galaxy) which are among the brightest galaxies in the whole A 209 field, as clear from the luminosity-weighted density image in panel *b*) of Figure 4.10. This substructure coincides with the south-eastern peak at RA = 01h 32m 55s, DEC =  $-13^{\circ} 35' 37''$  in the  $R < 23$  galaxy distribution from Paulin-Henriksson et al. (2007), reported in panel *c*) of Figure 4.10. Furthermore G1 appears associated also with the south-eastern peak of the reconstructed mass distribution from the weak lensing analysis performed by those authors;
- the secondary substructure G2 is located South-West of G1, at a projected distance of  $\sim 2'$  (i.e.  $\sim 400$  kpc), and contains 19 galaxies. Panel *b*) of Figure 4.10 indicates that G2 is mainly composed of bright galaxies, as observed for G1. This optical clump is only marginally visible in the galaxy density field from Paulin-Henriksson et al. (2007) (panel *c*) and no clear peak in the cluster mass distribution is associated with it;
- the presence of a third substructure (labelled as G3) is evident in the optical distribution based on the galaxy number (panel *a* of Fig. 4.10). Such substructure is at  $\sim 3'$  North-West from G1, corresponding to a projected distance of  $\sim 600$  kpc in the plane of the sky. G3 is also visible both in the galaxy density field and mass distribution in panel *c*. The little contribution of G3 to the luminosity-weighted galaxy distribution (panel *b*) reveals that this subclump is mostly built by faint galaxies.

On the basis of the luminosity-weighted number of galaxies in the main clump G1 and the subclump G2, we derived a rough estimate of the mass ratio between these substructures. We found that the mass of G1 is  $\lesssim 3$  times the mass associated with G2. No mass ratio estimate can be obtained for G1 and G3.

Using the spectroscopic and photometric catalogues in MGB03 and MBM04, we searched for possible redshift and colour segregations between the substructures detected in our analysis. We found 14 cluster members associated with G1, 14 with G2 and 10 with G3. No clear separation between G1, G2 and G3 was detected both in the velocity space and in the (B-R) colour distribution.

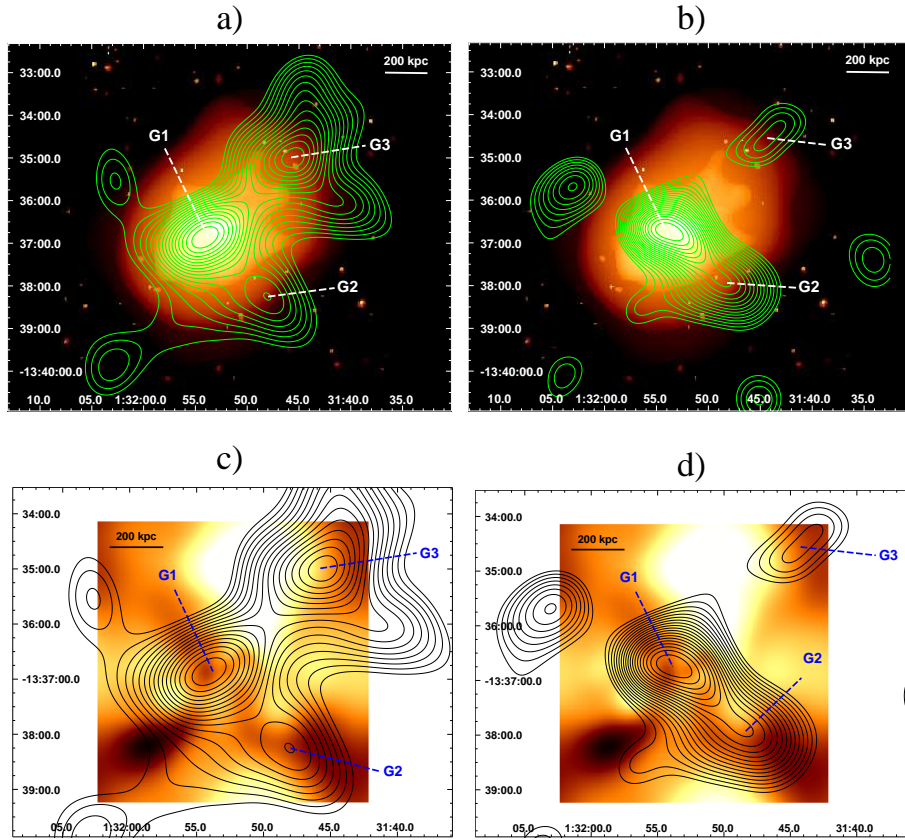


Figure 4.11: Isodensity contours of the reconstructed galaxy density field overlaid on the X-ray Chandra image (panels *a* and *b*) and hardness ratio image (panels *c* and *d*) of A 209. G1, G2 and G3 indicate the optical substructures. *Panels a and c*) – The optical density field is defined on the basis of the galaxy number, as in the panel *a*) of Fig. 4.10. *Panels b and d*) – The galaxy density image is luminosity-weighted, as in panel *b*) of Fig. 4.10.

## 4.5 Combined radio, optical and X-ray analysis

In order to complete the analysis of the merging properties of A 209 and investigate the origin of the central radio halo in connection with the cluster merger history, in this Section we combine the main results of our optical and X-ray analysis (Sec. 4.5.1), and perform a composite radio/X-ray study of the halo (Sec. 4.5.2).

### 4.5.1 Optical versus X-ray

In Figure 4.11 we show the isodensity contours of the APM galaxy density field (same as Fig. 4.10), overlaid on the cluster X-ray Chandra image of A 209 (same as Fig. 4.6) and to the hardness ratio image obtained in Section 4.3.2.

As clear from panel *a*) the optical distribution is roughly aligned with the major axis of the cluster hot gas distribution. The main optical clump (G1) is centered on

the X-ray brightest region, while the faint galaxies belonging to G3 are distributed along the low X-ray surface brightness tail extending toward North–West. Panel *b*) shows that G2 is not associated with any substructure in the cluster X-ray emission. Furthermore the axis connecting G1 and G2 is almost perpendicular to the X-ray axis.

Panel *c*) indicates that the hot region detected in the hardness ratio image (sector A in Fig. 4.8; see also Tab. 4.3) is located in the region between G1 and G3.

#### 4.5.2 Radio vs X-ray

In Figure 4.12 we report the the location of A 209 (cyan filled circle) on the  $\text{Log}L_X$ – $\text{Log}P_{1.4\text{GHz}}$  correlation found for all clusters known to host a giant radio halo (Sec. 1.7; see Cassano, Brunetti & Setti 2006 and references therein for the literature data).

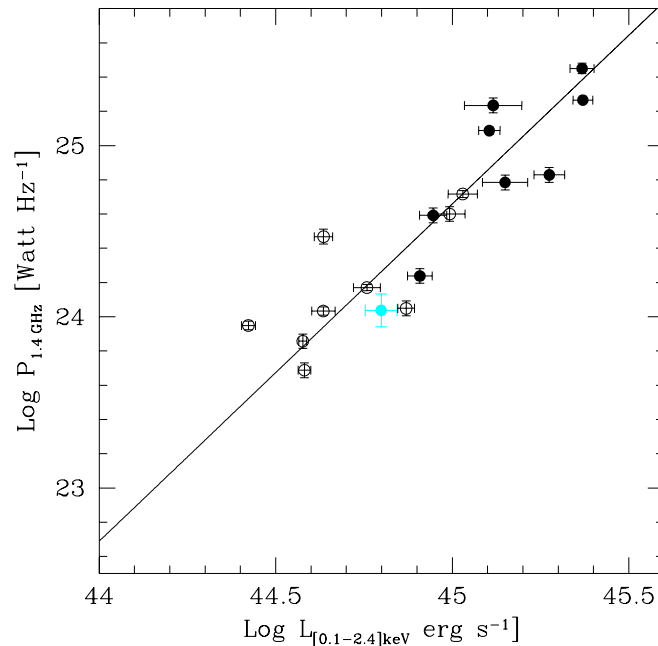


Figure 4.12:  $\text{Log}L_X$ – $\text{Log}P_{1.4\text{GHz}}$  diagram for the clusters with detected giant radio halos. Empty black circles represent the literature clusters at  $z < 0.2$ , and filled black circles the clusters at  $z > 0.2$ . The cyan filled circle shows the location of A 209. The solid line is the best–fit of the correlation found by Cassano, Brunetti & Setti (2006).

Empty and filled black circles represent the clusters at redshift  $z < 0.2$  and  $z > 0.2$

respectively. The solid line is the best-fit of the correlation found by Cassano, Brunetti & Setti (2006), i.e.  $P_{1.4\text{GHz}} \propto L_X^{1.97 \pm 0.25}$ .

Given the lack of a flux density value in Giovannini et al. (2006), we estimated the 1.4 GHz radio power of the halo in A 209 by scaling the measured flux density at 610 MHz (Tab. 4.2) with a spectral index  $\alpha = 1.2 \pm 0.2$  (the uncertainty assumed here dominates over the 610 MHz flux density error). The position of A 209 on the  $\text{Log}L_X\text{--Log}P_{1.4\text{GHz}}$  plane is in good agreement with the best-fit correlation for all literature clusters with a giant radio halo (solid line; Sec. 1.7).

In Figure 4.13 (upper panel) we show the GMRT 610 MHz contours of the halo (same as Fig. 4.5) on the Chandra image of A 209 (same as Fig. 4.6). The halo appears totally embedded within the cluster X-ray emission. Its central/southern brightest region coincides with the highest X-ray surface brightness, and follows (at least qualitatively) the distribution of the X-ray gas, as observed in other giant radio halos known in the literature (e.g. Govoni et al. 2004; see also Fig. 1.5 in Sec. 1.4).

The northern part of the halo does not show any association between higher radio brightness and higher X-ray emission. Furthermore, on the larger scale, the North–South elongation of the halo appears misaligned with respect to the X-ray axis. However, as discussed in Section 4.2.1, the peculiar double-peaked flux density distribution of the source may be driven by the presence of residual extended emission associated with the individual radio galaxies. In particular the northern peak of the halo may be due to the difficult subtraction of source C (lower panel of Fig. 4.13), which has no optical counterpart (see Fig. 4.4 and Tab. 4.2), but is associated with an X-ray point-like source.

## 4.6 The proposed merging scenario

On the basis of the results of our optical and X-ray analysis of A 209 (Secs. 4.3, 4.4 and 4.5.1), combined with the information from the literature, we propose that two main merging episodes occurred in the merging history of the cluster: (i) a past major merger and (ii) a more recent merger along a direction orthogonal to the old merger axis.

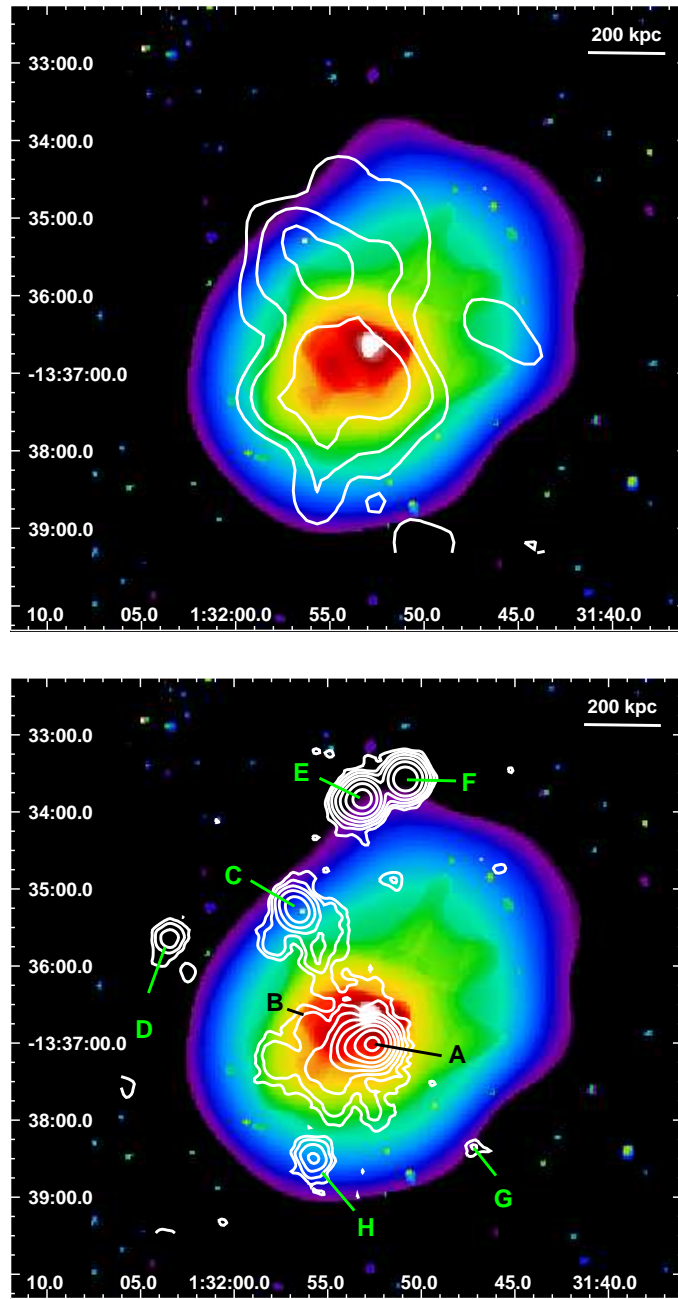


Figure 4.13: *Upper panel* – GMRT 610 MHz contours of the radio halo, superposed to the X-ray *Chandra* wavelet-reconstructed image of the cluster. The radio and X-ray images are the same as Figs. 4.5 and 4.6 respectively. *Upper panel* – GMRT 610 MHz contours of the radio emission in the A 209 region, on the X-ray *Chandra* wavelet-reconstructed image of the cluster. The radio and X-ray images are the same as Figs. 4.4 (lower panel) and 4.6 respectively. Letters from A to G indicate the individual radio galaxies.

#### i) The past major merger

The cluster may have experienced a past merger with a massive subcluster (mass ratio  $\gtrsim 1:3$ ) along the North-East/South-West direction. The substructure G2 in

Figure 4.10, which contains mainly bright galaxies, may be the remnant of the optical core of the infalling subcluster. Panel *d*) of Figure 4.10 shows that the dark matter distribution on the larger scale is elongated in the same direction as the axis connecting G1 to G2. The lack of an X-ray counterpart for G2 (Fig. 4.11) suggests that the merger is in a final stage, and the gaseous cores of the two subclusters have possibly completely merged after a phase of sloshing.

The spectroscopic and photometric properties of the red  $H_\delta$  strong galaxies belonging to A 209 suggest that the cluster may have indeed experienced a past merger with an infalling subcluster  $\sim 3.5\text{--}4.5$  Gyr ago (MGM04).

### ii) The recent merger

A more recent merging event may have occurred between G1 and G3 (Fig. 4.10) in a direction roughly orthogonal to old merger axis. G3 might have crossed the core region of A 209, coming from South-East. The comparison between the galaxy density field, the mass distribution (both in Fig. 4.10) and the X-ray emission (Fig. 4.11) suggests a decoupling between the galaxy and dark matter component and the hot gas, which has been stripped during the core crossing. Furthermore the hottest portion of the cluster (region A in Fig. 4.8) is approximately coincident with the region between G1 and G3. This region might have been heated by the passage of a shock developed during the collision between these two substructures. If we assume an impact velocity of the order of  $\sim 2000 \text{ km s}^{-1}$ , the projected distance between the G1 and G3 peaks implies that the cores have crossed each other  $\sim 0.5\text{--}1$  Gyr ago. In the estimate, we take into account possible projection effects, since the galaxy velocity gradient detected along the likely merger axis by MGB03 supports the idea that the process is not occurring in the plane of the sky.

## 4.7 Origin of the radio halo

On the basis of the merging history proposed for A 209 in Section 4.6, we attempt to explain the formation of the giant radio halo in this cluster in the framework of the re-acceleration model (Sec. 1.9.1).

A first injection of large scale turbulence might have occurred during the past major merger between the two massive subclusters G1 and G2. Once injected the turbulence eddies diffuse through the whole cluster volume and a turbulence cascade

from the large scale to smaller scale is developed. As shown by Cassano & Brunetti (2005), magneto-sonic (MS) waves with scales  $< 100$  kpc may efficiently re-accelerate relativistic electrons in the ICM up to the energies ( $\gamma \sim 10^4$ ) required to emit the synchrotron radiation detectable in the radio band (see also Sec. 1.9.1).

According to the calculations Cassano & Brunetti (2005), major mergers (i.e. with mass ratio of the order of  $\geq 1:5$ ) between massive clusters ( $M \geq 10^{15} M_{\odot}$ ) may provide the ingredients necessary to develop a giant radio halo (Sec. 1.9.1). Hence, given the estimated mass ratio for the merger between G1 and G2 ( $\gtrsim 1:3$ ), we might expect the formation of a giant radio halo as consequence of this first episode of the proposed merging history of A 209.

A further injection of fresh turbulence may be connected to the more recent merging event between G1 and G3. However, the mass ratio involved in such process is unknown. On the other hand, the turbulence driven by the past cluster major merger could have been not yet completely dissipated at the moment of the merging between G1 and G3. In this case, we might expect efficient particle re-acceleration also if the G1:G3 mass ratio is slightly lower than required value ( $\gtrsim 1:5$ ) to power a giant radio halo.

## Chapter 5

# The giant radio halo in A 697

In this Chapter we present the combined radio, X-ray and optical analysis of the merging galaxy cluster A 697. The cluster is at redshift  $z=0.282$  and has a high X-ray luminosity ( $L_{X[0.1-2.4\text{keV}]} \sim 1.1 \times 10^{45} \text{ erg s}^{-1}$ ) and virial mass ( $M_v \sim 2.2 \times 10^{15} M_\odot$ ). Its general properties are given in Table 2.1.

In the radio band, the cluster is characterised by the presence of a giant radio halo, which extends over the whole cluster central region. The existence of such diffuse radio emission was first suggested by Kempner & Sarazin (2001; hereinafter KS01) from inspection of the 327 MHz image from the Westerbork Northern Sky Survey (WENSS; Rengelink et al. 1997) and of the 1.4 GHz image from the NRAO VLA Sky Survey (NVSS; Condon et al. 1998). These images are also reported in Figure 5.1, superposed to the DSS optical frame. The presence of a giant radio halo was then confirmed by our high sensitivity GMRT observations at 610 MHz (Tab. 2.2), carried out within the GMRT Radio Halo Survey (Sec. 1.12).

With the aim to study the radio halo and its hosting cluster using a multiband approach, we combined our 610 MHz information with the Chandra data available in the public archive (Tab. 2.4), and optical information from the Sloan Digital Sky Survey (SDSS, data release DR5; Adelman-McCarthy et al. 2007), and from the literature (Girardi, Boschin & Barrera 2006; hereinafter GBB06).

The Chapter is organised as follows: the main properties of the merging environment of A 697, as provided by the literature, are described in Section 5.1; in Section 5.2 we present the radio analysis of the giant radio halo at the cluster centre; the X-ray Chandra analysis is given in Section 5.3, while the analysis of the

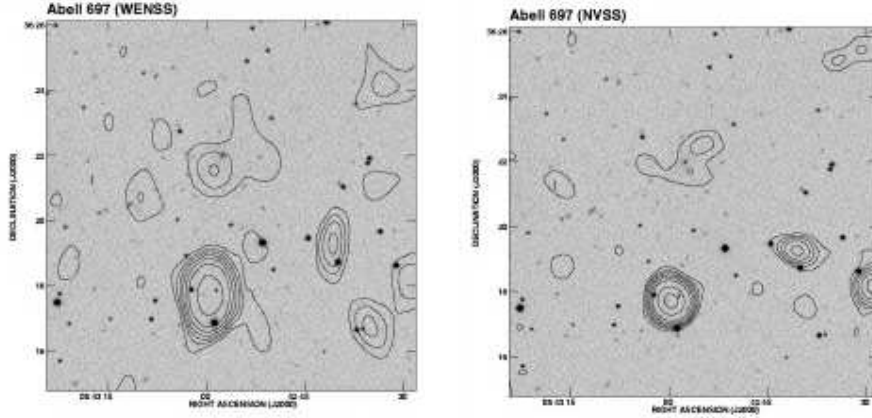


Figure 5.1: 327 MHz contours from the WENSS (left panel) and 1.4 GHz contours from the NVSS (right panel) of the A 697 region, superposed to the DSS optical image (from KS01). The rms level ( $1\sigma$ ) is  $\sim 3.6$  mJy  $\text{b}^{-1}$  in the WENSS image and  $\sim 0.45$  mJy  $\text{b}^{-1}$  in the NVSS. Radio contours are  $(2, 3.5, 5, 7, 10, 15, 30, 50, 100, 200, 500, \& 1000) \times 1\sigma$ . The  $3.5\sigma$  negative contour is also shown. The angular resolution is  $\sim 12'' \times 12''$  at 327 MHz and  $45'' \times 45''$  at 1.4 GHz.

optical SDSS data is performed in Section 5.4; in Section 5.5 we combine the results of our optical and X-ray analysis to complete the study of the merging environment of A 697 and discuss the radio halo properties in connection with the cluster X-ray properties; the proposed merging scenario and its connection with the formation of the radio halo are discussed in Sections 5.6 and 5.7 respectively.

The cosmology adopted in this work leads to a linear scale of  $4.26$  kpc  $\text{arcsec}^{-1}$  at the redshift of A 697 ( $z = 0.282$ ).

## 5.1 The merging environment of A 697

A clear indication that A 697 is very far from the dynamical equilibrium comes from the results of the recent optical and X-ray study by GBB06. In the optical band, they investigated the presence of substructures in the velocity and spatial distributions of the cluster members. They found that the cluster velocity distribution significantly deviates from a Gaussian, showing four distinct velocity clumps. However no substructure in the galaxy bi-dimensional distribution was found associated with these redshift clumps. This led GBB06 to suggest that the cluster is possibly experiencing a complex merging process, where the subclumps are mainly aligned along the line of sight (LOS).

The importance of the merger is still uncertain, since GBB06 found that the observed optical properties of A 697 might be explained as either an ongoing process of multiple accretion of small clumps by a very massive cluster, or the result of a past major merger. Alternatively, they proposed that, if the merger is still ongoing, it might be more important than a group accretion phenomenon, as also supported by the absence of a cool core in this cluster (Bauer et al. 2005). In this case, if such interaction is occurring along a direction close to the LOS, it might be difficult to identify it as a cluster merger.

In the X-ray band, GBB06 analysed the cluster Chandra observations available in the public archive. Their main result is the detection of three significant substructures in the inner  $\sim 200$  kpc radius region of the cluster. The main clump is approximately at the location of the central cD galaxy, while the other two structures are located North–West and South–East of the cluster centre, aligned along an S–shape structure. GBB06 noticed that such structure reminds the bi-dimensional distribution of the cluster galaxies on larger scale, and suggested that these clumps may be related to subgroups located (or projected onto) the cluster core.

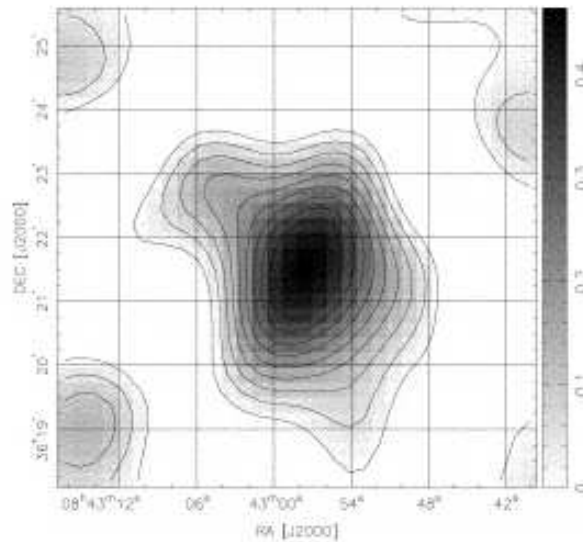


Figure 5.2: Projected mass density in the A 697 field, as inferred from the weak lensing analysis (from Dahle et al. 2002).

Important hints about the merger dynamics come from the weak lensing analysis by Dahle et al. (2002), who found that the cluster mass distribution is elongated in the North–North West/South–South East (NNW/SSE) direction (see Fig. 5.2 in

this work), which is parallel to the major axis of the central cD halo (Metzger & Ma 2000). On the basis of these results, Dahle et al. (2002) suggested a possible merging scenario, which involves a recent head-on collision of two massive clumps along the NNW/SSE direction.

The X-ray data may support the above scenario. The distribution of the cluster hot gas appears elliptical, with a similar position angle as the mass distribution, both in the ROSAT HRI (Dahle et al. 2002; Ota & Mitsuda 2004) and Chandra images (De Filippis et al. 2005; GBB06; this work).

## 5.2 The giant radio halo

The existence of extended radio emission on the cluster scale in A 697 was first suggested by KS01, who inspected the 327 MHz WENSS images to search for candidate radio halos and relics in all the Abell clusters in the survey. They classified such emission as uncertain (see left panel of Fig. 5.1), and measured a largest angular size (LAS) of  $\sim 2.9'$  (i.e.  $\sim 750$  kpc), and a total flux density of  $S_{327\text{ MHz}} = 29 \pm 6$  mJy.

### 5.2.1 GMRT 610 MHz observations

A 697 belongs to the sample of galaxy clusters selected for the GMRT Radio Halo Survey, described in Section 1.12. Within this project, the cluster was observed with the GMRT at 610 MHz for a total integration time of  $\sim 80$  minutes. Thanks to the high quality of the observations, and the lack of strong radio sources in the proximity of the cluster region, we reached a high sensitivity of the order of  $25 \mu\text{Jy b}^{-1}$  in the full resolution image ( $6.2'' \times 4.5''$ ). We refer to Table 2.2 and Section 2.2 for the details of the radio observations, and Section 2.4 for a description of the data reduction.

The GMRT 610 MHz full resolution image of the cluster virial region is shown in the upper panel of Figure 5.3. The cross indicates the cluster X-ray centre, and the radius of the solid circle corresponds to the virial radius ( $R_V = 2.9$  Mpc; Tab. 2.1). The dashed circle represents the portion of the cluster covered by the optical analysis in GBB06, and has a radius of  $\sim 1.3$  Mpc.

In the lower panel of Figure 5.3 we show a zoom of the same image, overlaid

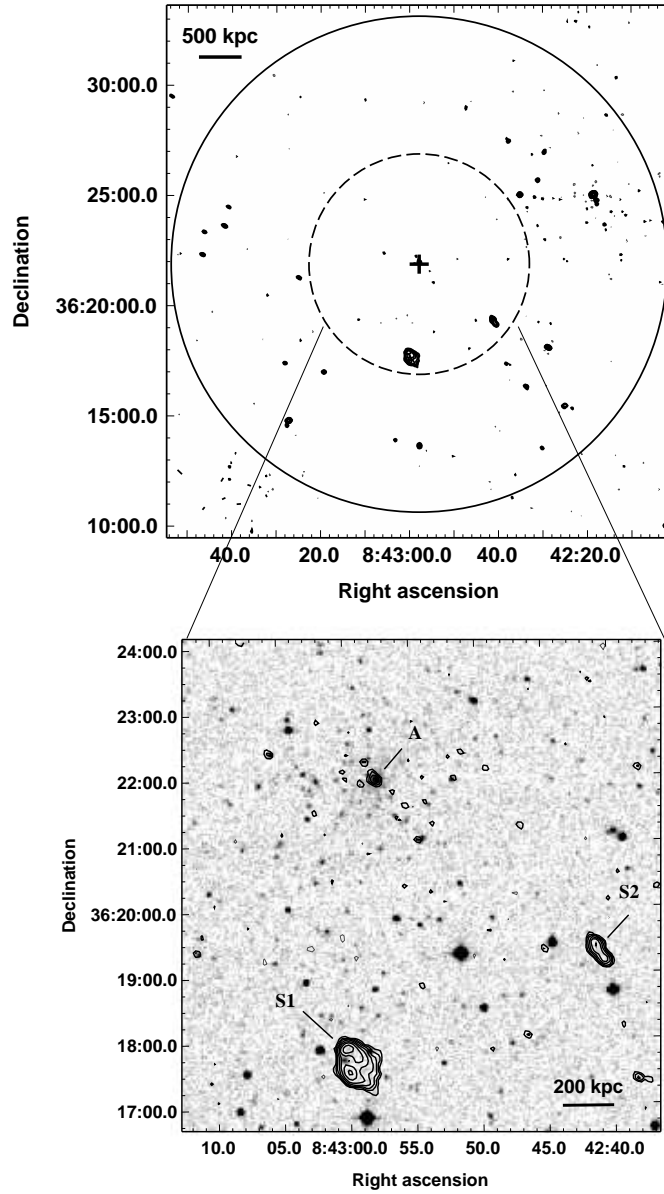


Figure 5.3: *Upper panel* – GMRT 610 MHz radio contours of the A 697 virial region. The noise level in the image is  $25 \mu\text{Jy b}^{-1}$ . Contours are scaled by a factor 2, starting from  $\pm 0.125 \text{ mJy b}^{-1}$ . The resolution is  $6.2'' \times 4.5''$ , p.a.  $65^\circ$ . The cross is the cluster X-ray centre. The solid circle has a radius corresponding to  $R_V = 2.9 \text{ Mpc}$ . The dashed circle is the region covered by the optical analysis in GBB06 and this work. *Lower panel* – Zoom of the central region of the cluster. The radio image is the same as the upper panel. Contours are scaled by a factor 2, starting from  $\pm 0.075 \text{ mJy b}^{-1}$ . The grey scale is the POSS-2 optical frame. The cluster central radio galaxy is labelled as A. S1 and S2 indicate the two extended radio galaxies detected in the Southern part of the cluster.

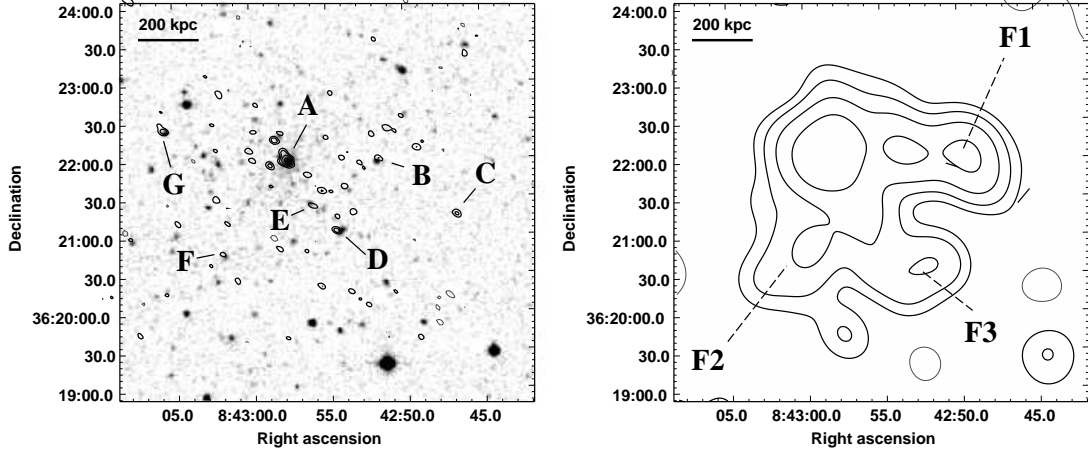


Figure 5.4: *Left panel* – Full resolution GMRT 610 MHz contours of the central region of A 697, superposed to the POSS-2 optical image. The resolution of the radio image is  $6.2'' \times 4.5''$ , p.a.  $65^\circ$ , the  $1\sigma$  level is  $25 \mu\text{Jy b}^{-1}$  and contours are spaced by a factor 2 starting from  $\pm 75 \mu\text{Jy b}^{-1}$ . Individual sources are labelled from A to H. *Right panel* – GMRT 610 MHz low resolution radio contours of the radio halo in A 697, after subtraction of the individual sources (from A to H in the left panel). The resolution of the radio image is  $40.0'' \times 35.0''$ , p.a.  $37^\circ$ . The  $1\sigma$  level in the image is  $50 \mu\text{Jy b}^{-1}$ . Contours are spaced by a factor of 2, starting from  $\pm 0.15 \text{ mJy b}^{-1}$ .

on the POSS-2 optical frame. At this resolution, a point like radio source (labelled as A) is identified with the central Brightest Cluster Galaxy (BCG). Two extended radio galaxies (labelled as S1 and S2) are located in the Southern part of the cluster. S1 is associated with a cluster member galaxy (#57 in the spectroscopic catalogue of GBB06); a galaxy with photometric redshift  $z_{\text{phot}} = 0.240 \pm 0.047$  from the SDSS, and thus a possible cluster member, is found within the radio isophotes of S2.

The innermost portion of the cluster is shown in Figure 5.4. The left panel gives the full resolution 610 MHz contours, overlaid on the POSS-2 optical image. The individual radio sources are labelled from A (same as lower panel of Fig. 5.3) to G. Optical counterparts for these sources were searched by inspecting the POSS-2 image, and by using the spectroscopic catalogue in GBB06 and the information from the SDSS. The sources are listed in Table 5.1, where we give their radio position and 610 MHz flux density, both measured on the full resolution image (left panel of Fig. 5.4), the optical catalogue, and coordinates and redshift of the optical counterpart. As clear from Table 5.1, all radio sources are identified with member galaxies of A 697, except for sources B and C, which are associated with a

Table 5.1: Individual radio galaxies at the A 697 centre.

Radio source	Radio position		$S_{610\text{ MHz}}$ mJy	Optical catalogue	Optical Position		z
	RA <sub>J2000</sub>	DEC <sub>J2000</sub>			RA <sub>J2000</sub>	DEC <sub>J2000</sub>	
A	08 42 57.70	+36 22 01	1.24	GBB#41	08 42 57.55	+36 22 00	0.281
B	08 42 51.73	+36 22 01	0.15	SDSS	08 42 51.86	+36 21 59	0.430 <sup>b</sup>
C	08 42 46.70	+36 21 16	0.21	SDSS	08 42 46.89	+36 21 16	0.163 <sup>b</sup>
D	08 42 54.54	+36 21 05	0.20	GBB#33	08 42 54.36	+36 21 03	0.274
E	08 42 56.04	+36 21 25	0.15	GBB#36	08 42 56.18	+36 21 27	0.285
F	08 43 01.95	+36 20 48	0.09	GBB#65	08 43 01.73	+36 20 46	0.284
G	08 43 05.65	+36 22 25	0.28	GBB#79	08 43 05.50	+36 22 24	0.267

(a) photometric redshift from the SDSS;

background and foreground galaxy respectively. All sources are undetected at the sensitivity limit of the 1.4 GHz Faint Images of the Radio Sky at Twenty-centimeters (FIRST) survey ( $\text{rms} \simeq 0.15 \text{ mJy b}^{-1}$ ).

In addition to the individual radio galaxies, positive residuals of radio emission are clearly visible in the high resolution image of Figure 5.4 (left panel). After subtraction of the flux density of sources A to G, which contribute for a total of 2.3 mJy, these residuals account for  $\sim 9 \text{ mJy}$ , suggesting the presence of very low surface brightness emission at the cluster centre. In order to highlight such emission, we subtracted all these individual sources ( Tab. 5.1) from the u–v data, and produced a low resolution image, convolved with a beam of  $40.0'' \times 35.0''$ . The image is shown in the right panel of Figure 5.4, and has a noise level of  $50 \mu\text{Jy b}^{-1}$ . It clearly confirms the existence of very extended emission at the cluster centre.

### 5.2.2 The morphology

The central diffuse source in Figure 5.4 (right panel) extends on largest angular size of  $\sim 3.5'$ , corresponding to a largest linear size (LLS) of  $\sim 890 \text{ kpc}$ . Its total flux density, after subtraction of the individual radio galaxies, is  $S_{610 \text{ MHz}} = 13 \pm 1 \text{ mJy}$ , which implies a total radio power of  $\log P_{610 \text{ MHz}} (\text{W Hz}^{-1}) = 24.54$ . The surface brightness is low, of the order of  $\sim 5 \times 10^{-4} \text{ mJy arcsec}^{-2}$ .

The source overall morphology is very complex. The innermost part, which permeates a region of  $\sim 1'$  (i.e.  $\sim 250 \text{ kpc}$ ) radius around the cluster centre, appears relatively regular and symmetric. On the larger scale a bright filament of emission (labelled as F1 in the right panel of Fig. 5.4) extends in the western direction, and two fainter filaments (F2 and F3) are located South of the cluster centre. Given the

Table 5.2: Parameters of the giant radio halo in A 697.

$S_{610\text{ MHz}}$ mJy	$S_{327\text{ MHz}}$ mJy	$\alpha_{327\text{ MHz}}^{610\text{ MHz}}$	$\log P_{610\text{ MHz}}$ $\text{W Hz}^{-1}$	LAS arcmin	LLS kpc	$B'_{eq}$ $\mu\text{G}$
$13 \pm 1$	$29 \pm 6$ <sup>(1)</sup>	$1.3 \pm 0.3$	24.54	$\sim 3.5$	$\sim 890$	1.2 <sup>(2)</sup>

(1) from the WENSS (KS01);

(2) see Section 5.2.3.

lack of an obvious optical counterpart, its low surface brightness and extent on the cluster scale, we classify this source as a giant radio halo (Sec. 1.4). Its main radio properties are summarised in Table 5.2.

We note that the extended emission detected at the sensitivity limit of the 327 MHz WENSS image ( $\simeq 3.6 \text{ mJy b}^{-1}$ ; see left panel of Fig. 5.1) appears elongated westward of the source peak. This elongation may correspond to the structure F1 observed at 610 MHz. The southern, lower brightness region of the halo, containing filaments F1 and F2, is undetected at the sensitivity limit of the WENSS.

We accurately inspected also the 1.4 GHz NVSS image. As clear from Figures 5.1 (right panel) and 5.5 (left panel), the structure of the candidate diffuse emission in the NVSS seems to significantly deviate from the WENSS image (left panel of Fig. 5.1) and the 610 MHz halo morphology in Figure 5.4 (right panel). In order to understand the origin of such difference, we calibrated and imaged the NVSS pointing containing the A 697 field (right panel of Fig. 5.5). No extended emission is detected at the cluster centre at the noise level of  $0.3 \text{ mJy b}^{-1}$ . Furthermore we found that the extended structure visible in the public NVSS image is actually coincident with a peak of a residual fringe, which crosses the image along the NW–SE direction, i.e. the same direction as the extent of the structure itself. For this reason we consider the NVSS image of this source unreliable, and will not use the NVSS information in the present work. Deep radio observations of A 697 are therefore fundamental to detect the halo at 1.4 GHz, and obtain information about its morphology and total flux density at this frequency.

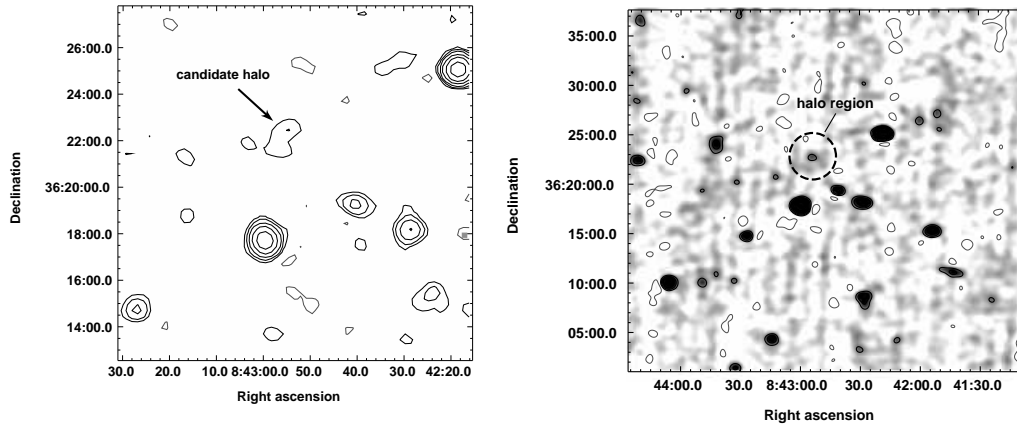


Figure 5.5: *Left panel* – Radio contours of the A 697 region from the public 1.4 GHz NVSS image. The  $1\sigma$  level is  $0.45 \text{ mJy b}^{-1}$ . Contour levels are spaced by a factor 2, starting from  $\pm 1 \text{ mJy b}^{-1}$ . The resolution is  $45'' \times 45''$ , p.a.  $0^\circ$ . *Right panel* – 1.4 GHz image (grey scale and contours) of the 1.4 GHz NVSS pointing containing A 697 after new calibration. The  $1\sigma$  level is  $0.3 \text{ mJy b}^{-1}$ . Contour levels are spaced by a factor 2, starting from  $\pm 0.9 \text{ mJy b}^{-1}$ . The resolution is  $60.0'' \times 48.0''$ , p.a.  $89^\circ$ . The black dashed circle indicate the region of the radio halo detected at 610 MHz (Fig. 5.4; right panel).

### 5.2.3 The radio spectrum

We estimated the slope of the integrated synchrotron spectrum of the radio halo in the frequency range 327 MHz–610 MHz, using the flux density values reported in Table 5.2. We obtained a spectral index  $\alpha = 1.3 \pm 0.3$  (also reported in Table 5.2), which is typical for this class of radio sources (Sec. 1.4).

We point out that the extent of the halo at 610 MHz (Fig. 5.4, right panel) is larger than in the WENSS image (Fig. 5.1, left panel), due to the source low surface brightness and to the higher sensitivity of the 610 MHz data. Therefore the estimated spectral index has to be considered as a lower limit.

High sensitivity GMRT observations at 327 MHz of A 697 (carried out in January 2007, during Cycle A011) will allow us to better constrain and study the total and point-to-point spectral index of the halo in the 327 MHz–610 MHz frequency range.

### 5.2.4 Equipartition magnetic field

Using the spectral index in Table 5.2, and under the assumption that the source is in a minimum energy condition (e.g. Pacholczyk 1970), we estimated the magnetic field associated with the giant radio halo. We considered a simple power law shape for the

energy spectrum of the relativistic electrons with slope  $\delta = 2\alpha + 1 = 3.58$  (Tab. 5.2), and adopted the standard equipartition equations, which are usually calculated in the 10 MHz–100 GHz frequency range. We obtained an equipartition magnetic field in the halo of  $B_{\text{eq}} \sim 0.3 \mu\text{G}$ . For this value of  $B_{\text{eq}}$ , the low frequency cut-off of 10 MHz corresponds to a low energy cut-off in the electron energy distribution of  $\gamma_{\text{min}} \sim 3 \times 10^3$ , being  $\gamma$  the electron Lorentz factor. In order to take into account the contribution of low energy electrons (i.e. with  $\gamma < 3 \times 10^3$ ), we computed the equipartition magnetic field by adopting the equations with a low energy cut-off in the particle energy spectrum (Brunetti, Setti & Comastri 1997). Assuming  $\gamma_{\text{min}} = 50$ , we obtained  $B'_{\text{eq}} \sim 1.2 \mu\text{G}$ , also reported in Table 5.2.

Both  $B_{\text{eq}}$  and  $B'_{\text{eq}}$  are in agreement with the magnetic field estimates reported in the literature for cluster radio halos (i.e.  $\sim 0.1\text{--}1 \mu\text{G}$ ; Sec. 1.3).

### 5.3 X-ray Chandra analysis

We re-analysed the X-ray data of A 697 available in the Chandra public archive (Obs. Id. 4271; exposure 19 ks). The details of the observation are given in Table 2.4 and the data re-processing is described in Section 3.5.2. The Chandra data were analysed also by GBB06 (Sec. 5.1). Here we present and discuss only the results of our analysis relevant for the study of the radio halo and its connection with the merging environment of the hosting cluster.

#### 5.3.1 Image analysis

In Figure 5.6 we show the Chandra wavelet-reconstructed image of the cluster. The image was obtained applying the wavelet decomposition tool (Vikhlinin et al. 1998) to the cluster image in the 0.5–5 keV energy band, after subtraction of the background and correction for the exposure map (see Sec. 2.6.1 for details).

As clear from Figure 5.6, the overall X-ray morphology of the cluster is elliptical, with the major axis aligned along the NNS/SSE direction. A striking and complex structure characterises the core region, where three significant bright substructures (labelled as X1, X2 and X3 in Fig. 5.6) are detected by the wavelet analysis within  $\sim 200$  kpc from the cluster centre. These clumps were also detected by GBB06, who suggested that they may be connected to small groups located within the cluster core.

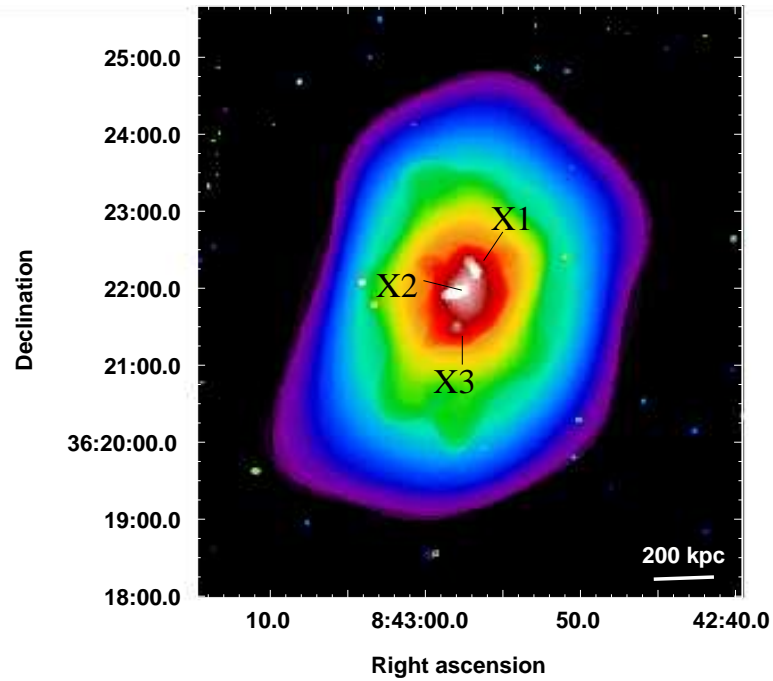


Figure 5.6: Wavelet-reconstructed Chandra image of A 697, in the 0.5–5 keV band. The image is divided for the exposure map and background subtracted. X1, X2 and X3 indicate the clumps at the cluster centre.

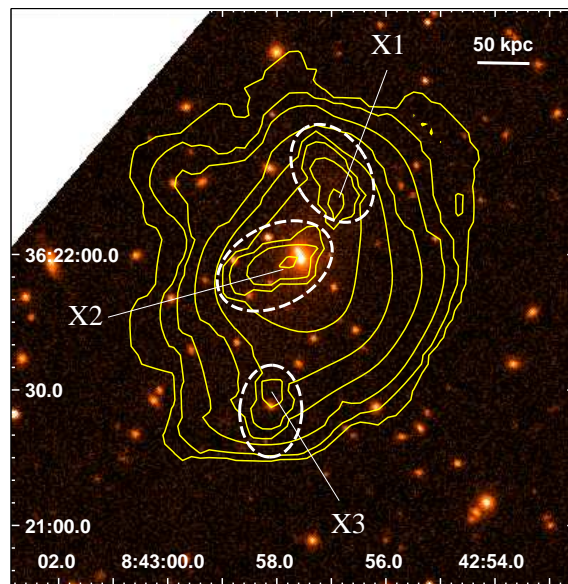


Figure 5.7: Optical *i*-band image from the SDSS of the central region of A 697. Overlaid are the linear-spaced contours of the inner part of the 0.5–9 keV wavelet-reconstructed Chandra image shown in Fig. 5.6. The dashed ellipses identify the three extended substructures detected by the wavelet analysis, labelled as X1, X2 and X3.

To highlight the complexity of this region, in Figure 5.7 we overlay the X-ray contours of the inner part of Figure 5.6, on the SDSS optical *i* frame. The white dashed ellipses show the location of the three clumps X1, X2 and X3. The structures have a largest linear size of  $\lesssim 100$  kpc. The central and brightest one (X2) is approximately located at the position of the BCG, as also noticed by GBB06. Its X-ray peak is slightly offset from the optical galaxy. No object is visible in the SDSS at the the location of X1, while a member galaxy (#46 in the GBB06 catalogue) is almost coincident with the X-ray peak of the southern substructure X3.

### 5.3.2 Spectral analysis

The spectra were extracted as described in Section 2.6.1, and fitted over the energy range 0.6–7.0 keV using the absorbed thermal model *wabs mekal* available in XSPEC (Sec. 2.6.1). The local absorption was fixed to the Galactic neutral hydrogen column density  $N_{\text{H}} = 3.4 \times 10^{20} \text{ cm}^{-2}$ , as obtained from the radio data (Dickey & Lockman 1990), and the redshift to  $z=0.282$ . Background spectra were extracted using the blank sky observations corresponding to the period of the observation (Sec. 2.6.1).

The  $\chi^2$  statistics was used to evaluate the goodness of the best-fit models. A consistency check of the results was carried out comparing them with the spectral results obtained using the Cash statistics. All errors are given at the 90% confidence level.

#### Cluster average temperature

We determined the average spectral properties of A 697 extracting the overall spectrum within the circular region shown in the left panel of Figure 5.8. The circle has a radius of  $r=3'$  ( $\sim 770$  kpc) and is centered on the cluster X-ray peak. The extracted spectrum, which contains about 15000 net counts (signal to noise ratio  $S/N \sim 115$ ), was grouped to obtain a minimum of 40 counts per bin. The spectrum and the best fit model are shown in the right panel of Figure 5.8. The best fit temperature and abundance values are given in Table 5.3, where we also report the  $S/N$  ratio in the region, and the reduced  $\chi^2$ , degree of freedom and null hypothesis probability of the best-fit model (see Sec. 2.6.1 for details).

No significant difference for the temperature value was found if the abundance was fixed to the canonical value of  $0.3 Z_{\odot}$ , and if a local background was used.

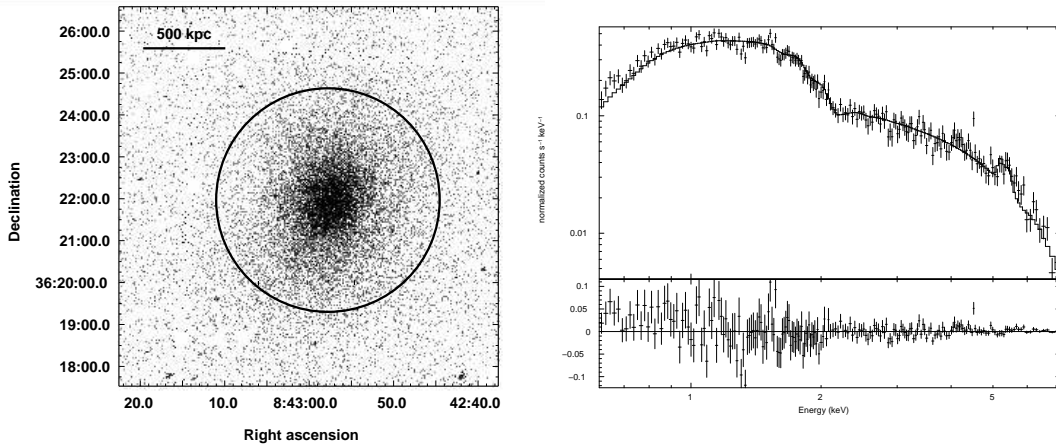


Figure 5.8: *Left panel* – Chandra image of A 697 in the 0.5–5 keV energy band. The image is background subtracted, vignetted corrected, and binned to  $1''$  pixels. The region used to estimate the cluster temperature is indicated by the circle, which has a radius of  $3'$  ( $\sim 770$  kpc). *Right panel* – Spectrum of A 697, extracted in the region reported in the left panel, with the thermal best fit model (solid line). The bottom section shows the residuals.

Furthermore, we obtained very consistent results using the Cash statistics.

We compared our temperature estimate with the values reported in the literature, and found agreement (within the errors) with the temperature obtained from ASCA data within the same region used here ( $8.2 \pm 0.8$  keV, Ota & Mitsuda 2004) and from the Chandra analysis in GBB06, who found  $10.2 \pm 0.8$  keV in the inner  $2'$  region of the cluster.

### Hardness ratio image

In order to derive hints about the nature of the X-ray clumps detected at the cluster centre (X1, X2 and X3 in Fig. 5.7), and search for indication of substructure in the gas temperature distribution, we produced the hardness ratio image of the cluster, as described in Section 2.6.1.

We used two images extracted in the 0.2–2.5 keV (*soft*) and 2.5–9 keV (*hard*) energy bands, both background subtracted and vignetted corrected. After removal of the individual point sources, the images were adaptively smoothed using the same scales, with a minimum significance of  $5\sigma$  and a maximum significance of  $10\sigma$ . Finally the hardness ratio image was produced by combining the smoothed images as  $(hard - soft)/(hard + soft)$ . The image is given in Figure 5.9, with the corresponding temperature calibration, carried out by means of the *fakeit* tool in

Table 5.3: Spectral fit results.

Region	T * keV	Z/Z <sub>⊙</sub> *	χ <sub>red</sub> <sup>2</sup> [d.o.f.]	Null-hyp. Prob.	S/N
Whole cluster (r=3')	9.3 <sup>+0.9</sup> <sub>-0.6</sub>	0.36 <sup>+0.11</sup> <sub>-0.10</sub>	1.19 [201]	0.332	115
A	10.3 <sup>+1.8</sup> <sub>-1.5</sub>	0.63 <sup>+0.30</sup> <sub>-0.23</sub>	1.16 [137]	0.100	62
B	8.0 <sup>+2.0</sup> <sub>-1.6</sub>	0.30 **	0.81 [66]	0.860	42
C	5.8 <sup>+2.0</sup> <sub>-1.2</sub>	0.30 **	1.09 [37]	0.319	30
D	14.5 <sup>+5.5</sup> <sub>-3.6</sub>	0.30 **	1.00 [78]	0.477	43
Ambient (r=2')	9.2 <sup>+1.5</sup> <sub>-1.0</sub>	0.42 <sup>+0.21</sup> <sub>-0.20</sub>	1.34 [151]	0.005	63

\* errors are at the 90% confidence level.

\*\* fixed in the fit.

XSPEC (see Sec. 2.6.1 for details).

Figure 5.9 shows that the core region of A 697 is relatively hot, with an average hardness ratio  $\langle \text{HR} \rangle \simeq -0.45$ , which corresponds to a temperature of  $T \simeq 10$  keV. This confirms the absence of a cool core in this cluster, as also found by Bauer et al. (2005). The three substructures detected by the wavelet analysis (Fig. 5.7) are reported as black dashed ellipses in Figure 5.9. There is a slight indication that the central and northern clumps are hotter ( $T \gtrsim 9$  keV) than the southern one ( $T \sim 8$  keV).

Figure 5.9 also shows the presence of a softer region West of the core ( $T \sim 5\text{--}6$  keV), while the southern part of the cluster appears hotter, with an average hardness ratio corresponding to a temperature  $T > 10$  keV.

In order to check the significance of these structures, we extracted the spectra in the regions reported in the right panel of Figure 5.9 and fitted them with the *wabs mekal* model (Sec. 2.6.1) in the 0.6–7.0 keV range.

Region A contains the three clumps detected by the wavelet analysis (black dashed ellipses). Unfortunately the statistics is not high enough to allow a spectral fit of these clumps individually. Therefore it is not possible to confirm the different

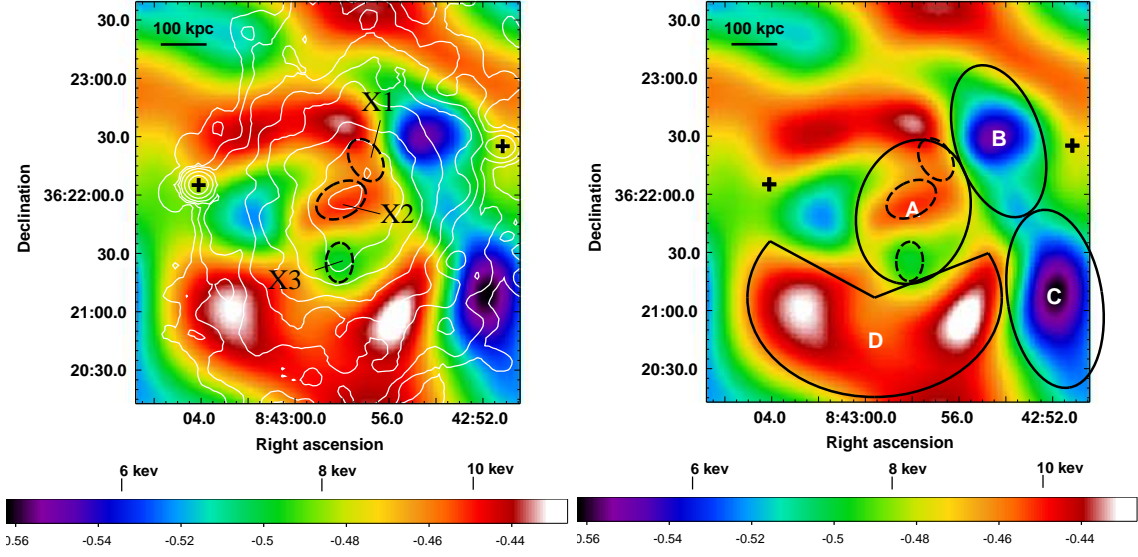


Figure 5.9: *Left panel* – Hardness ratio image of A 697 (colours) overlaid on the 0.5–5 keV brightness contours of the cluster (white), spaced by a factor of  $\sqrt{2}$ . The black dashed ellipses indicate the substructures X1, X2 and X3 detected in Fig. 5.6. The black crosses show the position of the point sources which were removed. The temperature calibration is reported. *Right panel* – Hardness ratio image of A 697 (same as *left panel*). A, B, C and D indicate the regions used for the spectral fits.

temperatures suggested by the hardness ratio image, and only the average value of the temperature within region A can be obtained a reasonably high level of significance. The results of the spectral fits for regions A, B, C, and D are summarised in Table 5.3.

In Figure 5.10 we compare the temperature associated with the regions in Figure 5.9 (right panel) with the average *ambient* gas temperature ( $T_{\text{amb}}$ ; Tab. 5.3) within  $2'$  from the cluster centre and determined after subtraction of regions A, B, C and D.

Table 5.3 and Figure 5.10 indicate that the temperature in regions A and B is consistent with  $T_{\text{amb}}$  within the errors, while region C is only slightly colder. On the contrary the southern region D is significantly hotter (at more than the 90% significance level), despite the large errors due to the low statistics.

## 5.4 Optical analysis

In the light of our results in the radio and X-ray bands, we re-analysed the behaviour of the optical galaxy distribution, using the SDSS-DR5 optical data and the bi-

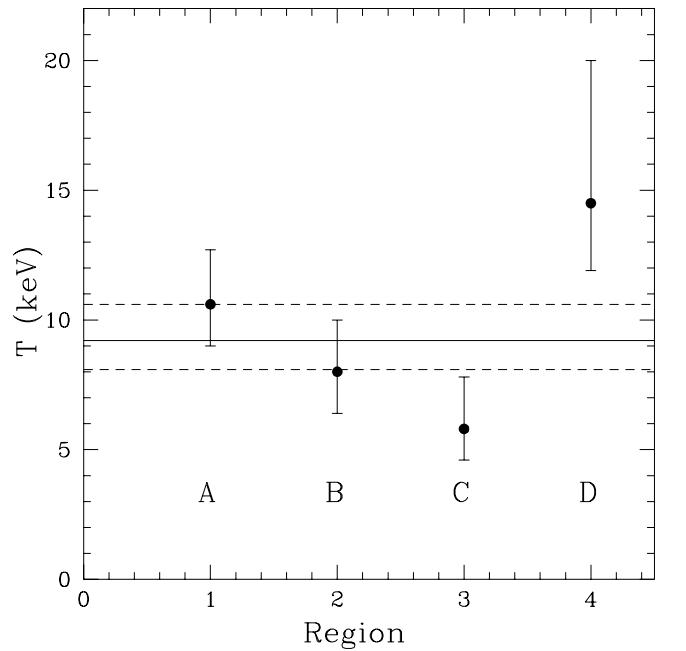


Figure 5.10: Best fit temperature associated with the X-ray regions defined in right panel of Figure 5.9. The ambient temperature (see text for details) and its error measurements are represented by the solid and dashed lines respectively. Errors are at the 90% confidence level.

dimensional version of the Adaptive Kernel Algorithm DEDICA (Bardelli et al. 1998a) to enhance possible substructures.

Although the velocity distribution of the member galaxies within  $\sim 1.3$  Mpc from the cluster centre (dashed circle in Fig. 5.3) shows four distinct components, GBB06 did not find evidence for any optical group associated (in the plane of the sky) with these redshift clumps (Sec. 5.1). Therefore only a bi-dimensional analysis could reveal the presence of possible substructures.

We extracted all objects in the SDSS within a region of  $\sim 10'$  radius (i.e.  $\sim 2.6$  Mpc) from the cluster centre, and limited our analysis to the optical magnitude  $i \leq 21$ . This choice represents the best compromise between the need for good statistics and the requirement to maximize the cluster member galaxies. From the  $i$  magnitude histogram, reported in the left panel of Figure 5.11, we determined that our sample is complete up to a magnitude 0.5 fainter than our limit (dashed line in the figure). The computation of the luminosity function (as difference between counts inside and outside a region of  $4'$  radius from the cluster centre) indicates that the cluster is visible in the magnitude range  $i = 18 \div 22$ . Moreover, the fraction

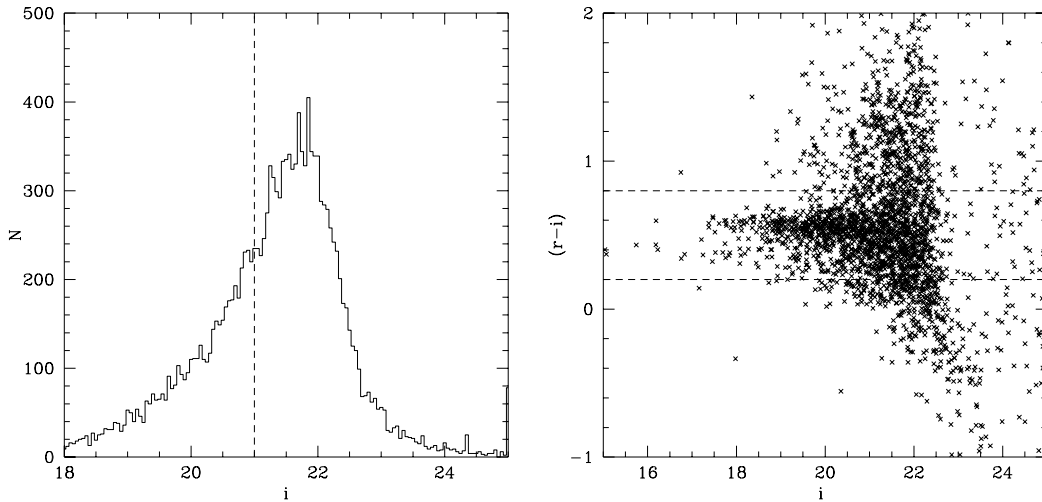


Figure 5.11: *Left panel* –  $i$  magnitude histogram for the objects extracted from the SDSS field. The dashed line represents the  $i = 21$  limit adopted for the analysis. *Right panel* – Color magnitude relation for the SDSS objects in the A 697 region. The dashed lines define the red sequence region.

of galaxies in the  $(r-i)-i$  color magnitude relation for cluster early type galaxies (defined as objects inside the dashed lines in the right panel of Fig. 5.11) is  $\sim 78\%$ .

According to Fukugita, Shimasaku & Ichikawa (1995), our limit is 0.25 magnitude brighter for ellipticals and 0.05 magnitude fainter for irregular galaxies with respect to the  $R \leq 21$  limit adopted by GBB06.

In Figure 5.12 we show the isodensity contours of the reconstructed galaxy density field from the SDSS sample, superposed to POSS-2 optical image of the A 697 region.

In panel *a*) the density map is defined on the basis of the galaxy number, while in panel *b*) the density is weighted for the galaxy luminosity, with a zero weight for objects with  $i > 16$  in order to minimize the interlopers. The isodensities in panel *c*) are computed by selecting all galaxies within the early type color-magnitude relation (Fig. 5.11, right panel). For comparison, in panel *d*) we report the galaxy density field of the cluster members with  $R \leq 21$  from GBB06.

As clear from Figure 5.12, the two-dimensional distribution of our sample is characterised by a number of subclumps, labelled from G1 to G6. All these substructures are significant at more than 95% level. In the following, we summarise the main properties of the overdensities visible in Figure 5.12:

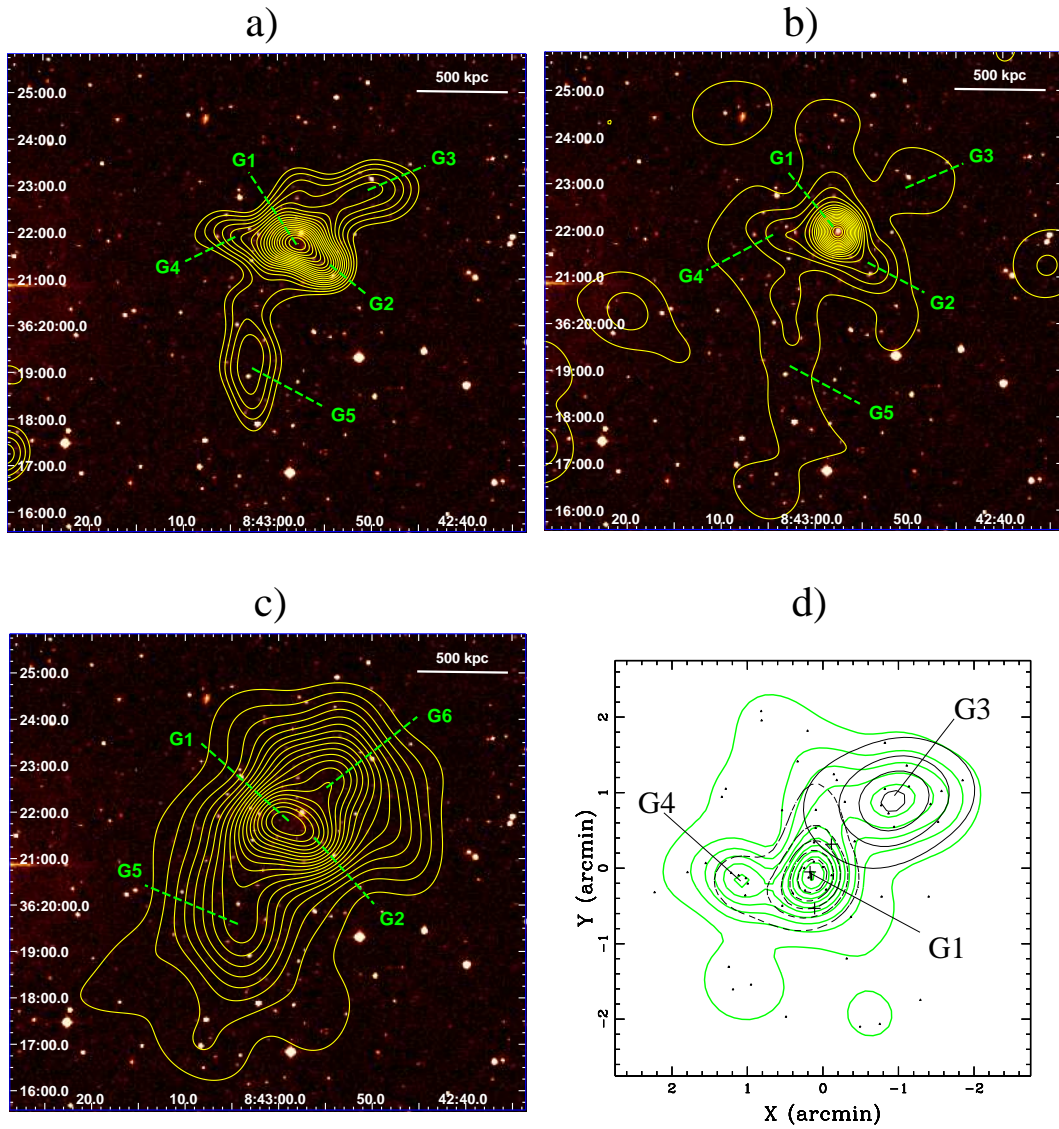


Figure 5.12: Panels a), b) and c) – Isodensity contours of the reconstructed galaxy density field (yellow) as derived from the  $i \leq 21$  SDSS sample, overlaid on the POSS-2 image of A 697 (colour). Labels from G1 to G6 indicate the optical substructures. In panel a) the density field is defined on the basis of the galaxy number. Panel b) shows the luminosity-weighted density image. Panel c) gives the red sequence density image. Panel d) – Isodensity contour map of the cluster members with  $R \leq 21$  (green contours) from GBB06. The black dashed and solid contours are the density image of the  $R \leq 20$  and  $20 < R \leq 21$  galaxies, respectively. The plot is centered on the cluster center. G1, G2 and G3 indicate the location of optical substructures detected in our analysis of the SDSS sample (see panels a, b and c).

1. Clump G1 : central region of the main cluster, composed of 20 galaxies, including the BCG. The luminosity-weighted galaxy distribution (Figure 5.12, panel *b*) is peaked on this galaxy. A slight offset is observed in the density field obtained from the whole sample (panel *a*), while the distribution of the red sequence galaxies appears shifted of  $\sim 20''$  ( $\sim 90$  kpc) from the peak in panel *b*). This region is evident also in the density field obtained from the GBB06 galaxy sample (panel *d*);
2. Clump G2: this substructure, containing 10 galaxies, is located at  $\sim 1'$  ( $\sim 260$  kpc) South-West of the cluster central region G1 (panel *a*). This overdensity is well visible also in the luminosity-weighted density field (*b*), and appears as an elongation in the red galaxy distribution in panel *c*). Although this clump is highly significant as a density peak (at the 99% level), it is not significantly segregated from the main cluster G1.
3. Clump G3: this structure appears as a clear overdensity in panel *a*), with a total of 10 galaxies. Its projected distance from centroid of the main clump G1 is  $\sim 500$  kpc. As clear from panel *d*), this clump was also detected by GBB06;
4. Clump G4: overdensity visible in the whole sample distribution (panels *a* and *b*), located East of the cluster centre, at  $\sim 400$  kpc (in the plane of the sky) from the G1 peak. This subclump is not clearly detectable in the red sequence sample (*c*), therefore it might be mostly composed by a rather blue galaxy population. This substructure was detected also by the optical analysis in GBB06 (panel *d*);
5. Clump G5: this substructure is significant at the 95% level, and extends South of the cluster core region, up to a distance of  $\sim 1$  Mpc from the peak of G1;
6. Clump G6: a shift of  $\sim 1'$  (i.e.  $\sim 260$  kpc) is observed between this overdensity (detected in the red sequence map in panel *c*) and the clump G3 (panel *a*). It is not clear whether these are different entities or the same group with a spatial offset between the red and blue galaxy populations.

We derived a rough estimate of the mass ratio between the main clump G1 and the subclump G2 on the basis of the luminosity-weighted number of galaxies in

these substructures. We obtained a mass ratio  $\gtrsim 1:3$ . No estimate can be obtained for G1 and the other optical clumps in Figure 5.12.

From inspection of Figure 5.2, which reports the cluster mass distribution, as reconstructed by the weak lensing analysis by Dahle et al. (2002), it is clear that the large scale distribution of the red galaxy sample (panel *c* in Figure 5.12) is similar to the dark matter density field.

## 5.5 Combined radio, optical and X-ray analysis

In this Section we combine the main results of our optical and X-ray analysis (Sec. 5.5.1) to complete the study of the merging environment of A 697. We also analyse the giant radio halo in connection with the X-ray properties of its hosting cluster (Sec. 5.5.2).

### 5.5.1 Optical versus X-ray

Figure 5.13 shows the isodensities of the SDSS galaxy density field (same as Fig. 5.12), superposed to cluster X-ray emission (left) and hardness ratio distribution (right), as derived by the Chandra observations (same as Figs. 5.6 and 5.9).

As clear from the overlay of the projected galaxy distribution on the cluster X-ray image, none of the optical substructures has an counterpart in the X-ray surface brightness, besides G1 which is clearly centered on the cluster core. An offset between the main X-ray peak (X2 in Fig. 5.6) and the G1 peak is observed both in panel *a*) and *c*), while the two peaks coincide in panel *b*), where the X-ray and optical distribution are both centered on the dominant cD galaxy.

On the large scale, the distribution of the hot gas is in rough agreement with the red galaxy density field (panel *c*, left), which is also similar to the mass distribution reported in Figure 5.2.

The comparison between the cluster hardness ratio image and the optical substructures (right panels of Fig. 5.13) shows that G2 is located (in projection) close to both the south-western hot region and eastern cold clump (respectively, regions D and C in Fig. 5.9). Furthermore, it is interesting that the peak of the optical substructure G6 coincides (on the plane of the sky) with the other cold region visible in the hardness ratio image (B in Fig. 5.9).

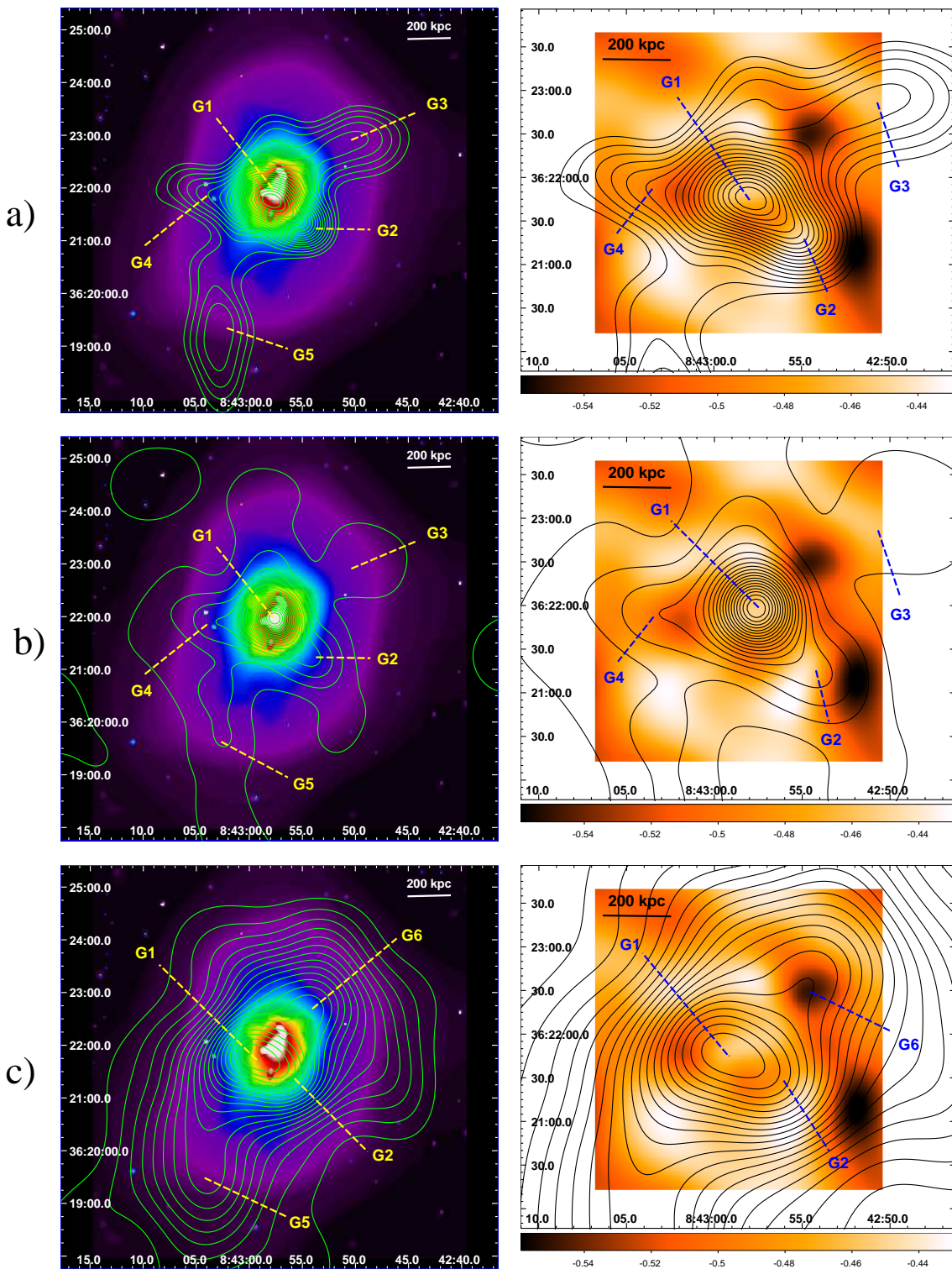


Figure 5.13: Isodensity contours of the SDSS galaxy density field overlaid on the X-ray Chandra image (left; same as Fig. 5.6) and hardness ratio image (right; same as Fig. 5.9). Labels from G1 to G6 indicate the optical substructures. *Panel a)* – The optical density field is based on the galaxy number, as in *a)* of Fig. 5.12. *Panel b)* – Luminosity-weighted density field, as in panel *b)* of Fig. 5.12. *Panel c)* – Red sequence density field, as in panel *c)* of Fig. 5.12.

### 5.5.2 Radio vs X-ray

It has been showed that the 1.4 GHz radio power of giant radio halos correlates with the X-ray luminosity of the hosting cluster (see Fig. 1.9 in Sec. 1.7). In particular the most powerful radio halos are hosted in the clusters with the highest X-ray luminosity.

In order to determine the behaviour of A 697 with respect to such correlation, we estimated the halo flux density at 1.4 GHz (and the corresponding radio power) on the basis of its 610 MHz flux density and spectral index in the 327–610 MHz frequency range (Tab. 5.2). We obtained  $S_{1.4\text{GHz}} = 4 \pm 1$  mJy and  $\log P_{1.4\text{GHz}} (\text{W Hz}^{-1}) = 24.08$ .

In Figure 5.14 we show as a magenta filled circle the the location of A 697 on the  $\text{Log}L_X\text{--}\text{Log}P_{1.4\text{GHz}}$  plane, along with all literature giant radio halo clusters (see Cassano, Brunetti & Setti 2006 and references therein for the literature data). Empty and filled black circles represent the clusters at redshift  $z < 0.2$  and  $z > 0.2$  respectively. The solid line is the best-fit of the correlation found by Cassano, Brunetti & Setti (2006), i.e.  $P_{1.4\text{GHz}} \propto L_X^{1.97 \pm 0.25}$  (see Sec. 1.7).

The location of A 697 is in agreement with the distribution of all clusters hosting a giant radio halo known so far.

In Figure 5.15 we show the overlay of the giant radio halo on the A 697 X-ray image. It is clear that the halo emission extends within the cluster thermal emission. The innermost and brightest region of the source, discussed in Section 5.2.2, permeates the whole core region, while the halo filaments (F1, F2 and F3 in the right panel of Fig. 5.4) extend outside the cluster core, where the X-ray surface brightness is lower.

## 5.6 Multiple group accretion or cluster major merger?

The large number of clumps detected in our optical analysis (Fig. 5.12) might suggest that not just a single merging process is ongoing in A 697, but repeated collisions between the main cluster and smaller units may be taking place. On the basis of the redshift information from GBB06 and from the SDSS, these clumps are not clearly segregated in the velocity space. Furthermore, none of them has a clear counterpart in the X-ray surface brightness distribution, although hints of a possible association

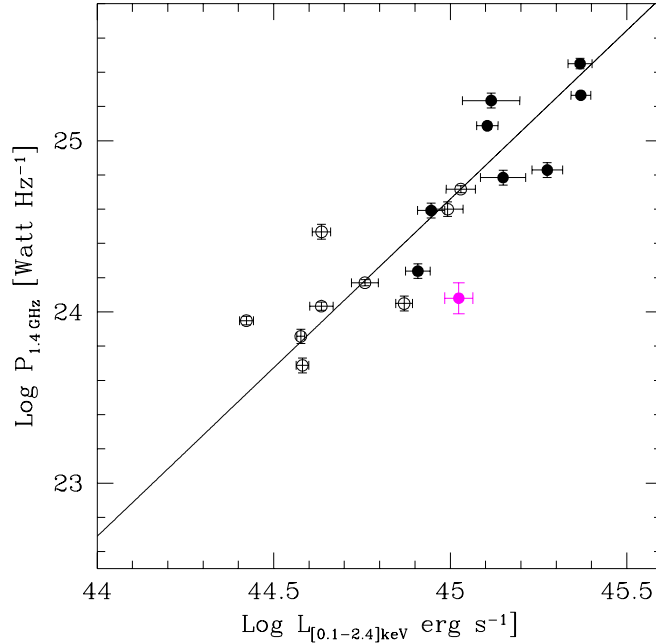


Figure 5.14:  $\text{Log}L_X\text{--}\text{Log}P_{1.4\text{GHz}}$  correlation for the clusters with detected giant radio halos. Empty black circles represent the literature clusters at  $z < 0.2$ , and filled black circles the clusters at  $z > 0.2$ . The magenta filled circle shows the location of A 697. The solid line is the best-fit of the correlation found by Cassano, Brunetti & Setti (2006).

of some clumps with the substructures detected in the hardness ratio image were found (Fig. 5.13).

An alternative possibility is that the observed complex optical and X-ray distributions are the result of a cluster major merger occurring along the line of sight. This scenario, which was also discussed by GBB06, may be supported by the following observational evidences:

- i. the cluster core region is hot and highly disturbed both in the X-ray surface brightness and hardness ratio distributions. As shown by the numerical simulations in Gómez et al. (2002), the core disruption occurs when a significant mass of the gas of the infalling subcluster reaches the core of the primary cluster. Hence a relatively high mass ratio for the merger is required to justify the complex structure observed in the A 697 core region;
- ii. the cluster X-ray emission, the mass distribution from the weak lensing analysis (Dahle et al. 2002) and the optical density field derived from the cluster

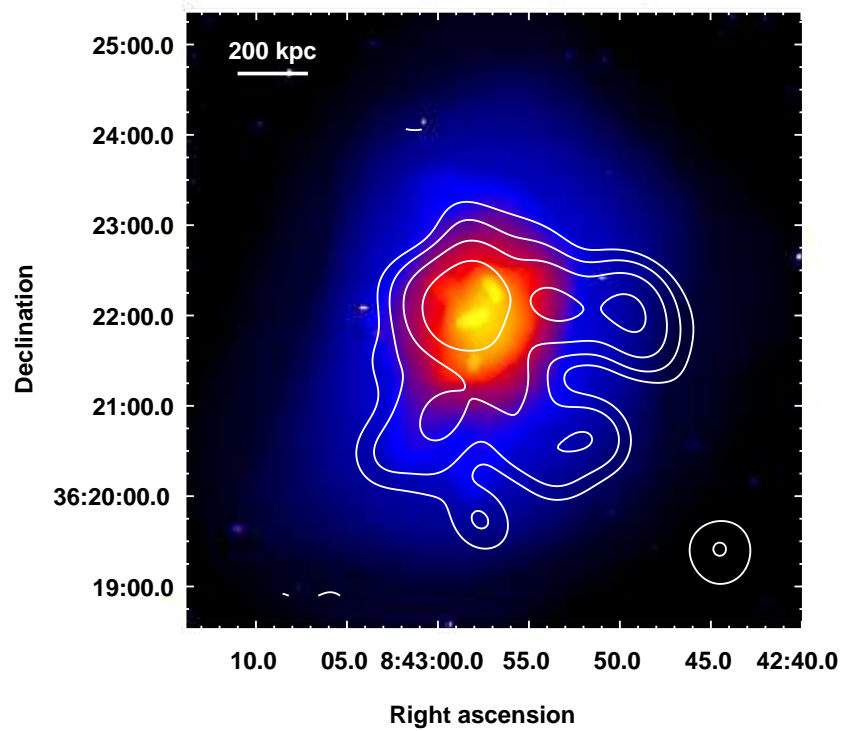


Figure 5.15: GMRT 610 MHz contours of the giant radio halo in A 697, overlaid on the 0.5–5 keV wavelet-reconstructed Chandra image of the cluster. The radio and X-ray images are the same as Figs. 5.4 and 5.6 respectively.

red galaxies all show a similar structure on the large scale, which is roughly elliptical with the major axis in the NNW/SSE direction. If the merger is in an advanced stage, as suggested by the core disruption, we might expect a decoupling between dark matter, galaxies and hot gas. However if the axis merger is mainly along the line of the sight, we could not be able to observe possible offsets existing between the three components;

- iii. the cluster is characterised by a very high LOS velocity dispersion ( $\sigma_v = 1334_{-95}^{+114}$  km s<sup>-1</sup>, GBB06), comparable to the highest values found in the literature for other merging clusters (e.g. Girardi & Mezzetti 2001);
- iv. the existence of redshift substructures mainly aligned along the line of sight was pointed out by GBB06. As clear from the velocity distribution determined by those authors (here reported in Fig. 5.16; see central panel), the main clump (centered at  $v \sim 85000$  km s<sup>-1</sup>) extends on a very broad velocity range, and has a velocity dispersion ( $\sigma_v \sim 600$  km s<sup>-1</sup>; GBB06) comparable to moderately massive clusters. A possible explanation for the complex velocity distribution in Figure 5.16 is a merger along the LOS between the main cluster and a second massive component which has already crossed the primary cluster core.

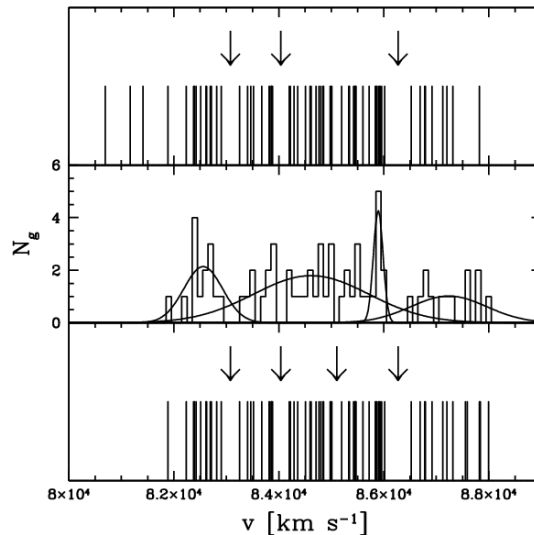


Figure 5.16: Distribution of radial velocities for the cluster members from GBB06. *Upper and lower panels:* stripe density plots where arrow indicate the position of the significant gaps. *Central panel:* velocity histogram with a binning of 100 km s<sup>-1</sup> with the Gaussians corresponding to the most significant Kaye mixture model (KMM; Ashman et al. 1994) partition for the GBB06 sample.

To conclude, we propose that A 697 is merging with a relatively massive subcluster along the line of sight. We also suggest that the first encounter between the cores may have already occurred and that the subcluster remnants are now oscillating around the mean velocity, before merging completely and recover the dynamical equilibrium.

## 5.7 Origin of the radio halo

A 697 is a massive galaxy cluster ( $M_v \sim 2.2 \times 10^{15} M_\odot$ ; Tab. 2.1) hosting a giant radio halo. According to the semi-analytical calculations in Cassano & Brunetti (2005) and Cassano, Brunetti & Setti (2006) in the framework of the re-acceleration model (Sec. 1.9), a recent merger of A 697 with a massive subcluster (i.e. mass ratio  $\gtrsim 1:5$ ) is required to explain the presence of such diffuse radio emission.

In Section 5.6 we proposed that the cluster may be indeed experiencing a major merger, which is expected to be in a relatively advanced stage. If such scenario is correct, we might expect that the subcluster infall has generated large scale turbulent motions in the gas of the main cluster (Sec. 1.1.2). Once the turbulent eddies have diffused over the whole cluster volume and decayed to the scales which are needed to efficiently re-accelerate relativistic electrons in the ICM ( $\lesssim 100$  kpc in the case of MS waves, Cassano & Brunetti 2005; see also Sec. 1.9.1), the giant radio halo was formed.

In this case the re-acceleration models predict the presence of a high frequency steepening in the integrated spectrum of the halo (Sec. 1.8; see also the A 3562 halo in Chapter 3). Unfortunately no spectral information over a wide range of frequencies is currently available for this source to test such prediction.

New 327 MHz observations of A 697, carried out with the GMRT during Cycle A011 (January 2007), combined with the 610 MHz data presented here, will allow us to better constrain the low frequency behaviour of the halo total spectrum and study the spectral index distribution in this source. However, high frequency observations are needed to determine the spectral index, as well as the morphology of the halo, at a frequency  $> 610$  MHz, and possibly confirm the presence of the expected high frequency steepening.

## Chapter 6

# The radio relic in Abell 521

Abell 521 is an X-ray luminous and massive galaxy cluster ( $L_{X[0.1-2.4\text{keV}]} \sim 8 \times 10^{44}$  erg s<sup>-1</sup>, virial mass  $M_v \sim 1.9 \times 10^{15} M_\odot$ ), at the redshift of  $z=0.247$ , which exhibits a variety of observational signatures of ongoing merging processes. Its general properties are reported in Table 2.1.

The complex merging activity of this cluster has been highlighted by the large amount of the X-ray (Arnaud et al. 2000, hereinafter AMS00; Ferrari et al. 2005, hereinafter FAE05) and optical data (Maurogordato et al. 2000, hereinafter MPB00; Ferrari et al. 2003, hereinafter FMC03, and Ferrari 2003, hereinafter F03) analysed in the literature. Multiple merging episodes are known to be occurring in this very disturbed cluster, whose properties are indicative of an object at an early phase of its dynamical evolution, and still growing by accreting a number of smaller mass concentrations.

Thanks to the wealth of the available optical and X-ray information, A 521 is an ideal environment to investigate the effects of cluster mergers on the radio emission properties of both the member galaxy population and the diffuse intracluster medium. In the present work we focus our attention on the most remarkable feature of the radio emission from A 521, i.e. the diffuse radio relic permeating a peripheral region of the cluster. A thorough multiband study of the relic and its surroundings is carried out using *i)* our GMRT 610 MHz and VLA 4.9 and 8.4 GHz observations of the relic region (Tab. 2.2), *ii)* VLA archival 1.4 GHz data (Tab. 2.2), *iii)* Chandra observations from the public archive (Tab. 2.4), and *iv)* the X-ray and optical information provided by the literature.

We discuss the source origin in the framework of the theoretical models for the cluster radio relic formation (Sec. 1.10), and in connection with the assessed merging

activity of the hosting cluster.

We also report on a multifrequency radio study of the source J0454–1016a, the most powerful radio galaxy in the cluster, which is located at a projected distance of  $\sim 1.5'$  from the relic. The connection between this radio galaxy and the nearby relic is investigated.

The analysis of the cluster radio galaxies was presented in Giacintucci et al. (2006; hereinafter GVB06), and will be not reported in the present work. The result found in GVB06 is that the number of the radio emitting early-type galaxies in A 521 is consistent (despite the large uncertainties due to the small number statistics) with the expectations from the standard radio luminosity function (RLF) for the local ( $z \leq 0.09$ ) cluster ellipticals. Since A 521 is at  $z=0.247$ , this result is striking if the positive evolution of the RLF for X-ray selected high redshift clusters is taken into account (Stocke et al. 1999; Branchesi et al. 2005). This led us to safely conclude that the merging events in A 521 are not increasing the AGN activity in the cluster early-type population compared to other less extreme environments, as already found in the complex merging environment of A 3558, in the central region of the Shapley Concentration (Venturi et al. 2000; Giacintucci et al. 2004).

The Chapter is organised as follows: in Section 6.1 we review the main optical and X-ray properties of A 521, as derived in the literature; the radio observations and data analysis of the relic and the nearby radio source J0454–1016a are reported in Section 6.2; in Section 6.3 we present the analysis of the integrated and point-to-point spectrum of the relic; the proposed scenarios for the relic origin are given in Section 6.4; in Section 6.5 we present the results of our re-analysis of the X-ray archival Chandra data; conclusions are summarised in Section 6.6.

At the redshift of A 521 ( $z=0.247$ ), the cosmology adopted in this work leads to a linear scale of  $1'' = 3.87$  kpc.

## 6.1 Multiple merging events in A 521

The extensive analysis performed at optical (MPB00, FMC03 and F03) and X-ray wavelengths (AMS00 and FAE05) reveals that A 521 is likely a young and still accreting galaxy cluster, whose physical state is very far from virialisation. Its

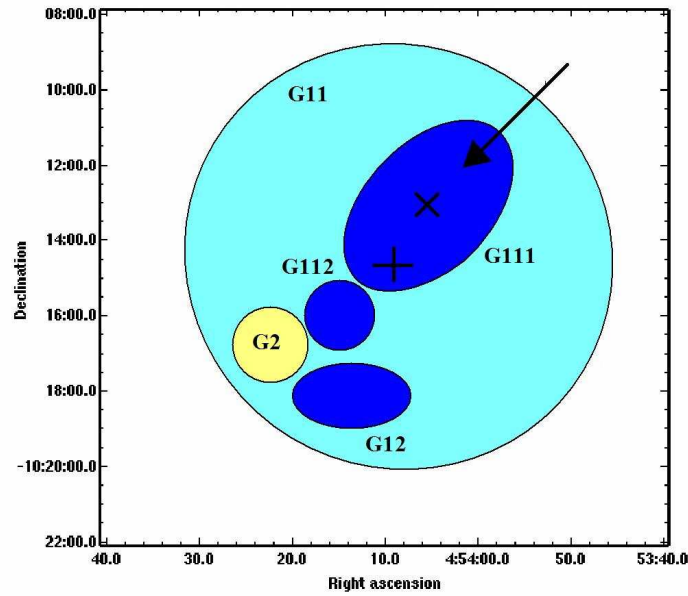


Figure 6.1: Cartoon representing the optical substructures in A 521. The cross marks the X-ray centre of the main cluster G11 (light blue). Blue ellipses indicate the location of the optical groups at the redshift of the cluster, while the yellow circle is an unbound substructure. The x-point is the centre of the X-ray compact subclump associated with the optical group G111 (AMS00; see also text). The arrow represents the likely infall direction of the group G111.

dynamics appears extremely complex, due to the multiple merging events which are significantly affecting the observed galaxy and hot gas distributions of the cluster. The cartoon in Figure 6.1 shows the location of the main optical substructures detected in the cluster region by MPB00 and FMC03, and sketches the merging scenario proposed by those authors.

The main merging episode is likely occurring between the main cluster (labelled as G11 in Fig. 6.1) and a northwestern group (G111), centered on the brightest cluster galaxy (BCG). The group is probably falling onto the cluster along the North West–South East direction, as indicated by the arrow in Figure 6.1. Many subcondensations can be clearly distinguished along the merger axis, both in the two-dimensional and redshift distribution of galaxies. In particular the following velocity substructures were indentified by FMC03 (see Fig. 6.1):

- G11: the main cluster with a mean velocity  $\langle v \rangle = 73965 \text{ km s}^{-1}$  and a relatively high velocity dispersion  $\sigma \sim 930 \text{ km s}^{-1}$ ;
- G111: a group dynamically bound to the BCG, with a very low velocity

dispersion ( $\sigma \sim 250 \text{ km s}^{-1}$ ) and a slightly higher mean velocity ( $\langle v \rangle = 74290 \text{ km s}^{-1}$ ) as compared to the main cluster G11. This group is probably falling onto the cluster from the NW direction. The small difference in the mean velocity between G111 and G11 may suggest that the merging is likely to be occurring on the plane of the sky;

- G112: a compact group bound to the cluster, whose velocity ( $\langle v \rangle = 74068 \text{ km s}^{-1}$ ,  $\sigma \sim 570 \text{ km s}^{-1}$ ) is similar to that of the infalling group G111. The virial masses estimated for G111 and G112 in FMC03 on the basis of the optical information are much smaller ( $\sim$  one order of magnitude) than that of the main cluster G11;
- G12: the lowest mass group bound to A 521, with higher velocity ( $\langle v \rangle = 75730 \text{ km s}^{-1}$ ) and  $\sigma \sim 120 \text{ km s}^{-1}$ .
- G2: a group South–East of A 521, at a projected distance of  $\sim 900 \text{ kpc}$  from the X–ray centre of the main cluster G11. This group has a mean velocity of  $\langle v \rangle = 78418 \text{ km s}^{-1}$  ( $\sigma \sim 500 \text{ km s}^{-1}$ ), which is much higher than the cluster velocity. On the basis of the two–body criteria, FMC03 concluded that this group is probably not bound to A 521.

Furthermore, FMC03 also found evidence of a filamentary structure of galaxies in the core region of the cluster, extending along the NE/SW direction, with velocity  $\langle v \rangle = 73625 \text{ km s}^{-1}$  and high velocity dispersion. This structure has been interpreted as evidence for a past merger, which occurred along a direction orthogonal to the axis of the current merging process.

The ROSAT–HRI observations analysed by AMS00 lead to a merging scenario which is consistent with that suggested by the optical data. The smoothed ROSAT–HRI image of A 521, extracted from the ROSAT public archive, is shown as green contours in Figure 6.2, superposed to the POSS–2 optical frame. A compact subclump was detected by AMS00 North–West of the centre of the cluster X–ray emission. The X–ray surface brightness distribution of this subclump is roughly peaked on the BCG, which belongs to the optical group G111 (Fig. 6.1). This X–ray substructure is therefore associated with the infalling group G111. The gas mass ratio between the main cluster G11 and the subclump G111 is  $M_{\text{gas, main}}/M_{\text{gas, sub}} \sim 7$

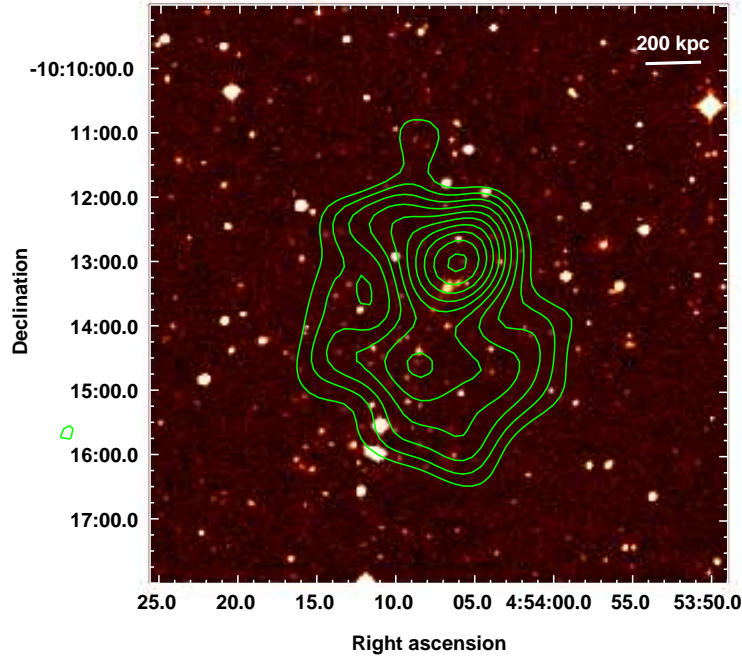


Figure 6.2: X-ray smoothed ROSAT-HRI image (green contours) of A 521 (from the ROSAT public archive), overlaid on the POSS-2 optical frame.

(AMS00). This value implies that we are witnessing an accretion process of a relatively massive galaxy group by the main cluster, rather than a major cluster merger.

In their more recent X-ray Chandra analysis, FAE05 brought further evidence favouring the above merging scenario and confirming the presence of a number of subclusters (G111 being the most massive one) observed at different stage of their infall onto the main cluster.

## 6.2 Radio analysis

### 6.2.1 GMRT observations at 610 MHz

The galaxy cluster A 521 was observed as part of the GMRT Radio Halo Survey at 610 MHz (Sec. 1.12). We refer to Table 2.2 and Section 2.2 for the details on the observations and Section 2.4 for the data reduction.

The most relevant result of these observations is the detection of a radio relic at the cluster outskirts. This source, visible also on the NVSS, was first imaged at high sensitivity at 1.4 GHz with the VLA (F03 and FAE05).

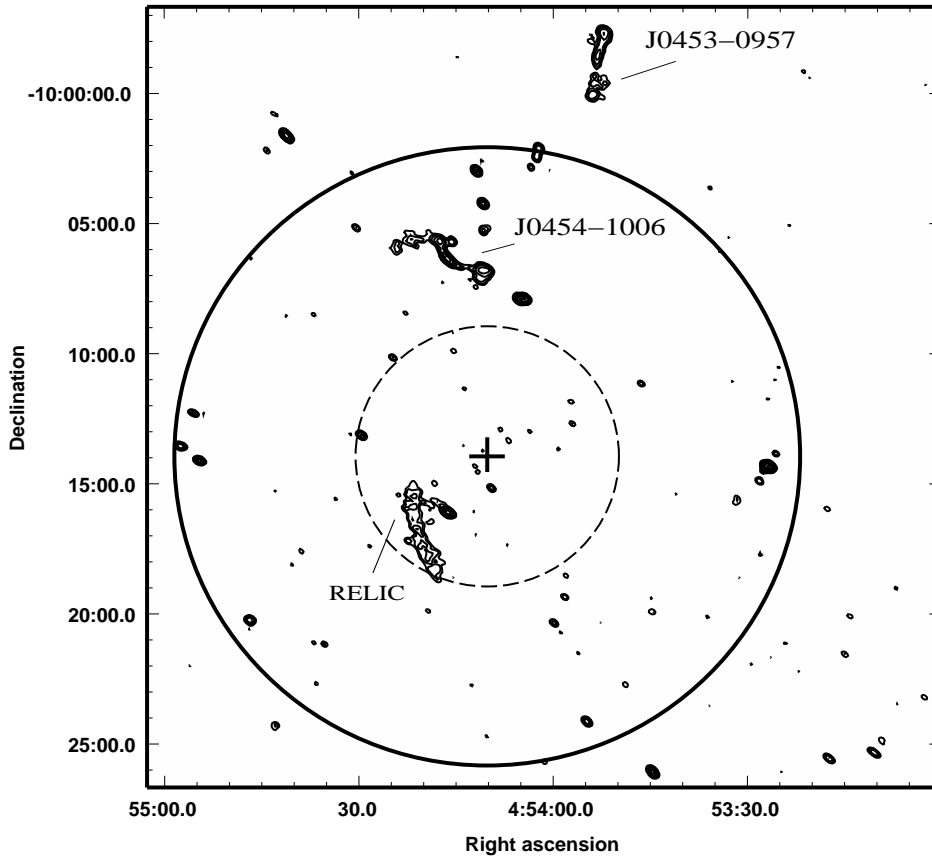


Figure 6.3: 610 MHz radio contours of the  $30' \times 30'$  region containing A 521. Contour levels are spaced by a factor 2, starting from  $5\sigma = 0.2 \text{ mJy b}^{-1}$ . The resolution is  $13.1'' \times 8.1''$ , in p.a.  $56^\circ$ . The cross marks the X-ray centre of the cluster. The radius of the solid circle corresponds to the cluster virial radius  $R_v = 2.8 \text{ Mpc}$ . The dashed circle has a radius of  $\sim 1 \text{ Mpc}$  and indicate the region covered by the optical analysis in FMC03.

In Figure 6.3 we show the image of the 610 MHz radio emission covering the region within the cluster virial radius (solid circle in the figure; see Tab. 2.1). The cross marks the X-ray centre of the cluster (Tab. 2.1). The dashed circle has a radius corresponding to  $\sim 1 \text{ Mpc}$ , and indicate the region covered by the optical analysis in FMC03. The image resolution ( $13.1'' \times 8.1''$ ) highlights the extended radio structures detected in the field, namely the radio relic in the south-eastern periphery of the cluster, and the two extended radio galaxies J0453-0957 and J0454-1006, located North of A 521, and analysed in GVB06.

As clear from Figure 6.3, the radio emission within the inner  $\sim 1 \text{ Mpc}$  radius region of the cluster is dominated by the diffuse radio relic. The source is located at a projected distance of  $\sim 4'$  (i.e.  $\sim 930 \text{ kpc}$ ) from the A 521 X-ray centre, and at

the border of the cluster X-ray emission, as detected by ASCA (Fig. 6.4). The relic is slightly misaligned with respect to the outer level of the ASCA X-ray isophotes.

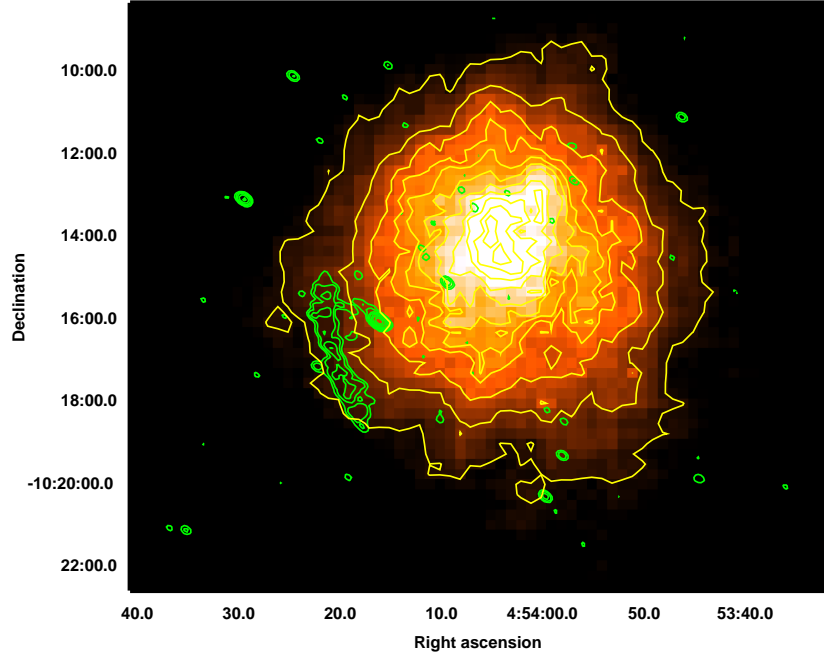


Figure 6.4: 610 MHz radio contours (green) of the A 521 region, overlaid on the X-ray smoothed ASCA image (colours and yellow contours) of the cluster, extracted from the ASCA public archive. The radio image is the same as Figure 6.3. The X-ray contours are  $3 \times 10^{-5} \div 2.4 \times 10^{-4}$  cts  $s^{-1}$  and are spaced of  $1.5 \times 10^{-5}$  cts  $s^{-1}$ .

### 6.2.2 The radio morphology

In Figure 6.5 we show the 610 MHz image of the diffuse radio source at the cluster outskirts. In the left panel, the relic (grey scale and contours) has an arc-shaped and highly elongated structure. The source major axis is  $\sim 4'$ , corresponding to a linear size of  $\sim 930$  kpc, and it is roughly perpendicular to the direction towards the cluster centre (Figs. 6.3 and 6.4). The maximum extent along the minor axis is  $\sim 50''$ , corresponding to  $\sim 200$  kpc only. The relic morphology and size at 610 MHz (Fig. 6.5) are in very good agreement with the 1.4 GHz image (FAE05 and Fig. 6.6 in this work). Its main radio properties are summarised in Table 6.1.

The 610 MHz full resolution image of the source, superposed on the POSS-2 optical frame in the right panel of Figure 6.5, allows to rule out the possibility that this object is a blend of different radio sources. If the individual radio

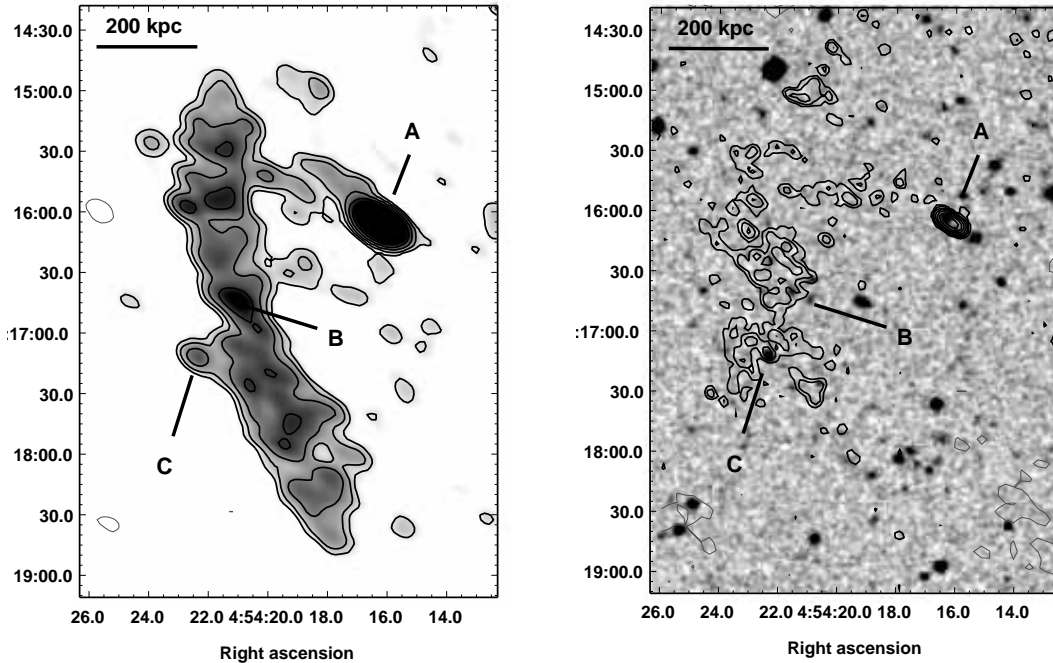


Figure 6.5: 610 MHz image of the radio relic in A 521. A, B and C indicate the position of the radio galaxies embedded in the relic emission. *Left panel* – Grey scale and contours of the relic at the resolution of  $13.1'' \times 8.1''$ , in p.a.  $56^\circ$ . The rms level is  $0.40 \text{ mJy b}^{-1}$ , and contours are spaced by a factor 2, starting from  $\pm 0.12 \text{ mJy b}^{-1}$ . *Right panel* – The relic contours are superposed to the POSS-2 optical image. The resolution is  $5.0'' \times 4.0''$ , in p.a.  $52^\circ$ . The rms level is  $0.30 \text{ mJy b}^{-1}$ . Contours are spaced by a factor 2, starting from  $\pm 0.12 \text{ mJy b}^{-1}$ .

galaxies embedded in the diffuse emission (labelled as A, B and C in Fig. 6.5) are excluded, the extended radio source does not appear to be associated with any optical counterpart.

Figure 6.5 also shows that the cluster radio galaxy J0454–1016a (labelled as A), i.e. the most powerful radio galaxy in A 521 (GVB06; see Tab. 6.2) is located  $1.5'$  only away from the relic (i.e.  $\sim 350 \text{ kpc}$  in the plane of the sky), and a faint bridge of low surface brightness emission seems to connect the two sources. In the full resolution image (Fig. 6.5, right panel) the source appears slightly extended. However the resolution is not high enough to confirm the presence of a physical relationship with the relic, for example in the form of bent jets and/or extended emission in the direction of the relic.

Even though projection effects in A 521 should be taken into account, this situation is similar to what is observed in the Coma cluster, where a bridge of

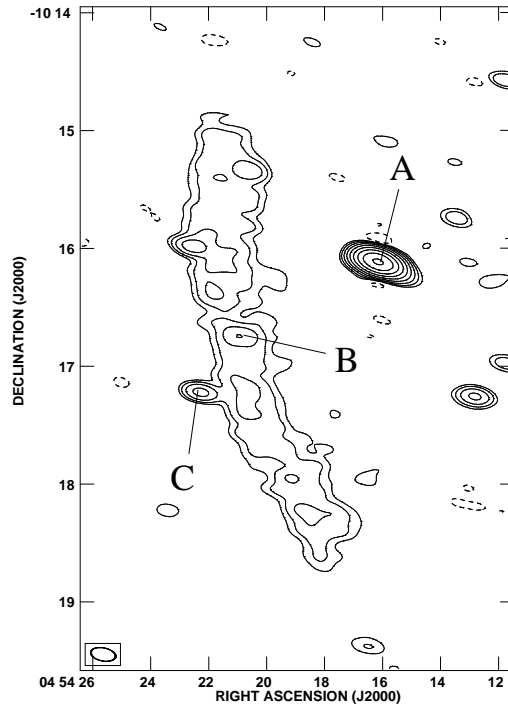


Figure 6.6: 1.4 GHz radio contours of the relic source in A 521 from VLA archival data. The rms level is  $15 \mu\text{Jy b}^{-1}$ . Contours are spaced by a factor 2, starting from  $\pm 0.045 \text{ mJy b}^{-1}$ . The resolution is  $12.8'' \times 6.7''$ , in p.a.  $79^\circ$ . A, B and C indicate the position of the radio galaxies embedded in the relic emission.

radio emission connects the tails of the radio galaxy NGC 4789 and the prototype relic source 1253+275 (see left panel of Fig. 1.7 in Sec. 1.5; Giovannini, Feretti & Stanghellini 1991).

### 6.2.3 VLA observations at 4.9 and 8.4 GHz

In order to image the sky region close to the relic and resolve the inner structure of the source J0454–1016a at higher frequency and resolution than the GMRT 610 MHz observations (Fig. 6.5), we observed the relic using the VLA at 4.9 GHz in the hybrid BnA and CnB configurations, and at 8.4 GHz in the BnA configuration. The details of the observations are given in Table 2.2, and the data reduction is described in Section 2.5.

Table 6.1: Properties of the relic source in A 521.

$S_{610\text{MHz}}$ (mJy)	$42 \pm 2$
$S_{1400\text{MHz}}$ (mJy)	$14 \pm 1$
$S_{4890\text{MHz}}$ (mJy)	$2.0 \pm 0.2$
$\alpha_{610}^{1400}$	$1.32 \pm 0.09$
$\alpha_{610}^{4890}$	$1.46 \pm 0.05$
$\log P_{610\text{MHz}}$ ( $\text{W Hz}^{-1}$ )	24.92
$\log P_{1400\text{MHz}}$ ( $\text{W Hz}^{-1}$ )	24.44
$\log P_{4980\text{MHz}}$ ( $\text{W Hz}^{-1}$ )	23.61
Linear size (kpc $\times$ kpc)	$\sim 930 \times 200$
axial ratio	$\sim 4.5$
d (arcmin) <sup>1</sup>	$\sim 4$
$B'_{\text{eq}}$ ( $\mu\text{G}$ ) <sup>2</sup>	3

<sup>1</sup> distance from the X-ray cluster centre (Tab. 2.1)

<sup>2</sup> see Section 6.3.1.

### 6.2.4 The radio relic

In Figure 6.7 we present the 4.9 GHz image of the relic (grey scale), obtained from the VLA–CnB observations, tapered to a resolution of  $22.0'' \times 15.0''$ , and with superposed the GMRT 610 MHz contours (same as Fig. 6.5). The faintest features of the relic emission are significant at the  $3\sigma$  level (i.e.  $45 \mu\text{Jy b}^{-1}$ ), and the peaks at the level of  $12\sigma$ . This is the second detection of a radio relic at a frequency as high as 4.9 GHz, after the relic source 1253+275 in the Coma cluster (Andernach et al. 1984; Thierbach, Klein & Wielebinski 2003; see also right panel of Fig. 1.7 in Sec. 1.5).

Future observations at 4.9 GHz with the VLA DnC configuration, which is more adequate to study the extended radio emission at this frequency and at the low declination of the source, are needed to properly image and analyse the relic morphology at 4.9 GHz.

### 6.2.5 The radio galaxy J0454–1016a

As pointed out in Section 6.2.2, the radio galaxy J0454–1016a is located at  $\sim 350$  kpc only (in projection) from the radio relic. This source has the highest radio power among the radio galaxies belonging to A 521 (GVB06; see also Tab. 6.2). It is identified with the galaxy #143 ( $v=74282 \text{ km s}^{-1}$ ,  $I=17.00$ ) in the FMC03 catalogue. No colour information is available in FMC03 for this galaxy, however on the basis of its featureless optical spectrum (FMC03), and of the  $(R-I)=1.26$  colour,

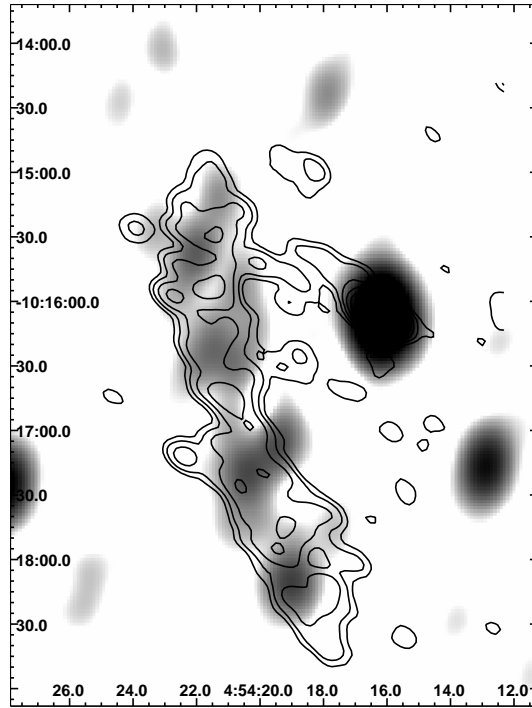


Figure 6.7: GMRT 610 MHz contours of the radio relic, overlaid on the 4.9 GHz VLA emission (grey scale). The resolution of the 4.9 GHz image is  $22.0'' \times 15.0''$ , and the  $1\sigma$  noise level is  $15 \mu\text{Jy b}^{-1}$ . The 610 MHz image is the same as Fig. 6.5.

as derived from the SuperCOSMOS/UKST catalogue (Hambly et al. 2001), it can be *bona fide* classified as an early-type galaxy (GVB06).

The CnB 4.9 GHz image of the source is given in panel *b*) of Figure 6.8, and the BnA higher resolution images at 4.9 and 8.4 GHz are presented in panels *c*) and *d*) respectively. For a proper comparison, we report the 610 MHz full resolution image of the relic and J0454–1016a in panel *a*). The highest resolution 8.4 GHz image (panel *d*) is suggestive of two radio jets starting from the northern compact component and sharply bent in the first few kpc from it. This leads us to conclude that the high frequency and arcsec resolution images of J0454–1016a are consistent with an head–tail morphology for the source. It appears extended in all the images, with a largest linear size of  $\sim 30$  kpc. The northern and most compact component, detected at both frequencies in the BnA images (panels *c* and *d*), is coincident with the nucleus of the host galaxy, and might host the radio core. However this component has a relatively steep spectrum between 4.9 and 8.4 GHz, with  $\alpha = 1.08 \pm 0.13$ . This suggests that the jet contribution is still dominant at the  $0.5''$  resolution, and higher resolution observations are needed to resolve the radio core.

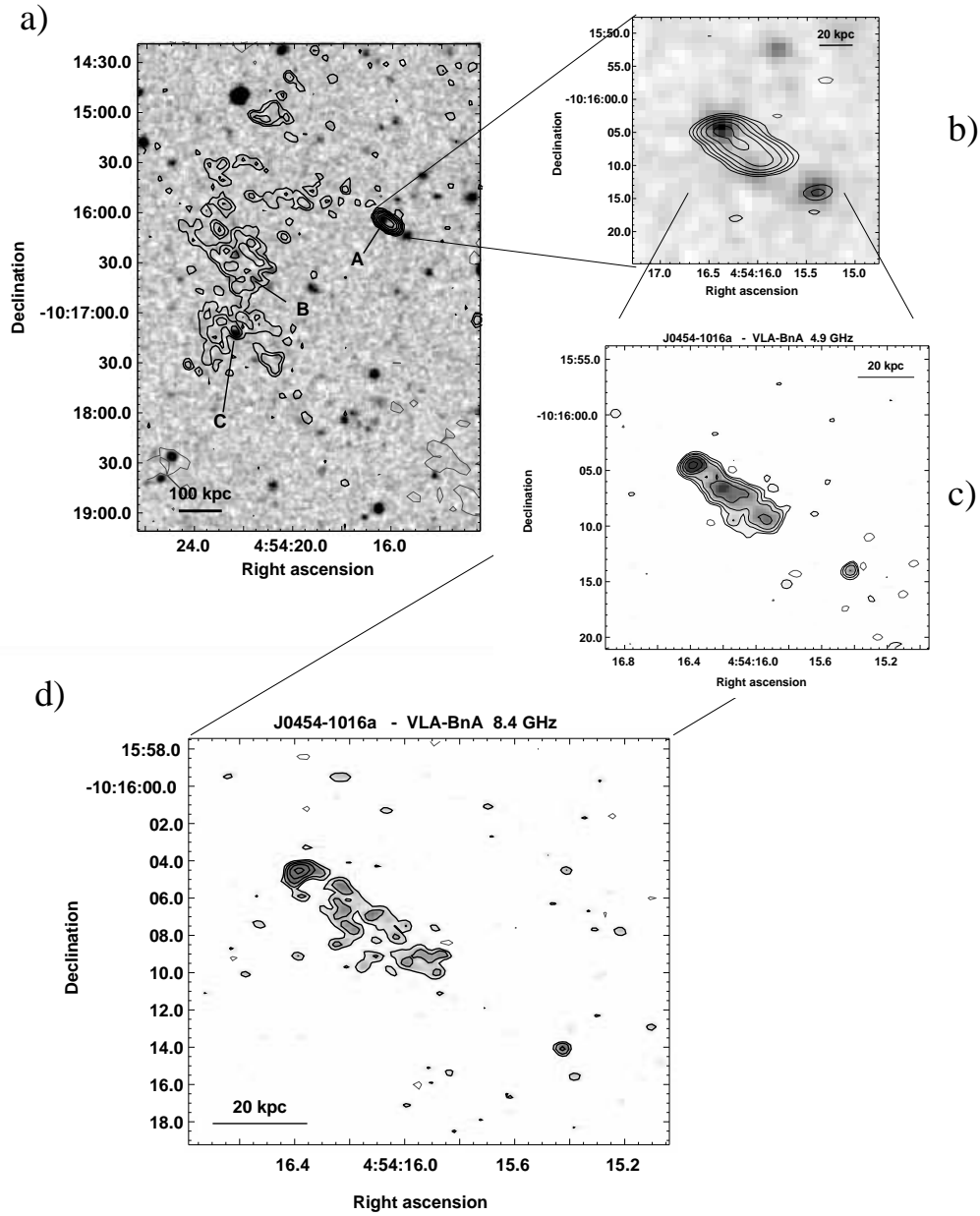


Figure 6.8: *Panel a)* – 610 MHz radio contours of the radio relic, overlaid on the POSS-2 optical image. The resolution is  $5.0'' \times 4.0''$ , in p.a.  $52^\circ$ . The radio contours are  $0.12 \times (-1, 1, 2, 4, 8, 16, 32, 64, 128, 256, 512) \text{ mJy b}^{-1}$ . A, B and C indicates the position of radio galaxies embedded in the relic emission. *Panel b)* – VLA-CnB 4.9 GHz contours of J0454-1016a. The resolution is  $4.0'' \times 2.0''$ , in p.a.  $-82^\circ$ . The contour levels are  $45 \times (-1, 1, 2, 4, 8, 16, 32) \mu\text{Jy b}^{-1}$ . *Panel c)* – VLA-BnA 4.9 GHz image (contours and grey scale) of J0454-1016a. The resolution is  $1.0'' \times 0.8''$ , in p.a.  $-84^\circ$ . The contour levels are  $30 \times (-1, 1, 2, 4, 8, 16, 32) \mu\text{Jy b}^{-1}$ . *Panel d)* – VLA-BnA 8.4 GHz image (contours and grey scale) of J0454-1016a. The resolution is  $0.6'' \times 0.5''$ , in p.a.  $82^\circ$ . The contour levels are  $24 \times (-1, 1, 2, 4, 8, 16) \mu\text{Jy b}^{-1}$ .

The extended emission is entirely located South–West of the compact component, and there is no evidence of any emission in the direction of the radio bridge detected at 610 MHz (see Fig. 6.5 and panel *a* of Fig. 6.8). Thus we can safely rule out any physical connection between the diffuse emission from the relic and this radio galaxy, whose tail extends (at least in projection) in a direction away from the relic region.

Table 6.2: Properties of the radio galaxy J0454–1016a.

$S_{610\text{MHz}}$ mJy	$S_{1.4\text{GHz}}$ mJy	$S_{4.9\text{GHz}}$ mJy	$S_{8.4\text{GHz}}$ mJy	$\log P_{1.4\text{GHz}}$ $\text{W Hz}^{-1}$	$\alpha_{610\text{MHz}}^{4.8\text{GHz}}$	$\alpha_{4.9\text{GHz}}^{8.4\text{GHz}}$
27.7	15.0	7.0*	3.6	24.41	$0.66 \pm 0.06$	$1.18 \pm 0.13$

\* from the VLA–CnB image in panel *b*) of Figure 6.8.

The flux densities of J0454–1016a and the relative spectral index values are summarised in Table 6.2. The 4.9 GHz flux reported in the table is measured on the CnB image (panel *b* of Fig. 6.8). The value obtained from the higher resolution image in panel *c*) is in very good agreement with the flux density given in Table 6.2.

### Connection with the radio relic

In GVB06 we proposed a possible scenario for the origin of the relic, based on the hypothesis of a physical connection between J0454–1016a and the diffuse emission, as suggested by the faint radio bridge between the two sources (Fig. 6.5). In particular, we proposed that the relic might be the result of the ram pressure stripping of the radio lobes of J0454–1016a by *i*) the group merging in the southern cluster region (see Fig. 6.1), or *ii*) the infall of the radio galaxy itself into the cluster. From internal and external pressure arguments, and given the projected distance of J0454–1016a from the relic, we found that the infall velocity of the merging group or of the galaxy itself should be  $\gtrsim 3000 \text{ km s}^{-1}$  (leading to shock with a Mach number  $M \gtrsim 2$ ) to allow the electrons in the radio lobes to still emit in the radio band.

However the high resolution and high frequency observations presented in Section 6.2.5 do not support the above scenario. In fact we can firmly rule out any physical connection between the relic and J0454–1016a, whose head–tail morphology is extended in a direction opposite with respect to the relic region

(Fig. 6.8).

## 6.3 Spectral analysis

### 6.3.1 Integrated radio spectrum of the relic

In order to properly determine the value of the total flux density of the relic at 610 MHz (Fig. 6.5) and 4.9 GHz (Fig. 6.7), we integrated over the whole region covered by its emission within the  $3\sigma$  level, and subtracted the flux density of the embedded point-sources (A, B and C in Figure 6.5), measured on the full resolution images. Following the same procedure, we obtained the relic flux density at 1.4 GHz from the image shown in Figure 6.6.

The derived flux densities, and the corresponding radio powers, calculated at the mean redshift of the cluster, are reported in Table 6.1. Using these values we determined the integrated synchrotron spectrum of the relic in the frequency range 610 MHz–4.9 GHz. The spectrum is plotted in Figure 6.9. As clear from the figure, the spectrum is steep with  $\alpha = 1.32 \pm 0.09$  between 610 and 1400 MHz, and it further steepens to  $\alpha = 1.46 \pm 0.05$  between 1.4 GHz and 4.9 GHz. These values are in agreement with the spectral index estimates found in the literature for cluster radio relics (i.e.  $\alpha \geq 1$ ; see Section 1.5).

In order to estimate the expected flux density of the relic at frequencies  $\nu < 610$  MHz, we extrapolated the 610–1400 MHz spectrum down to 74 MHz, assuming a power law with  $\alpha = 1.32$  (Tab. 6.1). The low frequency spectrum extrapolation is shown as a dashed line in Figure 6.9. The expected value of the relic flux density at 74 MHz is  $S_{74\text{ MHz, exp}} \simeq 680$  mJy. We used the  $80''$  resolution image from the VLA Low-frequency Sky Survey (VLSS<sup>1</sup>) to derive a rough measure of the relic flux density at 74 MHz. We integrated the VLSS image over the whole region covered by the relic at 610 MHz (Fig. 6.5), and subtracted the contribution of J0454–1016a (A in Fig. 6.5), estimated from its 610 MHz–4.9 GHz spectrum (Fig. 6.10 and Tab. 6.2). We obtained a value of  $S_{74\text{ MHz, obs}} \simeq 660$  mJy (indicated by the filled triangle in Figure 6.9), which is in reasonable agreement with the low frequency extrapolation of the relic spectrum. However this result has to be taken with care, since the structure detected in the VLSS image is not completely consistent with the relic morphology at higher frequencies, probably due to the different angular resolution

---

<sup>1</sup><http://lwa.nrl.navy.mil/VLSS/>

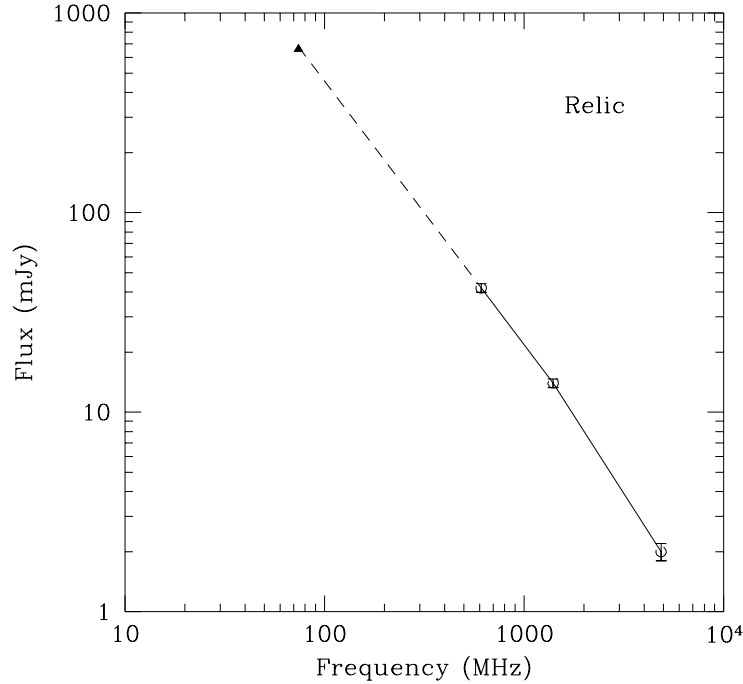


Figure 6.9: Radio spectrum of the radio relic between 610 MHz and 4.9 GHz. The dashed line represents the extrapolation of the 610 MHz–4.9 GHz spectrum down to 74 MHz. The filled triangle is the value measured on the 74 MHz VLSS image (see text for details).

and much lower sensitivity of the VLSS (average rms noise of the order of  $0.1 \text{ Jy b}^{-1}$ ). Therefore we will not use the 74 MHz data point in the discussion of the relic spectral properties and origin. GMRT observations at 327 MHz (performed during cycle A011, November 2006; data not yet available) will allow us to determine the real shape of the relic spectrum below 610 MHz.

### 6.3.2 Integrated radio spectrum of J0454–1016a

Using the flux densities reported in Table 6.2, we derived the integrated radio spectrum of the radio galaxy J0454–1016a (Fig. 6.10).

Between 610 MHz and 4.9 GHz, the spectrum has a power law shape with  $\alpha = 0.66 \pm 0.06$ . A steepening is observed for  $\nu > 4.9 \text{ GHz}$ , where the spectral index is  $\alpha = 1.18 \pm 0.13$  (Tab. 6.2). The spectral shape in Figure 6.10 is consistent with the spectrum observed in other active and low luminosity radio galaxies (e.g. Parma et al. 2002).

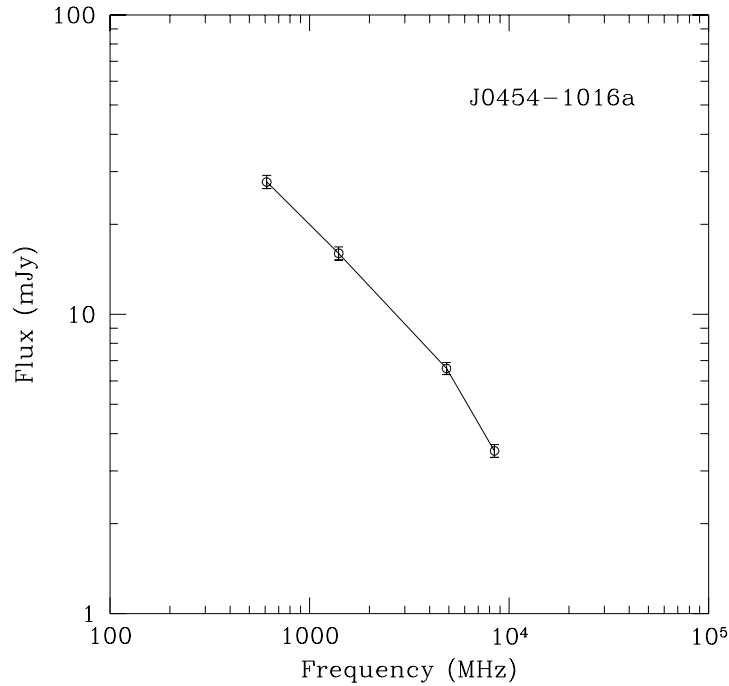


Figure 6.10: Integrated radio spectrum of J0454–1016a between 610 MHz and 8.4 GHz.

### 6.3.3 Spectral index image

The images of the spectral index distribution of radio relics and halos are a powerful tool to investigate and understand the origin and evolution of these sources, and their connection with the merging activity of the hosting cluster. In particular, the spectral index images provide important information on the energy spectrum of the radio emitting relativistic electrons and magnetic field distribution in these sources (see for example the study of the spectral properties of the radio halo in A 3562, Chapter 3).

The distribution of the spectral index over the radio relic in A 521 was determined by comparing our GMRT image at 610 MHz with the 1.4 GHz image obtained from the data available in the VLA archive (see Tab. 2.2). Both images were produced with the same cell size,  $u$ - $v$  range (0.3–32  $k\lambda$ ), and restoring beam ( $15'' \times 12''$ , p.a.  $75^\circ$ ). The noise level is  $35 \mu\text{Jy b}^{-1}$  in the 610 MHz image (not shown here) and  $15 \mu\text{Jy b}^{-1}$  in the 1.4 GHz image (Fig. 6.11). The images were

aligned, the pixels whose brightness was below the  $3\sigma$  level were blanked, and finally they were combined to create the spectral index image using the Synage++ package (Murgia 2001). The obtained image is shown in Figure 6.11, where we give the relic spectral index distribution (colours) with superposed the 1.4 GHz contours. As in Figure 6.5, the radio galaxies located within the relic emission are labelled as A, B, and C.

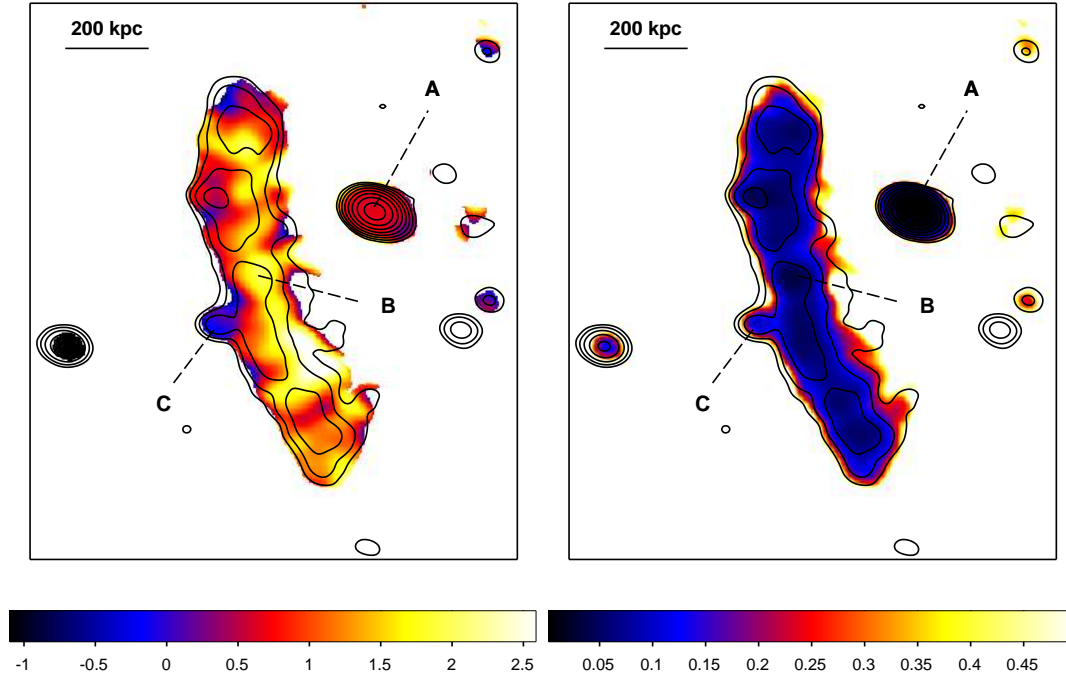


Figure 6.11: *Left panel* – Colour scale image of the spectral index distribution over the radio relic between 610 MHz and 1.4 GHz, as computed from images with a restoring beam of  $15'' \times 12''$ , p.a.  $75^\circ$ . Overlaid are the VLA 1.4 GHz radio contours at levels 0.075, 0.15, 0.30, 0.60, 1.20, 2.40, 4.80, and 9.6  $\text{mJy b}^{-1}$ . A, B and C indicate the position of the radio galaxies embedded in the relic emission (see also Fig. 6.5). *Right panel* – Color scale image of the spectral index uncertainty. Contours and labels are the same as right panel.

The overall spectral index image of the relic appears rather patchy, with the flattest knots characterised by  $\alpha \simeq 1.0 \pm 0.1$ , and the steepest regions reaching and exceeding  $\alpha \simeq 2.0 \pm 0.2$ . The radio galaxy labelled as C in Figure 6.11 has an inverted spectrum with  $\alpha = -0.5 \pm 0.1$ , while the spectral index of J0454–1016a (source A) is  $\alpha = 0.70 \pm 0.02$ , in very good agreement with the source integrated spectrum shown in Figure 6.10. We note that source B, which is totally embedded (in projection) by the relic emission, does not appear as a clear feature in the spectral index image, being  $\alpha$  in this region consistent with the average spectral index of the

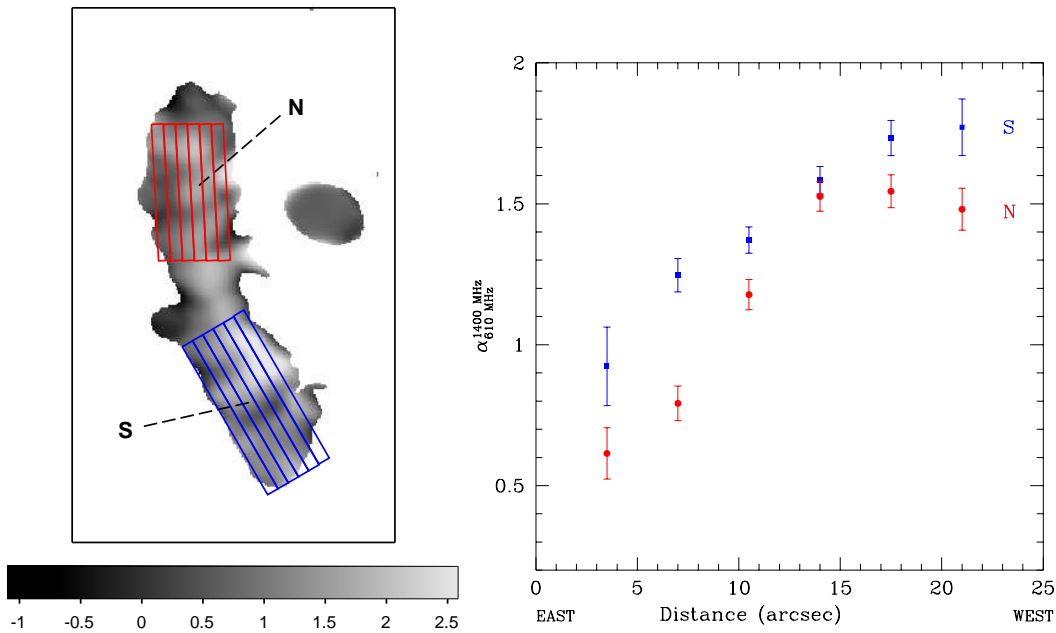


Figure 6.12: *Left panel* – Grid used to determine the 610–1400 MHz spectral index trend across the northern region (red, labelled as N) and southern region (blue, labelled as S) of the relic. The image of the spectral index distribution (grey scale) is the same as Figure 6.11. *Right panel* – Average spectral index between 610 and 1400 MHz in the  $7'' \times 80''$  and  $7'' \times 100''$  strips in the northern (red circles) and southern (blue squares) portions of the relic respectively (see left panel). The error bars represent the  $1\sigma$  error on the spectral index.

relic.

A more accurate inspection of Figure 6.10 suggests some hints of spectral steepening from the eastern edge of the relic toward the western border. In order to check the significance of such a trend, we determined the average spectral index in 6 strips of  $7'' \times 80''$  size in the northern region of the relic (red grid in the left panel of Fig. 6.12, labelled as N) and 6 strips of  $7'' \times 100''$  size in the southern part (blue grid, labelled as S). The strips were set parallel to the edge of the relic, i.e. at a position angle of  $3^\circ$  and  $30^\circ$  in the N and S regions respectively. For each strip we integrated the flux density on the 610 MHz and 1.4 GHz images individually, and then calculated the corresponding spectral index value. This procedure was adopted to reduce the bias toward steeper  $\alpha$  introduced in the outermost regions of the spectral index image by the higher sensitivity of the 1.4 GHz image.

The average spectral index in each strip is shown in the right panel of Figure 6.12, where red circles are related to the N region and blue squares to the S region (see left panel of the same figure). The spectral index trend shows a gradual steepening

going westwards in both regions. In particular from values of  $\alpha \simeq 0.6 \pm 0.1$  to  $\alpha \simeq 1.5 \pm 0.1$  in the southern part, and from  $\alpha \simeq 0.9 \pm 0.2$  to  $\alpha \simeq 1.7 \pm 0.1$  across the northern region.

A similar behaviour has been noticed also in other cluster radio relics (see Sec. 1.5, as for example in A 2744 (Orrú et al. 2007), A 2256 (Clarke & Ensslin 2006) and A 3667 (Rottgering et al. 1997).

### 6.3.4 Equipartition magnetic field

A zero-order estimate of the energy density of the relativistic plasma and magnetic field associated with the relic was obtained under the assumption of minimum energy conditions (e.g. Pacholczyk 1970). Assuming a power law energy spectrum from the electrons with a slope  $\delta = 2\alpha + 1 = 3.64$  (using  $\alpha = 1.32$ ; Table 6.1), and using the classical equipartition equations (normally computed in the frequency range between  $\nu_1 = 10$  MHz and  $\nu_2 = 100$  GHz), we obtained an equipartition magnetic field  $B_{eq} = 0.7 \mu\text{G}$ . Adopting the equipartition equations with a lower energy cut-off  $\gamma_{min}$  in the electron energy distribution (we used  $\gamma_{min} = 50$ ; see Sec. 5.2.4) we derived  $B'_{eq} \simeq 3 \mu\text{G}$ , also reported in Table 6.1.

Both values of the equipartition magnetic field are in agreement with the estimates found in the literature for radio relic sources and cluster radio halos, i.e. in the range 0.1 – few  $\mu\text{G}$  (see Section 1.3).

## 6.4 Origin of the radio relic

All the models developed so far to explain the origin of cluster radio relics (Sec. 1.10) invoke a connection between these sources and the presence of a shock wave driven by a merger episode and propagating within the X-ray emitting gas.

The hydrodynamic simulations of cluster mergers predict that the collision between two subclusters leads to the formation of two shocks (front and reverse shock; e.g. Ricker & Sarazin, 2001; see also Fig. 1.1 in Sec. 1.1.1).

A 521 is a very perturbed galaxy cluster with a complex dynamics (Sec. 6.1). The main cluster has a mass of the order of  $10^{15} M_{\odot}$  (Tab. 2.1), and is undergoing multiple minor merging events with groups whose mass is from  $\sim 1/7$  to  $\sim 1/10$  of the main cluster mass. On the basis of the dynamical analysis of MPB00, FMC03 and FAE05, and from inspection of Figure 6.1, a possible scenario is that the group

G111 is falling onto the main cluster G11, coming from North–West. The presence of the two optical groups G12 and G112 South–East of the central part of the cluster (see Fig. 6.1) suggests that also this region may be dynamically active.

Figure 6.4 shows that the relic (green contours) is located in projection at the border of the A 521 X–ray emission, as detected by ASCA (colour scale and yellow contours).

In the following we consider two possible scenarios for the formation of the radio relic in this merging cluster.

#### (a) Merger shock acceleration

A possibility to explain the formation of the radio relic in A 521 is the acceleration of electrons from the thermal pool up to ultrarelativistic energies by the passage of a strong merger shock (Ensslin et al. 1998; Rottgering et al. 1997; see also Sec. 1.10.1).

If the shock has a Mach number  $M$ , the energy spectrum of the generated radio emitting electrons<sup>2</sup> is a power law with slope  $\delta$  related to  $M$  by the equation (1.3) in Section 1.10.1.

In the case of A 521 the spectral index of the relic is  $\alpha = 1.32$  (Tab. 6.1), which provides  $\delta = 2\alpha + 1 = 3.64$ . This implies that the requested Mach number of the shock is  $M = 2.7$ . This Mach number is in reasonable agreement with the values expected for the shocks developed during cluster mergers ( $M \lesssim 3$ , Gabici & Blasi 2003; see also Sec. 1.1.1).

#### (b) Adiabatic compression of fossil electrons

As suggested by Ensslin & Gopal–Krishna (2001), a possible explanation for the origin of radio relics is the increase in the magnetic field strength and energy density of pre–existing relativistic electrons by the adiabatic compression exerted by a merger shock (Sec. 1.10.2). Such *fossil* electrons, whose energy is below the value required to emit synchrotron radiation detectable by the present radio instruments, may have been accumulating from past mergers or previous cycles of activity of a nearby radio galaxy.

---

<sup>2</sup>We do not consider the case of the reacceleration of a pre-existing population of relativistic electrons (see Markevitch et al. 2005 for a detailed discussion).

An important requirement in this scenario is the presence of a population of fossil relativistic electrons. In Section 6.2.2 we noted that the most powerful radio galaxy of A 521 (J0454–1016a) is located in the proximity of the relic (see for example Fig. 6.5 where J0454–1016a is labelled as A). A previous cycle of activity of this radio galaxy could have provided the fossil radio plasma in the intracluster medium, re-energized by the shock compression.

## 6.5 Is there a shock in the external region of A 521?

All the possibilities proposed in Section 6.4 to explain the formation of the radio relic require the presence of a shock in the external region of A 521, with Mach number  $M \lesssim 3$ . In search for an observational signature of a shock in the relic region, we re-analysed the public archive Chandra ACIS-I and ACIS-S observations (see Tab. 2.4 for details), analysed also in FAE05. We point out that the work in FAE05 is mainly restricted to the central and northern part of the cluster, and does not include the region which is relevant for the relic analysis. We refer to Section 2.6 for the X-ray data re-processing and reduction.

In Figure 6.13 we show the GMRT 610 MHz contours of the A 521 field (same as Fig. 6.3), superposed to the Chandra wavelet-reconstructed image of the cluster. The X-ray image was produced applying the wavelet decomposition tool (Vikhlinin et al. 1998; Sec. 2.6) to the cluster image obtained by combining the ACIS-I and ACIS-S images in the 0.5–5 keV energy band, both divided for the relative exposure maps and background subtracted.

On the unsmoothed 0.5–5 keV image (background-subtracted and exposure-corrected; not shown here), we extracted the radial X-ray surface brightness profile perpendicular to the relic source, using a  $80^\circ$  sector centered on the cluster centre and containing the relic.

The X-ray brightness profile does not show any evidence in support of the existence of a shock front at the projected location of the relic. However, this is not enough to rule out a connection between the relic and the presence of a shock wave. Two more issues should be considered. In particular:

- (a) the relic is very peripheral, therefore the X-ray surface brightness is very low at this distance from the cluster centre. Thus the possible density jump, associated with the presence of a shock discontinuity could be not revealed

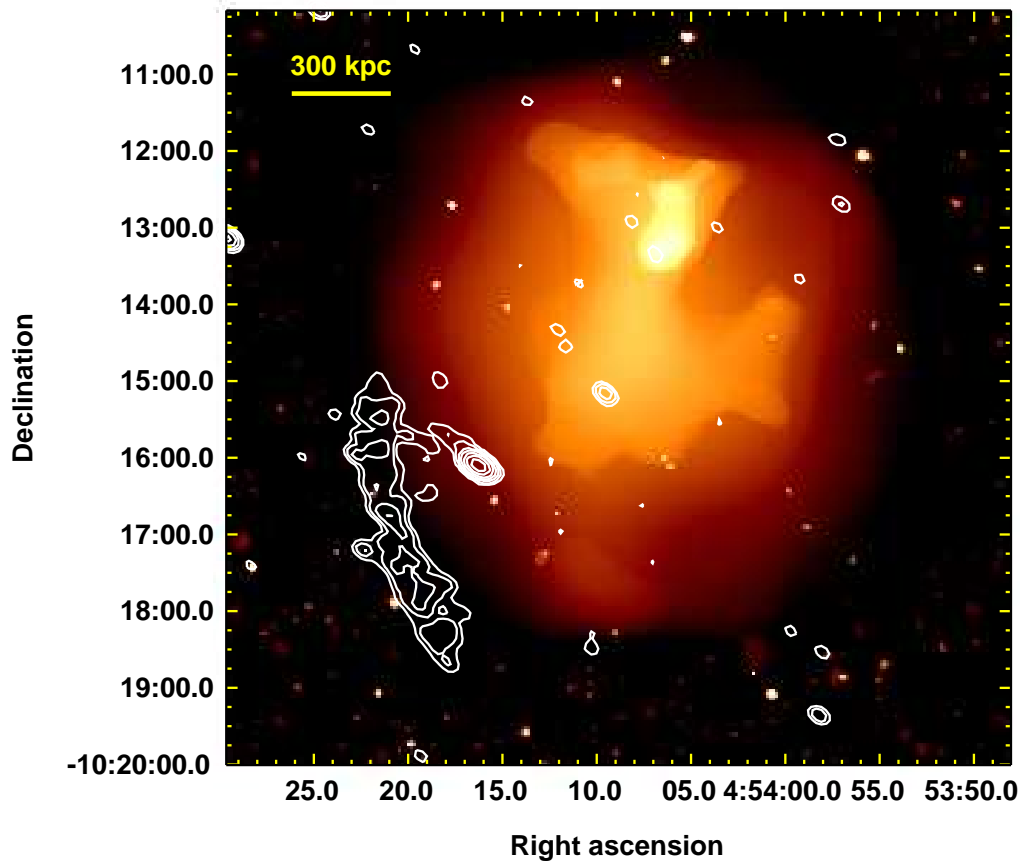


Figure 6.13: Wavelet-reconstructed Chandra image of A 521 in the 0.5–5 keV band. The image is obtained by the combination of the ACIS-I and ACIS-S images, both corrected for the exposure and background subtracted. Overlaid are the GMRT 610 MHz contours of A 521 field. The radio image is the same as Figure 6.3.

because of the low cluster X-ray emission and high level of the background in the relic region;

*b)* projection effects should also be taken into account in the analysis.

To underline the difficulty to detect a merger shock wave in a cluster using the present X-ray instruments (see Sec. 1.1.1 and the recent review by Markevitch & Vikhlinin 2007), we point out that only two unambiguous shock fronts, exhibiting both a sharp gas density edge and a clear temperature jump, have been found by Chandra so far, i.e. those in 1E 0657–56 (see Fig. 1.2 in Sec. 1.1.1; Markevitch et al. 2002 and 2006), and A 520 (Markevitch et al. 2005).

## 6.6 Summary and future perspectives

We studied the radio relic located in the south–eastern periphery of A 521 using high sensitivity radio observations, carried out at 610 MHz with the GMRT and at 4.9 and 8.4 GHz with the VLA. We combined our radio information with VLA 1.4 GHz and X–ray Chandra data from the public archives.

The main results of our analysis can be summarised as follows:

- i. the relic in A 521 is the second detected at a frequency as high as 4.9 GHz, after the source 1253+275 in the Coma cluster;
- ii. the relic integrated spectrum between 610 MHz and 4.9 GHz can be approximately described as a power law with steep spectral index ( $\alpha \sim 1.4$ ), although hints of a possible steepening at high frequency are found at  $\nu \geq 1.4$  GHz;
- iii. the image of the spectral index distribution between 610 MHz and 1.4 GHz over the relic region shows a significant steepening along the source minor axis, with the flattest region in the more external side of the relic with respect to the cluster centre. A similar spectral trend has been observed also in other few well–studied radio relics;
- iv. in GVB06 we suggested that the relic may be the result of the ram pressure stripping of the radio lobes of the nearby radio galaxy J0454–1016a as a consequence of group infalling/merger. This idea was suggested by the presence of a faint bridge of emission in the 610 MHz image which seems to connect the relic to this radio galaxy. However the higher frequency and higher resolution images of the relic region led us to firmly rule out any physical link between the two sources;
- v. the origin of the relic was discussed in connection to the presence of a shock wave in the south–eastern portion of the cluster, induced by the ongoing merger. Such shock may have accelerated thermal electrons up to ultra–relativistic energies or *revived* fossil radio plasma through adiabatic compression of the magnetic field. The radio properties of the relic require a Mach number  $M \lesssim 3$  for the shock;

- vi. the transversal steepening observed in the spectral index distribution of the relic may support such scenario: a steepening is indeed expected going from the current shock location to the trailing edge either in the shock acceleration model or the adiabatic compression hypothesis (Secs. 1.10.1 and 1.10.2). In the first case, the expected total spectrum of the relic is a power law, while in the adiabatic compression scenario the power-law constrain can be relaxed (see Markevitch et al. 2005 for a detailed discussion). Hence future observations at frequency  $> 1.4$  GHz, with an adequate u-v coverage to properly image the whole diffuse emission associated with the relic, are needed to determine the shape of the source spectrum in the high frequency regime and compare it to the theoretical expectations. Furthermore new GMRT observations at 327 MHz (performed during cycle A011, November 2006) will allow us to determine the low frequency behaviour of the source spectrum;
- vi. the analysis of the X-ray Chandra image of A 521 did not provide clear evidence for a shock front at the location of the relic. However projection effects should be taken into account for a more accurate study.

## Chapter 7

# The giant radio halo in RXCJ 2003.5–2323

RXCJ 2003.5–2323 belongs to the REFLEX subsample of the GMRT Radio Halo Survey (Sec. 1.12). Given its redshift  $z=0.317$ , it is among the most distant galaxy clusters in the sample, and the highest redshift object studied in the present work. The cluster is X–ray luminous and massive with  $L_{X[0.1-2.4\text{keV}]} \sim 9 \times 10^{44} \text{ erg s}^{-1}$  and virial mass  $M_v \sim 2 \times 10^{15} M_\odot$ . Table 2.1 summarises its main properties.

The knowledge of the dynamical status of RXCJ 2003.5–2323 is limited to the sparse information available in the literature. No deep optical and/or high resolution X–ray observations are available for this cluster, apart from the shallow ROSAT All Sky Survey (RASS), which does not provide any indication about the cluster dynamics.

The low frequency observations, carried out as part of the GMRT Radio Halo Survey at 610 MHz (Sec. 1.12), led us to discover a new giant radio halo in this cluster. This source is among the largest and most powerful halos known to date, and, due to the cluster redshift ( $z=0.317$ ), it is also one of the most distant. Hints of the presence of such diffuse radio emission were clear already from the inspection of the NVSS. In Figure 7.1 we overlay the 1.4 GHz NVSS contours of RXCJ 2003.5–2323 on the POSS–2 optical image. The central region of the cluster is covered by a very extended radio source, whose linear size exceeds the Mpc scale. This strongly suggests the existence of diffuse radio emission on the cluster scale.

Given the lack of deep optical and X–ray information, we study the cluster mainly in radio band, using our GMRT 610 MHz observations and 1.4 GHz data obtained from VLA observations in the hybrid CnB configuration (Tab. 2.2).

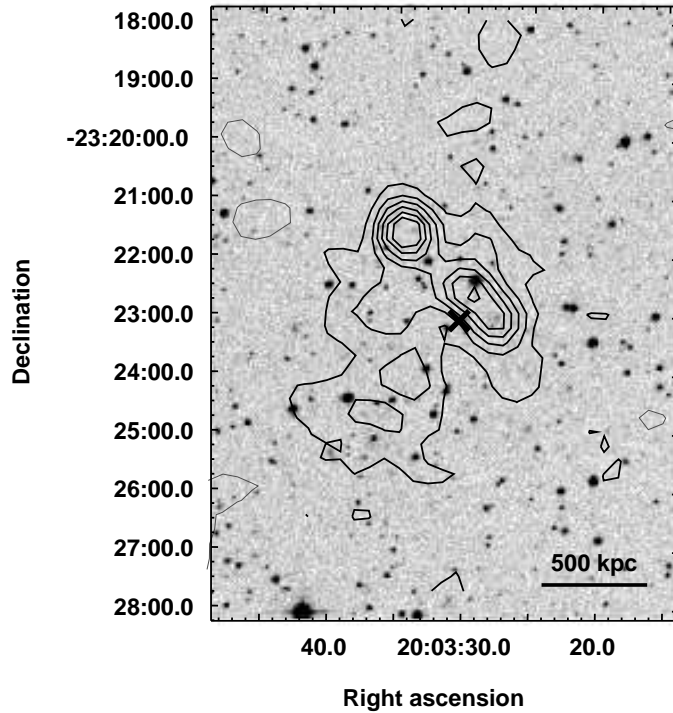


Figure 7.1: 1.4 GHz NVSS image of the diffuse source at the RXCJ 2003.5–2323 centre, overlaid on the POSS–2 optical frame. The  $1\sigma$  level in the image is  $0.45 \text{ mJy b}^{-1}$ . Contour levels are  $\pm 1, 2, 3, 4, 5, 6 \text{ mJy b}^{-1}$ . The resolution is  $45'' \times 45''$ , p.a.  $0^\circ$ . The cross indicates the X–ray centre of the cluster (Tab. 2.1).

The Chapter is organised as follows: the radio observations are presented in Section 7.1, where the GMRT 610 MHz images are shown in Section 7.1.1, and the VLA 1.4 GHz images are given in Section 7.1.2; Section 7.2 deals with the main observational properties of the halo; its polarisation properties are presented in Section 7.3, and its integrated spectrum is estimated in Section 7.4; finally in Section 7.5 we discuss the presence of an ongoing merger in the cluster, which may be responsible for the radio halo formation, and in Section 7.6 we discuss the origin of the peculiar radio morphology observed in this source; a summary is given in Section 7.7

At the redshift of RXCJ 2003.5–2323 ( $z=0.317$ ) the cosmology adopted in this work leads to a linear scale of  $1'' = 4.62 \text{ kpc}$ .

## 7.1 Radio observations

### 7.1.1 GMRT 610 MHz images

RXCJ 2003.5–2323 was observed with the GMRT at 610 MHz as part of the GMRT Radio Halo Survey (Sec. 1.12). The details of the observations are reported in Table 2.2 and Section 2.2. The data reduction was carried out as described in Section 2.4.

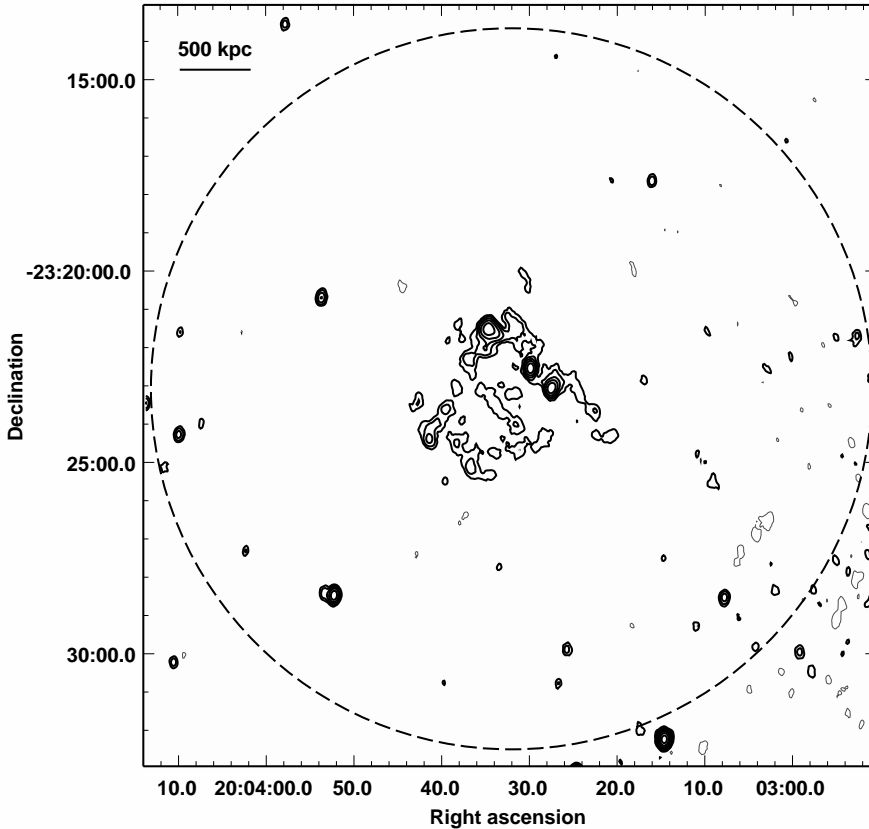


Figure 7.2: GMRT 610 MHz radio contours of the central  $20' \times 20'$  region containing RXCJ 2003.5–2323. The  $1\sigma$  level in the image is  $60 \mu\text{Jy b}^{-1}$ . Contour levels are scaled by a factor 2, starting from  $\pm 0.3 \text{ mJy b}^{-1}$ . The resolution is  $15.5'' \times 10.3''$ , p.a.  $-6^\circ$ . The dashed circle is centered on the X-ray centre of the cluster, and has a radius corresponding to the virial radius  $R_v = 9.91'$  (i.e. 2.75 Mpc).

We imaged the radio emission from the cluster at different angular resolutions, ranging from  $6.9'' \times 5.0''$  (full resolution, Tab. 2.2) to the lowest resolution of  $32.0'' \times 23.0''$ . The sensitivity achieved in the full resolution image is  $1\sigma = 40 \mu\text{Jy b}^{-1}$ , while higher noise levels are measured in the low resolution images ( $1\sigma = 60\text{--}100 \mu\text{Jy b}^{-1}$ ), obtained using the full array with a taper. The low resolution

images led us to firmly confirm the existence of a giant radio halo in this cluster, and allowed us to properly image and study its diffuse emission. The full resolution image allowed us to identify the individual radio galaxies located (in projection) within the halo.

An image at the resolution of  $15.5'' \times 10.3''$  of the 610 MHz emission within the cluster virial radius (Tab. 2.1) is shown in Figure 7.2. Besides the individual radio sources, the central region of the cluster is clearly permeated by very diffuse and low surface brightness radio emission.

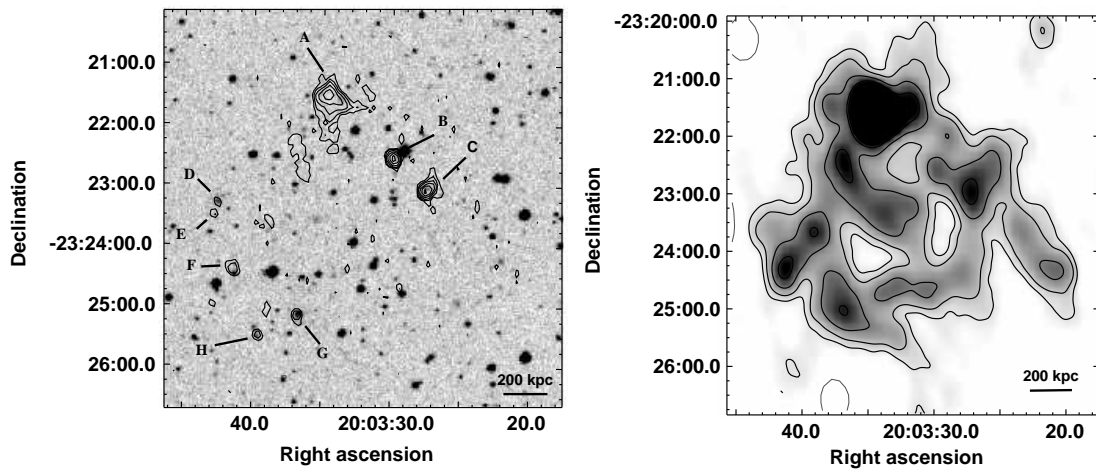


Figure 7.3: *Left panel* – Full resolution GMRT 610 MHz contours of the central region of RXCJ 2003.5–2323, superposed to the POSS–2 optical image. The resolution of the radio image is  $6.9'' \times 5.0''$ , p.a.  $-0.3^\circ$ . The  $1\sigma$  level is  $40 \mu\text{Jy/b}$ . Contours are spaced by a factor 2, starting from  $\pm 0.12 \text{ mJy b}^{-1}$ . Individual sources are labelled from A to H. *Right panel* – GMRT 610 MHz gray scale and radio contours of the giant radio halo in RXCJ 2003.5–2323 after subtraction of the individual sources (from B to H in the left panel). The resolution is  $32.0'' \times 23.0''$ , p.a.  $15^\circ$ . The  $1\sigma$  level in the image is  $100 \mu\text{Jy b}^{-1}$ . Contours are spaced by a factor 2, starting from  $\pm 0.3 \text{ mJy b}^{-1}$ .

The central portion of the cluster is shown in Figure 7.3. In the left panel we present the full resolution image, superposed to the POSS–2 optical frame, to highlight the individual radio sources at the cluster centre (labelled from A to H). We used the SuperCOSMOS Sky Survey (Hambly et al. 2001) to search for optical galaxies associated with these sources. The sources with a clear optical counterpart (B to H) are listed in Table 7.1, where we report the radio position, the 610 MHz and 1.4 GHz flux densities, measured on the full resolution images (see Sec. 7.1.2 for the 1.4 GHz information), and the coordinates and  $b_J$  magnitude of the optical identification. No obvious optical counterpart was found on the POSS–2 image and

Table 7.1: Individual radio galaxies at the RXCJ 2003.5–2323 centre.

Radio source	Radio position		$S_{610\text{ MHz}}$ mJy	$S_{1.4\text{ GHz}}$ mJy	Optical Position		$b_J$
	$RA_{J2000}$	$DEC_{J2000}$			$RA_{J2000}$	$DEC_{J2000}$	
B	20 03 29.87	−23 22 33	9.56	5.98	20 03 29.79	−23 22 32	22.07
C	20 03 27.57	−23 23 05	11.02	5.48	20 03 27.96	−23 23 11	21.03
D	20 03 42.57	−23 23 18	0.42	0.30	20 03 42.63	−23 23 17	19.75
E	20 03 42.83	−23 23 30	0.41	0.55	20 03 41.84	−23 23 25	21.09
F	20 03 41.44	−23 24 24	1.08	0.90	20 03 41.35	−23 24 28	18.27
G	20 03 36.72	−23 25 10	0.79	0.82	20 03 36.67	−23 25 08	18.15
H	20 03 39.59	−23 25 29	0.74	0.60	20 03 39.73	−23 25 29	20.79

SuperCOSMOS catalogue for source A.

In order to obtain the image of the extended emission only, we subtracted the sources in Table 7.1 from the  $u$ - $v$  data when producing the image shown in the right panel of Figure 7.3, which was convolved with a beam of  $32.0'' \times 23.0''$  in order to highlight the low surface brightness emission from the halo. Given the lack of optical identification, source A was not subtracted. This feature is considered as a peak in the diffuse emission.

### 7.1.2 VLA 1.4 GHz images

With the purpose to image and study the diffuse emission at the centre of RXCJ 2003.5–2323 at a frequency higher than our 610 MHz observations (7.1.1), we observed the cluster at 1.4 GHz using the VLA in the hybrid CnB configuration. The observations were performed in full polarisation mode for a total observing time of 9 hours on source. We refer to Table 2.2 for the summary of the observations and Section 2.5 for the data reduction.

The 1.4 GHz full resolution image ( $12.6'' \times 9.2''$ ) of the central region of RXCJ 2003.5–2323 is shown in the left panel of Figure 7.4, where the individual radio sources are labelled from A to H as in the left panel of Figure 7.3 (also reported in Tab. 7.1). Given the high sensitivity of this image ( $1\sigma = 20 \mu\text{Jy/b}$ ), the brightest regions of the halo are already well visible, despite the inadequate angular resolution. The image of the whole diffuse emission from the halo, after subtraction of the optically identified sources (Tab. 7.1), is given in the right panel of Figure 7.4. For a proper comparison with the GMRT 610 MHz image in Figure 7.3 (right panel), we show the 1.4 GHz image of the source convolved with the same beam of

$32.0'' \times 23.0''$  (p.a.  $15^\circ$ ).

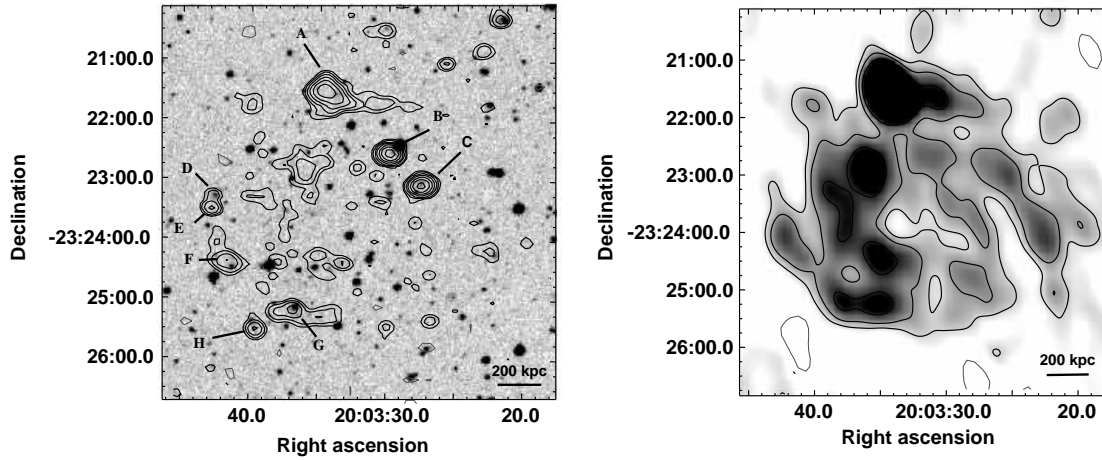


Figure 7.4: *Left panel* – Full resolution VLA 1.4 GHz contours of the central region of RXCJ 2003.5–2323, superposed to the POSS–2 optical image. The resolution of the radio image is  $12.6'' \times 9.2''$ , p.a.  $85^\circ$ . The  $1\sigma$  level is  $20 \mu\text{Jy/b}$ . Contours are spaced by a factor 2, starting from  $\pm 0.06 \text{ mJy b}^{-1}$ . Individual sources are labelled from A to H, as in Fig. 7.3. *Right panel* – VLA 1.4 GHz gray scale and radio contours of the giant radio halo after subtraction of the individual sources (from B to H in the left panel). The resolution is  $32.0'' \times 23.0''$ , p.a.  $15^\circ$ . The  $1\sigma$  level in the image is  $50 \mu\text{Jy b}^{-1}$ . Contours are spaced by a factor 2, starting from  $\pm 0.15 \text{ mJy b}^{-1}$ .

As clear from Figure 7.4 (right panel), the 1.4 GHz overall morphology of the halo is in general agreement with the 610 MHz image (Fig. 7.3, left panel). The halos shows a dishomogeneous structure at both frequencies, and extends on a scale of  $\sim 5'$ , corresponding to a linear size of  $\sim 1.4 \text{ Mpc}$ .

In Figure 7.5 we present a comparison between the halo images at 610 MHz (grey scale) and 1.4 GHz (red contours). The figure reveals that the images at the two frequencies differ in the fine structure of the halo surface brightness distribution. Most likely such discrepancy is due to the combination of the different sensitivity and u–v coverage of the two observations.

## 7.2 Observational properties of the radio halo

With its largest angular size of  $\sim 5'$ , corresponding to  $\sim 1.4 \text{ Mpc}$ , this source is among the largest radio halos imaged so far. One of the most striking features of this giant radio halo is its peculiar and complex morphology. Unlike most of the giant radio halos studied in the literature, which generally show a roughly regular

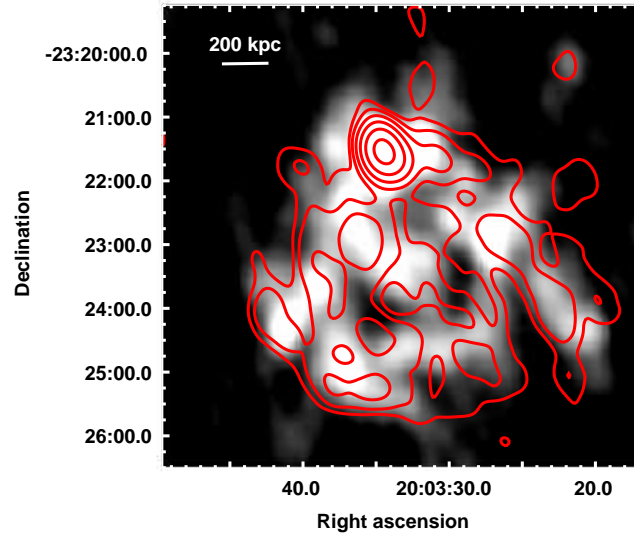


Figure 7.5: VLA 1.4 GHz contours (red) of the giant radio halo in RXCJ2003.5–2323, superposed to GMRT 610 MHz image (grey scale). The resolution of both images is  $32.0'' \times 23.0''$ , p.a.  $15^\circ$ . The  $1\sigma$  level is  $50 \mu\text{Jy b}^{-1}$  at 1.4 GHz and  $100 \mu\text{Jy b}^{-1}$  at 610 MHz. Contours are spaced by a factor 2, starting from  $\pm 0.15 \text{ mJy b}^{-1}$

and homogeneous radio brightness distribution (see for example Fig. 1.5 in Sec. ??), this halo exhibits clumps and filaments of emission extending on scales of the order of  $\sim 1'$  ( $\sim 270 \text{ kpc}$ ) and  $\sim 2 - 3'$  ( $\sim 550 - 830 \text{ kpc}$ ) respectively (Fig. 7.2 and right panels of Figs. 7.3 and 7.4). This complex morphology is reminiscent of the giant radio halo in A 2255 ( $z=0.08$ ), whose emission is characterised by the presence of filaments with a length of  $\sim 550 \text{ kpc}$  (Govoni et al. 2005).

The total flux density of the halo at 610 MHz and 1.4 GHz, after subtraction of the point sources (Tab. 7.1), is  $S_{610\text{MHz}} = 96.9 \pm 5.0 \text{ mJy}$  and  $S_{1.4\text{GHz}} = 34.9 \pm 1.7 \text{ mJy}$  respectively. The corresponding radio powers are  $\log P_{610\text{MHz}} (\text{W Hz}^{-1}) = 25.53$  and  $\log P_{1.4\text{GHz}} (\text{W Hz}^{-1}) = 25.09$ . These values are reported also in Table 7.2, where we summarise the main properties of the radio halo.

In Figure 7.6 we show as a green filled circle the location of RXCJ 2003.5–2323 in the  $\text{Log}L_X\text{--}\text{Log}P_{1.4\text{GHz}}$  plane, where all the giant radio halo clusters known in the literature are also reported (Sec. 1.7; see Cassano, Brunetti & Setti 2006 and references therein for the literature data). Clusters at redshift  $z < 0.2$  and  $z > 0.2$  are shown as empty and filled black circles respectively. The solid line is the best-fit of

Table 7.2: Properties of the giant radio halo in RXCJ2003.5–2323.

$S_{610\text{ MHz}}$ (mJy)	$96.9 \pm 5.0$
$S_{1400\text{ MHz}}$ (mJy)	$34.9 \pm 1.7$
$\alpha_{610\text{ MHz}}^{1400\text{ MHz}}$	$1.23 \pm 0.09$
$\log P_{610\text{ MHz}}$ ( $\text{W Hz}^{-1}$ )	25.53
$\log P_{1400\text{ MHz}}$ ( $\text{W Hz}^{-1}$ )	25.09
Linear size (Mpc)	$\sim 1.4$
$B'_{\text{eq}}$ ( $\mu\text{G}$ ) <sup>1</sup>	1.3

<sup>1</sup> estimated with a low energy cut-off in the electron spectrum (see text).

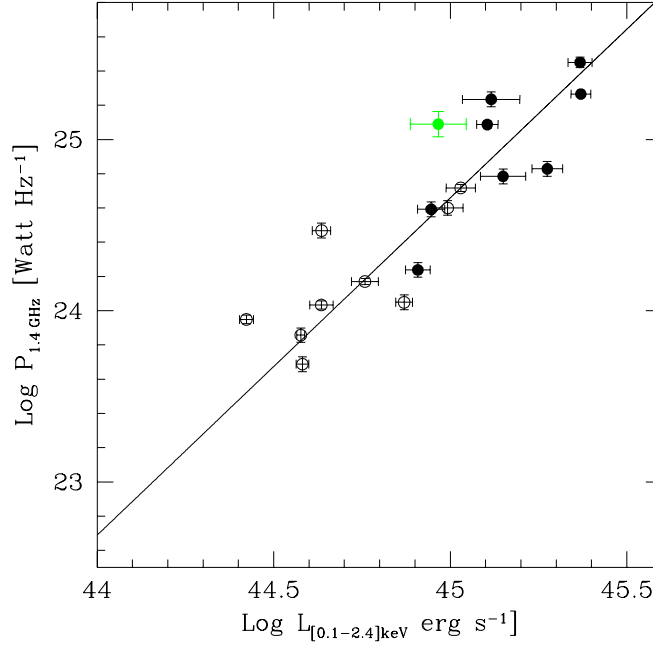


Figure 7.6:  $\text{Log}L_X$ – $\text{Log}P_{1.4\text{ GHz}}$  diagram for the clusters with detected giant radio halos. Empty black circles represent the literature clusters at  $z < 0.2$ , and filled black circles the clusters at  $z > 0.2$ . The green filled circle shows the location of RXCJ2003.5–2323. The solid line is the best-fit for the correlation found by Cassano, Brunetti & Setti (2006).

the correlation found by Cassano, Brunetti & Setti (2006), i.e.  $P_{1.4\text{ GHz}} \propto L_X^{1.97 \pm 0.25}$ . Despite some overlap, it is clear that the most powerful radio halos are hosted in the most X-ray luminous clusters, which are also the most distant. The location of RXCJ2003.5–2323 in the upper-right portion of the plot is in line with such behaviour, and is in good agreement with the distribution of all giant radio halos

known at present.

### 7.3 Polarisation properties of the halo

As noticed in Section 7.2, the filamentary flux density distribution of the giant radio halo in RXCJ 2003.5–2323 (Figs. 7.3 and 7.4, right panels) reminds the morphology of the halo in A 2255, where Govoni et al. (2005) detected with the VLA at 1.4 GHz filaments of emission extending on a scale of  $\sim 550$  kpc. Such filaments are strongly polarised (at levels of  $\sim 20 - 40\%$ ), while the upper limit to the fractional polarisation is  $\lesssim 15\%$  in the fainter regions of the halo (Govoni et al. 2005). The giant radio halo in RXCJ 2003.5–2323 appears even more clumpy and filamentary than A 2255. Hence, we used our VLA 1.4 GHz polarimetric observations (Tab. 2.2) to search for possible polarised emission associated with the filaments and clumps of this radio halo.

We did not detect any significant polarisation in the source. The upper limit ( $1\sigma$ ) to the fractional polarisation is  $\sim 2 - 3\%$  in the brightest regions of the halo (i.e. clumps and filaments), and  $\sim 15\%$  in the faintest regions, where the average total intensity emission is about  $0.15 \text{ mJy b}^{-1}$ .

### 7.4 The halo integrated spectrum and magnetic field

Using the flux density values in in Table 7.2, we derived the spectral index of the source between 610 and 1400 MHz. We obtained  $\alpha = 1.23 \pm 0.09$ , which is in agreement with the spectral indices reported in the literature for the halo sources (i.e.  $\alpha \geq 1$ ; Sect. 1.4).

Using this value of  $\alpha$ , we estimated the magnetic field associated with the halo. If we adopt the standard equipartition equations (computed in the frequency range 10 MHz–100 GHz), we obtained  $B_{\text{eq}} = 0.5 \mu\text{G}$ . If we take into account the contribution of low energy electrons ( $\gamma \lesssim 2 \times 10^3$ ), adopting the equipartition equations with a low energy cut-off of  $\gamma_{\text{min}} = 50$  in the particle energy spectrum (see Sec. 5.2.4), we obtain  $B'_{\text{eq}} = 1.7 \mu\text{G}$ , also reported in Table 7.2.

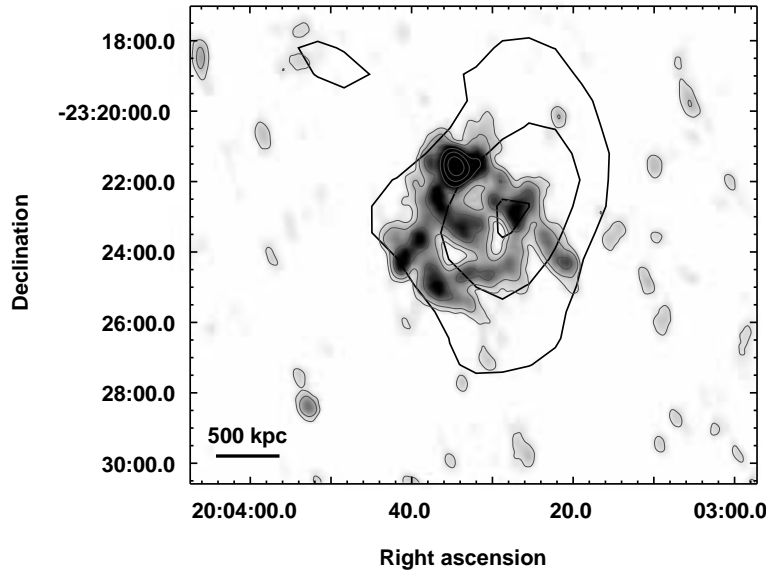


Figure 7.7: ROSAT All Sky Survey contours (black) of RXCJ 2003.5–2323 overlaid on the GMRT 610 MHz gray scale and contours (gray) of the radio halo. The X-ray contour levels are logarithmically spaced by a factor  $\sqrt{2}$ . The radio image is the same as right panel of Fig. 7.3.

## 7.5 Radio halo–cluster merger connection: is there a merger?

In the framework of the re-acceleration scenario (Sec. 1.9), the existence of a giant radio halo requires the presence of turbulence in the cluster volume, induced by a recent or still ongoing major merger event. The giant radio halo discovered in RXCJ 2003.5–2323 is one of the largest and most powerful known at present. Thus we expect a highly perturbed dynamics for the hosting cluster. Unfortunately no detailed information is available about the dynamical state of RXCJ 2003.5–2323, since no deep optical observations and/or high resolution X-ray data are present in the literature and public archives, apart the shallow image from the RASS, shown in Figure 7.7. The image does not provide any information about the presence of possible substructures in the hot gas distribution. It only suggests that the cluster X-ray emission is elongated along the North–West/South–East direction. Figure 7.7 also shows that the central radio halo is completely embedded within the outer level of the RASS X-ray isophote, which extends well beyond the halo extent.

Given the lack of high quality optical data, we searched for hints of substructures

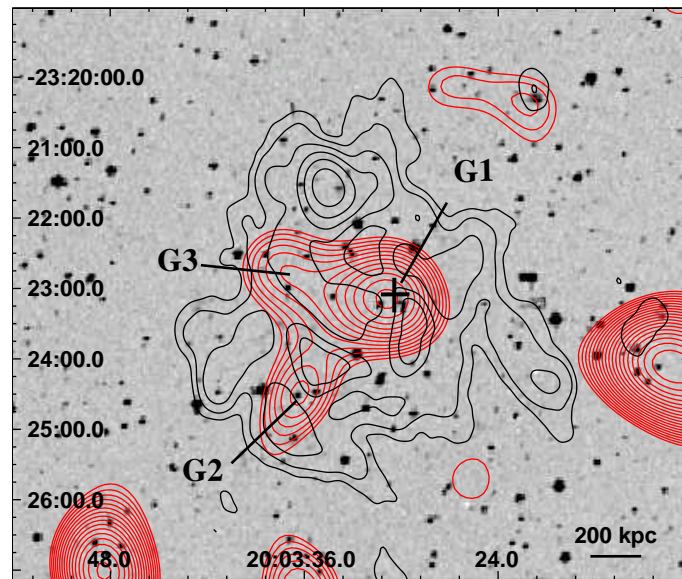


Figure 7.8: Distribution of the optical galaxies (red; from the APM to  $R < 20.5$ ) in the RXCJ 2003.5–2323 region, overlaid on the 610 MHz radio halo image (black contours) and the DSS optical frame (gray). The radio image is the same as right panel of Fig. 7.3. G1, G2 and G3 indicate the optical substructures.

in the galaxy bi-dimensional distribution, and hence for merging activity, using the information from the APM catalogue (Maddox et al. 1990).

The distribution of the optical galaxies from the APM (to the magnitude  $R \leq 20.5$ ) in the cluster region is shown as red contours in Figure 7.8, superposed to the 610 MHz image of the halo (black contours) and the DSS optical frame. The optical substructures are enhanced using an Adaptive Kernel algorithm (Bardelli et al. 1998a). A significant substructure (labelled as G2 in Fig. 7.8) is detected South–East of the central region (G1) of the cluster. A possible infalling/emerging sub-group (G3) is located East of the cluster core. This might be an indication for possible ongoing merging episodes, still in the phase to furnish energy to the intracluster medium in the form of shocks and turbulence.

Deeper observations both in the X–ray and optical bands are needed to confirm the presence of a strong merging activity in this cluster, and thus explain the existence of a giant radio halo. Forthcoming Chandra observations (50 ks) of RXCJ 2003.5–2323, scheduled during the Chandra Cycle 8, will allow us to study the surface brightness and temperature distribution of the X–ray emitting gas, and thus confirm the expected highly disturbed status of the cluster. Optical observations with the 3.6 m New Technology Telescope (NTT) will be carried out in April 2007

to obtain redshifts for a large number of galaxies in the RXCJ 2003.5–2323 region, and thus to reconstruct the cluster dynamics.

## 7.6 Origin of the clumps and filaments

The halo source in RXCJ 2003.5–2323 is very different from other giant radio halos, which typically exhibit a fairly regular and homogeneous morphology, with a flux density distribution usually peaked at the cluster centre and smoothly decreasing towards the cluster periphery (see Fig. 1.5 in Sec. 1.4). The structure and flux density distribution of the radio halo in RXCJ 2003.5–2323 are quite different. The halo has a striking clumpy/filamentary morphology, both at 610 MHz (Fig. 7.3, right panel) and 1.4 GHz (Fig. 7.4, right panel). Such clumps and filaments pose the question of their origin and connection with the intracluster medium distribution.

In the framework of the re-acceleration model (Sec. 1.9.1) the statistical properties of giant radio halos are expected to evolve with redshift. This is essentially due to the fact that as  $z$  increases it is more and more difficult for the acceleration mechanism to balance the Inverse Compton losses suffered by the radiating particles. Powerful giant radio halos at  $z > 0.2–0.3$  should be hosted by highly turbulent and dynamically disturbed clusters. The maximum efficiency in emitting synchrotron radiation in the re-acceleration model is obtained when the local magnetic field in the ICM equals the equivalent magnetic field of the Cosmic Microwave Background radiation (Brunetti et al. 2001; Cassano, Brunetti & Setti 2006), which is expressed as  $B_{cmb} \sim 3(1+z)^2 \mu\text{G}$ . Therefore, it is likely that only cluster regions close to this condition are able to emit synchrotron radiation at these redshifts. This implies that the synchrotron radio emission is expected to trace the peaks of the magnetic field intensity in the cluster, and this may result in a clumpy/filamentary radio brightness distribution. The peculiar radio morphology of the radio halo in RXCJ 2003.5–2323 may be in line with these expectations.

Furthermore, a spatial correlation between the radio halo and X-ray brightness has been found in a number of radio-halo clusters with deep radio observations and high resolution X-ray images (Sec. 1.7; see also the compared radio/X-ray analysis of the A3562 halo in Sec. 3.5). This suggests that the radio clumps and filaments observed in RXCJ 2003.5–2323 may have a counterpart in the X-ray surface brightness distribution. Our future Chandra observation will provide

insightful information about the hot gas distribution and will allow us to compare the cluster X-ray and radio brightness. Such comparison is a powerful tool to constrain the link between the cluster dynamics and non-thermal radio emission.

## 7.7 Summary of the analysis of RXCJ2003.5–2323

In this Chapter we presented the radio analysis of the galaxy cluster RXCJ 2003.5–2323. Our high sensitivity GMRT 610 MHz observations led to the discovery of a giant radio halo in this cluster. The source was also imaged and studied at high sensitivity using the VLA at 1.4 GHz, which confirmed the detection.

We can briefly summarise the most important features of this source as follows:

- 1) the largest linear size of this giant radio halo is  $\sim 1.4$  Mpc at both frequencies, i.e. it is one of the largest found so far;
- 2) with a radio power of  $\log P_{1.4\text{GHz}} (\text{W Hz}^{-1}) = 25.09$ , it is among the most powerful giant radio halos known to date, located in the upper end of the  $\text{Log}L_X\text{--Log}P_{1.4\text{GHz}}$  correlation.
- 3) given the redshift of the cluster ( $z=0.317$ ), this halo is also one of the most distant;
- 4) the most striking feature of this source is its complex and uncommon radio morphology. Clumps and filaments of emission on scales of the order of  $\sim 270$  kpc and  $\sim 550\text{--}830$  kpc respectively are clearly visible both at 610 MHz and 1.4 GHz. The observed structure is very different from that typically found for other giant radio halos, which are usually homogeneous, with the radio flux density peaked at the cluster centre and smoothly decreasing towards the outskirts.

In the framework of the re-acceleration scenario, the existence of a giant radio halo requires the presence of an ongoing or recent major merger in the hosting cluster. Unfortunately, no information on the X-ray gas distribution is available for RXCJ 2003.5–2323, except for the RASS image, which shows that the X-ray emission is strongly asymmetric and extends beyond the halo emission. The analysis of the bi-dimensional distribution of optical galaxies from the APM catalogue suggests the presence of two significant substructures, which may be interacting

with the cluster. However no redshift information is available at present to confirm such scenario. Forthcoming X-ray Chandra and optical NTT observations will allow us to study the dynamical state of the cluster, and possibly confirm its expected high merging activity.

A possible explanation for the complex morphology of the halo was proposed. Due to the relatively high redshift of the cluster, it is likely that the observed clumps and filaments trace the peaks of the magnetic field intensity in the cluster. This is expected in the framework of the re-acceleration model for the formation of giant radio halos.

## Chapter 8

# Multiple diffuse radio sources in RXCJ 1314.4–2515

RXCJ 1314.4–2515 is a rich galaxy cluster at redshift  $z=0.244$ , with a virial mass  $M_v = 2.3 \times 10^{15} M_\odot$ , high X-ray luminosity ( $L_X \sim 1.1 \times 10^{45} \text{ erg s}^{-1}$  in the 0.1–2.4 keV band), and high temperature (8.7 keV; Matsumoto et al. 2001). Its general properties are summarised in Table 2.1.

RXCJ 1314.4–2515 is the most remarkable galaxy cluster among the sample observed within the 610 MHz GMRT Radio Halo Survey (Sec. 1.12). At present it is the unique case of a cluster hosting a central radio halo and two peripheral relics, as first suggested by inspection of the 1.4 GHz NVSS image (Fig. 8.1), and then confirmed by VLA 1.4 GHz data (Feretti et al. 2005; hereinafter FSB05) and by our 610 MHz observations (Tab. 2.2). Given such complex and peculiar radio properties, RXCJ 1314.4–2515 represents a challenge for our understanding of the connection between cluster scale non-thermal phenomena and the physics of cluster mergers.

The little information available in the literature on the dynamical status of this cluster suggests clear hints of a high level of merging activity, as reported in the optical and X-ray analysis by Valtchanov et al. (2002; hereinafter VMP02). However a detailed analysis and a global understanding of the ongoing merger is still missing.

In the present work we perform a radio analysis of the extended sources in this cluster. The study is carried out using our GMRT 610 MHz observations (Tab. 2.2), combined with the VLA 1.4 GHz information from FSB05.

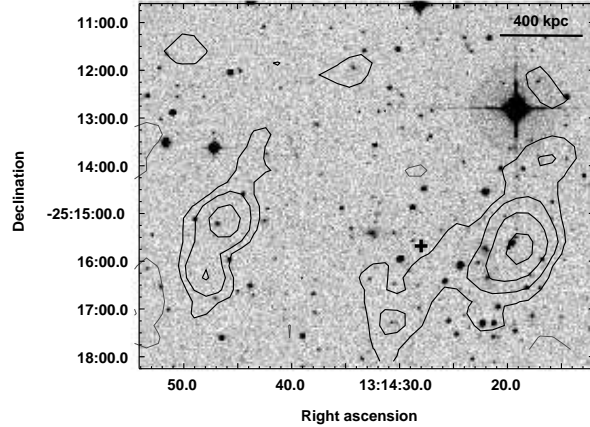


Figure 8.1: 1.4 GHz NVSS image of the complex diffuse emission in RXCJ 1314.4–2515, overlaid on the POSS–2 optical frame. The  $1\sigma$  level in the image is  $0.45 \text{ mJy b}^{-1}$ . Contour levels are spaced by a factor 2, starting from  $\pm 1 \text{ mJy b}^{-1}$ . The resolution is  $45'' \times 45''$ , p.a.  $0^\circ$ . The cross indicates the X–ray centre of the cluster (Tab. 2.1).

A re–analysis of the optical and X–ray properties of the cluster, as derived from the APM catalogue (Maddox et al. 1990) and ROSAT–HRI archival data respectively, is also presented.

The Chapter is organised as follows: in Section 8.1 we summarise the main observational evidence for an ongoing merger in RXCJ 1314.4–2515, as provided by the literature; our GMRT 610 MHz observations are presented in Section 8.2; the analysis of the relic sources is given in Section 8.3, while Section 8.4 deals with the central radio halo; the connection between these extended sources and the cluster merging environment is discussed in Section 8.5; in Section 8.6 we present the re–analysis of the optical and X–ray archival data; finally in Section 8.7 we summarise the main results of our study and the future development.

At the redshift of RXCJ 1314.4–2515 ( $z=0.244$ ), the cosmology adopted in this work leads to a linear scale of  $1'' = 3.84 \text{ kpc}$ .

## 8.1 Evidence for a merger in RXCJ 1314.4–2525

RXCJ 1314.5–2525 was studied with ROSAT–HRI in the X–ray band, and with the ESO–New Technology Telescope (NTT) in the optical by VMP02. Those

observations suggested that the cluster is very far from virialisation. We can briefly summarise the main results of the VMP02 analysis as follows:

- i. the redshift distribution of the member galaxies shows a bimodal behaviour, with two peaks separated in the velocity space by  $\sim 1700 \text{ km s}^{-1}$ ;
- ii. the bi-dimensional distribution of galaxies reveals the existence of two substructures along the East–West axis, which are associated with the clumps detected in the redshift space;
- iii. two dominant elliptical galaxies are clearly visible in the optical image of the cluster, separated by  $\sim 2.5'$  ( $\sim 560 \text{ kpc}$ ) in projected distance, and  $\sim 1000 \text{ km s}^{-1}$  in the velocity space. The brightest one is located within the eastern clump, while the other is a member of the western substructure;
- iv. the cluster X–ray emission is also bimodal and is elongated in the East–West direction, being the western peak the brightest;
- v. an offset between the X–ray peaks and the position of the two dominant galaxy is observed, being the X–ray centroid located between the two galaxies;
- vi. the elongation axis of the hot gas distribution is misaligned with respect to the axis defined by the optical galaxy distribution.

These results support the idea of a highly dynamically perturbed state for RXCJ 1314.4–2515, which is likely to be experiencing a merging process with a massive subclump along the E–W axis. The offset between the X–ray and optical peaks, as well as the misalignment between the axis of the X–ray and optical distributions, might be due to the decoupling between gas and galaxies during the merger.

## 8.2 GMRT 610 MHz observations

The GMRT 610 MHz observations of RXCJ 1314.4–2515 are part of the larger project of the GMRT Radio Halo Survey presented in Section 1.12. The observation details and description of the data reduction are given in Table 2.2 and Section 2.4 respectively.

We observed the cluster for a total of  $\sim 2.5$  hours and reached a sensitivity of the order of  $1\sigma = 60 \mu\text{Jy b}^{-1}$  in the full resolution image ( $8.0'' \times 5.0''$ ; Tab. 2.2). Using the full array with a taper, we produced the low resolution images (down to  $25.0'' \times 22.0''$ ), which are more adequate to image the regions of low surface brightness emission. An average noise level of  $\sim 60 \mu\text{Jy b}^{-1}$  was achieved also in these images.

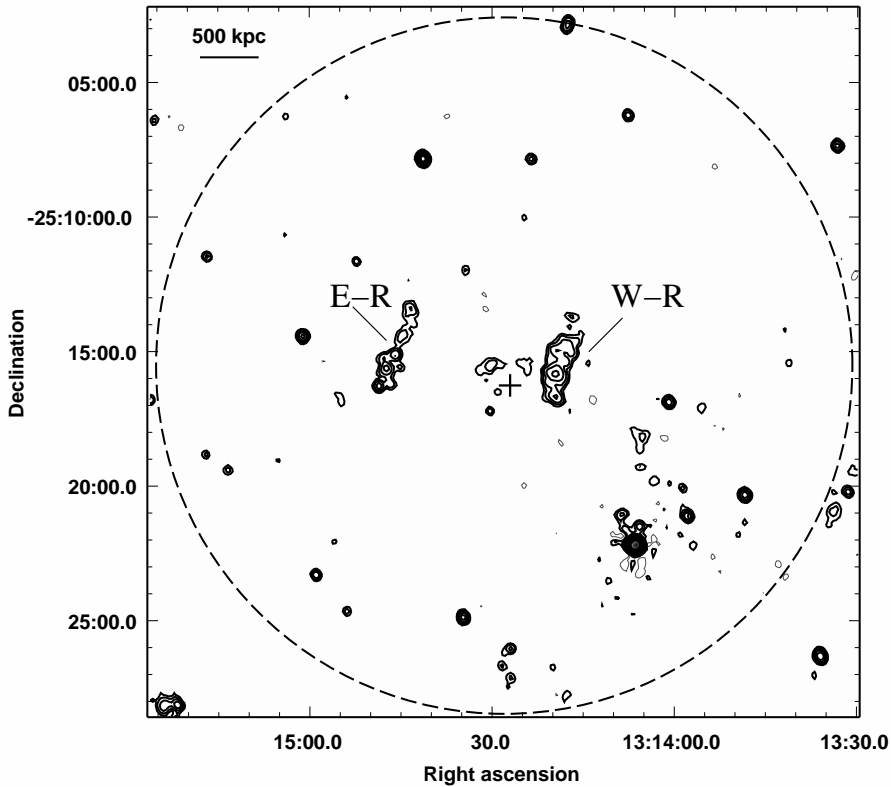


Figure 8.2: GMRT 610 MHz radio contours of the central  $25' \times 25'$  region containing RXCJ 1314.4–2515. The  $1\sigma$  level in the image is  $60 \mu\text{Jy b}^{-1}$ . Contour levels are scaled by a factor 2, starting from  $\pm 0.3 \text{ mJy b}^{-1}$ . The resolution is  $15.0'' \times 10.0''$ , p.a.  $-6^\circ$ . The dashed circle is centered on the cluster X-ray centre, indicated by the cross, and has a radius corresponding to the virial radius  $R_v = 12.93'$  (2.98 Mpc; Tab. 2.1). E-R and W-R indicate the western and eastern diffuse sources respectively.

Figure 8.2 shows the 610 MHz image of the virial region of RXCJ 1314.4–2515 at the resolution of  $15.0'' \times 10.0''$ . The dashed circle is centered on the cluster X-ray centre (cross) and has a radius equal to the virial radius of RXCJ 1314.4–2515 ( $R_v \sim 3 \text{ Mpc}$ ; Tab. 2.1). The lowest contour corresponds to  $5\sigma = 0.3 \text{ mJy b}^{-1}$ . The

southwestern portion of the field has a significantly higher noise level ( $\sim 0.1 \text{ mJy b}^{-1}$ ) due to the sidelobes of the bright point source located at  $\sim 8'$  from the cluster centre. The innermost part of the field is not strongly affected by the presence of such source. Two parallel bright features (labelled as E–R and W–R) are easily visible in the central region of Figure 8.2. Hints of the presence of very low surface brightness emission are also visible between these two structures.

Figure 8.3 zooms on the cluster inner region. The upper panel shows the full resolution image, superposed to the POSS–2 optical plate, while in the lower panel an image at the resolution of  $20.0'' \times 15.0''$  is displayed as grey scale and contours. Figure 8.3 (lower panel) confirms that RXCJ 1314.4–2515 has a very complex radio morphology, with the presence of three different regions of extended emission, labelled as E–R, W–R and RH.

The size and morphology of these extended structures are in very good agreement with the VLA 1.4 GHz image in FSB05, who ruled out any association of these diffuse sources with individual optical galaxies. On the basis of their overall morphology, coupled with their location with respect to the cluster centre, they classified the elongated and peripheral sources as radio relics (here referred to as E–R and W–R; Fig. 8.3) and the central source as radio halo (here referred to as RH).

## 8.3 The radio relics

### 8.3.1 The morphology

As clear from Figures 8.2 and 8.3, the two bright and roughly parallel relics (E–W and W–R) extend in the NNW–SSE direction for approximately  $4'$  each, which corresponds to a linear size of  $\sim 920 \text{ kpc}$  at the redshift of the cluster. The sources are very elongated, with an axial ratio of  $\sim 3$  for W–R and  $\sim 4.3$  for E–R, which are typical values for radio relics (see for example the A 521 relic in Chapter 6). Their projected distance from the cluster centre (cross in Fig. 8.2; Tab. 2.1) is  $\sim 2'$  (i.e.  $\sim 460 \text{ kpc}$ ) for W–R, and  $\sim 3.5'$  (i.e.  $\sim 800 \text{ kpc}$ ) for E–R. The main properties of these sources are given in Table 8.1.

The striking superposition of the radio contours at the resolution of  $25.0'' \times 22.0''$  on the X–ray archival ASCA image of RXCJ 1314.4–2515 (Fig. 8.4) clearly shows that the two relics are located at the border of the cluster X–ray emission detected by the satellite.

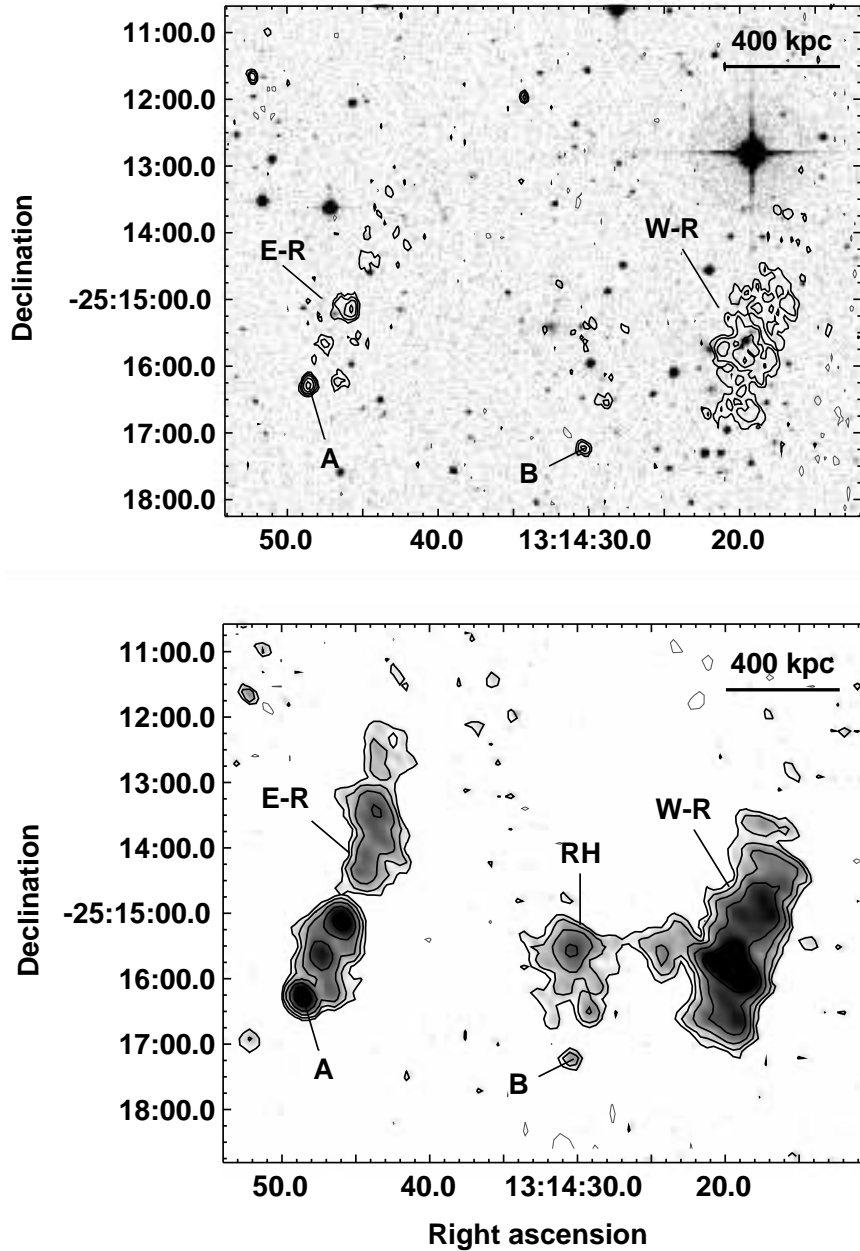


Figure 8.3: GMRT 610 MHz images of the central region of RXCJ 1314.4–2515. The  $1\sigma$  level is  $60 \mu\text{Jy b}^{-1}$ . Contours are spaced by a factor 2, starting from  $\pm 0.18 \text{ mJy b}^{-1}$ . E–R and W–R indicate the western and eastern relics respectively, the radio halo is labelled as RH, and the individual point sources in the relics/halo region are indicated as A and B. *Upper panel* – Full resolution radio contours ( $8.0'' \times 5.0''$ , p.a.  $15^\circ$ ) on the POSS–2 optical image. *Lower panel* – Grey scale and radio contours of the diffuse sources. The resolution is  $20.0'' \times 15.0''$ , p.a.  $39^\circ$ .

Table 8.1: Properties of the extended sources in RXCJ 1314.4–2515.

Source	$S_{610\text{ MHz}}$ mJy	$S_{1400\text{ MHz}}$ mJy	$\alpha_{610\text{ MHz}}^{1400\text{ MHz}}$	$\log P_{610\text{ MHz}}$ W Hz $^{-1}$	$\log P_{1400\text{ MHz}}$ W Hz $^{-1}$	LLS kpc	$B'_{\text{eq}}^{(1)}$ $\mu\text{G}$
W–R	$64.8 \pm 3.2$	$20.2 \pm 0.5$	$1.4 \pm 0.1$	25.03	24.60	920	3.1
E–R	$28.0 \pm 1.4$	$10.1 \pm 0.3$	$1.4 \pm 0.1^{(2)}$	24.67	24.30	920	2.6
RH	$10.3 \pm 0.3$	–	–	24.22	–	460	–

(<sup>1</sup>) estimated with a low energy cut-off in the electron spectrum (see text).

(<sup>2</sup>) value obtained including the contribution of source A (see text and Fig. 8.3).

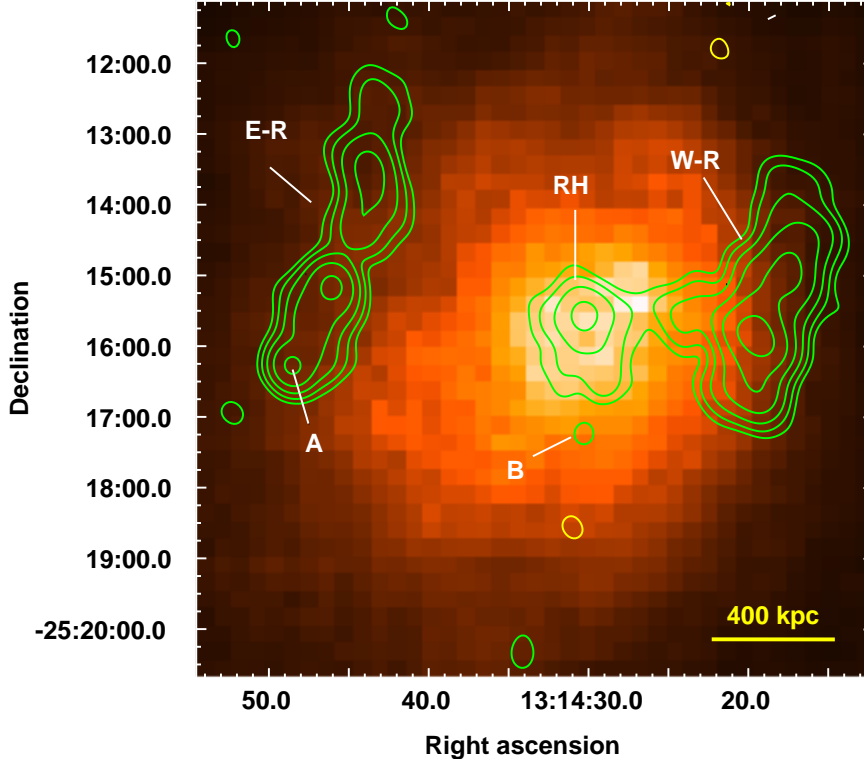


Figure 8.4: GMRT 610 MHz radio contours of RXCJ 1314.4–2515, overlaid on the X-ray archival ASCA image (colour). The  $1\sigma$  level in the image is  $60 \mu\text{Jy b}^{-1}$ . Contour levels are scaled by a factor 2, starting from  $\pm 0.2 \text{ mJy b}^{-1}$ . The resolution is  $25.0'' \times 22.0''$ , p.a.  $15^\circ$ . E–R and W–R indicate the western and eastern relics respectively, the radio halo is labelled as RH, and the individual point sources are indicated as A and B.

The 610 MHz flux density of the relics was measured on the low resolution images (lower panel of Fig. 8.3 and Fig. 8.4). We obtained  $S_{610\text{ MHz}} = 64.8 \pm 3.2$  mJy for the western relic and  $S_{610\text{ MHz}} = 28.0 \pm 1.4$  mJy for E–R (Tab. 8.1). The corresponding radio powers at the redshift of RXCJ 1314.4–2515 are given in Table 8.1. The flux density reported for E–R does not include the southern pointlike

source labelled as A in Figures 8.3 and 8.4. This source has no optical counterpart at the sensitivity of the POSS–2 image and in the SuperCOSMOS (Hambly et al. 2001) and APM catalogues. On the basis of the ATCA information at 2.5 GHz in VMP02, we estimated a 610 MHz–2.5 GHz spectral index of  $\alpha = 0.6$  for this source. This value is typical of active radio galaxies, rather than cluster scale diffuse radio sources, whose spectra are steep with  $\alpha > 1$  (Sec. 1.3). Hence we consider A as a background radio galaxy, unrelated to the diffuse emission associated with the eastern relic.

### 8.3.2 The integrated spectrum and magnetic field

Using the 1.4 GHz flux densities reported in FSB05 for the relics (also given in Tab. 8.1 with the corresponding radio powers), we derived their total spectral index between 1.4 GHz and 610 MHz. For a consistent comparison with FSB05, we included also the contribution of source A to the 610 MHz flux density of E–R, and obtained  $S'_{610\text{MHz}} = 32.8 \pm 1.6$  mJy. Our flux density measurements lead to the same spectral index in both features, i.e.  $\alpha = 1.4 \pm 0.1$  (Tab. 8.1). This value is typical for this class of radio sources (Sec. 1.3).

Using the spectral index between 610 MHz and 1.4 GHz (Tab. 8.1), we obtained an estimate of the magnetic field within the relic regions. The standard equipartition equations (computed in the frequency range 10 MHz–100 GHz), provide  $B_{\text{eq}} = 0.8 \mu\text{G}$  for W–R and  $B_{\text{eq}} = 0.6 \mu\text{G}$  for E–R. If we include the contribution of low energy electrons, adopting the equipartition equations with a low energy cut–off in the electron spectrum (we used  $\gamma_{\text{min}} = 50$ ; see Sec. 5.2.4), we obtain higher values, i.e.  $B'_{\text{eq}} = 3.1 \mu\text{G}$  and  $B'_{\text{eq}} = 2.6 \mu\text{G}$  for the western and eastern relics respectively, also reported in Table 8.1. Both values of the equipartition magnetic field are in agreement with the estimates found in the literature for radio relic sources and cluster radio halos, i.e. in the range 0.1 – a few  $\mu\text{G}$  (Sec. 1.3).

### 8.3.3 Origin of the relics

From a theoretical point of view, radio relics are thought to be connected with shock waves in the intracluster medium generated during merging phenomena (Sec. 1.1.1). According to the hydrodynamical simulations of cluster mergers (e.g. Ricker &

Sarazin 2001), we expect that the collision between two subclumps originates both a front shock, propagating along the infall direction of the secondary subcluster, and a back shock, which moves away in the opposite direction (see Fig. 1.1 in Sec. 1.1.1).

Figure 8.4 shows that the relics in RXCJ 1314.4–2515 are located at the border of the detected X–ray emission, and extend roughly parallel to each other. The projected location and orientation of these sources might be consistent with the presence of both a front and back shock, which are propagating toward the cluster outskirts along opposite directions. A possibility is that an approximately head–on collision between the X–ray/optical clumps detected by VMP02 along the East–West axis (Sec. 8.1) may have originated such shock waves. However, the available X–ray data lack the resolution and sensitivity to allow the detection of the expected temperature and density jumps at the location of the relics.

If the relics in RXCJ 1314.4–2515 are indeed connected to an underlying shock wave, two theoretical possibilities can be discussed for their origin: (i) shock acceleration of relativistic electrons; (ii) shock adiabatic compression of fossil radio plasma.

#### (i) Particle acceleration by a merger shock

As proposed by Röttgering et al. (1997) and Ensslin et al. (1998), the synchrotron radiation from cluster scale radio relics may be emitted by electrons accelerated from the thermal ICM up to ultra–relativistic energies by a merger shock (Sec. 1.10.1; see also the discussion on the relic origin in A 521, Sec. 6.4).

In this case the shape of the energy spectrum of the accelerated electrons<sup>1</sup> is a power law with slope  $\delta$ , which is related to the Mach number  $M$  of the shock by the equation (1.3) in Section 1.10.1.

Both relics in RXCJ 1314.4–2515 have a total spectral index between 610 MHz and 1.4 GHz of  $\alpha = 1.4 \pm 0.1$  (Tab. 8.1). For this value we find  $\delta = 2\alpha + 1 = 3.8$ , which implies that the requested Mach number of the shock is  $M = 2.4$  for both sources. This value is in good agreement with the Mach numbers expected for the shocks injected within the cluster atmosphere as consequence of mergers (i.e.  $M \lesssim 3$ ; see Section 1.1.1).

---

<sup>1</sup>the case of the re–acceleration of a pre–existing population of relativistic electrons is not considered here (see Markevitch et al. 2005 for a detailed discussion).

**(ii) Adiabatic compression of fossil radio plasma**

Merger shocks may adiabatically compress a region of pre-existing aged radio plasma, increase its magnetic field intensity and energy density, and thus re-energize the radio emitting relativistic electrons (Ensslin & Gopal-Krishna 2001; see Sec. 1.10.1 and also the analysis of the A 521 relic in Sec. 6.4.)

In the case of RXCJ 1314.4–2515, this scenario requires the existence of two regions of fossil relativistic electrons, located at the cluster outskirts, and opposite to each other. Furthermore two shock fronts are also required to revive these regions of aged radio plasma, and produce the relics at the observed positions.

The fossil electrons may have been released by a previous cycle of an active radio galaxy in the proximity of each relic, or by a single radio galaxy located in the region between the two sources. However no currently active source is observed near the western relic (Fig. 8.3), and source A, located South of E–R (Fig. 8.3), is likely associated with a background galaxy (see Sec. 8.3.1). Furthermore, there is a deficit of radio galaxies in this cluster, at least at the sensitivity limit of our GMRT 610 MHz observations ( $1\sigma \sim 60 \mu\text{Jy b}^{-1}$ ), apart source B (Fig. 8.3), which has no redshift information.

A possible alternative is that the fossil electrons may have been injected in the past, during the active phase of a radio galaxy which is presently switched-off. The existence of two radio galaxies, one for each relic and both dead at present, seems an unlikely possibility. The hypothesis of a single galaxy, located between the relics (e.g. the brightest cluster galaxy), and now in a quiescent phase of its radio activity may be more plausible. In this case, the two regions of aged radio plasma might be the old lobes of such radio galaxy, which have buoyantly moved to the cluster outskirts, and then been stretched and revived by the shock compression.

**8.4 The radio halo**

The halo is centered on the region of highest X-ray surface brightness (Fig. 8.4), and has a largest angular size of  $\sim 2'$ . The corresponding linear size ( $\sim 460$  kpc) implies that RH is not a giant radio halo (Sec. 1.4). The main radio properties of this source are summarised in Table 8.1.

The object B, South of the halo diffuse emission in Figures 8.3 and 8.4,

is an unrelated discrete radio source, identified with a  $b_J=20.77$  galaxy in the SuperCOSMOS catalogue. No redshift information is available for this source.

In Figures 8.3 and 8.4 the halo emission seems to blend with the western relic. However it is difficult to understand whether these structures are physically connected to each other or this feature is the result of projection effects, which are likely to play a role. This morphology is reminiscent of the complex diffuse source in the galaxy clusters A 754 (Kassim et al. 2001; Bacchi et al. 2003) and A 2256 (Clarke & Ensslin 2006; see also right panel of Fig. 1.8 in Sec. 1.5), which host a central radio halo and a more peripheral relic apparently connected to each other. Given the different polarisation properties of radio halos and relics (e.g. A 2256, Clarke & Ensslin 2006; see also Secs. 1.4 and 1.5), polarisation information would be necessary to clarify the halo–western relic connection in RXCJ 1314.4–2515.

The flux density of the halo is  $S_{610\text{MHz}} = 10.3 \pm 0.3$ , which implies a radio power of  $\log P_{610\text{MHz}} (\text{W Hz}^{-1}) = 24.72$  (Tab. 8.1). The halo flux density was measured on the low resolution image shown in Figure 8.4. No spectral index estimate between 610 MHz and 1.4 GHz can be derived, due to the lack of a flux density measurement at 1.4 GHz in FSB05, whose images do not allow to clearly separate the contribution of the halo and the western relic emission.

Figure 8.5 shows the  $\text{Log}L_X\text{--Log}P_{1.4\text{GHz}}$  correlation for all galaxy clusters known to host a radio halo, regardless of their size (Sec. 1.7). The clusters with a detected giant radio halo (i.e. with  $\text{LLS} \gtrsim 700$  kpc, see Sec. 1.4) are reported as black circles. The filled ones are the clusters at redshift  $z > 0.2$ , the empty circles are those at  $z < 0.2$  (see Cassano, Brunetti & Setti 2006 and references therein for the literature data). The cluster hosting a radio halo with  $\text{LLS} < 700$  kpc are shown as triangles. The black ones represent A 2218 ( $z=0.176$ ; Giovannini & Feretti 2000) and A 401 ( $z=0.0737$ ; Bacchi et al. 2003), while the red triangle is A 3562 ( $z=0.048$ ; Venturi et al. 2003; see also Chapter 3). The solid line is the best–fit of the correlation found for giant radio halos by Cassano, Brunetti & Setti (2006), i.e.  $P_{1.4\text{GHz}} \propto L_X^{1.97 \pm 0.25}$  (Sec. 1.7).

The location of the halo in RXCJ 1314.4–2515 is given by the blue triangle. Its radio power at 1.4 GHz was obtained by scaling the measured flux density at 610 MHz, obtained by integrating the image in Figure 8.4 over the whole region between the eastern border of the halo and the western relic. We obtained

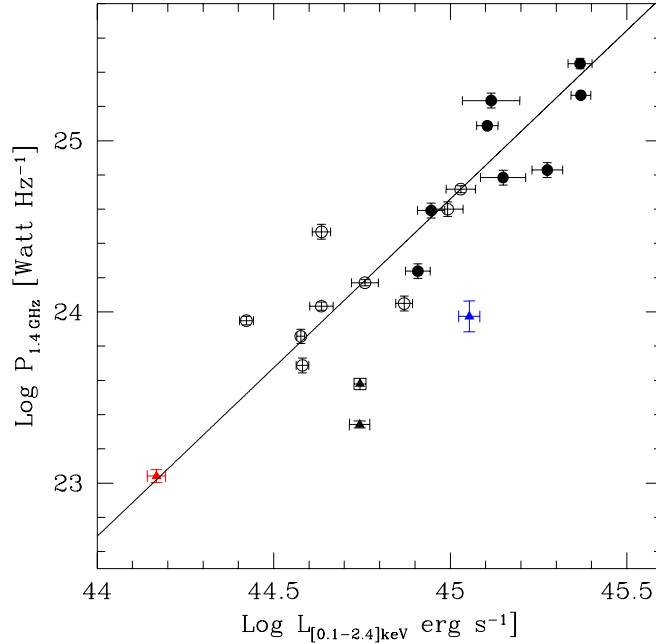


Figure 8.5:  $\text{Log}L_X\text{--}\text{Log}P_{1.4\text{ GHz}}$  diagram for all clusters with detected radio halos. Empty and filled black circles are the giant radio halos at  $z < 0.2$  and  $z > 0.2$  respectively. Black triangles are the radio halos in A 2218 (Giovannini & Feretti 2000) and A 401 (Bacchi et al. 2003). The red triangle is A 3562 (Venturi et al. 2003; Chapter 3). The blue triangle shows the location of RXCJ 1314.4–2515. The solid line is the best-fit found for giant radio halos by Cassano, Brunetti & Setti (2006).

$S'_{610\text{ MHz}} = 13.0 \pm 1.9$  mJy, where the large uncertainty reflects the difficulty in separating the contribution of the relic emission. The flux density given in Tab. 8.1 refers to the central portion of the halo, and does not include the bridge which connects the source to the western relic. We scaled  $S'_{610\text{ MHz}}$  adopting  $\alpha = 1.2 \pm 0.2$ , which is a typical value for radio halos (Sec. 1.4). The derived 1.4 GHz flux density is  $S_{1.4\text{ GHz}} = 4.8 \pm 0.8$  mJy, which implies  $\text{log}P_{1.4\text{ GHz}}(\text{W Hz}^{-1}) = 23.96$ .

As clear from Figure 8.5, the location of RXCJ 1314.4–2515 is consistent with the behaviour of A 2218 and A 401 (black triangles). All three clusters possess a radio halo, whose radio power is significantly smaller than the value expected from their X-ray luminosity on the basis of the best-fit correlation found for giant radio halos (solid line). On the contrary, the location of A 3562 (red triangle) is fully consistent with it, given the lower value of the cluster X-ray luminosity.

On the other hand, it has been recently found that the size of radio halos is

correlated to their radio power (Cassano 2007; Cassano et al. 2007). In particular, the 1.4 GHz radio power is  $\propto R_H^4$  for giant radio halos, where  $R_H$  is the halo radius. Compared to this law, the halo radio power in RXCJ 1314.4–2515, A 2218 and A 401 results considerably higher than what expected on the basis of their small size, while the A 3562 halo is in line with these expectations.

The link between the small size radio halos and the giant ones is still unclear, given also the small number involved. A possibility is that they may represent a different evolutionary stage of the radio halo phenomenon, but also a distinct class of extended radio sources.

#### 8.4.1 Origin of the radio halo

The radio halo is located within the central and brightest region of the X-ray distribution as imaged by ASCA (Fig. 8.4). It is also spatially coincident with the bulk of the optical galaxies, belonging to the eastern subclump found both in the bi-dimensional galaxy distribution and in the redshift space (VMP02; Sec. 8.1). The halo structure extends along the East–West axis, i.e. the same direction of the X-ray ROSAT–HRI elongation of the cluster central region (VMP02). It is possible that this direction also traces the merger axis. All these pieces of information suggest a tight connection between the origin of the halo and the ongoing merging process at the centre of the cluster.

In the hypothesis that a collision between two massive subclusters is ongoing in this region (Sec. 8.1), we expect that large scale turbulence is injected in the region swept by the infalling subclump (Sec. 1.1.2). Such large scale turbulence may efficiently diffuse over the whole volume between the cores of the two subclusters, and decay into smaller scale turbulence, which may re-accelerate relativistic electrons and produce the synchrotron radiation detected from the halo (re-acceleration scenario; see Secs. 1.8 and 1.9). In this case the spectrum of the electrons re-accelerated by turbulence shows a clear steepening at high radio frequencies (e.g. Coma, Thierbach et al. 2003; Sec. 1.8; see also the spectral analysis of the A 3562 halo in Chapter 3). However no spectral information is available for this halo to investigate this issue.

## 8.5 Need for an energetic cluster merger

RXCJ 1314.4–2515 is the third galaxy cluster imaged so far hosting a double relic, following the discoveries in A 3667 (Roettiger et al. 1999) and in A 3376 (Bagchi et al. 2005 and 2007). The overlay of the radio contours on the X-ray images of all three clusters are reported in Figure 8.6. RXCJ 1314.4–2515 is exceptional and unique in hosting two relic sources and a central radio halo.

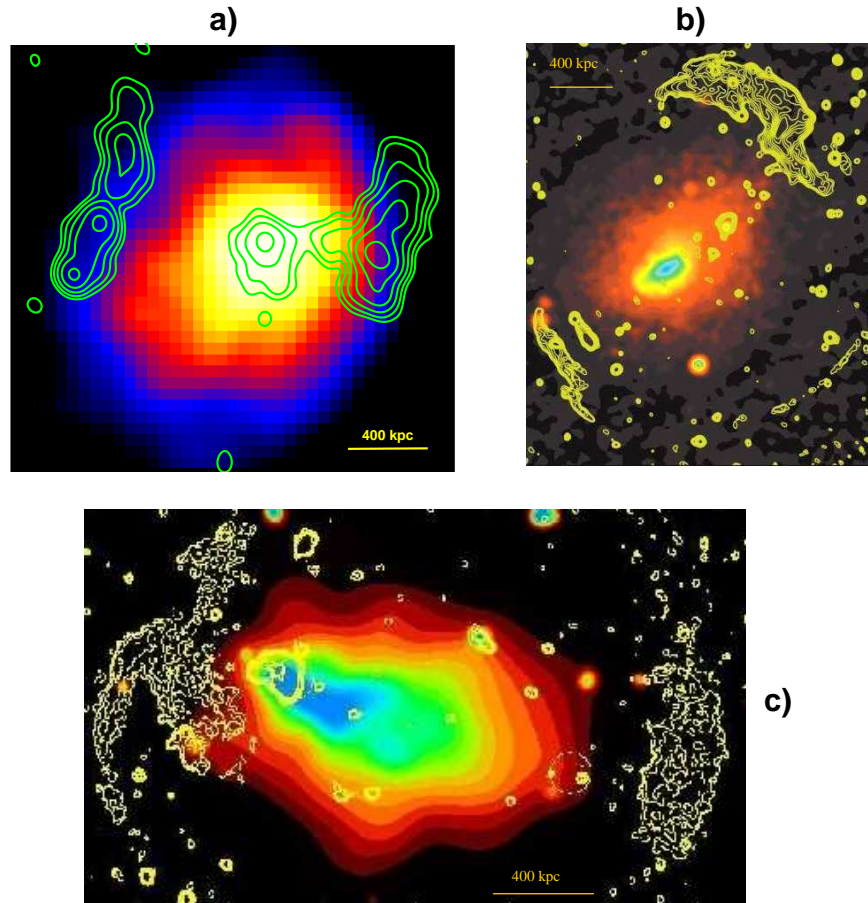


Figure 8.6: *Panel a)* – GMRT 610 MHz radio contours of RXCJ 1314.4–2515, overlaid on the smoothed X-ray ASCA image. The radio image is the same as Fig. 8.4. *Panel b)* – MOST 843 MHz radio contours (resolution  $43''$ ) of A 3667 (Röttgering et al. 1997) on the X-ray ROSAT PSPC image (composite image by M. Murgia, INAF–IRA, Bologna, Italy). *Panel c)* – VLA 1.4 GHz radio contours (resolution  $20''$ ) of A 3376 on the ROSAT PSPC image from Bagchi et al. (2005).

As pointed out in Section 1.6, halos and relics are thought to be related to cluster mergers, even though different physical processes may be at work for the two classes of radio sources: relics are expected to form in the proximity of shock fronts (Sec. 1.10), while halos are explained in the framework of particle re-acceleration

as powered by turbulence (Secs. 1.8 and 1.9). The existence of two relics and one radio halo in RXCJ 1314.4–2515 indicates that both mechanisms may be active in this cluster, and thus requires the presence of an ongoing energetic merger.

The optical and X-ray information available in the literature provide strong evidence for a high merging activity in this cluster (see Sec. 8.1). However they do not allow to determine the merging dynamics and derive the mass ratio of the involved subclusters, and thus to estimate the energetics of the ongoing merger.

## 8.6 Analysis of the cluster dynamics from archival data

In order to search for further clues about the cluster dynamics, we examined the bi-dimensional distribution of optical galaxies from the APM catalogue, and inspected the cluster ROSAT–HRI image.

### 8.6.1 Optical analysis

In Figure 8.7 we overlay the GMRT 610 MHz radio image (black contours) on the POSS–2 optical frame and isodensity contours (red) of the projected distribution of optical galaxies, as derived from the APM to the magnitude  $R < 20$ . Optical substructures are enhanced by an Adaptive Kernel Algorithm (Bardelli et al. 1998a). Three significant subclumps are clearly visible in the image, labelled as G1, G2 and G3. G1 and G2 coincide with the optical groups detected both in the velocity space and in the projected distribution of cluster members by VMP02 (Sec. 8.1). South of G2, we detect a possible infalling/outgoing subclump (G3). Unfortunately no redshift information is available to confirm whether this substructure is physically interacting with G1 and/or G2.

A rough estimate of the mass ratio between the main clump G1 and the subclumps G2 and G3 can be derived from the luminosity-weighted number of galaxies in these substructures. We found a ratio of  $\gtrsim 1:5$  for G1/G2 and  $\gtrsim 1:10$  for G1/G3.

On the basis of energetic arguments, the possibility to develop a giant radio halo is related to the efficiency of the turbulence injection and to the possibility to generate large enough ( $\geq$  Mpc size) turbulent regions in the cluster. The calculations in Cassano, Brunetti & Setti (2004 and 2006) and Cassano & Brunetti (2005) show that major cluster mergers (i.e. with mass ratio of the order of  $\geq 1:5$ ) between

massive clusters ( $M \geq 10^{15} M_{\odot}$ ) may provide the ingredients necessary to develop a giant radio halo (Sec. 1.9).

In the case of RXCJ 1314.4–2515, the cluster virial mass ( $M_v = 2.3 \times 10^{15} M_{\odot}$ ; Tab. 2.1) and the estimated mass ratio for the main merging process between G1 and G2 ( $\gtrsim 1:5$ ) are in line with the presence of a radio halo. For comparison, the formation of a radio halo is not expected in A 521 (Chapter 6). The virial mass of A 521 ( $M_v = 1.9 \times 10^{15} M_{\odot}$ ; Tab. 2.1) is similar to RXCJ 1314.4–2515, but the main merging event is occurring between the main cluster and a subcluster with a mass  $\sim 7$  times lower.

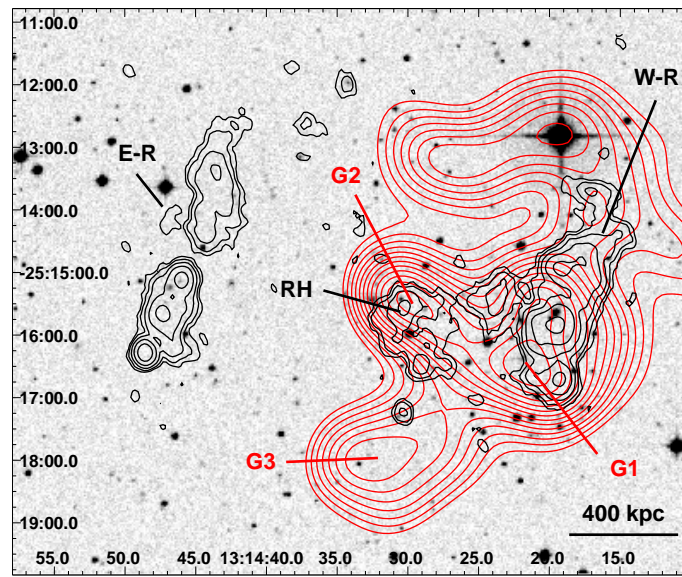


Figure 8.7: GMRT 610 MHz radio contours (black) overlaid on the POSS–2 optical frame and isodensity contours (red) of the optical galaxy distribution from the APM (to  $R < 20$ ). The resolution of the radio image is  $18.0'' \times 15.0''$ , p.a.  $15^\circ$ . Radio contours are spaced by a factor 2, starting from  $\pm 3\sigma = \pm 0.18 \text{ mJy b}^{-1}$ . E–R, W–R and RH indicate the western relic, eastern relic, and radio halo respectively. The optical substructures are labelled as G1, G2 and G3.

### 8.6.2 X–ray analysis

The smoothed ROSAT–HRI image of RXCJ 1314.4–2515 is shown as black contours in Figure 8.8, superposed to the 610 MHz image of the halo and relics (grey scale and red contours). The location of the main optical substructures G1, G2 and G3 (Fig. 8.7) is indicated by the blue crosses. As clear from the figure, the cluster has a complex and asymmetric X–ray surface brightness distribution. In the central part (i.e. the region between the relics), the X–ray emission extends approximately in the

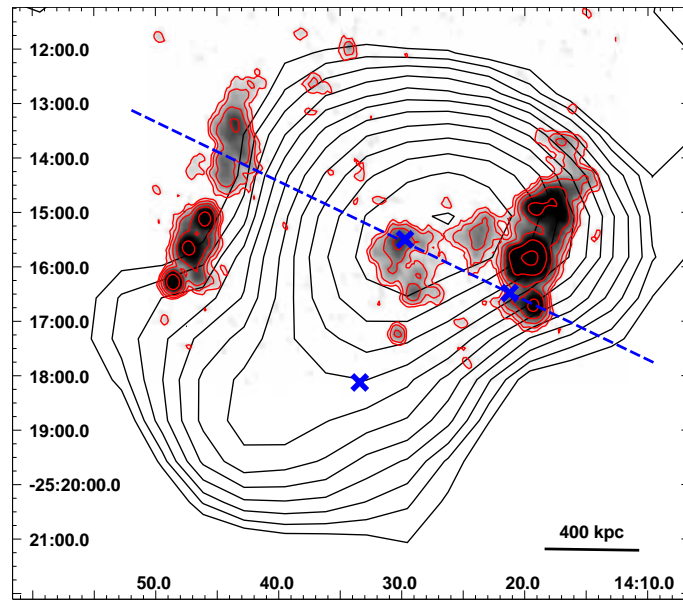


Figure 8.8: Smoothed ROSAT–HRI contours (black) overlaid on the GMRT 610 MHz radio image (grey scale and red contours). The radio image is the same as Fig. 8.7. The X–ray contour levels are logarithmically spaced by a factor  $\sqrt[4]{2}$ . Blue crosses show the location of the optical substructures labelled as G1, G2 and G3 in Fig. 8.7. The blue dashed line represents the axis connecting G1 and G2.

East–West direction. Its axis appears misaligned with respect to the axis connecting the optical groups G1 and G2 (blue dashed line in Fig. 8.8), as also noticed by VMP02 (Sec. 8.1). A tail of X–ray emission extending toward South–East is visible in the southern portion of the cluster. This structure seems associated with the optical clump G3, at least in projection onto the plane of the sky (Fig. 8.7), supporting the hypothesis that this is a subcluster which is falling onto RXCJ 1314.4–2515 or emerging from it.

In conclusion, the complex X–ray and optical properties of this cluster may be the result of a strong merging process between two or more massive subclumps.

## 8.7 Open issues and future observations

To summarise the results presented so far, the optical and X–ray information available in the literature and public archives are not deep enough to study the cluster dynamics in detail and provide support to the need of an energetic cluster merger, as required from the peculiar radio properties of RXCJ 1314.4–2515.

In particular the redshift information is missing to confirm whether the southern

optical (and possibly X-ray) substructure G3 is interacting with the cluster or is an unbound galaxy group. High resolution and high sensitivity X-ray images are needed to study the hot gas emission in more detail and search for evidence of shock fronts at the location of the relics.

For this reason we undertook a follow up study of this cluster. Thanks to forthcoming ESO EMMI–NTT observations (April 2007) we will perform optical spectroscopy of  $\sim 250$  galaxies in this cluster. This will allow us to determine the redshift of the southern substructure and reconstruct in detail the merger dynamics. Furthermore, coupled with our future X-ray XMM–Newton observations ( $\sim 50$  ks; scheduled during Cycle A06), these data will allow us to derive the energetics of the merger, to be related to the energy necessary for the particle re-acceleration responsible for the halo origin, as done in Chapter 3 for the A 3562 halo. Using the XMM–Newton observations we will also investigate the presence of large scale asymmetries in the surface brightness and gas temperature distributions, which may provide evidence for the presence of a shock at the location of the relics.

Further information is also required from the radio band. Low frequency observations carried out with the GMRT during cycle A011 (March 2007), will allow us to determine the integrated spectrum of the halo and relics over the 327 MHz–1.4 GHz frequency range, which will be compared with the expectations from the theoretical models.

## Chapter 9

# Final considerations and conclusions

The purpose of the present thesis was to carry out a comprehensive multiwavelength analysis of a number of galaxy clusters known to be undergoing merger events.

With this aim we selected four merging clusters with high quality data both in the optical and X-ray bands and performed high sensitivity GMRT and VLA radio observations in order to investigate the effect of the merging activity on the cluster radio properties. In particular, the radio observations aimed to test the presence of cluster scale diffuse radio emission in the form of a radio halo and/or a relic. Three of the selected clusters host a central radio halo, and a radio relic is found in the remaining one. Thanks to the multiband approach we attempted to connect the origin of these sources to the dynamical properties and time scale of the ongoing or recent merger event.

Two further galaxy clusters were studied in the present work: RXCJ 2003.5–2323 and RXCJ 1314.4–2515. They were observed at 610 MHz within the GMRT Radio Halo Survey (Sec. 1.12), which led us to detect diffuse radio emission on cluster scale in both clusters. However, the knowledge of their dynamical state is very poor, due to the lack of deep optical information and high resolution X-ray observations. Therefore, these clusters were analysed mainly in the radio band.

### 9.0.1 Summary of the observational results

We observed different situations in the studied galaxy clusters, which can be briefly summarised as follows:

- a radio halo is located at the centre of A 3562. Given its linear size of the order

of  $\sim 500$  kpc, this source is among the smallest radio halos known to date. The cluster has recently experienced a merger with a galaxy group three times less massive, which has passed North of the cluster core  $\sim 1$  Gyr ago. The northern portion of A 3562, which hosts the radio halo, has been significantly disturbed by such interaction, and the cluster core is now oscillating in the North–South direction in response to the recent merging event;

- a giant radio halo (LLS  $\sim 800$  kpc) was found in A 209. Our compared X–ray/optical analysis led us to propose that the cluster has experienced a past merger with a massive subcluster (mass ratio  $\gtrsim 1:3$ ), which is now in a very final stage, when the gaseous cores of the two subclusters have completely merged after a phase of sloshing around the mean velocity. A more recent merging event may have occurred in a direction orthogonal to the old merger axis. We estimated a time scale of the order of  $\sim 0.5$ – $1$  Gyr from the first encounter between the subcluster cores;
- a giant radio halo with LLS  $\sim 900$  kpc was found in A 697. In the light of our results in the X–ray and optical bands, we propose that the cluster is experiencing a major merger process along the line of sight. We also suggest that the first core crossing may have already occurred;
- a radio relic was detected at the outskirts of A 521. This cluster is accreting a number of smaller mass condensations. The most massive one (mass ratio  $\sim 1:7$ ) is falling into the cluster from the North West/South East direction.
- RXCJ 1314.4–2515 is the unique case known so far of a galaxy cluster hosting two peripheral radio relics (both with LLS  $\sim 900$  kpc) and one central small radio halo (LLS  $\sim 460$  kpc). Given such complex and peculiar radio properties, this cluster represents a challenge for our understanding of the connection between cluster scale radio sources and the physics of cluster mergers. The little information provided by the optical and X–ray data suggests the presence of an ongoing merging process between two relatively massive subclusters (mass ratio  $\gtrsim 1:5$ ), whose cores may have just crossed each other;
- RXCJ 2003.5–2323 hosts one of the largest and most powerful giant radio halos imaged so far. Furthermore it is also one of the highest redshift clusters known

to possess diffuse radio emission on the cluster scale. The halo morphology is extremely complex and peculiar, with the presence of bright filaments and clumps of emission. Such structure is very different from the typical morphology of radio halos, whose flux density distribution is usually peaked at the cluster centre and shows a smooth decrease toward the cluster outskirts.

### 9.0.2 The $\text{Log}L_X\text{--}\text{Log}P_{1.4\text{GHz}}$ correlation for radio halos

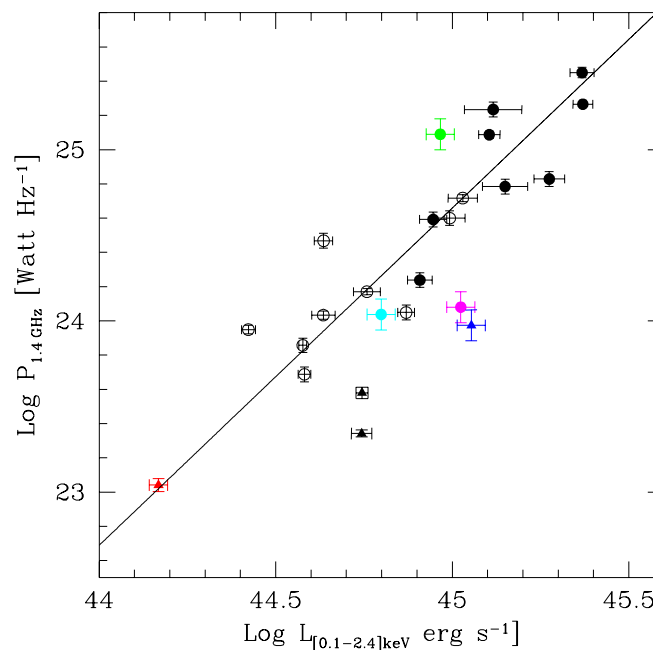


Figure 9.1:  $\text{Log}L_X\text{--}\text{Log}P_{1.4\text{GHz}}$  diagram for all clusters with detected radio halos. Empty and filled black circles are the giant radio halos at  $z < 0.2$  and  $z > 0.2$  respectively. The green circle is RXCJ 2003.5–2323, the magenta circle is A 697 and the cyan circle is A 209. Black triangles are the small radio halos in A 2218 (Giovannini & Feretti 2000) and A 401 (Bacchi et al. 2003). The red triangle is A 3562. The blue triangle is RXCJ 1314.4–2515. The solid line is the best-fit found for giant radio halos by Cassano, Brunetti & Setti (2006).

A correlation is known to exist between the 1.4 GHz radio power of halos and the X-ray luminosity of the hosting cluster (Sec. 1.7). In Figure 9.1 we show the location of the clusters with a radio halo studied in the present thesis on the  $\text{Log}L_X\text{--}\text{Log}P_{1.4\text{GHz}}$  diagram, along with all literature radio halo clusters (see figure caption for details).

The location of the giant radio halos in RXCJ 2003.5–2323 and A 209 (green and cyan solid circles respectively) is in good agreement with the distribution of all giant radio halos known at present (circles). In particular, the position of RXCJ 2003.5–2323 ( $z=0.317$ ) in the upper-right portion of the plot is in line with the behaviour of the most distant clusters (solid circles), which are found to host the most powerful halos. The location of A 697 (magenta) is below the best-fit correlation found for giant radio halos (solid line; see Sec. 1.7 for details), but within the scatter of the points.

The plot in Figure 9.1 includes also the small radio halos from the present work and from the literature (triangles). We note that A 3562 (red) and RXCJ 1314.4–2515 (blue) exhibit different behaviours.

Despite its small extent, the location of A 3562 is in very good agreement with the best-fit of the correlation for giant radio halos (solid line).

The position on the diagram of RXCJ 1314.4–2515 is consistent with the behaviour of the clusters hosting a small size radio halo (black triangles; see figure caption for details). All three clusters possess a source whose radio power is significantly smaller than the value expected from their X-ray luminosity on the basis of the best-fit correlation for giant radio halos.

It has been recently found that the size of radio halos is correlated to their radio power (Cassano 2007; Cassano et al. 2007). In particular, the 1.4 GHz radio power is  $\propto R_{\text{H}}^4$  for giant radio halos, where  $R_{\text{H}}$  is the halo radius. Compared to this law, the halo radio power in RXCJ 1314.4–2515, A 2218 and A 401 results considerably higher than what expected on the basis of their small size, while the A 3562 halo is in line with these expectations.

The link between the small size radio halos and the giant ones is still unclear, given also the small number involved. A possibility is that they may represent a different evolutionary stage of the radio halo phenomenon, but also a distinct class of extended radio sources.

### 9.0.3 Diffuse radio sources and cluster merger dynamics

In the framework of the re-acceleration scenario for the origin of diffuse radio emission in galaxy clusters, giant radio halos (i.e. with  $LLS_{\gtrsim 700 \text{ kpc}}$ ) are expected to be powered by turbulent particle re-acceleration in massive clusters ( $M_{\gtrsim 10^{15}}$

$M_{\odot}$ ), which are undergoing or have recently experienced an energetic merger event with a massive subcluster (mass ratio  $\gtrsim 1:5$ ).

The results of our multiband analysis and their interpretation in the framework of the re-acceleration scenario can be summarised as follows:

- the existence of a giant radio halo in A 697 is expected, since a major merger is likely to be ongoing in this massive galaxy cluster ( $M_v \sim 2.2 \times 10^{15} M_{\odot}$ ). Furthermore, the merger stage may be relatively advanced, and thus enough time may have elapsed since the injection of large scale turbulent motions and the decay of the turbulent eddies to the small scales needed to re-accelerate relativistic electrons in the ICM;
- the presence of a giant radio halo in A 209 ( $M_v \sim 1.6 \times 10^{15} M_{\odot}$ ) might be similarly explained, if part of the turbulence generated during the past major merger has not been completely dissipated at the moment of the new ongoing merging event, expected to be injecting further fresh turbulence which may refurnish the radio halo;
- no giant radio halo is expected in A 521, which indeed does not exhibit diffuse emission at its centre. Although the mass of this cluster ( $M_v \sim 1.9 \times 10^{15} M_{\odot}$ ) is above the mass threshold to form a radio halo, the mass ratio of the main ongoing merging process is  $\sim 1:7$ . According to the semi-analytical calculations in Cassano & Brunetti (2005; see Sec. 1.9.1), such mass ratio is expected to reflect into a low re-acceleration efficiency for the injected turbulence.

A 521 hosts a radio relic at its outskirts. A possible explanation for its origin requires the presence of a shock front at the location of the source. Such shock may have been generated by the ongoing merger, whose axis is roughly perpendicular to the relic extent. The spectral properties of the relic may support such interpretation and require a Mach number  $\lesssim 3$  for the shock;

- a different situation is observed in the case of the small radio halo in A 3562. The cluster mass ( $M_v = 5.9 \times 10^{14} M_{\odot}$ ) is below the threshold to form a radio halo, however the cluster has experienced a merger with a mass ratio  $\sim 1:3$ . In this case we might expect that a by-product of such event (and of the consequent sloshing of the cluster core) may have been the

injection of a non-negligible fraction of turbulence and the amplification of the magnetic field strength in the Northern region of the cluster, which is indeed entirely permeated by the diffuse emission from the halo. On the basis of the reconstructed dynamics of the merger, we showed that there has been enough time for the development of a turbulence cascade, necessary for particle acceleration; at the same time, the epoch of turbulence injection is recent enough to expect that it is not yet completely dissipated at present. The clear steepening of the radio spectrum of this source supports such interpretation, since it proves that the energy of the electrons accelerated in the core region is just sufficient to emit synchrotron radiation up to frequencies around 1 GHz. Furthermore, the small size of the halo is due to the fact that the synchrotron emission is likely to be emitted only in the cluster region where the magnetic field intensity is stronger (i.e. North of the core) and that, even assuming that the acceleration efficiency is maintained outside the radio emitting region, a drop in the magnetic field strength by a factor of  $\sim 2$  outside this region would cause a sharp decrement of the synchrotron emissivity at 610 MHz (of a factor of  $\sim 7 - 8$ ).

#### 9.0.4 Future perspectives

The little information available in the optical and X-ray bands for RXCJ 2003.5–2323 and RXCJ 1314.4–2515 did not allow us to obtain a detailed picture of the merger dynamics and to estimate the involved energetics, which has to be compared to the needed energy for the electron re-acceleration responsible for the observed diffuse emission. For this reason we undertook a follow up study of these clusters both in the optical and X-ray bands.

Thanks to forthcoming ESO EMMI–NTT observations (April 2007) we will perform optical spectroscopy of a large number of galaxies in these clusters, which will allow us to reconstruct in detail the merger dynamics.

Coupled with our future X-ray XMM–Newton observations of RXCJ 1314.4–2515 ( $\sim 50$  ks; scheduled during Cycle A06), these data will allow us to derive the energetics of the ongoing merger and to investigate the presence of large scale asymmetries in the surface brightness and gas temperature distributions, which may provide evidence for the presence of a shock at the location of the relics.

Similarly, the combination of the NTT data with forthcoming Chandra observations of RXCJ 2003.5–2323 (50 ks; scheduled during Cycle 8) will provide insightful information about the cluster dynamical state, leading to possibly confirm the expected major merger in this cluster.

Further information is also required from the radio band for all the sources studied in the present work, except for A 3562 which has been already observed at five different frequencies going from 235 MHz to 1.4 GHz.

Low frequency observations at 327 MHz were carried out with the GMRT during cycle A011 for A 521, A 209 (November 2006), A 697 (January 2007) and RXCJ 1314.4–2515 (March 2007). Observations at 235 MHz for RXCJ 1314.4–2515 and at 235 and 327 MHz for RXCJ 2003.5–2323 were recently requested for the GMRT cycle A012. These observations will allow us to study the morphology of the halos and relics at frequencies  $< 610$  MHz and derive the integrated and point-to-point spectrum of these sources in the low frequency range.

On the other hand, high frequency data are also needed in order (i) to detect and image the A 697 halo at 1.4 GHz and study its spectral properties in the 327–1.4 GHz range; (ii) to image the diffuse emission associated with the relics in A 521 and RXCJ 1314.4–2515 at frequencies  $\nu > 1.4$  GHz and determine the shape of their spectrum over a wide range of frequency, to be compared to the theoretical expectations. Future observations with the ATCA and VLA will be planned for these sources.



# Bibliography

- Abell G.O., 1958, ApJ Suppl., 3, 211
- Abell G.O., Corwin H.G.Jr., & Olowin R.P., 1989, ApJ Suppl., 70, 1
- Adami C., Biviano A., Durret F., Mazure, A., 2005, A&A, 443, 17
- Adelmann–McCarthy J.K., Agüeros M.A, Allam S.S., et al. 2007, ApJS, submitted
- Andernach H., Feretti L., & Giovannini G., 1984, A&A, 133, 252
- Arnaud M., Maurogordato S., Slezak E., Rho J., 2000, A&A, 355, 461 (AMS00)
- Ashman K.M., Bird C.M., Zepf S.E, 1994, AJ, 108, 2348
- Bacchi M., Feretti L., Giovannini G., Govoni F., 2003, A&A, 400, 465
- Bagchi J., Durret F., Lima Neto G.B, Paul S., Chavan S., Proceedings of the 29th International Cosmic Ray Conference. August 2005, Pune, India, 2005, Vol. 3, p.241
- Bagchi J., Durret F., Lima Neto G.B., Paul S., 2006, Sci, 314, 791
- Balestra I., Tozzi P., Ettore S., Rosati P., Borgani S., Norman V., Mainieri C., Viola M., 2007, A&A, 462, 429
- Ballarati B., Feretti L., Ficarra A., Giovannini G., Nanni M., Olori C., Gavazzi G., 1981, A&A, 100, 323
- Bardelli S., Zucca E., Malizia A., et al., 1996, A&A, 305, 435
- Bardelli S., Pisani A., Ramella M., Zucca E., Zamorani G., 1998a, MNRAS, 300, 589
- Bardelli S., Zucca E., Zamorani G., Vettolani G., Scaramella R., 1998b, MNRAS, 296, 599
- Bardelli S., Zucca E., Zamorani G., Moscardini L., Scaramella R., 2000, MNRAS, 312, 540
- Bardelli S., De Grandi S., Ettore S., Molendi S., Zucca E., Colafrancesco S., 2002, A&A, 382, 17
- Bartelmann M., & Schneider P., 2001, Phys. Reports, 340, 291

- Bauer F. E., Fabian A. C., Sanders J. S., Allen S. W., Johnstone R. M., 2005, MNRAS, 359, 1481
- Beck R., & Krause M., 2005, AN, 326, 414
- Bertschinger E., 1998, ARA&A, 36, 599
- Biviano A., Durret F., Gerbal D., Le Fevre O., Lobo C., Mazure A., Slezak E., 1996, A&A 311, 95
- Blandford R., & Eichler D., 1987, Phys. Rep., 154, 1
- Blasi P., Colafrancesco S., 1999, APh, 12, 169
- Blasi P., 2004, JKAS, 37, 483
- Böhringer, H., Schuecker, P., Guzzo, L., et al., 2004, A&A, 425, 367
- Borgani S., Murante G., Springel V., et al. 2004, MNRAS, 348, 1078
- Boschin W., Girardi M., Barrena R., Biviano A., Feretti L., Ramella M., 2004, A&A, 416, 839
- Branchesi M., Gioia I.M., Fanti C., Fanti R., Perley R.A., 2006, A&A 446, 97
- Bridle A.H., & Fomalont E.B., 1976, A&A, 52, 107
- Briel U.G., Finoguenov A., Henry J.P., 2003, Workshop on Galaxies and Clusters of Galaxies, Shuzenji, 2003, p.149
- Brunetti G., Setti G., Comastri A., 1997, A&A, 325, 898
- Brunetti G., Setti G., Feretti L., Giovannini G., 2001, MNRAS, 320, 365
- Brunetti G., 2003, ASPC, 301, 349
- Brunetti G., in *Outskirts of galaxy clusters: intense life in the suburbs*, IAU colloquium 195, Ed. A. Diaferio, 2004, p. 148
- Brunetti G., Blasi P., Cassano R., Gabici S., 2004, MNRAS, 350, 1174
- Buote D.A., 2001, ApJ, 553, 15
- Burns J.O., Sulkanen M.E., Gisler G.R., Perley R.A., 1992, ApJ, 388, L49
- Cassano R., Brunetti G. & Setti G., 2004, JKAS, 37, 589
- Cassano R., & Brunetti G., 2005, MNRAS, 357, 1313
- Cassano R., Brunetti G. & Setti G., 2006, MNRAS, 369, 1577
- Cassano R., 2007, Ph.D Thesis, University of Bologna
- Cassano R., Brunetti G., Setti G., Govoni F., Dolag K., 2007, MNRAS, submitted
- Churazov E., Forman W., Jones C., Böhringer H., 2003, ApJ, 590, 225
- Clarke T.E., & Ensslin T.A., 2006, AJ, 131, 2900
- Colafrancesco S. & Blasi P., 1998, APh, 9, 227

- Colafrancesco S., in *Diffuse thermal and relativistic plasma in galaxy clusters*, 1999 Eds. H.Böhringer, L.Feretti & P.Schuecker, Garching, Germany
- Condon J.J., Cotton W.D., Greisen E.W., Yin Q.F., Perley R.A., Taylor G.B., Broderick J.J., 1998, AJ, 115, 1693
- Dahle H., Kaiser N., Irgens R.J., Lilje P.B, Maddox S.J., 2002, ApJS, 139, 313
- De Filippis E., Sereno M., Bautz M.W., Longo G., 2005, ApJ, 625, 108
- Deiss B.M., Reich W., Lesch H., Wielebinski R., 1997, A&A, 321, 55
- Dennison B., 1980, ApJ, 239, 93
- Dickey J. M., & Lockman F.J., 1990, ARA&A 28, 215
- Dolag K., Bartelmann M., & Lesch H., 1999, A&A, 348, 351
- Dolag K. & Enßlin T.A., 2000, A&A, 362, 151
- Dolag K., Bartelmann M., & Lesch H., 2002, A&A, 387, 383
- Dolag K., Vazza F., Brunetti G., Tormen G., 2005, MNRAS, 364, 753
- Durret F., Forman W., Gerbal D., Jones C., Vikhlinin A., 1998, A&A, 335, 41
- Ebeling H., Voges W., Böhringer H., Edge A.C., Huchra J.P., Briel U.G., 1996, MNRAS, 281, 799
- Ebeling H., Edge A.C., Böhringer H., et al., 1998, MNRAS, 301, 881
- Ebeling H., Edge A.C., Allen S.W. et al. , 2000, MNRAS, 318, 333
- Edge A.C., Stewart G.C., & Fabian A.C., 1992, MNRAS, 258, 177
- Enßlin T.A., Biermann P.L., Klein U., Kohle S., 1998, A&A, 332, 395
- Enßlin T.A., in *Diffuse thermal and relativistic plasma in galaxy clusters*, Eds. H. Böhringer, L. Feretti & P. Schuecker, 1999, p.275
- Enßlin T.A. & Gopal-Krishna, 2001, A&A, 366, 26
- Enßlin T.A. & Brüggen M, 2002, MNRAS, 331, 1011
- Enßlin T.A., 2004, JKAS, 37, 439
- Ettori S., Fabian A.C., White D.A., 1997, MNRAS289, 787
- Ettori S., Bardelli S., De Grandi S., Molendi S., Zamorani G., Zucca E., 2000, MNRAS, 318, 239
- Feretti L., Giovannini G. & Böhringer H., 1997, NewA, 2, 501
- Feretti L., in *Diffuse thermal and relativistic plasma in galaxy clusters*, eds. H. Böhringer, L. Feretti & P. Schuecker, 1999, MPE report, 271, 3
- Feretti L., Fusco-Femiano R., Giovannini G., Govoni F., 2001, A&A, 373, 107
- Feretti L., 2003, ASP Conf. Series, 310, 143

- Feretti L., Orrù E., Brunetti G., Giovannini G., Kassim N., Setti G., 2004, *A&A*, 423, 111
- Feretti L., Schuecker P., Böhringer H., Govoni F., Giovannini G., 2005, *A&A*, 444, 157 (FSB05)
- Ferrari C., Maurogordato S., Cappi, A., Benoist C., 2003, *A&A*, 399, 813 (FMC03)
- Ferrari C., 2003, PhD thesis, University of Nice–Sophia Antipolis, France (F03)
- Ferrari C., Arnaud, M., Etori S., Maurogordato, S., Rho, J., 2005, *A&A*, 446, 417 (FAE05)
- Finoguenov A., Henriksen M.J., Briel U.G., de Plaa J., Kaastra J. S., 2004, *ApJ*, 611, 811 (FHB04)
- Finoguenov A., Böhringer H. & Zhang Y.-Y., 2005, *A&A*, 442, 827
- Fujita Y., Takizawa M. & Sarazin C., 2003, *ApJ*, 584, 190
- Fukugita M., Shimasaku K., Ichikawa T., 1995, *PASP*, 107, 945
- Fusco–Femiano R., Dal Fiume D., Feretti L., Giovannini G., Grandi P., Matt G., Molendi S., Santangelo A., 1999, *ApJ*, 513, L21
- Fusco–Femiano R., Dal Fiume D., De Grandi S., Feretti L., Giovannini G., Grandi P., Malizia A., Matt G., Molendi S., 2000, *ApJ*, 543, L7
- Fusco–Femiano R., Dal Fiume D., Orlandini M. et al., 2003, in *Matter and Energy in Clusters of Galaxies*, ASP Conf. Series, 301, 109, eds. S.Boeyer & C.–Y.Hwang
- Fusco–Femiano R., Orlandini M., Brunetti G., Feretti L., Giovannini G., Grandi P., Setti G., 2004, *ApJ*, 602, L73
- Fusco–Femiano R., Landi R. & Orlandini M., 2005, *ApJ*, 624, 69
- Fusco–Femiano R., Landi R. & Orlandini M., *ApJ*, 654, 9
- Gabici S., & Blasi P., 2003, *ApJ*, 583, 695
- Gastaldello F., & Molendi S., 2004, *ApJ*, 600, 670
- Giacintucci S., Venturi T., Bardelli S., Dallacasa D., Zucca E., 2004, *A&A*, 419, 71 (GVB04)
- Giacintucci S., Venturi T., Bardelli S., Brunetti G., Cassano R., Dallacasa, D., 2006, *NewA*, 11, 437 (GVB06)
- Gioia I.M., Braitto V., Branchesi M., Della Ceca R., Maccacaro T., Tran K.–V., 2004, *A&A*, 419, 517
- Giovannini G., Feretti L. & Stanghellini, 1991, *A&A*, 252, 528
- Giovannini G., Feretti L., Venturi T., Kim K.T., Kronberg P.P., 1993, *ApJ*, 406,

399

- Giovannini G., Tordi M., & Feretti L., 1999, *NewA*, 4, 141
- Giovannini G., & Feretti L., 2000, *NewA*, 5, 335
- Giovannini G., & Feretti L., 2002, in *Merging Processes in Galaxy Clusters*, vol. 272, p. 197, eds. L.Feretti, I.M.Gioia & G.Giovannini
- Giovannini G., & Feretti L., 2004, *JKAS*, 37, 323
- Giovannini G., Feretti L., Govoni F., et al., in *Origin and Evolution of Cosmic Magnetism*, 2006, *Astron. Nachr.*, 327, 563
- Girardi M., Escalera E., Fadda D., Giuricin G., Mardirossian F., Mezzetti M., 1997, *ApJ*, 482, 41
- Girardi M. & Mezzetti M., 2001, *ApJ*, 548, 79
- Girardi M., & Biviano A., 2002, in *Merging Processes in Galaxy Clusters*, Eds. L.Feretti, I.M.Gioia & G.Giovannini, Vol. 272, p. 39
- Girardi M., Bosch W., Barrena R., 2006, *A&A*, 455, 45 (GBB06)
- Gitti M., Brunetti G., & Setti G., 2002, 2002, *A&A*, 386, 456
- Gómez P.L., Pinkney J., Burns J.O., Wang Q., Owen F.N., Voges W., 1997, *ApJ*, 474, 580
- Gómez P.L., Loken C., Roettiger K., Burns, J.O., 2002, *ApJ*, 569, 122
- Gonzalez-Casado G., Mamon G.A. & Salvador-Sole E., 1994, *ApJ*, 433, 61
- Govoni F., Feretti L., Giovannini G., Böhringer H., Reiprich T.H., Murgia M., 2001a, *A&A*, 376, 803
- Govoni F., Enßlin T.A., Feretti L., Giovannini G., Böhringer H., Reiprich T.H., 2001b, *A&A*, 369, 441
- Govoni F., & Feretti L., 2004, *Journal of Mod. Phys.*, Vol. 13, Issue 8, p. 1549
- Govoni F., Markevitch M., Vikhlinin A., VanSpeybroeck L., Feretti L., Giovannini G., 2004, *ApJ*, 605, 695
- Govoni F., Murgia M., Feretti L., Giovannini G., Dallacasa D., Taylor G.B., 2005, *A&A*, 430, 5
- Inogamov N.A. & Sunyaev R.A., 2003, *Astron. Lett.* 29, 791
- Hambly N.C., MacGillivray H.T., Read M.A., et al., 2001, *MNRAS*, 326, 1279
- Haines, C.P., Mercurio, A., Merluzzi, P., La Barbera F., Massarotti M., Busarello G., Girardi M, 2004, *A&A*, 425, 783
- Henry J.P., & Briel U.G., 1995, *ApJ*, 443, L9

- Henry J.P., & Briel U.G., 1996, *ApJ*, 472, 137
- Henry J.P., Finoguenov A., & Briel U.G., 2004, *ApJ*, 615, 181
- Herbig T. & Birkinshaw M., 1994, *BAAS*, 26, 1403
- Hwang C–Y, 2004, *JKAS*, 37, 461
- Jaffe W.J., 1977, *ApJ*, 212, 1
- Jee M.J., White R.L., Ford H.C., Blakeslee J.P., Illingworth G.D., Coe D.A., Tran K.–V.H., 2005, *ApJ*, 634, 813
- Jeltema T.E., Canizares C.R., Bautz M.W., Malm M.R., Donahue M., Garmire G.P., 2001, *ApJ*, 562, 124
- Johnston–Hollitt M., Ekers R.D. & Hunstead R.W., 2001, *ASPC*, 250, 432
- Jones C. & Forman W., 1999, *ApJ*, 511, 65
- Kaiser C.R., Schoenmakers A.P., & Röttgering H.J.A., 2000, *MNRAS*, 315, 381
- Katz N. & White S.D.M., 1993, *ApJ*, 412, 455
- Kellogg E., Gursky H., Tananbaum H., Giacconi R., Pounds K., 1972, *ApJ*, 174, 65
- Kempner J.C., & Sarazin C.L., 2001, *ApJ*, 548, 639 (KS01)
- Kempner J.C., & David L.P., 2004, *MNRAS*, 349, 385
- Kim K.T., Kronberg P.P., Dewdney P.E., Landecker T.L., 1990, *ApJ*, 355, 29
- Komissarov S.S. & Gubanov A.G., 1994, *A&A*, 285, 27
- Krivonos R.A., Vikhlinin A., Markevitch M., Pavlinsky M.N., 2003, *Astronomy Letters*, 29, 425
- Kull A. & Böhringer H., 1999, *A&A*, 341, 23
- Kuo P–H., Hwang C–Y., Ip W–H., 2003, *ApJ*, 594, 732
- Liang H., Hunstead R.W., Birkinshaw M., Andreani P., 2000, *ApJ*, 544, 686
- Locken C., Roettiger K., Burns J.O., Norman M., 1995, *ApJ*, 445, 80
- Maddox S.J., Efstathiou G., Sutherland W.J., Loveday J., 1990, *MNRAS*, 243, 692
- Markevitch M., Sarazin C.L., & Irwin J.A, 1996, *ApJ*, 472, L17
- Markevitch M., Forman W.R., Sarazin C.L., Vikhlinin A., 1998, *ApJ*, 503, 77
- Markevitch M., Sarazin C.L., & Vikhlinin A., 1999, *ApJ*, 521, 526
- Markevitch M., Ponman T.J., Nulsen P.E.J., Bautz M.W., Burke D.J. et al., 2000, *ApJ*, 541, 542
- Markevitch M., & Vikhlinin A., 2001, *ApJ*, 563, 95

- Markevitch M., Gonzalez A. H., David L., Vikhlinin A., Murray S., Forman W., Jones C., Tucker W., 2002, *ApJ*, 567, 27
- Markevitch M., Vikhlinin A., & Forman W.R., 2003, in *Matter and Energy in Clusters of Galaxies*, Taiwan, ASP Conf. Series, eds. S.Bowyer & C.Y.Hwang, 301, 37 (astro-ph/0208208)
- Markevitch M., Govoni F., Brunetti G., Jerius D., 2005, *ApJ*, 627, 733
- Markevitch M., 2006, in *The X-ray Universe 2005*, El Escorial, Spain (astro-ph/0511345)
- Markevitch M., & Vikhlinin A., 2007, *Physics Reports*, in press (astro-ph/0701821)
- Marty P.B., Kneib J.P., Sadat R., Bardeau S., Czoske O., Ebeling H., Smail I., 2003, in *New X-ray Results from Clusters of Galaxies and Black Holes*, eds. C. Done, E.M. Puchnarewicz, M.J. Ward, in Proc. of 34th COSPAR Scientific Assembly (astro-ph/0309054)
- Maurogordato S., Proust D., Beers T.C., Arnaud M., Pelló R., Cappi A., Slezak E., Kriessler J.R., 2000, *A&A*, 355 848 (MPB00)
- Mathews T., Morgan W., & Schmidt M., 1964, *ApJ*, 140, 35
- Matsumoto H., Pierre M., Tsuru T.G., Davis D.S., 2001, *A&A*, 374, 28
- Mazzotta P., Fusco-Femiano R. & Vikhlinin A., 2002, *ApJ*, 569, 31
- Mercurio, A., Girardi, M., Boschini, W., Merluzzi P., Busarello G., 2003, *A&A*, 397, 431 (MGB03)
- Mercurio, A., PhD thesis, 2004, University of Trieste, astro-ph/0412077 (M04)
- Mercurio A., Busarello, G., Merluzzi, P., La Barbera F., Girardi M., Haines C.P., 2004b, *A&A*, 424, 79 (MBM04)
- Metzger M.R., & Ma C.P., 2000, *AJ*, 120, 2879
- Miniati F., Ryu D., Kang H., Jones T.W., Cen R., Ostriker J.P., 2000, *ApJ*, 542, 608
- Miniati F., Jones T.W., Kang H., Ryu D., 2001, *ApJ*, 562, 233
- Mitchell R.J., Culhane J.L., Davison P.J.N., Ives J.C., 1976, *MNRAS*, 175, 29
- Molendi S., 2004, in *Plasmas in the laboratory and in the Universe: New Insights and New Challenges*, AIP Conf. Proceedings, 703, 345
- Mohr J.J., Mathiesen B., & Evrard A.E., 1999, *ApJ*, 517, 627
- Murgia M., 2001, Ph.D Thesis, University of Bologna

- Oegerle W.R., & Hill J.M., 2001, ApJ, 122, 2858
- Ohno H., Takizawa M., & Shibata S., 2002, ApJ, 577, 658
- Okabe N. & Umetsu K., 2007, PASJ, submitted (astro-ph/0702649)
- Orrú M., Feretti L., Govoni F., Murgia M., Giovannini G., Brunetti G., Setti G., 2006, AN, 327, 565
- Orrú M., Murgia M., Feretti L., Govoni F., Brunetti G., Giovannini G., Girardi M., Setti G., 2007, A&A, in press, astro-ph/0701776
- Ota N., & Mitsuda K., 2004, A&A, 428, 757
- Pacholczyk A.G., *Radio Astrophysics*, 1970, Freeman Eds.
- Parma P., Murgia, M., de Ruiter, H. R., Fanti, R., 2002, NewAR 46, 313
- Paulin-Henriksson S., Antonuccio-Delogu V., Haines C.P., Radovich M., Mercurio A., Becciani U, 2007, A&A, in press (astro-ph/0701799)
- Petrosian V., 2001, ApJ, 557, 560
- Pisani A., 1996, MNRAS, 278, 697
- Pfrommer C., Springel V., Enßlin T.A., Jubelgas M., 2006, MNRAS, 367, 113
- Pfrommer C. & Enßlin T.A., 2004, MNRAS, 352, 76
- Press W.H. & Schechter P., 1974, ApJ, 187, 425
- Randall S.W., Sarazin C.L., & Ricker P.M., 2002, ApJ, 577, 579
- Reid A.D., Hunstead R.W., Lemonon L. et al., 1999, MNRAS, 302, 571
- Reimer A., Reimer O., Schlickeiser R., Iyudin A., 2004, A&A, 424, 773
- Reiprich, T.H., & Böhringer, H., 2002, ApJ, 567, 716
- Rengelink R.B., Tang Y., de Bruyn A.G., Miley G.K., Bremer M.N., Röttgering H.J.A., Bremer M.A.R., 1997, A&AS, 124, 259
- Rephaeli Y., Gruber D.E., & Blanco P., 1999, ApJ, 511, L21
- Rephaeli Y., & Gruber D.E., 2002, ApJ, 579, 587
- Rephaeli Y., & Gruber D.E., 2003, ApJ, 595, 137
- Ricker P.M., & Sarazin C.L., 2001, ApJ, 561, 621
- Rizza, E., Burns, J.O, Ledlow, M.J, Owen F.N., Voges W., Bliton M., 1998, MNRAS, 301, 328
- Roettiger K., Loken C. & Burns J.O., 1997, ApJS, 109, 307
- Roettiger K., Burns J.O. & Stone, J.M., 1999, ApJ, 518, 603
- Roettiger K., Stone J.M & Burns J.O., 1999, ApJ, 518, 594
- Roland J., 1981, A&A, 93, 407

- Rottgering H.J.A., Wieringa M.H., Hunstead R.W., Ekers R.D., 1997, MNRAS, 290, 577
- Rossetti M., & Molendi S., 2004, A&A, 414, 41
- Rossetti M., Ghizzardi S., Molendi S., Finoguenov A., 2006, A&A in press (astro-ph/0611056)
- Ryu D., Kang H., Hallman E., Jones T.W., 2003, ApJ, 593, 599
- Sarazin C.L., 1999, ApJ, 520, 529
- Sarazin C.L., in *Merging Processes in Clusters of Galaxies*, eds. L. Feretti, I.M. Gioia & G. Giovannini, Kluwer Academic Publishers, 2002, Vol. 272, p. 1
- Schindler S. & Müller E., 1993, A&A, 272, 137
- Schlickeiser R., Sievers A. & Thiemann H., 1987, A&A, 182, 21
- Schuecker P., Böhringer H., Reiprich T.H., Feretti L., 2001, A&A, 378, 408
- Schuecker P., Finoguenov A., Miniati F., Böhringer H., Briel U.G., 2004, A&A, 426, 387
- Serlemitsos P.J., Smith B.W., Boldt E.A., Holt S.S., Swank J.H., 1977, ApJ, 211, L63
- Sijbring D., 1993, *A Radio Continuum and HI Line Study of the Perseus Cluster*, PhD Thesis, Groningen
- Smith G.P., Edge A.C., Eke V.R., Nichol R.C., Smail I., Kneib J.P., 2003, ApJ, 590, L79
- Stoke J.T., Perlman E.S., Gioia I.M., Harvanek M., 1999, AJ, 117
- Struble M., & Rood H., 1991, ApJS, 77, 363
- Sunyaev R.A., Norman M.L., & Brian G.L., 2003, Astronomy Letters, 29, 783
- Takizawa M., 2005, ApJ, 629, 791
- Thierbach M., Klein U., Wielebinski, R., 2003, A&A, 397, 53
- Tribble P.C., 1993, MNRAS, 263, 31
- Valtchanov I., Murphy T., Pierre M., Hunstead R., Lémonon L., 2002, A&A 392, 795 (VMP02)
- Vazza F., Tormen G., Cassano R., Brunetti G., Dolag K., 2006, MNRAS, 369, 14
- Venturi T., Bardelli S., Morganti R., Hunstead R.W., 2000, MNRAS, 314, 594 (VBM00)
- Venturi T., Bardelli S., Dallacasa D., Brunetti G., Giacintucci S., Hunstead R.W., Morganti R., 2003, A&A, 402, 913 (VBD03)

- Venturi T., Giacintucci S., Brunetti G., Cassano R., Bardelli S., Dallacasa D., Setti G., 2007, *A&A*, 463, 937
- Vikhlinin A., Forman W., & Jones C., 1997, *ApJ*, 474, L7
- Vikhlinin A., McNamara B.R., Forman W., Jones C., Quintana H., Hornstrup A., 1998, *ApJ*, 502, 558
- Vikhlinin A., Markevitch M., & Murray S.S., 2001, *ApJ*, 551, 160
- Vikhlinin A., Markevitch M., Murray S.S., Jones C., Forman W., Van Speybroeck L., 2005, *ApJ*, 628, 655
- Vikhlinin A., Kravtsov A., Forman W., Jones C., Markevitch M., Murray S.S., VanSpeybroeck L., 2006, *ApJ*, 640, 691
- White S.D.M., Briel U.G., & Henry J.P., 1993, *MNRAS*, 261, L8
- Willson M., 1970, *MNRAS*, 151, 1
- Yan H., & Lazarian A., 2004, *ApJ*, 614, 757
- Zucca E., Zamorani G., Scaramella R., Vettolani G., 1993, *ApJ*, 407, 470
- Zwicky F., 1973, *ApJ*, 86, 217